

# EXPERIMENTAL INVESTIGATION OF THE FREE-END PRESSURE DISTRIBUTION FOR SURFACE-MOUNTED FINITE-HEIGHT SQUARE PRISMS

A Thesis Submitted to the  
College of Graduate and Postdoctoral Studies  
in Partial Fulfillment of the Requirements  
for the degree of Master of Science  
in the Department of Mechanical Engineering  
University of Saskatchewan  
Saskatoon

By  
Herman GY Heng

©Herman GY Heng, Nov/2019. All rights reserved.

# PERMISSION TO USE

In presenting this thesis in partial fulfilment of the requirements for a Postgraduate degree from the University of Saskatchewan, I agree that the Libraries of this University may make it freely available for inspection. I further agree that permission for copying of this thesis in any manner, in whole or in part, for scholarly purposes may be granted by the professor or professors who supervised my thesis work or, in their absence, by the Head of the Department or the Dean of the College in which my thesis work was done. It is understood that any copying or publication or use of this thesis or parts thereof for financial gain shall not be allowed without my written permission. It is also understood that due recognition shall be given to me and to the University of Saskatchewan in any scholarly use which may be made of any material in my thesis.

Requests for permission to copy or to make other use of material in this thesis in whole or part should be addressed to:

Head of the Department of Mechanical Engineering  
College of Engineering  
University of Saskatchewan  
57 Campus Drive  
Saskatoon, Saskatchewan S7N 5A9  
Canada

or

Dean of the College of Graduate and Postdoctoral Studies  
116 Thorvaldson Building  
University of Saskatchewan  
110 Science Place  
Saskatoon, Saskatchewan S7N 5C9  
Canada

# ABSTRACT

An experimental investigation was performed to study the mean free-end surface pressure distribution for surface-mounted finite-height square prisms. The prism aspect ratio (AR) was varied from 1 to 11, with a small increment of 0.5. For each aspect ratio, the effect of incidence angle ( $\alpha$ ) on the mean pressure distribution was investigated from  $0^\circ$  to  $45^\circ$ , with a small increment of  $1^\circ$ . Integration of the free-end pressure distribution was performed to determine the normal force coefficient due to pressure ( $C_{N,p}$ ). Measurements were also performed for the mean drag and lift force coefficients ( $C_D$  and  $C_L$ ) and Strouhal number (St) from  $\alpha = 0^\circ$  to  $45^\circ$ , and vortex formation length at mid-span and at  $\alpha = 0^\circ$ . The freestream velocity ( $U_\infty$ ) used was 22.5 m/s (equivalent to a Reynolds number of  $Re = 6.5 \times 10^4$ ) for all the measurements, except for the measurement of forces, where  $U_\infty = 40.0$  m/s (equivalent to a Reynolds number of  $Re = 1.1 \times 10^5$ ) was used. The boundary layer thickness developed on the ground plane (relative to the width of the prism) ( $\delta/D$ ) varied from 0.8 to 2.6 for five different cases.

The results demonstrated that the most complex pressure distributions, based on the range of pressures encountered and the severity of the pressure gradients, tend to occur at the highest incidence angles, and were most pronounced for the lowest and highest aspect ratios tested, which suggests the existence of three distinct flow regimes based on the pressure distribution. The effect of the boundary layer on the pressure distribution varies at different incidence angles, with the most appreciable impact is observed at  $\alpha = 0^\circ$  and  $45^\circ$ . There are seven different critical incidence angles determined in the present study, based on the minimum  $C_D$ , maximum  $C_D$ , maximum magnitude of  $C_L$ , positive  $C_L$ , primary and secondary peaks of  $C_{N,p}$ , and maximum St. Based on the results of  $C_D$  and St, there are only two flow regimes identified (instead of three regimes as based on the pressure distribution). The first flow regime is where the boundary layer effect dominates the flow, and results in high sensitivity of  $C_D$ ,  $C_L$  to AR, but no well-defined peak is identified in the power spectra. The second flow regime shows the forces and dominant vortex shedding frequency are insensitive to the aspect ratio. The vortex formation length at mid-span was found to be maximum when  $AR = 9$  for  $\delta/D = 0.8$ .

# ACKNOWLEDGEMENTS

First and foremost, I would like to express my greatest gratitude to my research supervisor, Prof. David Sumner, for your consistent and professional support given to me throughout my M.Sc. program. Your advice, encouragement, enthusiasm, and financial support are greatly appreciated. You have contributed tremendously to the successful completion of my program, and it is undoubtedly a rewarding experience working with you.

My appreciation also goes to Mr. Shawn Reinink, the Departmental Assistant of Thermofluids, for your technical guidance in the experimental setup, as well as in the LabVIEW and MATLAB programming. The research was completed ahead of schedule on account of your prompt response in resolving all the technical issues. The additional technical assistance received from Mr. Rob Peace (Departmental Assistant of Applied Mechanics), Mr. Blair Cole (Engineering Shops Manager), and Mr. Daniel Vessey (Instrument Maker of Engineering Shops) in manufacturing and modification of the test models is also recognized.

I would also like to thank my advisory committee, Prof. James Bugg and Prof. Kerry Mazurek for giving their precious comments and opinions to improve the quality of my work. In addition, the administrative support given by the Graduate Student Commons Office and relevant staffs in the Department of Mechanical Engineering is also appreciated. A similar appreciation is also given to some university resources that have contributed to my program, such as University Library (mainly on organizing graduate writing workshops), Student Wellness Center, and Gwenna Moss Centre for Teaching and Learning.

I also acknowledge Mr. Hayden Reitenbach who has given a great amount of peer support, both technically and spiritually. There is also a lot of non-academic support received from various friends, classmates, and elders. Although this support is non-academic related, these invaluable friendships have greatly improved my mental health and have helped me to succeed in the research indirectly.

Last but not least, a big thank you shall go to the Department of Mechanical Engineering and the Natural Sciences and Engineering Research Council of Canada (NSERC) for providing the financial support (via the Devolved Scholarship Program) in this project.

# DEDICATION

This thesis is dedicated to those vulnerable people who undergo a great amount of struggle and difficulty in their journey of education. I am blessed to be given an opportunity to receive an education at the postgraduate level, and to obtain a life-long precious experience from my M.Sc. program. However, it is also acknowledged that there is a significant amount of other unfortunate people in this world who are greatly in thirst of knowledge, but are not given an equal opportunity in receiving the education due to demographic factors, financial capability, or sometimes the lack of enthusiasm of educators. By dedicating this thesis to those vulnerable people, I am committed to (should any opportunity arise) supporting the work of education in a realistic and achievable manner. I strongly believe in the power of education in changing one's life (and so the community and society). Thus, it is my vision that education is treated as a human right, instead of as a privilege, and that the opportunity of basic education should be granted to everyone regardless of ethnicity, nationality, gender, gender identity, sexual orientation, religion, age, disability, or socioeconomic status.

# CONTENTS

PERMISSION TO USE	i
ABSTRACT	ii
ACKNOWLEDGEMENTS	iii
DEDICATION	iv
CONTENTS	v
LIST OF TABLES	viii
LIST OF FIGURES	x
NOMENCLATURE	xxii
<b>1 INTRODUCTION</b>	<b>1</b>
1.1 Background . . . . .	1
1.2 Motivation . . . . .	5
1.3 Objectives . . . . .	6
1.4 Scope . . . . .	7
1.5 Thesis outline . . . . .	11
<b>2 LITERATURE REVIEW</b>	<b>12</b>
2.1 Introduction . . . . .	12
2.2 The flow around an infinite square prism . . . . .	12
2.3 The flow around a finite-height square prism . . . . .	17
2.3.1 Flow structure at $\alpha = 0^\circ$ . . . . .	18
2.3.2 The effect of aspect ratio . . . . .	22
2.3.3 The effect of incidence angle . . . . .	24
2.4 The flow near to free-end surface . . . . .	27
2.4.1 Flow field above the free end . . . . .	27

2.4.2	Surface pressure at the free end . . . . .	32
2.5	Aerodynamic forces . . . . .	39
2.5.1	Drag force coefficient . . . . .	40
2.5.2	Lift force coefficient . . . . .	44
2.6	Strouhal number . . . . .	46
2.7	Vortex formation length . . . . .	54
2.8	Summary and identified gaps in the literature . . . . .	58
<b>3</b>	<b>METHODOLOGY AND EXPERIMENTAL SETUP</b>	<b>64</b>
3.1	Introduction . . . . .	64
3.2	Wind tunnel . . . . .	64
3.3	Freestream conditions and Pitot-static probe . . . . .	65
3.4	Boundary layer characteristics . . . . .	67
3.5	Square prism models . . . . .	72
3.6	Measurement of $C_P$ by ZOC17 pressure scanner . . . . .	75
3.7	Measurement of $C_D$ , $C_L$ , and $C_N$ by force balance . . . . .	78
3.8	Measurement of $\delta$ , $St$ and $L_f$ by hotwire probe . . . . .	82
3.9	Measurement uncertainty . . . . .	84
<b>4</b>	<b>RESULTS AND DISCUSSION</b>	<b>88</b>
4.1	Mean free-end surface pressure distribution . . . . .	88
4.1.1	The effect of incidence angle . . . . .	89
4.1.2	The effect of aspect ratio . . . . .	96
4.1.3	The effect of boundary layer thickness . . . . .	105
4.2	Comparison of $C_P$ distribution between cylinder and square prism . . . . .	113
4.3	Aerodynamic forces . . . . .	121
4.3.1	Drag force coefficient . . . . .	121
4.3.2	Lift force coefficient . . . . .	128
4.3.3	Normal force coefficient . . . . .	132
4.3.4	Point of action . . . . .	137
4.4	Strouhal number . . . . .	141

4.5	Vortex formation length . . . . .	150
<b>5</b>	<b>CONCLUSIONS, CONTRIBUTIONS, AND RECOMMENDATIONS</b>	<b>154</b>
5.1	Conclusions . . . . .	154
5.2	Contributions of the present work . . . . .	158
5.3	Recommendations for future work . . . . .	160
	<b>REFERENCES</b>	<b>162</b>
	<b>APPENDIX A MEAN FREE-END <math>C_P</math> DISTRIBUTION</b>	<b>166</b>
	<b>APPENDIX B CENTERLINE <math>C_P</math> PROFILES</b>	<b>202</b>
	<b>APPENDIX C COMPARISON OF THE <math>C_P</math> PROFILES FOR THE CYLINDER AND SQUARE PRISM</b>	<b>210</b>
	<b>APPENDIX D PERMISSION AGREEMENTS</b>	<b>218</b>

# LIST OF TABLES

1.1	Manipulated, fixed and measured variables in the experiment . . . . .	10
2.1	Different flow regimes for an infinite-height square prism at $\alpha = 0^\circ$ to $45^\circ$ , identified by Igarashi (1984), Huang et al. (2010), and Yen and Yang (2011).	16
2.2	Summary of various experimental investigations related to the surface pressure measurement at the free end of finite-height square prisms. . . . .	38
2.3	Summary of critical angles, $\alpha_c$ for different experimental investigations based on minimum $C_D$ . The values shown are estimated by visually inspecting the $C_D$ versus $\alpha$ curve in the studies listed below. . . . .	43
2.4	Summary of critical angles, $\alpha_c$ for different experimental investigations based on minimum $C_L$ . The values shown are estimated by visually inspecting the $C_L$ versus $\alpha$ curve in the studies listed below. . . . .	46
2.5	Summary of critical angles, $\alpha_c$ for different experimental investigations based on maximum $St$ . The values shown are estimated by visually inspecting the $St$ versus $\alpha$ curve in the studies listed below. . . . .	53
2.6	Summary of the vortex formation length at the mid-span location of the prism, at $\alpha = 0^\circ$ . The values shown are estimated based on visually inspecting on the $z/D$ (or $z/H$ ) versus $L_f/D$ ( $L_f/H$ ) curve in the studies listed below. . .	57
3.1	Characteristics of the undisturbed boundary layer developed from the ground plane (with the prism removed) for five different cases. . . . .	71
3.2	Maximum experimental uncertainties for the measured variables. . . . .	87
4.1	The ranges of AR for two characteristics and three regimes of the free-end mean $C_P$ distribution at four selected incidence angles: $\alpha = 0^\circ$ , $15^\circ$ , $30^\circ$ and $45^\circ$ . . . . .	103
4.2	The influence of the boundary layer on the cylinder, and square prism at $\alpha = 0^\circ$ and $45^\circ$ based on the centerline $C_P$ profiles along $x$ -axis and $y$ -axis. . . .	119

4.3	Summary of the critical aspect ratio based on the maximum vortex formation length at the mid-span location for cylinder and square prism at $\alpha = 0^\circ$ . . .	152
5.1	Summary of critical aspect ratios based on different observations in the present study and the study of Beitel et al. (2019). . . . .	157
A.1	Free-end mean pressure distribution (contour lines of constant $C_P$ ) at $\alpha = 0^\circ$ for AR = 1 to 11. The flow is from left to right. See page 173 for the scale. .	166
A.2	Free-end mean pressure distribution (contour lines of constant $C_P$ ) at $\alpha = 10^\circ$ for AR = 1 to 11. The flow is from left to right. See page 180 for the scale. .	174
A.3	Free-end mean pressure distribution (contour lines of constant $C_P$ ) at $\alpha = 15^\circ$ for AR = 1 to 11. The flow is from left to right. See page 187 for the scale. .	181
A.4	Free-end mean pressure distribution (contour lines of constant $C_P$ ) at $\alpha = 30^\circ$ for AR = 1 to 11. The flow is from left to right. See page 194 for the scale. .	188
A.5	Free-end mean pressure distribution (contour lines of constant $C_P$ ) at $\alpha = 45^\circ$ for AR = 1 to 11. The flow is from left to right. See page 201 for the scale. .	195
B.1	Centerline mean $C_P$ profiles (where $X =$ is a coordinate fixed to the prism free-end surface, and rotates with the prism) at (a) AR = 1, (b) AR = 1.5, (c) AR = 4.5, (d) AR = 7, (e) AR = 9, and (f) AR = 11 at selected $\alpha = 0^\circ$ , $15^\circ$ , $30^\circ$ and $45^\circ$ . . . . .	202
C.1	Comparison of $x$ -axis and $y$ -axis centerline $C_P$ profile between square prisms at $\alpha = 0^\circ$ (blue square) and $\alpha = 45^\circ$ (normalized with projected width, $D'$ ) (red diamond), and circular cylinder studied by Beitel (2017) (green circle), for AR = 1 to 11. $Re = 6.5 \times 10^4$ for both studies. Open symbol and dashed line represent the thin boundary layer ( $\delta/D = 0.8$ (present) and 0.6 (Beitel (2017))); solid symbol and solid line represent the thick boundary layer ( $\delta/D = 2.6$ (present) and 1.9 (Beitel (2017))). . . . .	210

# LIST OF FIGURES

1.1	Application of flow around a square prism in (a) high-rise building (b) automobile (c) offshore structure (d) bridges. Photos taken by the author. . . . .	3
1.2	Flow around a surface-mounted finite-height square prism - reproduced from Wang and Zhou (2009) with permission of Cambridge University Press. . . .	4
1.3	Schematic diagram of the experiment set-up. $H$ is the height of the prism, $D$ is the width of the prism, $U_\infty$ is the freestream velocity, $U(z)$ is the mean streamwise velocity profile of the boundary layer on the ground plane, $\delta$ is the boundary layer thickness, $\alpha$ is the incidence angle, $x$ , $y$ , and $z$ are the Cartesian coordinates with origin at the root of the prism (the prism-wall junction). . .	5
2.1	Geometry and symbols associated with the flow around an infinite-height square prism with the prism rotated in the clockwise direction. Note that $\alpha = 0^\circ$ corresponds to side A-D oriented normal to the approaching flow. . .	13
2.2	Four flow regimes for an infinite square prism identified by Igarashi (1984): (a) perfectly separated flow (symmetric), (b) perfectly separated flow (asymmetric), (c) reattached flow, and (d) wedge type flow - figure of D. Sumner; used with permission. . . . .	14
2.3	Three flow regimes for an infinite-height square prism and the distribution based on various $Re$ and $\alpha$ - reproduced from Yen and Yang (2011) with permission of Elsevier. The symbol $\theta$ is denoted by $\alpha$ in the present thesis. .	17
2.4	Different vortex structures associated with the flow around a finite-height square prism - figure of D. Sumner; used with permission. . . . .	18
2.5	Two types of flow structure proposed by Wang and Zhou (2009) and used with permission of Cambridge University Press: (a) symmetrically arranged two spanwise vortex roll (b) staggered arranged spanwise vortex. The coordinate system $(x, y, z)$ is the same as the present thesis as described in Section 1.1.	20

2.6	Different flow models proposed by (a) Bourgeois et al. (2011): alternating half-loop flow structure with principal core and streamwise connector strand, and (b) Rastan et al. (2017): hairpin vortex structure with top and isometric view, colored by streamwise vorticity. Used with permission of AIP Publishing.	21
2.7	The flow structure identified by Kindree et al. (2018) with three pairs of vortex cores, colored by streamwise vorticity, $\Omega_x$ , for a square prism with $AR = 3.91$ . $Re = 1.05 \times 10^4$ , $\delta/D = 0.21$ . The main vortex cores labeled with $D+$ and $D-$ indicate different directions of vorticity. The coordinate system $(x, y, z)$ is the same as the present thesis as described in Section 1.1. Used with permission of Springer Nature.	22
2.8	Mean streamwise vorticity contours in $y$ - $z$ planes at $x/D = 1, 3$ , and $5$ , for $AR = 3, 5$ and $7$ , at $Re = 9.3 \times 10^3$ and $\delta/D = 1.4$ - reproduced from Wang and Zhou (2009) with permission of Cambridge University Press. The symbols $x^*$ , $y^*$ and $z^*$ are denoted by $x/D$ , $y/D$ , and $z/D$ , respectively in the present thesis.	24
2.9	Mean streamwise vorticity contours in $y$ - $z$ planes at $x/D = 10$ ( $Re = 3.7 \times 10^4$ , $\delta/D = 1.5$ ) for $AR = 7$ : (a) $\alpha = 0^\circ$ , (b) $\alpha = 15^\circ$ , (c) $\alpha = 30^\circ$ , and (d) $\alpha = 45^\circ$ . Red contours indicate the vorticity in counter-clockwise direction; blue contours indicate the clockwise direction; green circle lines indicate the pairs of streamwise vortices - reproduced from Unnikrishnan et al. (2017) with permission of Elsevier.	26
2.10	Flow profile around a cube ( $AR = 1$ ) with separation and reattachment locations at the free end - reproduced from Nakamura et al. (2001) with permission of Elsevier.	28
2.11	Formation of conical vortices above the free-end surface for a finite-height square prism of $AR = 4$ at $\alpha = 10^\circ$ to $15^\circ$ - reproduced from Okuda and Taniike (1993) with permission of Elsevier.	29
2.12	Mean velocity and vorticity field above the free end of a finite-height square prism with $AR = 9$ , $Re = 4.2 \times 10^4$ , $\delta/D = 1.7$ , at (a) $\alpha = 0^\circ$ and (b) $\alpha = 45^\circ$ - reproduced from McClean and Sumner (2014) with permission of ASME.	30

2.13	Mean streamline profile above the free end for finite-height square prism of (a) $AR = 3$ , (b) $AR = 5$ , (c) $AR = 7$ , and (d) $AR = 9$ , with the foci of the mushroom vortex indicated in green circles and saddle points indicated in blue circles ( $Re = 4.2 \times 10^4$ , $\delta/D = 1.5$ ) - reproduced from Sumner et al. (2017) with permission of Elsevier. . . . .	31
2.14	Mean streamline profile above the free end for a square prism of $AR = 3$ at $\alpha = 0^\circ$ investigated by (a) Sumner et al. (2017) using PIV measurement ( $Re = 4.2 \times 10^4$ , $\delta/D = 1.5$ ) (b) Cao et al. (2019) using numerical simulation ( $Re = 5 \times 10^4$ , $\delta/D = 20$ ). The reverse flow is from right to left. Used with permission of Elsevier. . . . .	32
2.15	Mean streamline profile at the free end for square prism of $AR = 3$ at $\alpha = 15^\circ$ . Note that the direction of rotation is opposite to the clockwise direction denoted in Figure 2.1. The red lines denote the streamline direction. The notation "a.l" in blue denotes the attachment lines. The numbers 1, 2, 3, 0(4) indicate different corners of the prism, which are denoted by A, B, C, D, respectively, in Figure 2.1. The flow is from left to right - reproduced from Cao et al. (2019) with permission of Elsevier. . . . .	33
2.16	Mean $C_P$ contours around a cube ( $AR = 1$ ), $Re = 3.1 \times 10^4$ , $\delta/D = 1.5 - 1.83$ , for: (a) $\alpha = 0^\circ$ , and (b) $\alpha = 45^\circ$ - reproduced from Nakamura et al. (2001) and Nakamura et al. (2003) with permission of Elsevier. S in the right figure indicates a pair of separation lines. . . . .	34
2.17	$C_P$ centerline profile for front, top, and rear surfaces of a cube ( $AR = 1$ ) at $\alpha = 0^\circ$ , $Re = 4.6 \times 10^4$ , $\delta/D \gg 1$ - reproduced from Lee et al. (2016) with permission of Techno-Press. The numbers on the $x$ -axis denote different locations of the surfaces. 0 to 1 and 2 to 3 represents the front surface and rear surface, respectively, which are not the scopes of this thesis. The number 1 to 2 represents the top surface. The symbol $x/h$ on the $x$ -axis is denoted by $X/D$ in the present thesis. . . . .	35

2.18	$C_P$ centerline profile for front, top, and rear surfaces of a cube ( $AR = 1$ ) at various $\alpha$ , $Re = 4.6 \times 10^4$ , $\delta/D \gg 1$ - reproduced from Lim and Ohba (2015) with permission of Techno-Press. The numbers on the $x$ -axis denote different locations of the surfaces. 0 to 1 represents the front surface, while 2 to 3 represents the rear surface which are not the scope of this thesis. The number 1 to 2 represents the top surface. The symbol $x/h$ on the $x$ -axis is denoted by $X/D$ in the present thesis. . . . .	36
2.19	Mean free-end $C_P$ distribution for a square prism with $AR = 0.5$ at (a) $\alpha = 0^\circ$ , and (b) $\alpha = 45^\circ$ , and $C_P'$ contours for the same prism at (c) $\alpha = 0^\circ$ , and (d) $\alpha = 45^\circ$ , sampled in an atmospheric boundary layer condition. The black arrow indicates the flow direction - reproduced from Chen et al. (2018) with permission of Elsevier. . . . .	39
2.20	Mean drag force coefficient, $C_D$ versus $\alpha$ experimentally investigated by (a) McClean and Sumner (2014) ( $Re = 7.3 \times 10^4$ , $\delta/D = 1.5$ ) (used with permission of ASME) and (b) Sakamoto (1985) ( $Re = 3.3 \times 10^4$ , $\delta/H = 0.7$ ) (used with permission of Elsevier). The symbol $\phi$ and $h/w$ in the right diagram represent the incidence angle and aspect ratio, respectively, which are denoted by $\alpha$ and $AR$ in the present thesis. McClean and Sumner (2014) changed $AR$ by varying $H$ , while Sakamoto (1985) changed $AR$ by varying $D$ . . . . .	42
2.21	Mean lift force coefficient, $C_L$ versus $\alpha$ experimentally investigated by (a) McClean and Sumner (2014) ( $Re = 7.3 \times 10^4$ , $\delta/D = 1.5$ ) (used with permission of ASME) and (b) Sakamoto (1985) ( $Re = 3.3 \times 10^4$ , $\delta/H = 0.7$ ) (used with permission of Elsevier). The symbol $\phi$ and $h/w$ in the right diagram represent the incidence angle and aspect ratio, respectively, which are denoted by $\alpha$ and $AR$ in the present thesis. McClean and Sumner (2014) changed $AR$ by varying $H$ , while Sakamoto (1985) changed $AR$ by varying $D$ . . . . .	45

2.22	Power spectral density reproduced from Wang and Zhou (2009) at three streamwise location and four spanwise locations; used with permission of Cambridge University Press. The symbols $x^*$ and $z^*$ are denoted by $x/D$ and $z/D$ in the present thesis. The symbol of $f^*$ is the dimensionless frequency, which is the Strouhal number, St. The notation $E_u$ is the power spectral density, and the small letter $d$ is the width of the prism and same as the capital letter $D$ in the present thesis. . . . .	48
2.23	Power spectral density versus the St experimentally obtained by Porteous et al. (2017) for (a) waterfall diagram based on a wide range of aspect ratio ( $0.29 \leq AR \leq 22.9$ ), and (b) selected aspect ratios only. The symbols $L$ , $W$ , and $V_\infty$ in the diagram correspond to the symbols of $H$ , $D$ , and $U_\infty$ used in the present thesis. Used with permission of Cambridge University Press. . . . .	49
2.24	The variation of St with AR based on the peaks identified in different shedding regimes - reproduced from Porteous et al. (2017) with permission of Cambridge University Press. The symbols of R0, RI, RII and RIII denote different shedding regimes; the symbols P1, P2, P3 represent the different series of St based different peaks observed; the symbols $L$ , $W$ , and $V_\infty$ in the diagram correspond to the symbols of $H$ , $D$ , and $U_\infty$ used in the present thesis. . . . .	50
2.25	Strouhal number, St versus $\alpha$ experimentally investigated by (a) McClean and Sumner (2014) ( $Re = 7.3 \times 10^4$ , $\delta/D = 1.5$ ) (used with permission of ASME) and (b) Sakamoto (1985) ( $Re = 3.3 \times 10^4$ , $\delta/H = 0.7$ ) (used with permission of Elsevier). The symbol $\phi$ and $h/w$ in the right diagram represent the incidence angle and aspect ratio, respectively, which are denoted by $\alpha$ and AR in the present thesis. McClean and Sumner (2014) changed AR by varying $H$ , while Sakamoto (1985) changed AR by varying $D$ . . . . .	52

2.26	Vortex formation length (based on PIV measurement) at different spanwise locations experimentally investigated by (a) Wang and Zhou (2009) and (b) Sumner et al. (2017). The symbols $x^*$ and $z^*$ in the left figure represents the dimensionless distances, which are denoted by $x^*/D$ and $z/D$ in the present thesis; the symbol $d$ is the same as the notation $D$ in the present thesis, which represents the width of the prism. Used with permissions of Cambridge University Press and Elsevier. . . . .	56
3.1	Schematic diagram of the low-speed, closed-return wind tunnel facility at the University of Saskatchewan. . . . .	65
3.2	Normalized boundary layer profile for five different cases listed in Table 3.1. The closed symbols represent the velocity profile ( $u/U_\infty$ ), while the open symbols represent the turbulence intensity profile ( $u'/U_\infty$ ) denoted by abbreviation ‘TI’ on the $x$ -axis. For each case, the profiles are presented in three streamwise locations: $x/D = -5$ (red left triangle), 0 (black square), and $+5$ (green right triangle). . . . .	70
3.3	Square prism model of the experiment in (a) front view and (b) 3D view. The front view is shown in an exploded view, while the 3D view shows the full assembly. The mounting bracket (below the turntable) is not seen in the 3D view. . . . .	73
3.4	(a) Pressure tap distribution at the free end with detailed dimensions ( $D$ is the width of the prism). (b) Surface pressure distribution in each quadrants. Holes in orange represent the surface distribution for quadrant 1, blue for quadrant 2, red for quadrant 3, green for quadrant 4, and yellow for origin. . . . .	74
3.5	Pressure measurement system in the present experimental investigation. There are 8 yellow pressure lines connected to the pressure scanner 1, and 8 blue pressure lines connected to the pressure scanner 2. . . . .	75

3.6	The experimental steps in the pressure measurement based on the limitation of available input of the pressure scanners and the maximum allowable rotation of the force balance of $180^\circ$ . The abbreviation ‘Q’ indicates quadrant, and different lines of urethane flexible tubing are represented by the word ‘Tap’.	76
3.7	Schematic diagram of the full pressure measurement system in the present experimental investigation. The pictorial diagram of the instruments circled in the red dashed lines is provided in Figure 3.5.	78
3.8	Force balance (located underneath of the ground plane) which is used for the measurement of the aerodynamic forces.	79
3.9	Definition of the aerodynamic forces and moments associated with the flow around a surface-mounted finite-height square prism in the present study.	80
3.10	Calibration of the hotwire anemometer probe in the boundary layer measurement, where $E$ is on the $x$ -axis and $u$ is on the $y$ -axis in the curve fitting.	83
4.1	Free-end mean pressure distribution (contour lines of constant $C_P$ ) for a prism of $AR = 1$ (cube): (a) $\alpha = 0^\circ$ , (b) $\alpha = 10^\circ$ , (c) $\alpha = 15^\circ$ , (d) $\alpha = 20^\circ$ , (e) $\alpha = 30^\circ$ , and (f) $\alpha = 45^\circ$ . The flow is from left to right.	90
4.2	Free-end mean pressure distribution (contour lines of constant $C_P$ ) for a prism of $AR = 6$ : (a) $\alpha = 0^\circ$ , (b) $\alpha = 10^\circ$ , (c) $\alpha = 15^\circ$ , (d) $\alpha = 20^\circ$ , (e) $\alpha = 30^\circ$ , and (f) $\alpha = 45^\circ$ . The flow is from left to right.	92
4.3	Free-end mean pressure distribution (contour lines of constant $C_P$ ) for a prism of $AR = 11$ : (a) $\alpha = 0^\circ$ , (b) $\alpha = 10^\circ$ , (c) $\alpha = 15^\circ$ , (d) $\alpha = 20^\circ$ , (e) $\alpha = 30^\circ$ , and (f) $\alpha = 45^\circ$ . The flow is from left to right.	93
4.4	Centerline mean $C_P$ profiles (where $X$ is a coordinate fixed to the prism free-end surface, and rotates with the prism) at (a) $AR = 1$ , (b) $AR = 1.5$ , (c) $AR = 4.5$ , (d) $AR = 7$ , (e) $AR = 9$ , and (f) $AR = 11$ at selected $\alpha = 0^\circ$ , $15^\circ$ , $30^\circ$ and $45^\circ$ .	95
4.5	Free-end mean pressure distribution (contour lines of constant $C_P$ ) at $\alpha = 0^\circ$ : (a) $AR = 1$ , (b) $AR = 2$ , (c) $AR = 4.5$ , (d) $AR = 7$ , (e) $AR = 9$ , and (f) $AR = 11$ . The flow is from left to right.	97

4.6	Free-end mean pressure distribution (contour lines of constant $C_P$ ) at $\alpha = 15^\circ$ : (a) AR = 1, (b) AR = 1.5, (c) AR = 3, (d) AR = 8, (e) AR = 9.5, and (f) AR = 11. The flow is from left to right. . . . .	99
4.7	Free-end mean pressure distribution (contour lines of constant $C_P$ ) at $\alpha = 30^\circ$ : (a) AR = 1, (b) AR = 1.5, (c) AR = 4, (d) AR = 7, (e) AR = 9.5, and (f) AR = 11. The flow is from left to right. . . . .	100
4.8	Free-end mean pressure distribution (contour lines of constant $C_P$ ) at $\alpha = 45^\circ$ : (a) AR = 1, (b) AR = 2, (c) AR = 4.5, (d) AR = 7, (e) AR = 9, and (f) AR = 11. The flow is from left to right. . . . .	102
4.9	Centerline mean $C_P$ profiles (where $X$ is a coordinate fixed to the prism free-end surface, and rotates with the prism) at (a) $\alpha = 0^\circ$ , (b) $\alpha = 15^\circ$ , (c) $\alpha = 30^\circ$ , and (d) $\alpha = 45^\circ$ for AR = 1 to 11, with increment of 1. . . . .	104
4.10	Free-end mean pressure distribution (contour lines of constant $C_P$ ) at $\alpha = 0^\circ$ : (a) present study (AR = 1, $\delta/D = 0.8$ , $\text{Re} = 6.5 \times 10^4$ ), (b) present study (AR = 1, $\delta/D = 2.6$ , $\text{Re} = 6.5 \times 10^4$ ), (c) Nakamura et al. (2001) (AR = 1, $\delta/D = 1.5 - 1.83$ , $\text{Re} = 3.1 \times 10^4$ ), and (d) Chen et al. (2018) (AR = 0.5, $\delta/D > 1$ , $\text{Re} = 8.4 \times 10^4$ ). The flow is from left to right. The reproduced figures are used with permission of Elsevier. . . . .	106
4.11	Free-end mean pressure distribution (contour lines of constant $C_P$ ) at $\alpha = 0^\circ$ : (a)(b) AR = 1.5, (c)(d) AR = 4.5, (e)(f) AR = 10.5. $\delta/D = 0.8$ and 2.6 for the diagrams on the left and right, respectively. The flow is from left to right. . . . .	108
4.12	Free-end mean pressure distribution (contour lines of constant $C_P$ ) for AR = 2: (a)(b) $\alpha = 15^\circ$ , (c)(d) $\alpha = 25^\circ$ , and (e)(f) $\alpha = 35^\circ$ . $\delta/D = 0.8$ and 2.6 for the diagrams on the left and right, respectively. The flow is from left to right. . . . .	109
4.13	Free-end mean pressure distribution (contour lines of constant $C_P$ ) at $\alpha = 45^\circ$ : (a)(b) AR = 1, (c)(d) AR = 4, (e)(f) AR = 7. $\delta/D = 0.8$ and 2.6 for the diagrams on the left and right, respectively. The flow is from left to right. . . . .	111

- 4.14 Centerline mean  $C_P$  profiles (where  $X =$  is a coordinate fixed to the prism free-end surface, and rotates with the prism) for (a) present study ( $AR = 1$ ,  $\delta/D = 0.8$ ,  $Re = 6.5 \times 10^4$ ), (b) present study ( $AR = 1$ ,  $\delta/D = 2.6$ ,  $Re = 6.5 \times 10^4$ ), and (c) Lim and Ohba (2015) ( $AR = 1$ ,  $\delta/D \gg 1$ ,  $Re = 4.6 \times 10^4$ ) - used with permission of Techno-Press, refer to Figure 2.18 for the full caption. 112
- 4.15 Comparison of  $x$ -axis centerline  $C_P$  profile between square prisms in the present study at  $\alpha = 0^\circ$  (blue square) and  $\alpha = 45^\circ$  (normalized with projected width,  $D'$ ) (red diamond), and circular cylinder studied by Beitel (2017) (green circle): (a)  $AR = 1$ , (b)  $AR = 3$ , (c)  $AR = 5$ , (d)  $AR = 7$ , (e)  $AR = 9$ , and (f)  $AR = 11$ .  $Re = 6.5 \times 10^4$  for both studies. Open symbol and dashed line represent the thin boundary layer ( $\delta/D = 0.8$  (present) and  $0.6$  (Beitel (2017))), while solid symbol and solid line represent the thick boundary layer ( $\delta/D = 2.6$  (present) and  $1.9$  (Beitel (2017))). . . . . 116
- 4.16 Comparison of  $y$ -axis centerline  $C_P$  profile between square prisms in the present study at  $\alpha = 0^\circ$  (blue square) and  $\alpha = 45^\circ$  (normalized with projected width,  $D'$ ) (red diamond), and circular cylinder studied by Beitel (2017) (green circle): (a)  $AR = 1$ , (b)  $AR = 3$ , (c)  $AR = 5$ , (d)  $AR = 7$ , (e)  $AR = 9$ , and (f)  $AR = 11$ .  $Re = 6.5 \times 10^4$  for both studies. Open symbol and dashed line represent the thin boundary layer ( $\delta/D = 0.8$  (present) and  $0.6$  (Beitel (2017))), while solid symbol and solid line represent the thick boundary layer ( $\delta/D = 2.6$  (present) and  $1.9$  (Beitel (2017))). . . . . 120
- 4.17 Mean drag force coefficient,  $C_D$ , versus  $\alpha$  (colored by the magnitude of  $C_D$ ) for all the tested aspect ratios in two boundary layers conditions: (a)  $\delta/D = 0.8$  and (b)  $\delta/D = 2.0$  at  $Re = 1.1 \times 10^5$ . . . . . 122
- 4.18 Critical incidence angles,  $\alpha_c$  based on the minimum  $C_D$  and maximum  $C_D$  at the region of the plateau formation for all the tested aspect ratios in both cases of boundary layers ( $\delta/D = 0.8$  and  $2.0$ ) at  $Re = 1.1 \times 10^5$ . The results are also compared with previous studies of Sakamoto (1985) ( $\delta/H = 0.7$ ;  $Re = 3.3 \times 10^4$ ) and McClean and Sumner (2014) ( $\delta/D = 1.5$ ;  $Re = 7.3 \times 10^4$ ). 123

4.19	Mean drag force coefficient, $C_D$ , versus $\alpha$ for selected aspect ratios and both boundary layers ( $\delta/D = 0.8$ and $2.0$ ) at $\text{Re} = 1.1 \times 10^5$ . . . . .	125
4.20	Mean drag force coefficient, $C_D$ , at various $\alpha$ for all the tested aspect ratios in both cases of boundary layers ( $\delta/D = 0.8$ and $2.0$ ) at $\text{Re} = 1.1 \times 10^5$ . The results are also compared with previous studies of Sakamoto (1985) ( $\delta/H = 0.7$ ; $\text{Re} = 3.3 \times 10^4$ ) and McClean and Sumner (2014) ( $\delta/D = 1.5$ ; $\text{Re} = 7.3 \times 10^4$ ). . . . .	126
4.21	Free-end mean pressure distribution (contour lines of constant $C_P$ ) at $\alpha = 10^\circ$ : (a) $\text{AR} = 1$ , (b) $\text{AR} = 1.5$ , (c) $\text{AR} = 4.5$ , (d) $\text{AR} = 7.5$ , (e) $\text{AR} = 8.5$ , and (f) $\text{AR} = 11$ . The flow is from left to right. . . . .	127
4.22	Comparison of $C_D$ between cylinder (Beitel et al. (2019) - green circle), and square prisms at $\alpha = 0^\circ$ (blue square) and $\alpha = 45^\circ$ (red diamond) of $\text{AR} = 1$ to $11$ in two boundary layers conditions: $\delta/D = 0.8$ (present) and $0.6$ (Beitel et al. (2019)); $\delta/D = 2.0$ (present) and $1.9$ (Beitel et al. (2019)). $\text{Re} = 1.1 \times 10^5$ and $6.5 \times 10^4$ , for the present study and the study of Beitel et al. (2019), respectively. . . . .	128
4.23	Mean lift force coefficient, $C_L$ , versus $\alpha$ (colored by the magnitude of $C_L$ ) for all the tested aspect ratios in two boundary layers conditions: (a) $\delta/D = 0.8$ and (b) $\delta/D = 2.0$ . . . . .	129
4.24	Critical incidence angles, $\alpha_c$ based on the maximum magnitude of $C_L$ for all the tested aspect ratios in both cases of boundary layers ( $\delta/D = 0.8$ and $2.0$ ) at $\text{Re} = 1.1 \times 10^5$ . The results are also compared with previous studies of Sarode et al. (1981) ( $\delta/D = 20$ ; $\text{Re} = 2.2 \times 10^4$ ), Sakamoto (1985) ( $\delta/H = 0.7$ ; $\text{Re} = 3.3 \times 10^4$ ), and McClean and Sumner (2014) ( $\delta/D = 1.5$ ; $\text{Re} = 7.3 \times 10^4$ ). . . . .	130
4.25	Mean lift force coefficient, $C_L$ , versus $\alpha$ for selected aspect ratios and both boundary layers ( $\delta/D = 0.8$ and $2.0$ ) at $\text{Re} = 1.1 \times 10^5$ . . . . .	131
4.26	Mean normal suction force coefficient, $C_{N,p}$ , versus $\alpha$ (colored by the magnitude of $C_{N,p}$ ) for all the tested aspect ratios in two boundary layers conditions: (a) $\delta/D = 0.8$ and (b) $\delta/D = 2.6$ . . . . .	132

4.27	Critical incidence angles, $\alpha_c$ based on the maximum magnitudes of $C_{N,p}$ at two regions of the plateau formation. The black squares represent $\alpha_c$ based on the primary peak formation, while the blue circles represent $\alpha_c$ based the secondary peak. The data are presented for all the tested aspect ratios in both cases of boundary layers ( $\delta/D = 0.8$ (open symbol) and $2.6$ (solid symbol)) at $\text{Re} = 6.5 \times 10^4$ . . . . .	134
4.28	Mean normal suction force coefficient, $C_{N,p}$ , versus $\alpha$ for selected aspect ratios and both boundary layers ( $\delta/D = 0.8$ and $2.6$ ) at $\text{Re} = 6.5 \times 10^4$ . . . . .	135
4.29	Comparison between the mean normal suction force coefficient computed by integration ( $C_{N,p}$ - open symbol) and resultant normal force measured by force balance ( $C_N$ - solid symbol) for the cylinder (Beitel et al. (2019) - green circle), and square prisms at $\alpha = 0^\circ$ (blue square), and $\alpha = 45^\circ$ (red diamond) of $\text{AR} = 1$ to $11$ in two boundary layers conditions: (a) $\delta/D = 0.8$ (present) and $0.6$ (Beitel et al. (2019)) (b) $\delta/D = 2.0$ (present - force balance), $2.6$ (present - integration), and $1.9$ (Beitel et al. (2019)). $\text{Re} = 1.1 \times 10^5$ for the $C_N$ data of the prisms, and $\text{Re} = 6.5 \times 10^4$ for the remaining data. . . . .	137
4.30	Point of action of $C_{N,p}$ for selected aspect ratios: (a) $\text{AR} = 1$ , (b) $\text{AR} = 3$ , (c) $\text{AR} = 5$ , (d) $\text{AR} = 7$ , (e) $\text{AR} = 9$ , and (f) $\text{AR} = 11$ at $\alpha = 0^\circ$ to $45^\circ$ (represented by $z$ -axis) in both cases of boundary layer ( $\delta/D = 0.8$ (red sphere) and $2.6$ (green cube); $\text{Re} = 6.5 \times 10^4$ ). . . . .	139
4.31	Point of action of $C_{N,p}$ for selected incidence angles: (a) $\alpha = 0^\circ$ , (b) $\alpha = 10^\circ$ , (c) $\alpha = 15^\circ$ , (d) $\alpha = 20^\circ$ , (e) $\alpha = 30^\circ$ , and (f) $\alpha = 45^\circ$ for $\text{AR} = 1$ to $11$ (represented by $z$ -axis) in both cases of boundary layer ( $\delta/D = 0.8$ (red sphere) and $2.6$ (green cube); $\text{Re} = 1.1 \times 10^5$ ). . . . .	140
4.32	Strouhal number, $\text{St}$ , versus $\alpha$ (colored by the magnitude of $\text{St}$ ) for all the tested aspect ratios in two boundary layers conditions: (a) $\delta/D = 0.8$ and (b) $\delta/D = 2.2$ at $\text{Re} = 6.5 \times 10^4$ . . . . .	141

4.33	Critical incidence angles, $\alpha_c$ based on the maximum St for all the tested aspect ratios in both cases of boundary layers ( $\delta/D = 0.8$ and $2.2$ ) at $Re = 6.5 \times 10^4$ . The results are also compared with previous studies of Sakamoto (1985) ( $\delta/H = 0.7$ ; $Re = 3.3 \times 10^4$ ) and McClean and Sumner (2014) ( $\delta/D = 1.5$ ; $Re = 7.3 \times 10^4$ ). . . . .	142
4.34	Strouhal number, St, versus $\alpha$ for selected aspect ratios and both boundary layers: (a) $\delta/D = 0.8$ and (b) $\delta/D = 2.2$ at $Re = 6.5 \times 10^4$ . . . . .	143
4.35	Comparison of St between cylinder (Beitel et al. (2019) - green circle), and square prisms at $\alpha = 0^\circ$ (blue square) and $\alpha = 45^\circ$ (red diamond) of AR = 1 to 11 in two boundary layers conditions: $\delta/D = 0.8$ (present) and $0.6$ (Beitel et al. (2019)), and $\delta/D = 2.2$ (present) and $1.9$ (Beitel et al. (2019)). $Re = 6.5 \times 10^4$ for both studies. . . . .	145
4.36	Power spectra of the velocity fluctuations at the mid-span as a function of incidence angle for selected aspect ratios (AR = 1 to 11, with increment of 2): (a) $\delta/D = 0.8$ and (b) $\delta/D = 2.2$ at $Re = 6.5 \times 10^4$ . . . . .	148
4.37	Power spectra of the velocity fluctuations at the mid-span as a function of aspect ratio for selected incidence angles ( $\alpha = 0^\circ$ to $45^\circ$ , with increment of $15^\circ$ ): (a) $\delta/D = 0.8$ and (b) $\delta/D = 2.2$ at $Re = 6.5 \times 10^4$ . . . . .	149
4.38	Comparison of vortex formation length at the mid-span between cylinder (Beitel et al. (2019) - green circle) and square prisms at $\alpha = 0^\circ$ (blue square) of AR = 1 to 11 in two boundary layers conditions: $\delta/D = 0.8$ (both studies), and $\delta/D = 2.6$ (present) and $3.0$ (Beitel et al. (2019)). $Re = 6.5 \times 10^4$ for both studies. Open and solid symbols represent the thin and thick boundary layer, respectively. . . . .	151

# NOMENCLATURE

## English Symbols

$AR$	Aspect ratio, $H/D$
$C_D$	Mean drag force coefficient
$C_L$	Mean lift force coefficient
$C_N$	Mean normal force coefficient
$C_{N,p}$	Mean normal force coefficient due to suction pressure [N]
$C_P$	Mean surface pressure coefficient
$C_P'$	Fluctuation of the surface pressure coefficient
$D$	Width of square prism [mm]
$D'$	Projected width of square prism [mm]
$E$	Voltage output of hotwire [V]
$f$	Vortex shedding frequency [Hz]
$F_D$	Mean drag force [N]
$F_L$	Mean lift force [N]
$F_N$	Mean normal force [N]
$F_{N,p}$	Mean normal force due to suction pressure [N]
$H$	Height of square prism [mm]
$L_f$	Vortex formation length [mm]
$L_{f,max}$	Maximum vortex formation length [mm]
$M_P$	Pitching moment [Nm]
$M_R$	Rolling moment [Nm]
$M_Y$	Yawing moment [Nm]
$P$	Mean local static pressure [Pa]
$P_{rms}$	Root-mean-square local static pressure [Pa]
$P_0$	Stagnation pressure [Pa]
$P_\infty$	Freestream static pressure [Pa]
$q_\infty$	Freestream dynamic pressure [Pa]
$R$	Specific gas constant in ideal gas law [ $\text{Jkg}^{-1}\text{K}^{-1}$ ]

$Re$	Reynolds number based on prism width
$S$	Temperature constant in Sutherland's Law [K]
$St$	Strouhal number
$T_0$	Standard temperature in Sutherland's Law [K]
$T_\infty$	Freestream temperature [K]
$u$	Local streamwise velocity [m/s]
$u'$	Local streamwise velocity fluctuation [m/s]
$\langle u' \rangle^2$	Reynolds stress based on $u'$ [m <sup>2</sup> /s <sup>2</sup> ]
$\langle u' \rangle_{max}^2$	Maximum Reynolds stress based on $u'$ [m <sup>2</sup> /s <sup>2</sup> ]
$U_\infty$	Freestream velocity [m/s]
$U(z)$	Boundary layer mean velocity profile [m/s]
$X$	$x$ -coordinate fixed to the free-end surface [mm]
$Y$	$y$ -coordinate fixed to the free-end surface [mm]
$X_{ac}$	$x$ -coordinate of point of action on the free-end surface [mm]
$Y_{ac}$	$y$ -coordinate of point of action on the free-end surface [mm]
$x$	Streamwise coordinate [mm]
$y$	Transverse (cross-stream) coordinate [mm]
$z$	Spanwise (vertical) coordinate [mm]

## Greek Symbols

$\alpha$	Incidence angle [°]
$\alpha_c$	Critical incidence angle [°]
$\delta$	Ground plane boundary layer thickness [mm]
$\delta^*$	Ground plane boundary layer displacement thickness [mm]
$\epsilon()$	Uncertainty of individual parameter (specified in the bracket)
$\theta$	Ground plane boundary layer momentum thickness [mm]
$\mu_0$	Air dynamic viscosity at standard temperature [Pa·s]
$\mu_\infty$	Freestream dynamic viscosity [Pas]
$\rho_\infty$	Freestream density [kg/m <sup>3</sup> ]

**Word Abbreviation**

FS	Full Scale
LC	Load Cell
PIV	Particle Image Velocimetry
Q	Quadrant
U of S	University of Saskatchewan
TI	Turbulence Intensity
ZOC	Zero-Operate-Calibrate

# 1 INTRODUCTION

## 1.1 Background

The flow around a bluff body has become of interest to researchers and scientists mainly because of its wide application in many industries. A bluff body is an object with a non-streamlined shape profile which leads to significant flow separation from its surface. On account of the flow separation, a pronounced wake region is generated downstream of the bluff body. The wake generation is one of the reasons for aerodynamic forces and moments experienced by bluff-body structures. Additionally, the flow separation from different surfaces of the bluff body often results in the formation of a pair of shear layers. The interaction between the two separated shear layers leads to periodic alternate vortex shedding, which may result in flow-induced vibration. Both aerodynamic forces and vortex shedding are important features to be considered in engineering structural design in the context of safety. The characteristics of the flow separation, wake formation, aerodynamic forces, and vortex shedding frequency are greatly dependent on the shape of the bluff body.

The Department of Mechanical Engineering at the University of Saskatchewan (U of S) has more than 20 years of experience in conducting research to investigate the flow around various bluff-body shapes. The research group is particularly interested in two types of bluff-body shapes: the circular cylinder and square prism, which are the two most common shapes studied in fundamental bluff-body aerodynamics research. The flow around a bluff body in the shape of a circular cylinder is popular in many engineering applications, such as the design of pipelines, heat exchangers, and cooling towers. There have been several experimental investigations conducted by the bluff-body research group at the U of S to study the flow around a surface-mounted finite-height circular cylinder. Heseltine (2003) and Adaramola (2008) extensively studied the wake structure behind surface-mounted finite-height circular

cylinders of different aspect ratios. The results were mainly presented in the velocity and vorticity field contour plots, with some additional information about the effect of aspect ratio on the vortex shedding frequency and formation length. The investigation of Beitel (2017), on the other hand, focused more on the flow structure above the free end for surface-mounted finite-height cylinders, and the results were presented as free-end surface pressure distributions. Igbalajobi (2011) investigated the reduction in shedding frequency and aerodynamic forces by installing a splitter plate at the downstream centerline location of circular cylinders. The consideration of interference between structures was also studied by Reitenbach (2018), who provided information about the variation in aerodynamic forces and vortex shedding frequency around two surface-mounted finite-height cylinders arranged in tandem, side-by-side, and staggered positions. The aspect ratios used were 3, 5, 7, and 9 for all the studies above-mentioned, except for Beitel (2017) who used 22 different aspect ratios ranging from 0.5 to 11, with 0.5 increment.

The flow around a square prism is also evident in many engineering applications, which include but are not limited to the design of high rise buildings, bridges, offshore structures, and automobiles. Figure 1.1 provides some common structures in daily life which require the application of bluff-body aerodynamics with square prisms. However, in comparison to the flow around a circular cylinder, the flow around a square prism has not been as extensively studied. The bluff-body research group at the U of S has been attempting to fill this gap, and has completed some research related to the flow around surface-mounted finite-height square prisms. The thesis of Unnikrishnan (2016) explained the near wake structure of surface-mounted, finite-height square prisms, somewhat similar to the works of Heseltine (2003) and Adaramola (2008), but with different bluff-body shapes. Ogunremi (2014) also performed similar experiments as Igbalajobi (2011) in investigating the effect of using a splitter plate on the vortex shedding frequency and forces, but the work was performed for finite-height square prisms. Numerical simulation work was also carried out by Einian (2012) to study the wake structure for finite-height square prisms using large eddy simulation (LES). Rostamy (2012) provided more information about the flow field behind and above the free end for both surface-mounted finite-height circular cylinders and square prisms. The experiments were carried out by using particle image velocimetry (PIV). The work of Rostamy (2012)

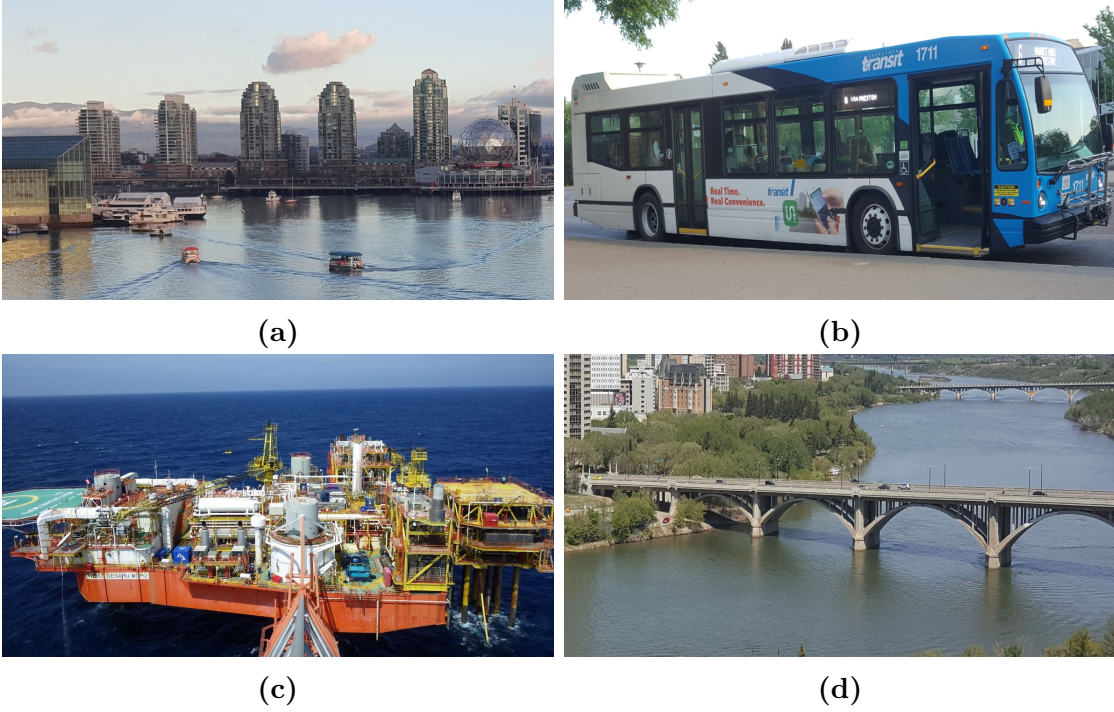


**Figure 1.1:** Application of flow around a square prism in (a) high-rise building (b) automobile (c) offshore structure (d) bridges. Photos taken by the author.

was further complemented by Chakravarty (2018) who performed numerical simulation to investigate the flow over finite-height circular cylinders and square prisms. Similar to the investigations for finite-height cylinders aforementioned, the aspect ratios used were 3, 5, 7, and 9 for all these studies. To date, the research group has yet to adopt a wide range of aspect ratios to investigate the flow around a surface-mounted finite-height prism. Hence, the present thesis intends to mirror the research of Beitel (2017), but performs the work for surface-mounted finite-height square prisms, with objectives and detailed scope outlined in Sections 1.3 and 1.4, respectively.

The flow structure around a finite-height square prism is rather more complicated than that around an “infinite” (two-dimensional) square prism. An infinite square prism indicates that the prism is sufficiently long so that the free-end and ground-plane effects are negligible over much of the span or height. The most significant feature of the flow around an infinite square prism is the Karman (spanwise) vortices which are formed due to the alternating rolling up behavior of the separated shear layers along the two sides of the prism. When a finite-height square prism is used, the effect of the free end is no longer trivial due to the

formation of tip vortices from the flow separation at the top surface of the prism. The ground plane effect is also significant on account of the formation of base vortices and horseshoe vortices. Wang and Zhou (2009) illustrated the formation of these vortices as shown in Figure 1.2. Therefore, the flow around a finite-height square prism is undoubtedly more complicated owing to the interaction between the Karman (spanwise) vortices, tip and base vortices, and horseshoe vortex on the ground plane.

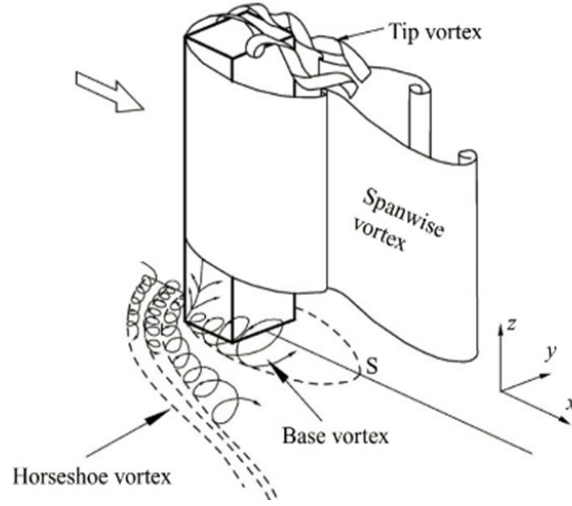


**Figure 1.2:** Flow around a surface-mounted finite-height square prism - reproduced from Wang and Zhou (2009) with permission of Cambridge University Press.

Due to this complexity, there is a relative lack of research on the flow around a finite-height square prism, in comparison to an infinite prism, although the flow around a finite-height prism is more practical in industrial applications. Thus, the proposed research presents an experimental investigation of the flow around surface-mounted finite-height square prisms, with the main focus to investigate the pressure distribution on the top surface (free end) of the square prism. The free-end pressure distribution of the square prism is expected to be strongly affected by several parameters: the aspect ratio of the square prism ( $AR = H/D$ , where  $H$  is the height of the prism and  $D$  is the width of the prism), incidence angle ( $\alpha$ ), and the boundary layer thickness developed on the ground plane ( $\delta/D$ ). The present study investigates the effect of these parameters on the free-end pressure distribution. The schematic diagram of the experiment set-up and the coordinate system used are shown in Figure 1.3.

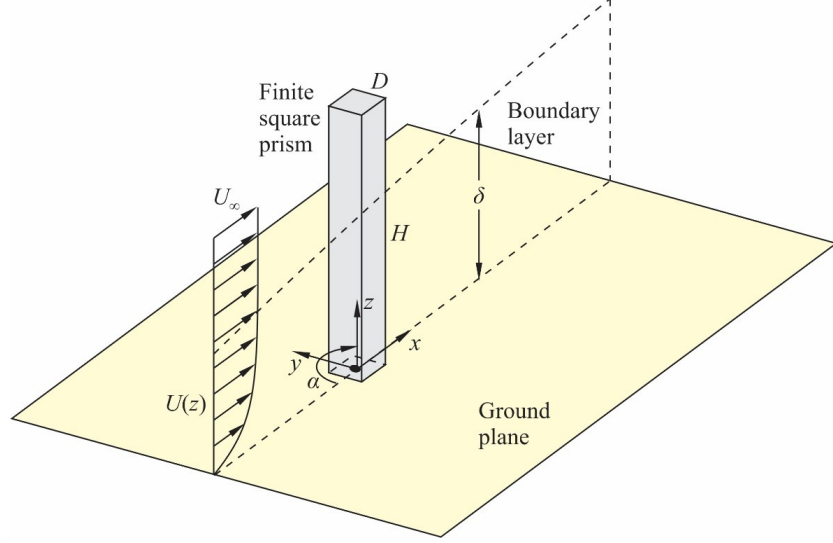


**Figure 1.3:** Schematic diagram of the experiment set-up.  $H$  is the height of the prism,  $D$  is the width of the prism,  $U_\infty$  is the freestream velocity,  $U(z)$  is the mean streamwise velocity profile of the boundary layer on the ground plane,  $\delta$  is the boundary layer thickness,  $\alpha$  is the incidence angle,  $x$ ,  $y$ , and  $z$  are the Cartesian coordinates with origin at the root of the prism (the prism-wall junction).

## 1.2 Motivation

The thesis is focused on surface-mounted finite-height square prisms with many practical applications, particularly in buildings and offshore structures. The pressure field of a square prism bluff body is important for determining the wind loading and regions of disturbed flow. For buildings in particular, information on the rooftop pressure distribution and regions of disturbed flow are needed to properly locate heating and air conditioning units, intake and exhaust ducts, rooftop solar panels, small wind turbines, and other equipment and structures. The characteristics of the disturbed flow includes the region with significant flow separation. The flow separation results in low surrounding suction pressure which may increase the energy consumption of some equipment such as air compressors. The disturbed flow may also indicate regions with significant formation of vortices which may affect the energy efficiency of certain equipment such as wind turbines due to high turbulence intensity. Proper location of these devices, outside regions of disturbed flow and in a favorable pressure field, is needed to maximize performance, minimize energy costs, and reduce carbon emission. Energy usage optimization and saving can be achieved by locating various facilities at suitable positions

on the rooftop based on the desired operating surrounding pressure. The present research results may enable design engineers to better understand how the aspect ratio of the building, incidence angle of wind, and boundary layer condition, will influence the pressure distribution on a building. The investigation on the effect of aspect ratio is essential, considering buildings can be designed in a wide range of dimensions. Likewise, considering wind is coming from various directions, the effect of the incidence angle on the pressure distribution is worth investigating. The effect of the boundary layer thickness is also worth investigating to understand the influence of low-momentum fluid on the pressure distribution.

It should be noted that the present work is somewhat different from the conventional wind engineering experiment, where an atmospheric boundary layer is adopted in the investigation. The highlighted applications above are more relevant to the wind engineering experiment. However, it should be recognized that the present work serves as a fundamental study that answers some research questions related to the effect of aspect ratio, incidence angle, and boundary layer on the trend of the pressure distribution and aerodynamic forces.

### 1.3 Objectives

The objectives of this research were driven from the motivation outlined in Section 1.2, as well as several identified gaps in the literature, which will be discussed in Chapter 2. Although the main objective is focused on the free-end surface pressure distribution, some investigations on aerodynamic forces, vortex shedding frequency, and vortex formation length were also performed to complement the results of the pressure distribution. The specific objectives of the present experimental investigation are to study:

- The mean free-end surface pressure distribution, mean aerodynamic forces, and vortex shedding frequency of surface-mounted finite-height square prisms by varying:
  - ◊ the aspect ratio from  $AR = 1$  to 11, with an increment of 0.5;
  - ◊ the incidence angle from  $\alpha = 0^\circ$  to  $45^\circ$ , with an increment of  $1^\circ$ ; and
  - ◊ the boundary layer thickness,  $\delta/D$ , with and without a tripping fence installed on the ground plane upstream of the square prism.

- The vortex formation length of surface-mounted finite-height square prisms at mid-span and at  $\alpha = 0^\circ$  by varying:
  - ◊ the aspect ratio from  $AR = 1$  to 11, with an increment of 0.5; and
  - ◊ the boundary layer thickness,  $\delta/D$ , with and without a tripping fence installed on the ground plane upstream of the square prism.
- Any critical incidence angles and aspect ratios based on critical behavioural changes of the pressure distributions, aerodynamic forces, vortex shedding frequency, and vortex formation length investigated.
- Any relationship between the behavioural changes of those parameters aforementioned.

## 1.4 Scope

The main scope of this thesis is similar to the work of Beitel (2017), which is to investigate the flow above the free-end surface only, through measuring the mean free-end surface pressure distribution. The difference between the present thesis and the thesis of Beitel (2017) is the shape of the bluff body. The flow around a surface-mounted finite-height cylinder was investigated by Beitel (2017) while the present thesis research is focused on the free-end surface pressure for a surface-mounted finite-height square prism. The surface pressure is presented in dimensionless form as the pressure coefficient  $C_P$  as shown in Equation 1.1. In this equation,  $C_P$  is the local pressure coefficient,  $P$  is the local static pressure,  $P_\infty$  is the freestream static pressure,  $\rho_\infty$  is the freestream density, and  $U_\infty$  is the freestream velocity.

$$C_P = \frac{P - P_\infty}{\frac{1}{2}\rho_\infty U_\infty^2} \quad (1.1)$$

The output of  $C_P$  is presented in two different forms: contour plots showing lines of constant  $C_P$  on the free end and centerline  $C_P$  profiles. The  $C_P$  contour plots illustrate the full pressure distribution based on all the measurement points on the free-end surface, while the centerline  $C_P$  profiles only show the curve of  $C_P$  versus  $X$  location along the centerline of

the prism, where  $X$  is the coordinate fixed to the free-end surface based on the prism width. The centerline profiles along the  $x$ - and  $y$ -axis defined in Figure 1.3 are also presented at two incidence angles of  $\alpha = 0^\circ$  and  $\alpha = 45^\circ$ . Using the contour and profile plots, changes in the  $C_P$  distribution on the top surface of the square prisms were specifically investigated by several approaches as follows:

- comparing the change in the minimum  $C_P$  value with changes in AR,  $\alpha$  and  $\delta/D$ ;
- contrasting the change of the minimum  $C_P$  location with changes in of AR,  $\alpha$  and  $\delta/D$ ;
- evaluating the change of the  $C_P$  contour shapes with changes in AR,  $\alpha$  and  $\delta/D$ ; and
- identifying any critical regions, such as regions with significant pressure recovery behavior or high density of contour lines, with changes in AR,  $\alpha$ , and  $\delta/D$ .

This research also investigated the effect of AR,  $\alpha$ , and  $\delta/D$  on the mean aerodynamic forces, vortex shedding frequency, and vortex formation length. These parameters (except for the formation length) were also investigated by Beitel (2017) for the finite-height circular cylinder. The mean aerodynamic forces investigated were the mean drag force ( $F_D$ ) that is parallel to the flow and acts towards downstream, the mean lift force ( $F_L$ ) that acts sideways of the prism, and the mean normal force ( $F_N$ ) that acts perpendicularly upwards from the free-end surface. The forces are measured by a force balance. Similar to the pressure coefficient, the aerodynamic forces are presented in dimensionless form as shown in Equations 1.2 to 1.4. In these equations,  $C_D$  is the drag force coefficient,  $C_L$  is the lift force coefficient, and  $C_N$  is the normal force coefficient. Note that the reference area used in  $C_N$  is the free-end surface area ( $D^2$ ), and is different from the definition of  $C_D$  and  $C_L$ , where the frontal area ( $HD$ ) of the prism is used.

$$C_D = \frac{F_D}{\frac{1}{2}\rho_\infty H D U_\infty^2} \quad (1.2)$$

$$C_L = \frac{F_L}{\frac{1}{2}\rho_\infty H D U_\infty^2} \quad (1.3)$$

$$C_N = \frac{F_N}{\frac{1}{2}\rho_\infty D^2 U_\infty^2} \quad (1.4)$$

The vortex shedding frequency was measured by hotwire anemometry, and its dimensionless form is represented by the Strouhal number which is shown in Equation 1.5. In this equation,  $f$  is the vortex shedding frequency.

$$St = \frac{fD}{U_\infty} \quad (1.5)$$

The vortex formation length was also measured by hotwire anemometry, and was scaled with the prism width ( $L_f/D$ ). This research limits the vortex formation length measurements to  $\alpha = 0^\circ$  only. It is known that the vortex formation length varies with the spanwise location. As the instrument used for the vortex formation length was hotwire anemometry instead of particle image velocimetry (PIV), the formation length measurement was limited to the mid-span location only. The scope of the formation length measurements is somewhat similar to Unnikrishnan (2016), except that thesis contained more information about the formation length at other spanwise locations, and the formation length was measured by a seven-hole pressure probe. Conversely, the present thesis has more detailed information about the formation length for a wider range (by 7 times) of aspect ratio.

As mentioned in Section 1.1, three parameters, AR,  $\alpha$  and  $\delta/D$ , need to be changed to study the effect of these parameters on all the above-mentioned measured variables. The range of the aspect ratio is limited to AR = 1 to 11 with 0.5 increments (which corresponds to 21 square prism models in total), although testing more prisms with higher aspect ratio is more desirable with the possibility that more flow regimes can be identified (Porteous et al. (2017)). The range of the incidence angle is limited to  $\alpha = 0^\circ$  to  $45^\circ$ , which is the same as most of the literature. The increment of the incidence angle is  $1^\circ$ , which is relatively smaller in comparison to that in most of the literature. The effect of the boundary layer was investigated in two different cases. For the first case, the experiment was conducted without a boundary layer trip installed at the upstream of the flow. The boundary layer thickness in this case (at the location of the prism) was about  $\delta/D = 0.8$ . With a boundary layer trip

installed upstream of the flow, the incoming flow formed a thicker boundary layer, ranging from  $\delta/D = 2.0$  to  $2.6$ . The details of the boundary layer are discussed further in Section 3.4.

In short, there are three manipulated variables in this experiment, which are aspect ratio (AR), incidence angle ( $\alpha$ ), and boundary layer thickness ( $\delta/D$ ). Also, there are six measured variables, which include the pressure coefficient ( $C_P$ ) distribution, mean drag force coefficient ( $C_D$ ), mean lift force coefficient ( $C_L$ ), mean normal force coefficient ( $C_N$ ), Strouhal number (St), and vortex formation length ( $L_f$ ). This experimental investigation also limits the incoming wind speed by fixing the freestream velocity to  $U_\infty = 22.5$  m/s and  $40.0$  m/s. The latter value was selected in the measurement of aerodynamic forces, while the former value was used for rest of the measurements (discussed further in Section 3.4). These freestream velocities correspond to  $Re = 6.5 \times 10^4$  and  $1.1 \times 10^5$ , respectively. The width of the square prism was also fixed in this experiment to  $D = 48$  mm, and therefore the aspect ratio was varied by changing the height,  $H$ , of the prism. Table 1.1 summarizes all the manipulated, fixed, and measured variables, and the corresponding measurement devices in the present experimental investigation. The details of the measurement devices will be discussed in Chapter 3.

**Table 1.1:** Manipulated, fixed and measured variables in the experiment

	<b>Variable</b>	<b>Range</b>
Manipulated Variable	Aspect ratio, AR	1 - 11 (with 0.5 increment)
	Incidence angle, $\alpha$	$0^\circ$ to $45^\circ$ (with $1^\circ$ increment)
	Boundary layer thickness, $\delta/D$	0.8 and 2.0 - 2.6
Fixed Variable	Freestream velocity, $U_\infty$	22.5 and 40.0 m/s
	Diameter, $D$	48 mm
	<b>Variable</b>	<b>Measurement Devices</b>
Measured Variable	Pressure coefficient, $C_P$	Pressure transducer
	Drag force coefficient $C_D$	Force balance
	Lift force coefficient $C_L$	Force balance
	Normal force coefficient $C_N$	Force balance
	Strouhal number, St	Hotwire anemometry
	Vortex formation length, $L_f/D$	Hotwire anemometry

## 1.5 Thesis outline

The thesis consists of five main chapters. After introducing the motivation, objectives, and scope of the experimental investigation in this Chapter 1, a literature review is provided in Chapter 2 that presents a general review on the flow around an infinite square prism and a finite square prism, as well as specific reviews which specially focus on the free-end surface pressure distribution, aerodynamic forces, Strouhal number and formation length of the finite-height square prism. Chapter 2 also discusses some gaps in the literature that were identified, and the expected contributions from this research work. Chapter 3 focuses on the methodology which includes details related to the experimental set-up and the instrumentation used in this research work. The design of the pressure taps and measurement locations will also be discussed in Chapter 3. Chapter 4 presents the results and discussion of this experimental investigation. The results include the effect of aspect ratio, incidence angle and boundary layer thickness on the free-end pressure distribution, aerodynamic forces, vortex shedding frequencies, and also the vortex formation length at mid-span. Chapter 5 concludes this experimental investigation, reiterates the contributions of the present work, and provides some recommendations for future work which could complement the results of this present study.

Several appendices are also included in this thesis. The full results of the mean free-end surface pressure distribution for all the tested aspect ratios at five selected incidence angles ( $\alpha = 0^\circ, 10^\circ, 15^\circ, 30^\circ$ , and  $45^\circ$ ) are presented in Appendix A. Similarly, the full results of the centerline pressure profile are shown in Appendix B for all tested aspect ratios at four selected incidence angles ( $\alpha = 0^\circ, 15^\circ, 30^\circ$ , and  $45^\circ$ ). The present thesis also compares the results of the centerline pressure profile along the  $x$ - and  $y$ -axis defined in Figure 1.3 between the finite square prism and the finite cylinder studied in the thesis of Beitel (2017). The results of this comparison are available in Appendix C. It should also be noted that the present thesis uses several figures from different publications. Permission to use these figures has been obtained from relevant publishers and the agreements are shown in Appendix D.

## 2 LITERATURE REVIEW

### 2.1 Introduction

The literature review in this chapter begins with a general overview of the flow around an infinite square prism (Section 2.2) and a finite-height square prism (Section 2.3). The effect of the incidence angle and aspect ratio on the flow structure around the finite-height prism is also presented. The review is then shifted to some specific areas of research that are more related to the present thesis, such as the flow field above the free end, and information on the mean free-end surface pressure distribution (Section 2.4). Next, the review covers some other measured variables (outlined in Section 1.4), such as the aerodynamic forces (Section 2.5), Strouhal number (Section 2.6) and vortex formation length (Section 2.7). Lastly, based on the studies reviewed in this chapter, a summary is given with the identification of several gaps in the literature (Section 2.8), which further support the objectives (detailed in Section 1.3) of the present study.

### 2.2 The flow around an infinite square prism

An infinite square prism simply indicates that the prism is sufficiently slender ( $H \gg D$ ) so that the flow features associated with the free-end and ground-plane effect are negligible over most of the height or span. The flow around the infinite prism is considered to be free of appreciable end effects and strongly two-dimensional. Hence, for an infinite square prism, the flow features around the four sides of the prism are typically the main focus in the literature. The main difference between the flow features around the square prism and circular cylinder are the locations of the separation points. The flow characteristics of the square prism are relatively insensitive to the Reynolds number in comparison to the circular

cylinder, on account of the flow separation occurs at the sharp corners of the square prism, while the location of the separation points for the circular cylinder is greatly dependent on the Reynolds number. Therefore, many studies of the square prism in the literature investigated the flow separation and reattachment characteristics at various incidence angles instead of at different Reynolds numbers. The incidence angle is the angle measured between the flow direction and the square cross-section centerline, and often increased in clockwise direction for most studies, following the convention adopted in aerodynamics textbooks for the angle of attack of an aerofoil. Figure 2.1 shows a common geometry and some symbols associated with the flow around a square prism, where the incidence angle,  $\alpha$  increases in the clockwise direction.

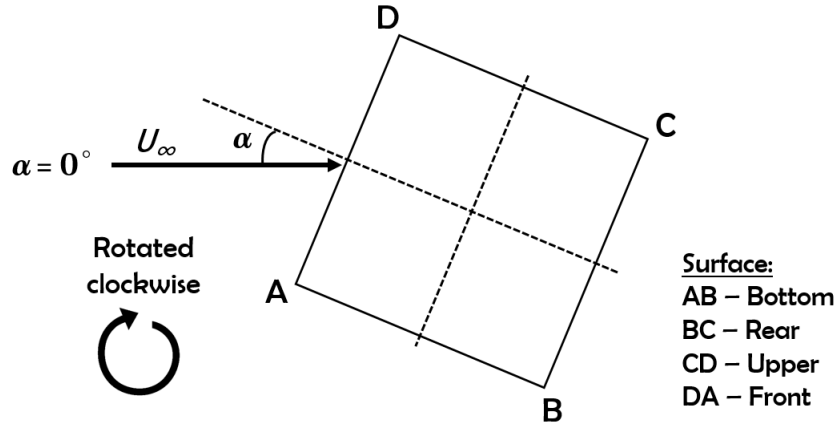


**Figure 2.1:** Geometry and symbols associated with the flow around an infinite-height square prism with the prism rotated in the clockwise direction. Note that  $\alpha = 0^\circ$  corresponds to side A-D oriented normal to the approaching flow.

Based on the clockwise rotation of the square prism and with the flow from left to right (as shown in Figure 2.1), the surface which would experience the most rapid change on the flow behavior (with respect to the increase of  $\alpha$ ) is the bottom surface (side A-B in Figure 2.1). Igarashi (1984) has performed flow visualization by using an oil film method at  $Re = 3.7 \times 10^4$  to investigate the flow patterns on this bottom surface at  $\alpha = 0^\circ$  to  $45^\circ$ , with  $5^\circ$  increment. At  $\alpha = 0^\circ$ , Igarashi (1984) observed that the flow was separated at both sharp corners of the leading edge and formed a shear layer. The shear layer rolled up and reattachment occurred on the rear surface (side B-C in Figure 2.1) of the prism. This observation is the first flow regime identified by Igarashi (1984) where the flow is considered “perfectly and symmetrically

separated” and no significant flow reattachment was observed on the upper (C-D) and bottom (A-B) surfaces of the prism. This first flow regime occurred at a range of small incidence angle ( $0^\circ \leq \alpha \leq 5^\circ$ ). For  $\alpha = 5^\circ$  and  $10^\circ$ , Igarashi (1984) found the velocity of reverse flow (from the rear surface B-C) along the bottom surface A-B increased, and resulted in slight increase in the pressure coefficient on the bottom surface. Igarashi (1984) classified this flow regime as “perfectly and asymmetrically separated flow”. This flow regime started at  $\alpha = 5^\circ$ , and ceased when the shear layer started to reattach at the trailing edge (corner B) of the bottom surface at  $\alpha = 15^\circ$ , and resulted in significant changes in the surface pressure profile, both quantitatively and qualitatively. The pressure coefficient on the bottom surface generally increased drastically starting at  $\alpha = 15^\circ$ , and the formation of a separation bubble was evident due to the reattachment of the shear layer onto the bottom surface. Igarashi (1984) classified this flow regime as “reattachment flow pattern” for  $15^\circ \leq \alpha \leq 35^\circ$ . The location of the reattachment point at this regime generally moved closer to the leading edge (corner A) when the incidence angle increased. The fourth flow regime classified by Igarashi (1984) was the “wedge type flow” for  $35^\circ \leq \alpha \leq 45^\circ$ , where the flow profiles were almost identical and insensitive to the change of the incidence angle. Figure 2.2 summarizes the four flow pattern identified by Igarashi (1984) for an infinite square prism.

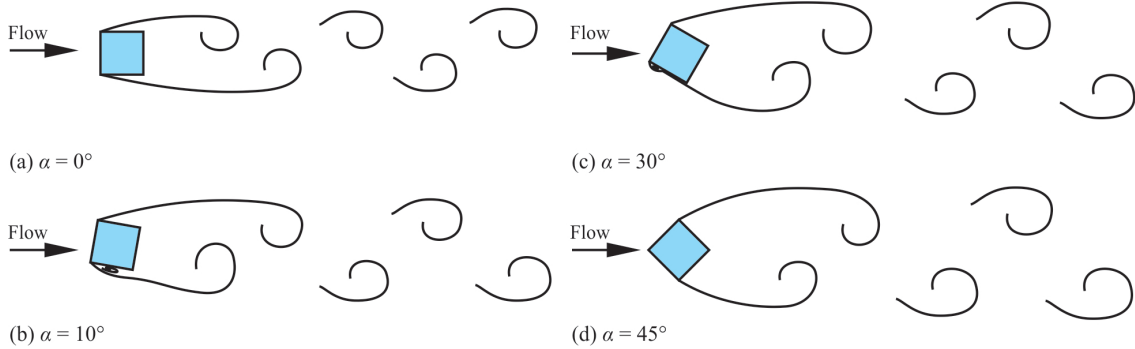


**Figure 2.2:** Four flow regimes for an infinite square prism identified by Igarashi (1984): (a) perfectly separated flow (symmetric), (b) perfectly separated flow (asymmetric), (c) reattached flow, and (d) wedge type flow - figure of D. Sumner; used with permission.

Huang et al. (2010) and Yen and Yang (2011) have also demonstrated a systematic illustration in their experimental investigations to classify different flow regimes based on flow separation and reattachment characteristics. Both of the studies adopted smoke-wire techniques, at different Reynolds numbers of  $Re = 2 \times 10^4$  and  $Re = 6.3 \times 10^3$  for Huang

et al. (2010) and Yen and Yang (2011), respectively. Both studies concluded three distinct flow regimes, instead of four regimes as identified by Igarashi (1984). Huang et al. (2010) named the first flow regime as “subcritical flow”, where there was no flow reattachment observed on the bottom surface of the prism. A similar flow regime was observed by Yen and Yang (2011), and they named this regime as “leading-edge separation” which occurs at small incidence angles ( $0^\circ \leq \alpha \leq 12^\circ$ ). The second flow regime identified by Huang et al. (2010) was “supercritical flow”, where the shear layer reattachment on the bottom surface of the prism is pronounced. Huang et al. (2010) identified the critical angle of  $\alpha_c = 15^\circ$ , where they started observing the formation of a separation bubble on the bottom surface. Huang et al. (2010) classified the flow for  $\alpha > \alpha_c$  as “supercritical flow”. On the other hand, for  $12^\circ \leq \alpha \leq 30^\circ$ , Yen and Yang (2011) classified the flow as “separation bubble mode”, where the separation bubble formed between the shear layer and the bottom surface of the square prism. The flow is considered fully attached to the bottom surface of the prism for  $\alpha \geq 30^\circ$  and Yen and Yang (2011) described this phenomena as “attached flow”.

The separation and reattachment profiles obtained were somewhat similar between different studies by Igarashi (1984), Huang et al. (2010), and Yen and Yang (2011). The flow regimes of “perfectly separated flow (symmetric)” and “perfectly separated flow (asymmetric)” as identified by Igarashi (1984) were combined into one flow pattern by Huang et al. (2010) as “subcritical flow”, and Yen and Yang (2011) as “leading-edge separation”. The “reattached flow” identified by Igarashi (1984) was similar to the “separation bubble mode” classified by Yen and Yang (2011), where the shear layer started reattaching to the bottom surface of the prism and leading to the formation of separation bubble. Likewise, the “wedge flow pattern” identified by Igarashi (1984) and the “attached flow pattern” identified by Yen and Yang (2011) were similar, where both patterns showed the shear layer almost fully reattached along the bottom surface of the prism with no evidence of the separation bubble. Huang et al. (2010), on the other hand, combined both “separation bubble mode” and “attached flow” into one flow regime of “supercritical flow”, and only assigned the “wedge flow pattern” to describe the flow feature at  $\alpha = 45^\circ$  where the flow attached along both leading edges facing to the flow (surface A-B and D-A in Figure 2.1) and not separated until the rear edges. Table 2.1 summarizes different flow regimes identified by all the studies above-mentioned.

**Table 2.1:** Different flow regimes for an infinite-height square prism at  $\alpha = 0^\circ$  to  $45^\circ$ , identified by Igarashi (1984), Huang et al. (2010), and Yen and Yang (2011).

Study	Re	$\alpha$ range	Flow mode
Igarashi (1984)	$3.4 \times 10^4$	$0^\circ - 5^\circ$	Perfectly separated flow (symmetric)
		$5^\circ - 15^\circ$	Perfectly separated flow (asymmetric)
		$15^\circ - 35^\circ$	Reattachment flow
		$35^\circ - 45^\circ$	Wedge flow
Huang et al. (2010)	$2.0 \times 10^4$	$0^\circ - 15^\circ$	Subcritical flow
		$15^\circ - 45^\circ$	Supercritical flow
		$45^\circ$	Wedge flow
Yen and Yang (2011)	$6.3 \times 10^3$	$0^\circ - 12^\circ$	Leading-edge separation
		$12^\circ - 30^\circ$	Separation bubble
		$30^\circ - 45^\circ$	Attached flow

Similar experiments were also performed by Dutta et al. (2003) using a smoke tunnel at  $Re = 3.9 \times 10^3$  at four incidence angles of  $\alpha = 0^\circ, 30^\circ, 45^\circ, 60^\circ$ . The adoption of incidence angle at  $\alpha = 60^\circ$  is relatively less common in the literature as the flow characteristics at this angle mirror the behaviour at  $\alpha = 30^\circ$ . Although Dutta et al. (2003) did not specifically classify the flow modes into different categories, their flow visualization results complemented the flow regimes identified by Igarashi (1984), Huang et al. (2010) and Yen and Yang (2011). At  $\alpha = 0^\circ$ , Dutta et al. (2003) made similar statements about the flow separation at both corners of the leading edge which exposed to the flow, which corresponds to the “perfectly separated flow (symmetric)” named by Igarashi (1984), and “leading-edge separation” named by Yen and Yang (2011). At  $\alpha = 30^\circ$  and  $45^\circ$ , the flow visualization of Dutta et al. (2003) showed significant flow attachment on the bottom surface, which is similar to the “wedge type flow” identified by Igarashi (1984) for  $35^\circ \leq \alpha \leq 45^\circ$  and Huang et al. (2010) at  $\alpha = 45^\circ$ , and “attached flow” mode identified by Yen and Yang (2011) for  $30^\circ \leq \alpha \leq 45^\circ$ .

Yen and Yang (2011) also performed further investigation on the effect of Reynolds number, by varying the Re range from 4,000 to 36,000. The three distinct flow regimes were still evident, except the critical angle between the two subsequent flow regimes varied

slightly with the changes of  $Re$ . Figure 2.3 shows the distribution of the flow regimes at various  $Re$  and  $\alpha$ . The result shows that the critical angle for the flow to switch from the leading-edge separation to separation bubble mode is highly insensitive to the change of  $Re$ . On the other hand, the critical angle where the separation bubble mode turned to the attached flow decreased almost linearly for low  $Re$  region ( $Re < \sim 2.3 \times 10^4$ ), and remained nearly consistent once  $Re > \sim 2.3 \times 10^4$ . The Reynolds number effect on the critical angle is only somewhat pronounced in the attached flow region (at higher  $\alpha$ ). This observation again confirmed the argument about the flow feature around a square prism is nearly independent to  $Re$  on account of the flow separation at the sharp corners.

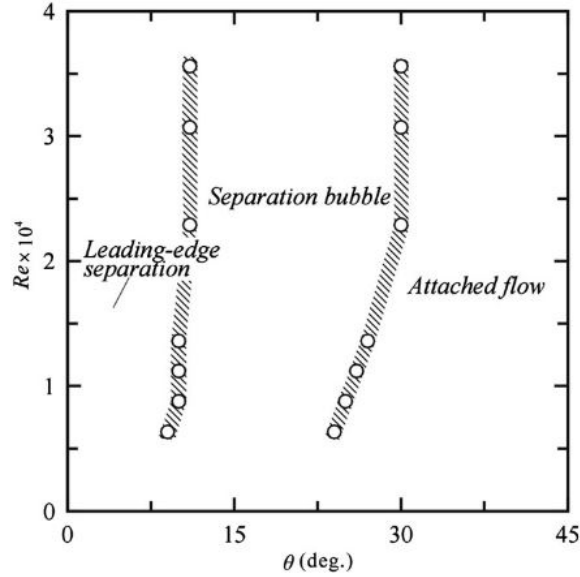


**Figure 2.3:** Three flow regimes for an infinite-height square prism and the distribution based on various  $Re$  and  $\alpha$  - reproduced from Yen and Yang (2011) with permission of Elsevier. The symbol  $\theta$  is denoted by  $\alpha$  in the present thesis.

## 2.3 The flow around a finite-height square prism

There is a wide range of the research scope related to the flow around a finite-height square prism. Thus, this section intends to organize different scopes of the research accordingly. Subsection 2.3.1 focuses on the flow model at  $\alpha = 0^\circ$  only, which is the most common incidence angle in most studies. The effects of aspect ratio (at  $\alpha = 0^\circ$ ) and incidence angle on the wake structure are reviewed in subsections 2.3.2 and 2.3.3, respectively.

### 2.3.1 Flow structure at $\alpha = 0^\circ$

The separated flow from the square prism surface discussed in Section 2.2 is associated with periodic alternate formation and shedding of Karman vortices. The Karman vortex street contains the main vortex structures in the context of the flow around an infinite square prism. However, with the adoption of a finite-height square prism, other types of vortices form behind the prism due to the influence of the free end and ground plane, such as the common tip vortices which are formed due to the flow separation at the free end, base vortex structures which are emerging from the ground plane, and the horseshoe vortex which rolls around the wall junction of the prism. Figure 2.4 shows the different types of vortex structures for the flow around a finite-height square prism. It should be noted that for clarity purposes, the vortex structures illustrated in Figure 2.4 are shown in imagined shapes (not as per actual flow model) without considering the interaction between those different vortices structures (similar to the simpler model shown in Figure 1.2). It is also worth pointing out the formation of the Karman vortices only occurs if the aspect ratio of the prism exceeds the critical aspect ratio so that the boundary layer effect does not dominate the flow structure.

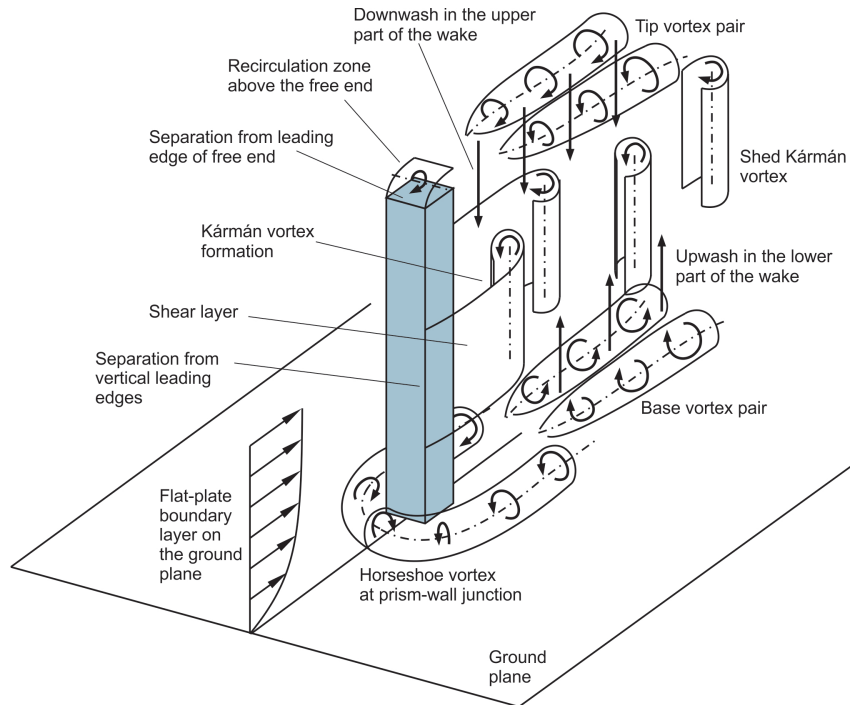


**Figure 2.4:** Different vortex structures associated with the flow around a finite-height square prism - figure of D. Sumner; used with permission.

Some studies have provided more detail about the flow structure with the consideration of the interaction between the different vortex structures above-mentioned. Wang and Zhou (2009) introduced two types of flow structure around a square prism with  $AR = 7$ , which are a symmetrically arranged two spanwise vortex roll and a staggered arranged spanwise vortex. The symmetrically arranged structure consists of a pair of vortices that are bent concavely towards downstream and joined together near to the free end. The bending of the vortices is due to the tip vortices emerging from the free end and base vortices generated from the ground plane. Wang and Zhou (2009) describe that the tip vortices are connected to downwash flow, while the base vortices form upwash flow. In this type of flow structure, both tip and base vortices symmetrically intersect with the same  $y$ - $z$  plane (Figure 2.5). The occurrence of the first type of the flow structure is less common according to Wang and Zhou (2009). The second type of the flow structure introduced by Wang and Zhou (2009), the staggered arranged spanwise vortex roll, shows that the spanwise vortices do not intersect symmetrically in the  $x$ - $y$  plane. Additionally, both pairs of tip and base vortices are formed in a staggered position in the  $y$ - $z$  plane, with one pair formed downstream of the  $y$ - $z$  plane, and the other one located upstream of the plane. In both flow structures, the presence of the horseshoe vortex was also observed by Wang and Zhou (2009) which rolls around the wall-junction of the prism in a boundary layer with thickness of  $\delta/D = 2.6$ .

Bourgeois et al. (2011) conducted an experimental investigation by using PIV for a finite square prism with  $AR = 4$ , and proposed the other flow structure named “alternating half-loop structures” which consists of leading principal cores and streamwise connector strands. The leading principal core is almost vertical to the ground plane and retains its shape during different phases of the flow, while the connector strand deforms and reforms throughout various timescales of the flow. Once the connector strand is fully formed, it was observed by Bourgeois et al. (2011) that the strand connects the bottom of one of the principal cores to the top of the other principal core downstream. Two principal cores connected by the strand are located at different sides of the shed structure, with one oriented in the  $+y$  direction and the other one in the  $-y$  direction. The illustration of the alternating-half loop structure is shown in Figure 2.6 (a). In comparison to the flow model of Wang and Zhou (2009), the presence of the horseshoe vortex was not evident based on the model proposed

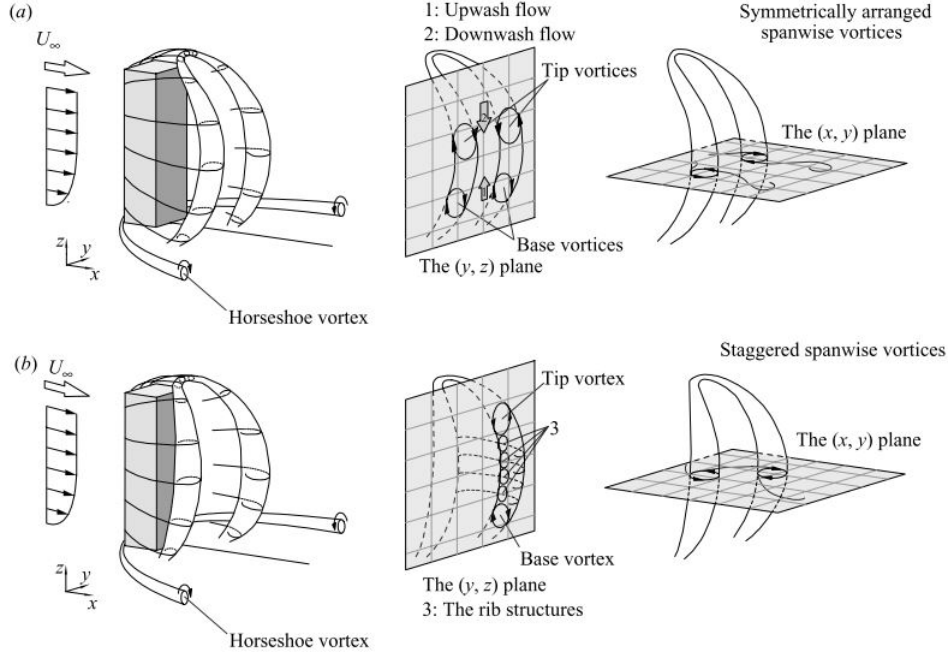


**Figure 2.5:** Two types of flow structure proposed by Wang and Zhou (2009) and used with permission of Cambridge University Press: (a) symmetrically arranged two spanwise vortex roll (b) staggered arranged spanwise vortex. The coordinate system  $(x, y, z)$  is the same as the present thesis as described in Section 1.1.

by Bourgeois et al. (2011) on account of the adoption of a relatively thinner boundary layer of  $\delta/D = 0.18$ .

Recent studies by Rastan et al. (2017), Zhang et al. (2017), and Kindree et al. (2018) have also proposed some low-Reynolds-number flow models for a finite-height square prism. Rastan et al. (2017) and Zhang et al. (2017) conducted numerical simulations and observed a flow model named “hairpin vortices” at  $Re = 85$  and  $150$ , respectively. The hairpin structure proposed by Rastan et al. (2017) (as shown in Figure 2.6 (b)) did not show an obvious half-loop, and also the formation of the principal core (as identified by Bourgeois et al. (2011)) was not evident. Rastan et al. (2017) claimed that the wake transition region from low  $Re$  to high  $Re$  is necessary to develop the hairpin-shaped vortices from “small curved legs” to “full curved legs”. Zhang et al. (2017) claimed that the hairpin vortex model is a phenomenon which indicates a weak spanwise vortex shedding at low  $Re$ . Nevertheless, despite a low  $Re$  used by Rastan et al. (2017) and Zhang et al. (2017), the hairpin structures identified in their studies still share some similarities as the “half-loop alternating structure” proposed by Bourgeois et al. (2011), where both vortex structures were formed close to the

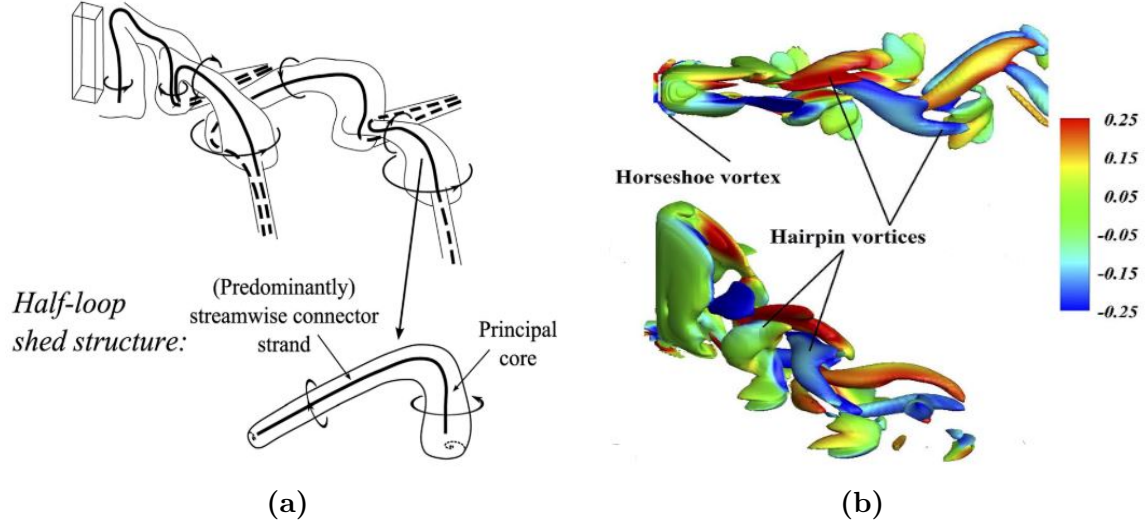


**Figure 2.6:** Different flow models proposed by (a) Bourgeois et al. (2011): alternating half-loop flow structure with principal core and streamwise connector strand, and (b) Rastan et al. (2017): hairpin vortex structure with top and isometric view, colored by streamwise vorticity. Used with permission of AIP Publishing.

ground plane and shed alternatively between different transverse directions ( $+y$  to  $-y$  and vice versa). These two studies also provided physical explanations about the formation of their flow models which are related to the interaction between the shear layers, upwash flow (base vortices), and downwash flow (tip vortices). On the other hand, Kindree et al. (2018) conducted an experimental investigation by using PIV for a finite square prism with  $AR = 3.91$  at  $Re = 1.05 \times 10^4$ . Based on the flow model of Kindree et al. (2018), there was a pair of vortices with different directions of streamwise vorticity observed in the wake region as shown in Figure 2.7. Kindree et al. (2018) also observed another pair of vortex cores located below the main vortex core (labeled as  $D+$  and  $D-$  in Figure 2.7) with the same direction of streamwise vorticity. The third pair of vortex cores observed by Kindree et al. (2018) (although it was not too evident) was located near to the ground plane, and this pair of vortex cores had the same direction of rotation as the main vortex cores. Notably, the sense of rotation observed by Kindree et al. (2018) was different that those of Wang and Zhou (2009) and Bourgeois et al. (2011). Kindree et al. (2018) showed that for all three pairs of the vortices, all the vortices at the  $+y$  location rotated clockwise, while all the vortices at the  $-y$  location rotated counter-clockwise. On the other hand, Wang and Zhou (2009) and Bourgeois et al. (2011) observed different senses of rotation for different vortices despite

the vortices were formed at the same  $y$  location. Kindree et al. (2018) explained the main reason for such occurrence was the adoption of low  $Re$  in their investigation which led to a laminar boundary layer condition. Although the sense of rotation of the various vortices was different for these studies, the flow structure related to the formation of the base vortices and tip vortices was somewhat identical. It was noticed that the pair of main vortices was emerging from the free end. Additionally, the flow model shape of Kindree et al. (2018) was very similar to the mean vortex structure identified in the study of Bourgeois et al. (2011). Although the Reynolds number adopted by Kindree et al. (2018) was remarkably lower than that of Wang and Zhou (2009) and Bourgeois et al. (2011), the flow models proposed for these studies did not vary significantly, which suggests that the effect of  $Re$  on the flow may be relatively trivial as compared to other parameters such as  $AR$  and  $\alpha$ .

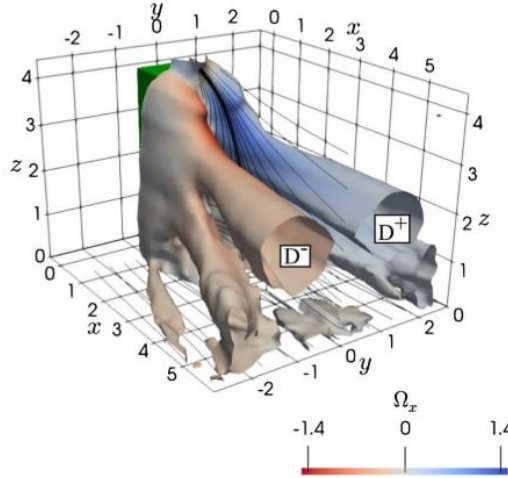


**Figure 2.7:** The flow structure identified by Kindree et al. (2018) with three pairs of vortex cores, colored by streamwise vorticity,  $\Omega_x$ , for a square prism with  $AR = 3.91$ .  $Re = 1.05 \times 10^4$ ,  $\delta/D = 0.21$ . The main vortex cores labeled with  $D^+$  and  $D^-$  indicate different directions of vorticity. The coordinate system  $(x, y, z)$  is the same as the present thesis as described in Section 1.1. Used with permission of Springer Nature.

### 2.3.2 The effect of aspect ratio

The various flow models proposed by Bourgeois et al. (2011), Rastan et al. (2017), and Kindree et al. (2018) were investigated at a single aspect ratio of  $AR = 4$ , 7, and 3.91 respectively. Wang and Zhou (2009) provided additional information about the variation of

the flow structure due to the effect of aspect ratio, by presenting the time-averaged vorticity contours for  $AR = 3, 5$  and  $7$  at different streamwise locations of  $x/D = 1, 3$ , and  $5$ . It was observed that the near-wake structure (at  $x/D = 1$ ) was qualitatively identical where one pair of tip vortices was observed near to the free end, and one pair of base vortices was formed near to the ground plane. The strength of the vorticity increased with the aspect ratio of the prism, and the pair of base vortices diminished towards downstream. Wang and Zhou (2009) observed that for the smallest aspect ratio tested ( $AR = 3$ ), the base vortices were not pronounced at  $x/D = 3$ , and completely absent at  $x/D = 5$ . For  $AR = 5$  and  $7$ , although the decay of the base vortices can still be observed, the presence of the base vortices at  $x/D = 5$  were still evident. Also, Wang and Zhou (2009) observed that the strength of the tip vortices was stronger than the base vortices, and the base vortices decayed at an earlier streamwise location than the tip vortices. The results of Wang and Zhou (2009) showed that the aspect ratio has strong impact on the strength of vorticity and formation of the base vortices. Stronger vorticity was observed with higher aspect ratio of the prism for both tip and base vortices, and it appeared that the base vortices at  $x/D = 3$  were only evident after the critical aspect ratio of  $AR = 5$ . Thus, the secondary vortex pairs identified by Kindree et al. (2018) might not be evident if a lower aspect ratio was used.

Unnikrishnan et al. (2017) conducted similar experiments as Wang and Zhou (2009) to investigate the variation of the wake vorticity field with aspect ratio at a larger downstream location of  $x/D = 10$ , for four aspect ratios ( $AR = 3, 5, 7, 9$ ) at  $Re = 3.7 \times 10^4$  and  $\delta/D = 1.5$ . It was observed from their experiments that the wake structures for  $AR = 3$  and  $5$  were different than those of  $AR = 7$  and  $9$ , where the vorticity contours for  $AR = 3$  and  $5$  were more circular in shape in comparison to the contours for  $AR = 7$ , and  $9$ . Furthermore, a pair of induced vortices was observed by Unnikrishnan et al. (2017) near to the ground plane, starting at  $AR = 5$ , which suggests the transition of wake structure after this critical aspect ratio. The other crucial effect of the aspect ratio identified by Unnikrishnan et al. (2017) was the increase of the downwash strength with higher aspect ratio of the prism. It was interestingly observed that the maximum value of the downwash flow increases with  $AR$ , and the downwash reached the ground plane for the lowest aspect ratio tested ( $AR = 3$ ), based on their result of mean velocity vector field measured by a seven-hole pressure probe.

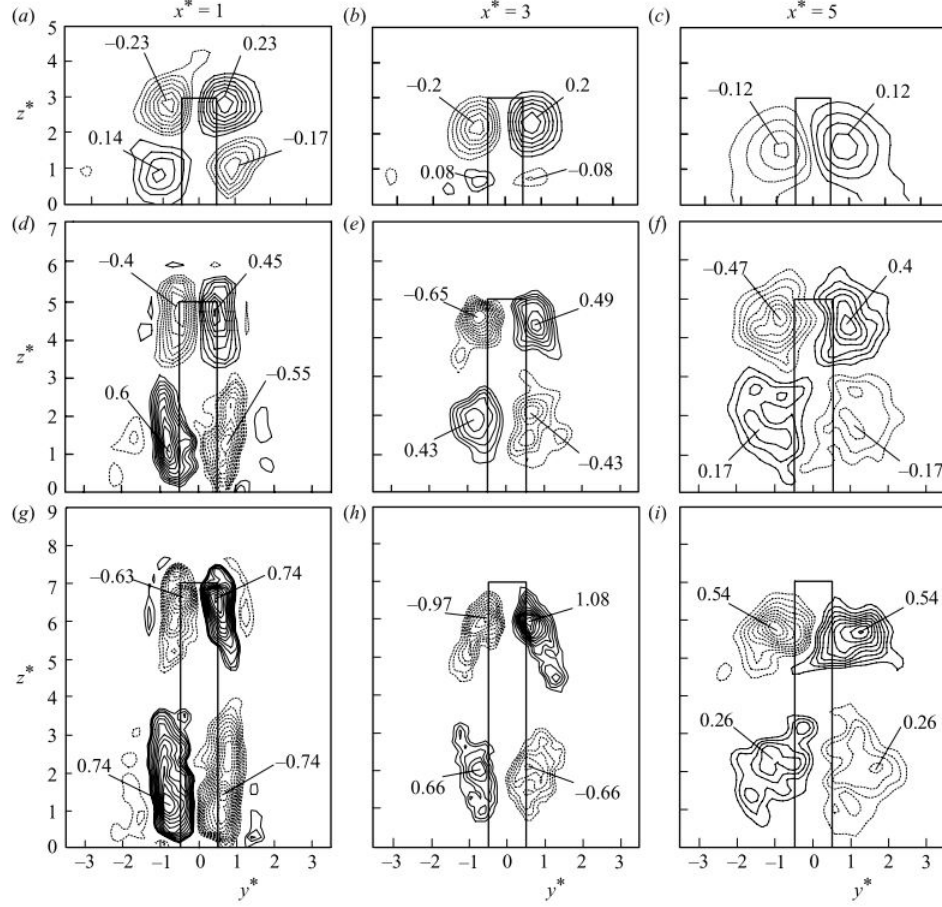


**Figure 2.8:** Mean streamwise vorticity contours in  $y$ - $z$  planes at  $x/D = 1, 3$ , and  $5$ , for  $AR = 3, 5$  and  $7$ , at  $Re = 9.3 \times 10^3$  and  $\delta/D = 1.4$  - reproduced from Wang and Zhou (2009) with permission of Cambridge University Press. The symbols  $x^*$ ,  $y^*$  and  $z^*$  are denoted by  $x/D$ ,  $y/D$ , and  $z/D$ , respectively in the present thesis.

### 2.3.3 The effect of incidence angle

The effect of the incidence angle has been discussed in Section 2.2 for the flow around an infinite square prism. In this subsection, the review on the effect of the incidence angle will be further enhanced with the consideration of downwash flow owing to the free-end effect. It should be noted that all the flow models proposed in different studies as described in subsection 2.3.1 were performed at  $\alpha = 0^\circ$ . The flow visualization or structure at other incidence angles has not been extensively investigated to date. A few studies which discussed the effect of incidence angles on the flow structure were performed by Unnikrishnan et al. (2017) and Sohankar et al. (2018).

Sohankar et al. (2018) investigated the wake profile for three incidence angles,  $\alpha = 0^\circ$ ,  $15^\circ$ , and  $45^\circ$  at two streamwise location of  $x/D = 3$  and  $5$ . Their result of time-averaged streamwise velocity, sampled at  $Re = 2 \times 10^4$  and  $\delta/D = 0.5$ , showed that the “double peaks profile” was formed for all three  $\alpha$  at  $x/D = 3$ , measured at the mid-span location. As suggested by Sohankar et al. (2018), the formation of the double peak profile was due to the downwash flow which descended from the free end into the wake and extended until the mid-span location. This observation further conformed the tip vortex structure described in subsection 2.3. The location of the lower peak was near to the centerline of the prism for  $\alpha = 0^\circ$  and  $45^\circ$ , which suggests that the mean wake structure was symmetric at  $\alpha = 0^\circ$  and  $45^\circ$ , and the downwash flow induced by the tip vortices had dominated the centerline location. For a non-symmetrical orientation of  $\alpha = 15^\circ$ , the location of the lower peak shifted towards the  $+y$  direction, which indicated that the downwash flow was no longer dominating the wake at the centerline location, but was more biased towards the  $+y$  direction. Sohankar et al. (2018) also discovered that for  $\alpha = 15^\circ$ , the downwash flow did not reach the mid-span location at a relatively further streamwise distance of  $x/D = 5$  due to the absence of the double peaks profile at this angle. Similarly, the double peak formation for  $\alpha = 0^\circ$  at  $x/D = 5$  was much less pronounced in comparison to  $x/D = 3$ , but the downwash effect at  $x/D = 5$  for  $\alpha = 0^\circ$  was still evident because the profile did not show a clear single peak (as the profile of  $\alpha = 15^\circ$ ) that suggests the wake is nearly independent of the downwash effect. On the other hand, the velocity profile at  $\alpha = 45^\circ$  showed a lower peak with relatively higher streamwise velocity magnitude at  $x/D = 5$  as compared to  $x/D = 3$ , which indicated that the downwash effect is relatively stronger at further streamwise distance for  $\alpha = 45^\circ$ .

Unnikrishnan et al. (2017) provided a more comprehensive study about the variation of the wake profile at  $\alpha = 0^\circ$  to  $45^\circ$ , with a  $5^\circ$  increment. From the mean velocity and vorticity contours, the wake structure was observed to be symmetric at  $\alpha = 0^\circ$ . The wake structure began to shift upwards and towards  $+y$  direction for the incidence angle range of  $5^\circ \leq \alpha \leq 15^\circ$ , with the highest asymmetry observed at  $\alpha = 15^\circ$ . Notably, the occurrence of the highest asymmetrical wake at  $\alpha = 15^\circ$  was close to the critical angles identified by Igarashi (1984), Huang et al. (2010), and Yen and Yang (2011) discussed in Section 2.2. The wake structure slowly regained its symmetry starting from  $\alpha = 20^\circ$  until the wake profile was fully

symmetric at  $\alpha = 45^\circ$ . The vorticity contours presented by Unnikrishnan et al. (2017) also showed that the tip vortex structures were relatively concentrated and more circular in shape at  $\alpha = 0^\circ$  as compared to the elongated vorticity profiles at  $\alpha = 45^\circ$ . Figure 2.9 shows the variation of the wake structure (based on the vorticity contours) at various incidence angles studied by Unnikrishnan et al. (2017) for  $AR = 7$ . Unnikrishnan et al. (2017) highlighted that the occurrence of the wake shifting towards  $+y$  direction from  $\alpha = 5^\circ$  to  $15^\circ$  can still be observed for the other aspect ratios of  $AR = 3, 5$  and  $9$ . Additionally, for all aspect ratios tested, the most remarkable asymmetrical wake profile was still observed at  $\alpha = 15^\circ$ . The main difference between different aspect ratios is the formation of secondary vortices, below the main tip vortex pair, that was only observed for high aspect ratio ( $AR = 7$  and  $9$ ), and the secondary vortices were most obvious at  $\alpha = 45^\circ$ . Also, the induced vorticity (as described in subsection 2.3.2) was absent for  $AR = 3$  regardless of the incidence angle owing to close proximity of the tip vortices to the ground plane.

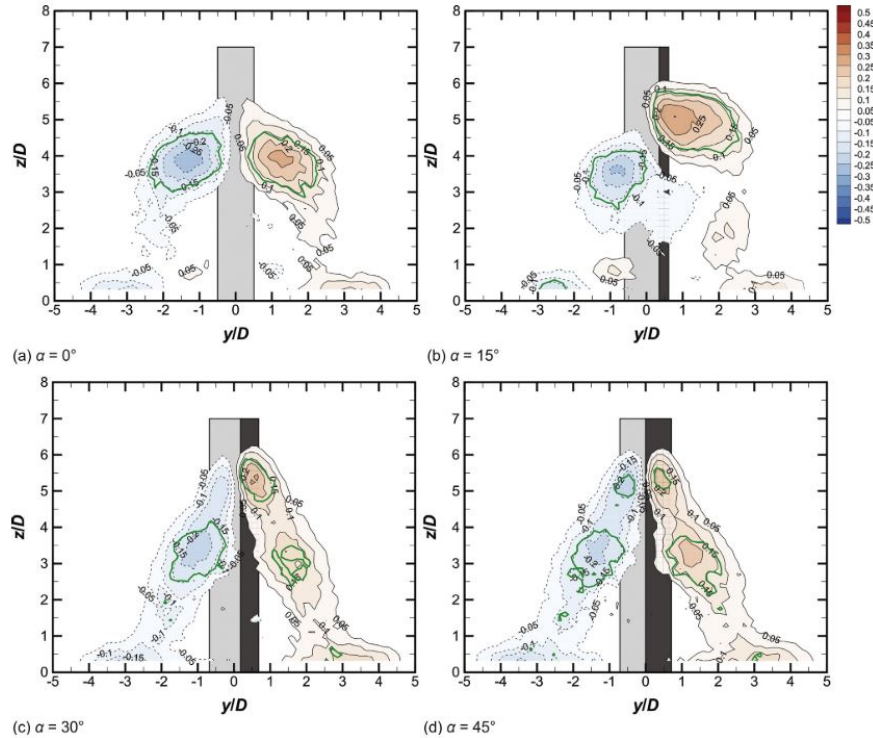


**Figure 2.9:** Mean streamwise vorticity contours in  $y$ - $z$  planes at  $x/D = 10$  ( $Re = 3.7 \times 10^4$ ,  $\delta/D = 1.5$ ) for  $AR = 7$ : (a)  $\alpha = 0^\circ$ , (b)  $\alpha = 15^\circ$ , (c)  $\alpha = 30^\circ$ , and (d)  $\alpha = 45^\circ$ . Red contours indicate the vorticity in counter-clockwise direction; blue contours indicate the clockwise direction; green circle lines indicate the pairs of streamwise vortices - reproduced from Unnikrishnan et al. (2017) with permission of Elsevier.

## 2.4 The flow near to free-end surface

In this section, the scope of the review will be narrowed into the studies which are related to the flow above the free-end surface. Although the main measured variable in the current study is the mean surface pressure at the free end, but it is also worth reviewing some studies which investigated the velocity flow field above the free-end surface, as these studies would be beneficial in providing some fundamental physical explanations about the surface pressure profile discovered in the present thesis. Subsection 2.4.1 reviews some experimental investigations which provided extensive details about the flow field above the free-end surface of the prism, while subsection 2.4.2 provides the review on a few available studies about the surface pressure at the free end, which are directly related to the main scope of the present thesis as outlined in Section 1.4.

### 2.4.1 Flow field above the free end

The flow field near to different faces of a cube ( $AR = 1$ ) at  $\alpha = 0^\circ$  was investigated by Nakamura et al. (2001) using the oil film method and smoke visualization. At the free-end surface, Nakamura et al. (2001) observed significant reverse flow due to the flow separation at the leading edge. Notably, the separated shear layer reattached at the downstream of the top surface which was very close to the trailing edge (as shown in Figure 2.10). The reverse flow inside the recirculation region also separated at the location of  $(1/6)D$  measured from the leading edge. This flow pattern was obtained experimentally at  $Re = 3.1 \times 10^4$  and  $\delta/D = 1.5 - 1.83$ . In a separate study by Nakamura et al. (2003), similar experimental methods were used to investigate the flow field near to different faces of a cube ( $AR = 1$ ) positioned at  $\alpha = 45^\circ$ . At this angle, Nakamura et al. (2003) observed a pair of separation lines extending from the leading edge apex, and a pair of reattachment lines which was formed inside the separation lines. The pair pattern of the separation and reattachment line for  $\alpha = 45^\circ$  was different than the line pattern for  $\alpha = 0^\circ$ , where only single separation and reattachment lines were observed. Nakamura et al. (2003) described the characteristic of this flow pattern as similar to the behavior of the conical vortices pattern of a delta wing at high  $\alpha$ .

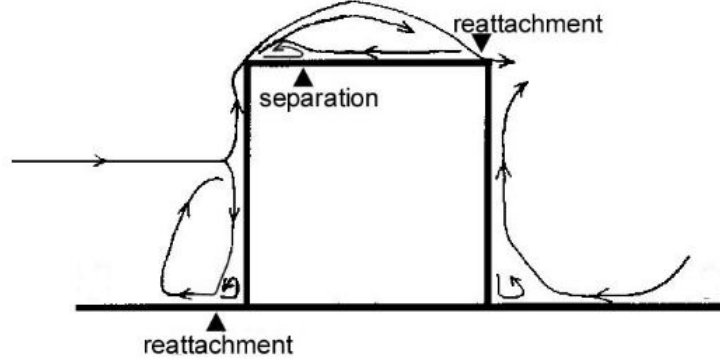


**Figure 2.10:** Flow profile around a cube ( $AR = 1$ ) with separation and reattachment locations at the free end - reproduced from Nakamura et al. (2001) with permission of Elsevier.

Okuda and Taniike (1993) provided more detailed information about the conical vortices formation at various  $\alpha$  above the top surface through their flow visualization experiment at  $Re = 1.6 \times 10^4$ , and for three different boundary layers,  $\delta/D = 0.4, 2.1$ , and  $6.9$ . The aspect ratio used by Okuda and Taniike (1993) was  $AR = 4$ , which was higher than the cube model adopted by Nakamura et al. (2001) and Nakamura et al. (2003). At  $\alpha = 0^\circ$  to  $5^\circ$ , the flow was separated from the leading edge and the separated shear layer bent downward towards the top surface. This observation is similar to the study of Nakamura et al. (2001) as shown in Figure 2.10. It was interestingly observed that at  $\alpha = 10^\circ$  to  $15^\circ$ , a single conical vortex was formed at the free end which was emerging from the windward corner (corner A in Figure 2.1). Okuda and Taniike (1993) described that the formation of this conical vortex was due to the bifurcation of the separated shear layer at the windward corner. The shear layer was divided into two different flow structures after striking the upper windward corner: the conical vortices above-mentioned which were rolling above the windward corner and towards downstream direction, and a “standing conical vortex on the side” as named by Okuda and Taniike (1993), which was another conical vortex driving below the windward corner. Figure 2.11 illustrates the flow model near to the free end proposed by Okuda and Taniike (1993) at  $\alpha = 10^\circ$  to  $15^\circ$ . For  $\alpha = 20^\circ$  to  $45^\circ$ , a pair of conical vortices (similar structure as the single conical vortex formed above the windward corner at  $15^\circ$ ) was observed. It is also worth mentioning that the characteristics of the conical vortices at various angles, from  $\alpha = 0^\circ$  to  $45^\circ$ , were identical for two different boundary layer thicknesses,  $\delta/D = 0.4$  (or  $\delta/H = 0.1$ )

and  $\delta/D = 2.1$  (or  $\delta/H = 0.5$ ), based on the experimental results of Okuda and Taniike (1993). The flow visualization for the third boundary layer thickness  $\delta/D = 6.9$  (or  $\delta/H = 1.7$ ) was not conclusive due to high turbulence components in the approaching flow. Also, as the experiment was carried out at a single aspect ratio of  $AR = 4$ , it remains vague if the flow model shown in Figure 2.11 can still be observed for a square prism with  $AR < 4$ .

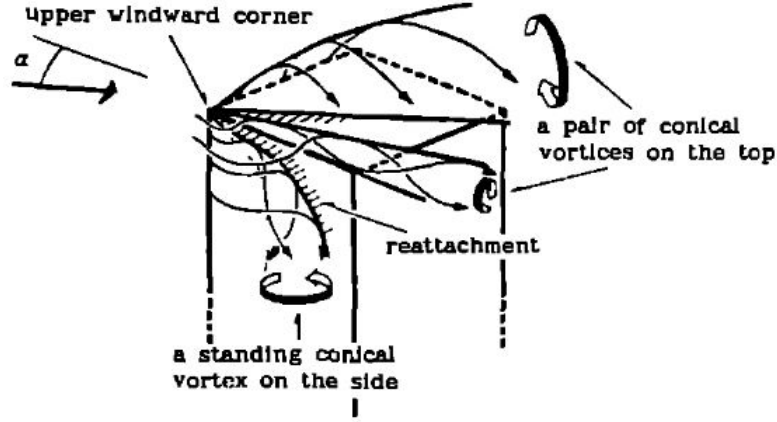


**Figure 2.11:** Formation of conical vortices above the free-end surface for a finite-height square prism of  $AR = 4$  at  $\alpha = 10^\circ$  to  $15^\circ$  - reproduced from Okuda and Taniike (1993) with permission of Elsevier.

The effect of incidence angle on the flow above the free end was also briefly provided by McClean and Sumner (2014), who performed PIV measurements to describe the flow field above the free end at two incidence angles,  $\alpha = 0^\circ$  and  $45^\circ$ . Based on their experimental results of mean velocity and vorticity fields, it was observed a significantly larger recirculation zone above the free end at  $\alpha = 0^\circ$  as compared to  $\alpha = 45^\circ$  as shown in Figure 2.12. This observation indicates that at  $\alpha = 45^\circ$ , the region of the separation flow was squeezed into a narrower region, and the downwash originates at a spanwise location closer to the trailing edge, as compared to  $\alpha = 0^\circ$ . This observation was in line with the experimental investigation of Banks et al. (2000) which showed that the height of the vortex core (measured from the free end) significantly decreased with the incidence angle. The PIV results of McClean and Sumner (2014) also inferred that the downwash flow has relatively stronger effect on the near wake region behind the prism, and this inference supports the observation of Sohankar et al. (2018) (in subsection 2.3.3), where the mean streamwise velocity profile in the near wake region showed much more remarkable double peaks formation at  $\alpha = 45^\circ$  than  $\alpha = 0^\circ$ .

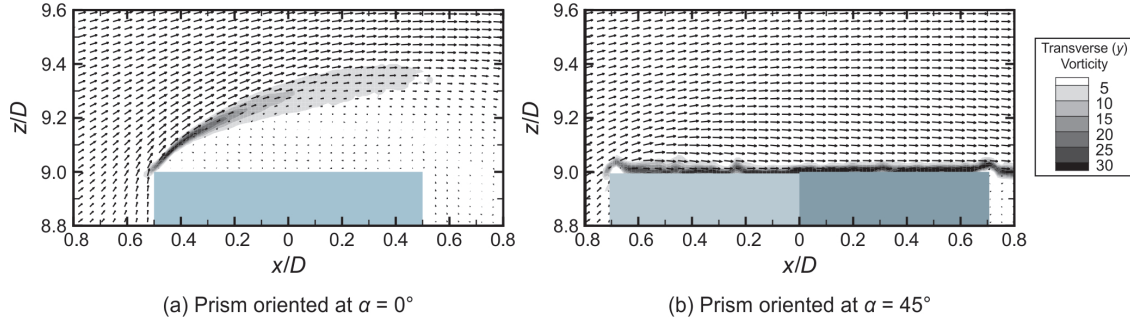


**Figure 2.12:** Mean velocity and vorticity field above the free end of a finite-height square prism with  $AR = 9$ ,  $Re = 4.2 \times 10^4$ ,  $\delta/D = 1.7$ , at (a)  $\alpha = 0^\circ$  and (b)  $\alpha = 45^\circ$  - reproduced from McClean and Sumner (2014) with permission of ASME.

The other experimental investigation which provided extensive details about the flow field above the free end was performed by Sumner et al. (2017). This study presented the velocity and vorticity fields above the free end in  $x$ - $y$ ,  $y$ - $z$  and  $x$ - $z$  planes, for four aspect ratios ( $AR = 3, 5, 7, 9$ ), at  $\delta/D = 1.5$  and  $Re = 4.2 \times 10^4$ . The effect of  $AR$  on the flow above the free end was studied, however, the investigation was solely performed at  $\alpha = 0^\circ$ . For all aspect ratios tested, similar results were observed as Okuda and Taniike (1993) and McClean and Sumner (2014) at  $\alpha = 0^\circ$ , where the separated shear layer from the leading edge did not reattach onto the free end but directly entered into the near-wake region. This result is different from the finding of Nakamura et al. (2001) for cube ( $AR = 1$ ), where a reattachment point close to the trailing edge can be observed (Figure 2.10), despite the values of  $\delta/D$  and  $Re$  were similar between the studies. Figure 2.13 shows the streamline profile above the free end for four aspect ratios and the location of the focus point of the mushroom vortex. Sumner et al. (2017) showed that the vortex centre (in the recirculation zone) moved downstream and upwards (further away from the free end), when  $AR$  decreased from  $AR = 9$  to 3. Also, based on the mean streamline profile in the  $x$ - $y$  plane, the magnitude of the maximum reverse flow (just above the free end) was found strongest for  $AR = 3$ , while the flow patterns for  $AR = 5, 7, 9$  were almost similar. Moreover, it was observed that the entrainment of the flow (from other regions) into the recirculation bubble, and the mean streamwise vorticity above the free end were significantly weaker for  $AR = 3$ , compared to  $AR = 5, 7, 9$ . Sumner et al. (2017) therefore suggested that the separated flow above the free end experienced different flow regimes when the aspect ratio of the prism lies below the critical aspect ratio (between

AR = 3 and AR = 5). Notably, the thickness of the separated flow region was not remarkably affected by AR, although a slight decrease in the maximum thickness between the free end and separated layer was observed for AR = 9.

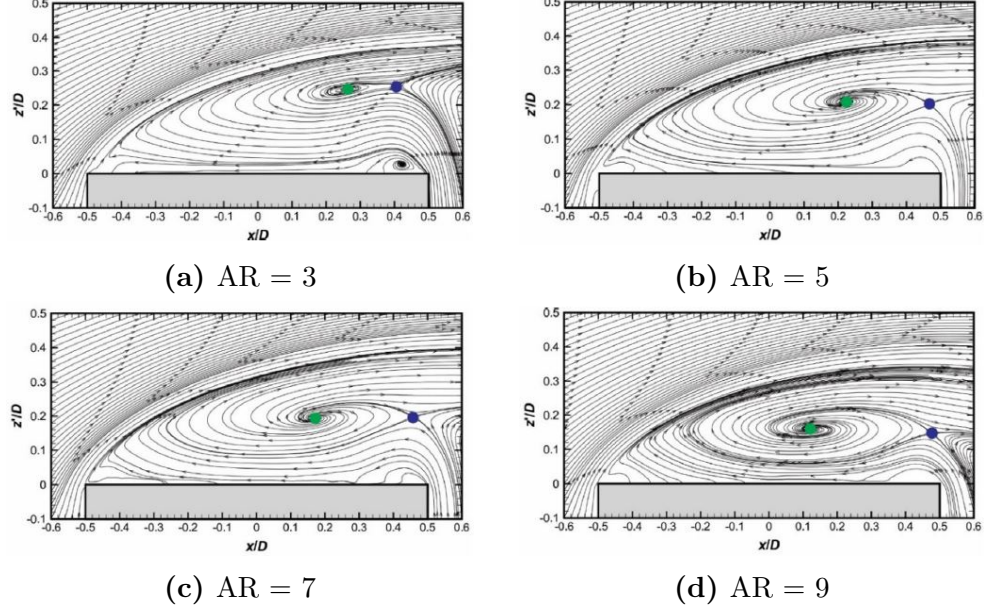


**Figure 2.13:** Mean streamline profile above the free end for finite-height square prism of (a) AR = 3, (b) AR = 5, (c) AR = 7, and (d) AR = 9, with the foci of the mushroom vortex indicated in green circles and saddle points indicated in blue circles ( $Re = 4.2 \times 10^4$ ,  $\delta/D = 1.5$ ) - reproduced from Sumner et al. (2017) with permission of Elsevier.

In view of the limited available experimental investigation on the flow above the free end in the literature, some studies also provided this information by using numerical simulation (Saha (2013), Zhang et al. (2017), and Cao et al. (2019)) at  $\alpha = 0^\circ$ . Zhang et al. (2017) suggested that no separation was observed at a sufficiently small Reynolds number of  $Re = 50$ . With the increase of  $Re$ , the flow separation at the free end began and the area of the recirculation region increases with  $Re$ . The flow field pattern obtained by Zhang et al. (2017) at  $Re = 250$  was similar to Saha (2013), where a pair of spiral-flow centers (symmetric at the centerline) was observed closed to the leading edge. This pair of spiral-flow centers was absent in all of the experimental investigations above-mentioned, which might be due to the remarkable difference in Reynolds number. However, the location of the separation line of the reverse flow was similar to the experimental investigation of Nakamura et al. (2001), which was close to the leading edge. On the other hand, the numerical simulation of Cao

et al. (2019) at  $Re = 5 \times 10^4$  for  $AR = 3$  was qualitatively identical with the experimental investigation of Sumner et al. (2017). For both studies, when the reverse flow approached the leading edge, the streamline deflected away from the centerline, as shown in Figure 2.14.

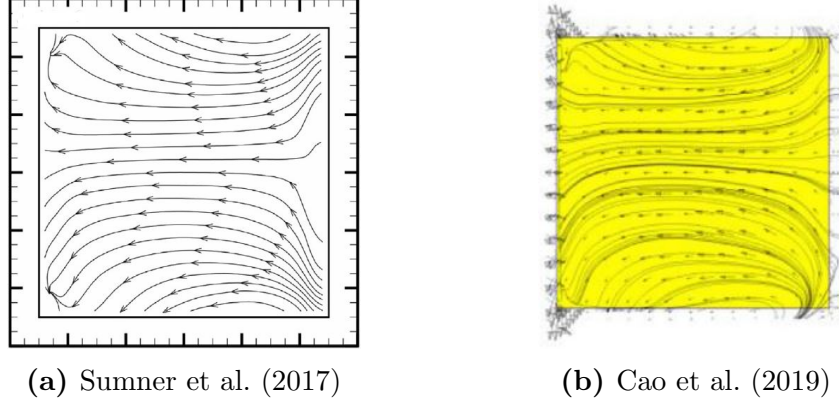


**Figure 2.14:** Mean streamline profile above the free end for a square prism of  $AR = 3$  at  $\alpha = 0^\circ$  investigated by (a) Sumner et al. (2017) using PIV measurement ( $Re = 4.2 \times 10^4$ ,  $\delta/D = 1.5$ ) (b) Cao et al. (2019) using numerical simulation ( $Re = 5 \times 10^4$ ,  $\delta/D = 20$ ). The reverse flow is from right to left. Used with permission of Elsevier.

It is worth mentioning that although the methodology of numerical simulation used by Cao et al. (2019) was different than the experimental investigation of the present thesis, the study of Cao et al. (2019) is still worth referring to, because it provided the information of the flow field at the top surface for non-zero angle of  $\alpha = 15^\circ$ , an incidence angle which has been neglected in the literature to date. Figure 2.15 shows the flow field based on their study at  $\alpha = 15^\circ$ . The streamline pattern seems more denser closer to the windward corner, and there are two reattachment lines located at upper-right region of the surface, which seems to support the observation of Okuda and Taniike (1993) about the formation of a single conical vortex emerging from the windward corner at  $\alpha = 15^\circ$ .

## 2.4.2 Surface pressure at the free end

After reviewing the flow field above the free end in subsection 2.4.1, this subsection focuses solely on the details of surface pressure on the free end of a finite square prism. The studies which specifically focus on the surface pressure measurement at the free end are relatively limited in the literature compared to other research scopes mentioned in Section 2.2 and 2.3. Some of the available studies which consist of the information about the free-end surface

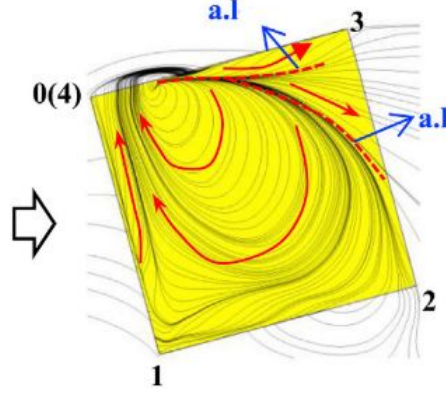


**Figure 2.15:** Mean streamline profile at the free end for square prism of  $AR = 3$  at  $\alpha = 15^\circ$ . Note that the direction of rotation is opposite to the clockwise direction denoted in Figure 2.1. The red lines denote the streamline direction. The notation “a.l” in blue denotes the attachment lines. The numbers 1, 2, 3, 0(4) indicate different corners of the prism, which are denoted by A, B, C, D, respectively, in Figure 2.1. The flow is from left to right - reproduced from Cao et al. (2019) with permission of Elsevier.

pressure are Baines (1963), Castro and Robins (1977), Sitheeq et al. (1997), Nakamura et al. (2001), Nakamura et al. (2003), Lim and Ohba (2015), and Lee et al. (2016), each with different focuses and scopes. For all the studies above-mentioned, the surface pressure was measured in the dimensionless form of  $C_P$  (defined in Equation 1.1). Also, all these studies showed that  $C_P$  on the top surface at all locations was negative because the flow separates from the leading edge corner of the prism. The negative  $C_P$  values imply a vertical, upwards suction force is experienced on the top surface of the prism.

The most simple study about the surface pressure measurement at the free end was investigated by Nakamura et al. (2001) for a cube at  $\alpha = 0^\circ$ , and Nakamura et al. (2003) for a cube at  $\alpha = 45^\circ$ . It should be noted that the main focus of these studies was the local heat transfer around a cube, but part of the studies of Nakamura et al. (2001) and Nakamura et al. (2003) showed full pressure contour patterns for different surfaces of a cube ( $AR = 1$ ) at  $\alpha = 0^\circ$ , and  $\alpha = 45^\circ$ , respectively. For  $Re = 3.1 \times 10^4$  and  $\delta/D = 1.5 - 1.83$  (which was higher than the cube height), Nakamura et al. (2001) observed the  $C_P$  value at the top surface was maximum near to the flow field reattachment line (as described in previous subsection 2.4.1). Additionally, the surface pressure distribution at the top showed the most negative  $C_P$  at the location nearer to the leading edge, and there was a slow pressure recovery in

the downstream direction (Figure 2.16(a)). The pressure contour for  $\alpha = 45^\circ$  investigated by Nakamura et al. (2003), on the other hand, showed highly dense contour lines near to the apex leading edge and sparsely populated contour line towards the downstream of the surface (Figure 2.16(b)). The most negative  $C_P$  was also found close to the sharp leading edge corner, and the low pressure region further extended downstream along the pair of separation lines (as described in previous subsection 2.4.1). The  $C_P$  contours for  $\alpha = 0^\circ$  and  $\alpha = 45^\circ$  both showed symmetrical patterns, but the pressure contours at  $\alpha = 45^\circ$  seemed much more complicated at the top surface which imprints the formation of the pair of conical vortices at this angle described by Okuda and Taniike (1993) (subsection 2.4.1).

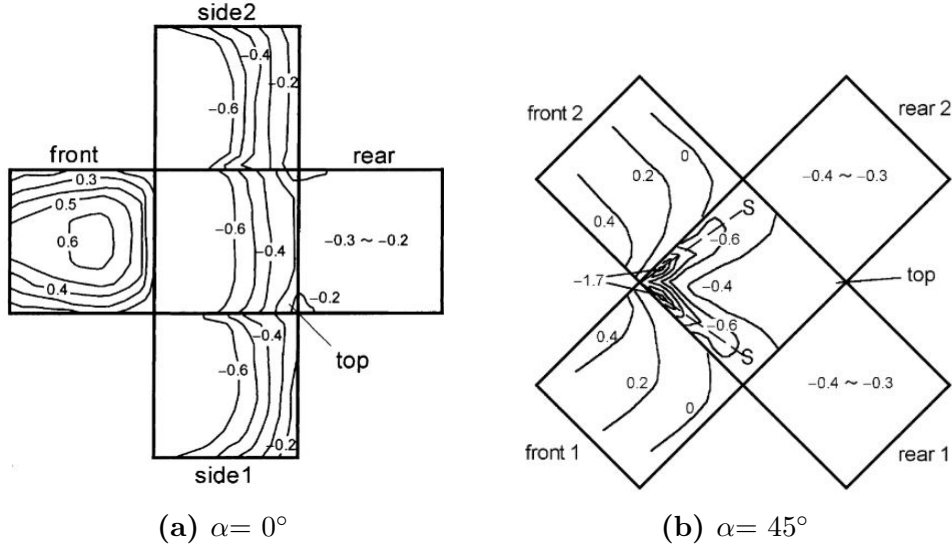


**Figure 2.16:** Mean  $C_P$  contours around a cube ( $AR = 1$ ),  $Re = 3.1 \times 10^4$ ,  $\delta/D = 1.5 - 1.83$ , for: (a)  $\alpha = 0^\circ$ , and (b)  $\alpha = 45^\circ$  - reproduced from Nakamura et al. (2001) and Nakamura et al. (2003) with permission of Elsevier. S in the right figure indicates a pair of separation lines.

citeBaines1963 presented full pressure contours for  $AR = 1$  and 8, and their results showed that the complexity of the free-end  $C_P$  contour for  $AR = 1$  is more complicated than that of  $AR = 8$ . Lim and Ohba (2015) and Lee et al. (2016), on the other hand, only presented the centerline pressure profile instead of full pressure contours, but they provided more details about the effect of  $AR$  and  $\alpha$  on the free-end pressure distribution. Both of these studies adopted a very similar methodology, where the Reynolds number was  $Re = 4.6 \times 10^4$ , and the aspect ratio of the prism was controlled by changing the length and width of the prism

(instead of varying the height,  $H$ , as in the present thesis). The research scopes for both studies were also almost identical, except that Lim and Ohba (2015) provided some additional details about the velocity flow field around the cube (similar to the flow visualization shown by Nakamura et al. (2001) described in subsection 2.4.1). The effect of AR for both studies was only limited at  $\alpha = 0^\circ$ . From the centerline pressure profile at  $\alpha = 0^\circ$ , the substantial pressure recovery trend along the downstream for both studies was still apparent as shown in Figure 2.17, which reflects the pressure contour pattern illustrated by Nakamura et al. (2001) in Figure 2.16(a). By varying the length of the prism (normal to the flow), the centerline profiles were still qualitatively similar for both studies with substantial pressure recovery along downstream. Quantitatively, the profile showed the  $C_P$  became lower (more suction effect) when the length of the free end surface normal to the flow increased. By varying the width,  $D$ , of the prism (parallel to the flow), the prism with the shortest width generally showed slightly higher  $C_P$ . Also, the pressure recovery trend was not observed for the prism with the shortest width which suggests that the reattachment did not occur when the streamwise distance of the free end surface is not sufficiently long.

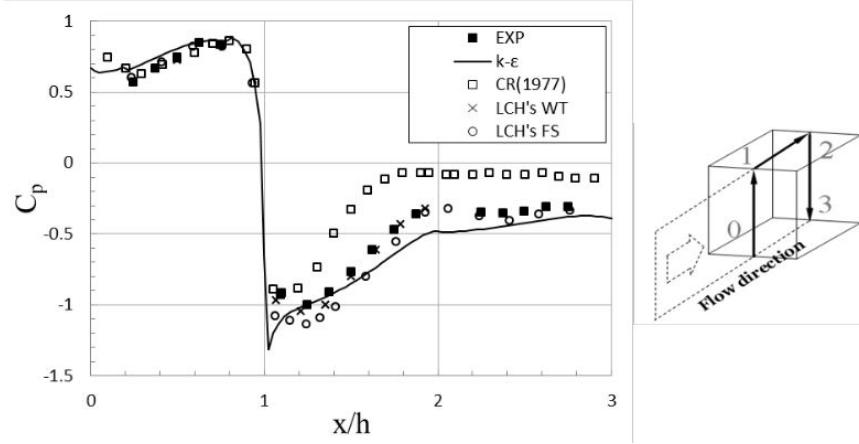


**Figure 2.17:**  $C_P$  centerline profile for front, top, and rear surfaces of a cube ( $AR = 1$ ) at  $\alpha = 0^\circ$ ,  $Re = 4.6 \times 10^4$ ,  $\delta/D \gg 1$  - reproduced from Lee et al. (2016) with permission of Techno-Press. The numbers on the  $x$ -axis denote different locations of the surfaces. 0 to 1 and 2 to 3 represents the front surface and rear surface, respectively, which are not the scopes of this thesis. The number 1 to 2 represents the top surface. The symbol  $x/h$  on the  $x$ -axis is denoted by  $X/D$  in the present thesis.

The effect of the incidence angle on the surface pressure distribution was experimentally investigated by Castro and Robins (1977), and Lim and Ohba (2015). Castro and Robins

(1977) only investigated two incidence angles,  $\alpha = 0^\circ$  and  $45^\circ$ , while the study of Lim and Ohba (2015) covered five incidence angles of  $\alpha = 0^\circ, 10^\circ, 20^\circ, 30^\circ$ , and  $45^\circ$ . For both studies, the centerline pressure profiles of  $C_P$  versus  $X/D$  (note that capital letter  $X$  is the fixed coordinate with the free-end surface, and different from the small letter  $x$  in Figure 1.3 that indicates the fixed coordinate parallel to the ground plane), the most negative  $C_P$  can still be observed near to the leading edge due to flow separation, and a slow pressure recovery can be found with increasing downstream distance. With a relatively smaller increment of  $\alpha$ , the results of Lim and Ohba (2015) showed that the value of  $C_P$  generally increased (became less negative) when the incidence angle increased as illustrated in Figure 2.18. Regardless of the increase of  $C_P$  with the incidence angle, the value of  $C_P$  still lied below zero, which indicates that the flow separation was still significant despite the incidence angle varied. At  $\alpha = 45^\circ$ , the pressure recovered relatively more rapidly near to the oblique leading edge, but the pressure recovery trend was not too apparent towards the oblique trailing edge as shown in Figure 2.18. The variation of the centerline pressure profile at various incidence angles was also numerically simulated in the study Lee et al. (2016), and the their result was similar to the experimental investigation by Lim and Ohba (2015) as shown in Figure 2.18.

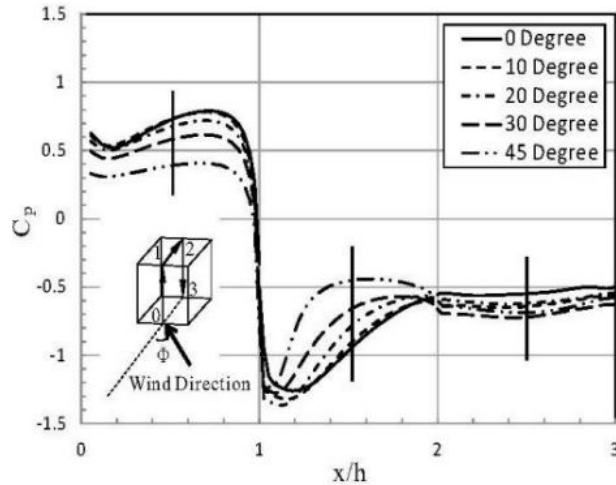


**Figure 2.18:**  $C_P$  centerline profile for front, top, and rear surfaces of a cube ( $AR = 1$ ) at various  $\alpha$ ,  $Re = 4.6 \times 10^4$ ,  $\delta/D \gg 1$  - reproduced from Lim and Ohba (2015) with permission of Techno-Press. The numbers on the  $x$ -axis denote different locations of the surfaces. 0 to 1 represents the front surface, while 2 to 3 represents the rear surface which are not the scope of this thesis. The number 1 to 2 represents the top surface. The symbol  $x/h$  on the  $x$ -axis is denoted by  $X/D$  in the present thesis.

The effect of boundary layer thickness on the mean free-end surface pressure has not been extensively studied. It seems to date the experimental investigation of Castro and Robins (1977) and Sitheeq et al. (1997) are the only available studies that reviewed the boundary layer effect on the free-end surface pressure distribution of a finite square prism. Both studies looked at the cube ( $AR = 1$ ) and presented only the centerline profile to illustrate the pressure distribution instead of the full  $C_P$  contours. Castro and Robins (1977) performed the experimental investigation with two different boundary layer thicknesses,  $\delta/D = 0$  (uniform upstream flow) and 10 (atmospheric boundary layer). For  $\alpha = 0^\circ$ , Castro and Robins (1977) observed that the trend of the  $C_P$  became more sensitive to the streamwise distance when the prism was immersed in an atmospheric boundary layer. For the case of uniform upstream flow, the trend of pressure recovery along downstream was not evident. With a significantly thicker (atmospheric) boundary layer used, the pressure recovery trend can be observed from  $C_P = \sim -1$  near to the leading edge to  $C_P = \sim 0$  at the location close to the trailing edge. For  $\alpha = 45^\circ$ , the boundary layer thickness had relatively lesser impact on the variation of  $C_P$  on the top face in comparison to the case when  $\alpha = 0^\circ$ . A significant pressure variation can still be observed in the case of uniform upstream flow. For both incidence angles investigated, the common difference between both cases of the boundary layer thickness was the magnitude of  $C_P$ , where  $C_P$  was found lower (more suction effect) when a thinner boundary layer (with uniform upstream flow) was adopted. The study of Sitheeq et al. (1997) investigated the effect of the boundary layer at only one incidence angle,  $\alpha = 0^\circ$ . However, Sitheeq et al. (1997) measured more centerline profiles at different transverse locations, and adopted three boundary layer thicknesses,  $\delta/D = 5, 8, 12$  or  $\delta/H = 2.0, 3.2, 4.8$ . The study of Sitheeq et al. (1997) also showed substantial pressure recovery trend towards downstream at  $\alpha = 0^\circ$ , which is similar to other above-mentioned studies. However, the results of Sitheeq et al. (1997) did not illustrate a significant difference between different cases of boundary layer thickness, although a slightly lower  $C_P$  can still be observed for the case of thinnest boundary layer  $\delta/D = 5$ . For each case of boundary layer thickness, the pressure profiles at different transverse locations were also almost identical. Comparing to the study of Castro and Robins (1977), the boundary layer thicknesses adopted by Sitheeq et al. (1997) were all above the cube height, and the difference in boundary layer thickness for each case was relatively

smaller, which might be the reasons for lesser variation in the pressure profile between each cases of boundary layer. Various experimental investigations related to the free-end surface pressure measurement of a square prism are summarized in Table 2.2.

**Table 2.2:** Summary of various experimental investigations related to the surface pressure measurement at the free end of finite-height square prisms.

<b>Study</b>	<b>AR</b>	<b><math>\alpha</math></b>	<b><math>\delta/D</math></b>	<b><math>C_P</math> output</b>
Baines (1963)	1, 8	$0^\circ$	$\sim 0, \gg 1$	Full contours
Castro and Robins (1977)	1	$0^\circ, 45^\circ$	$\sim 0, \gg 1$	Centerline profile
Sitheeque et al. (1997)	2.5	$0^\circ$	5, 8, 12	Centerline profile
Nakamura et al. (2001)	1	$0^\circ$	1.5 - 1.83	Full contours
Nakamura et al. (2003)	1	$45^\circ$	1.5 - 1.83	Full contours
Lim and Ohba (2015)	0.5, 1, 2	$0^\circ$	$\gg 1$	Centerline profile
Lim and Ohba (2015)	1	$0^\circ, 10^\circ, 20^\circ, 30^\circ, 45^\circ$	$\gg 1$	Centerline profile
Lee et al. (2016)	0.5, 1, 2	$0^\circ$	$\gg 1$	Centerline profile

It should be noted that there are also some other studies which provided information about the free-end surface pressure for a finite-height square prism, but are not listed in Table 2.2 on account of different methodology or research focus. For instance, the studies of Lim et al. (2009) and Chen et al. (2018) provided mean and fluctuating pressure contours at the top surface. However, part of the study of Chen et al. (2018) did provide some information on the mean and fluctuating pressure contours for  $\alpha = 0^\circ$  and  $45^\circ$  as shown in Figure 2.19. The results of Chen et al. (2018) were identical to Lim et al. (2009) and also to those studies reviewed previously (listed in Table 2.2), but Chen et al. (2018) provided additional information about the pressure fluctuations contours which were qualitatively similar to the mean pressure contour. The other investigation which mainly focused on the effect of structure interference was the study of Lim et al. (2014), where part of their study presented the mean and fluctuating surface pressure centerline profiles, which complement the full contour results of Chen et al. (2018) as shown in Figure 2.19.

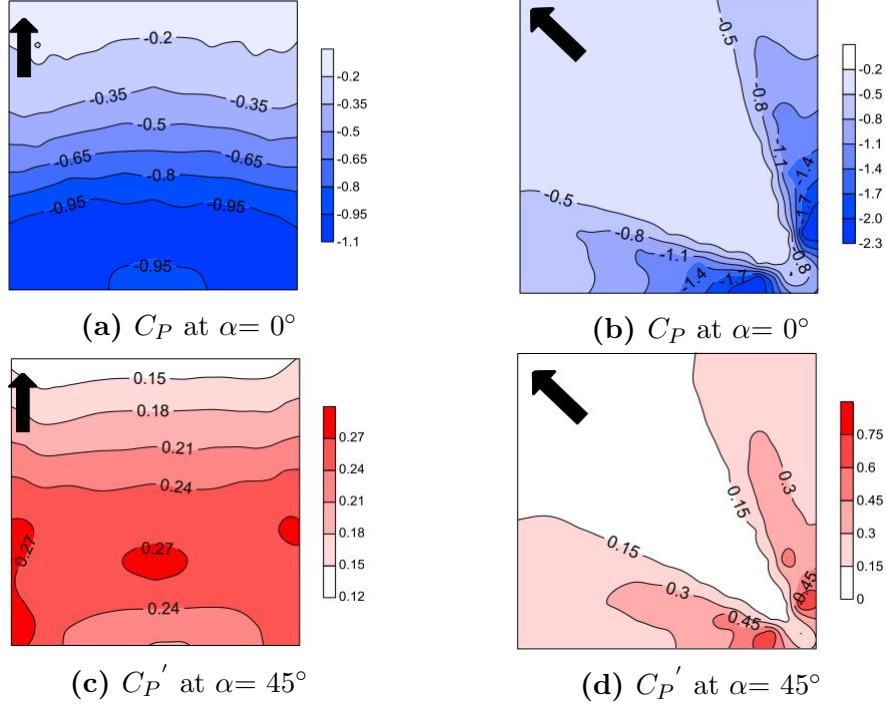


**Figure 2.19:** Mean free-end  $C_P$  distribution for a square prism with AR = 0.5 at (a)  $\alpha = 0^\circ$ , and (b)  $\alpha = 45^\circ$ , and  $C_P'$  contours for the same prism at (c)  $\alpha = 0^\circ$ , and (d)  $\alpha = 45^\circ$ , sampled in an atmospheric boundary layer condition. The black arrow indicates the flow direction - reproduced from Chen et al. (2018) with permission of Elsevier.

## 2.5 Aerodynamic forces

The aerodynamic forces experienced by the square prism result from the pressure and shear stress distributions on the surfaces of the prism. Two forces which are always associated with the flow around a bluff body are lift and drag forces. Lift force acts in the direction perpendicular to the flow, while drag force acts in the direction parallel to the flow. Most of the articles in the literature present the drag and lift forces as dimensionless parameters, which are the drag coefficient,  $C_D$  (Equation 1.2), and lift coefficient,  $C_L$  (Equation 1.3). There is also a third force, which is the normal force, which acts normal to the free-end surface of the prism. However, the normal force is commonly neglected in the literature. This section is therefore divided into two different subsections, which will review the two most common forces discussed in the literature: drag force coefficient (subsection 2.5.1) and lift force coefficient (subsection 2.5.2). The studies reviewed in this section mainly focus on the time-averaged mean drag and lift force coefficients, although some studies included some

details about the fluctuations in the drag and lift force coefficients (Sakamoto and Oiwake (1984) and Sakamoto (1985)).

### 2.5.1 Drag force coefficient

The drag force coefficient is a strong function of aspect ratio, incidence angle and boundary layer thickness, and a relatively weaker function of the Reynolds number. Wang et al. (2017) performed an experimental investigation from  $Re = 0.68 - 6.12 \times 10^5$  and concluded that the mean drag coefficient did not vary significantly with  $Re$  for both an infinite-prism and a finite-height square prism with  $AR = 5$ . The experiment results of McClean and Sumner (2014) and Wang et al. (2017) showed that the  $C_D$  for a finite square prism was always less than that of an infinite square prism.

The effect of the aspect ratio on the drag force coefficient was experimentally investigated by Akins and Paterka (1977), Sarode et al. (1981), Sakamoto and Oiwake (1984) and Sakamoto (1985), and McClean and Sumner (2014). Akins and Paterka (1977) measured the drag force coefficient for different combinations of aspect ratio and boundary layer thickness. The aspect ratio was adjusted by varying both  $D$  and  $H$ , and therefore the study investigated on both square and rectangular prisms. By changing the aspect ratio through  $D$  (and formed different rectangular prisms with different free-end areas), Akins and Paterka (1977) observed the change in  $C_D$  was more significant, in comparison to the case where  $AR$  was changed by varying  $H$ . Sakamoto (1985) also evaluated the trend of  $C_D$  at 18 different aspect ratios from  $AR = 1$  to 6 (changed by varying  $D$ ). The results of Sakamoto (1985) showed higher sensitivity of  $C_D$  to the change of  $AR$ , as compared to Akins and Paterka (1977). By increasing the  $AR$  through increasing the width of the prism, Sakamoto (1985) observed the magnitude of  $C_D$  at  $\alpha = 0^\circ$  increased with  $AR$  of the rectangular prism. This increase trend was most pronounced at low  $AR$  region ( $AR = 1$  to 3), and the increase rate became less rapid at a higher range of aspect ratios tested ( $AR = 3$  to 6). Sakamoto (1985) explained that the increase in  $C_D$  with  $AR$  was due to the decrease in surface pressure,  $C_P$ , on the rear surface of the prism when  $AR$  was higher. The  $C_P$  on the rear surface was measured at  $z/H = 0.75$ . On the other hand, Sarode et al. (1981) and Sakamoto (1985) changed the aspect ratio by varying the height of the prism, and observed a similar remarkable increase

trend in drag force coefficient with AR for both  $\alpha = 0^\circ$  (for both studies) and  $45^\circ$  (Sarode et al. (1981) only). McClean and Sumner (2014) provided more detailed information about the trend of  $C_D$  for five aspect ratios (AR = 3, 5, 7, 9, and 11 - changed by varying the height,  $H$ ) for a wide range of incidence angles,  $\alpha = 0^\circ$  to  $45^\circ$ . A similar trend of the increase in  $C_D$  with AR was observed, but the result of McClean and Sumner (2014) also interestingly showed a fairly sharp plateau in the  $C_D$  versus  $\alpha$  curve at  $\alpha \simeq 10^\circ$  for the prisms with higher aspect ratio (AR = 9 and 11). Also, the mean  $C_D$  of the smallest AR tested (AR = 3) was relatively insensitive to the change of  $\alpha$  as compared to other prisms with higher AR.

The variation of  $C_D$  with the incidence angle was further investigated by Akins and Paterka (1977), Sarode et al. (1981), Sakamoto (1985), and McClean and Sumner (2014). Out of all these studies, only the study of Akins and Paterka (1977) showed that  $C_D$  generally decreased with  $\alpha$ , while the rest showed that  $C_D$  decreased with  $\alpha$  until the critical angle,  $\alpha_c$ , and then the  $C_D$  increased again gradually until  $\alpha = 45^\circ$ , and therefore the curve of  $C_D$  versus  $\alpha$  formed a minimum peak at  $\alpha_c$ . For the study of Sarode et al. (1981), the critical angle (where minimum  $C_D$  value was attained) was not apparent for the lower aspect ratio prisms (AR  $\leq 3.64$ ), while the critical angle for the other prisms with higher aspect ratios (AR = 6.36 and 10) lied between the range of  $10^\circ \leq \alpha \leq 25^\circ$  (but the absolute single value for  $\alpha_c$  was still undefined due to the absence of a well-defined peak). The incidence angle increment adopted by Sarode et al. (1981) was  $5^\circ$ , which was the same as Sakamoto (1985). Nevertheless, the results of Sakamoto (1985) showed a much higher variation in mean  $C_D$  with  $\alpha$ . There was a minimum peak observed between  $\alpha_c = 13^\circ$  (for smallest AR tested, AR = 1) to  $17^\circ$  (for largest AR tested, AR = 5). McClean and Sumner (2014) adopted a smaller increment in  $\alpha$  ( $1^\circ$ ), and plotted the  $C_D$  versus  $\alpha$  curve for five aspect ratios (AR = 3, 5, 7, 9, and 11). McClean and Sumner (2014) found that the variation of  $C_D$  with  $\alpha$  of a finite-height prism was less sensitive as compared to the infinite square prism. The  $\alpha_c$  identified by McClean and Sumner (2014) were  $\alpha_c = 16^\circ$  for AR = 11, 9, 5, and 3;  $\alpha_c = 18^\circ$  for AR = 7. The comparison of the  $C_D$  versus  $\alpha$  curve for both studies of Sakamoto (1985) and McClean and Sumner (2014) is shown in Figure 2.20.

Both Sakamoto (1985) and McClean and Sumner (2014) explained that the decrease of  $C_D$  before these critical angles was due to the reattachment of the shear layer separated at

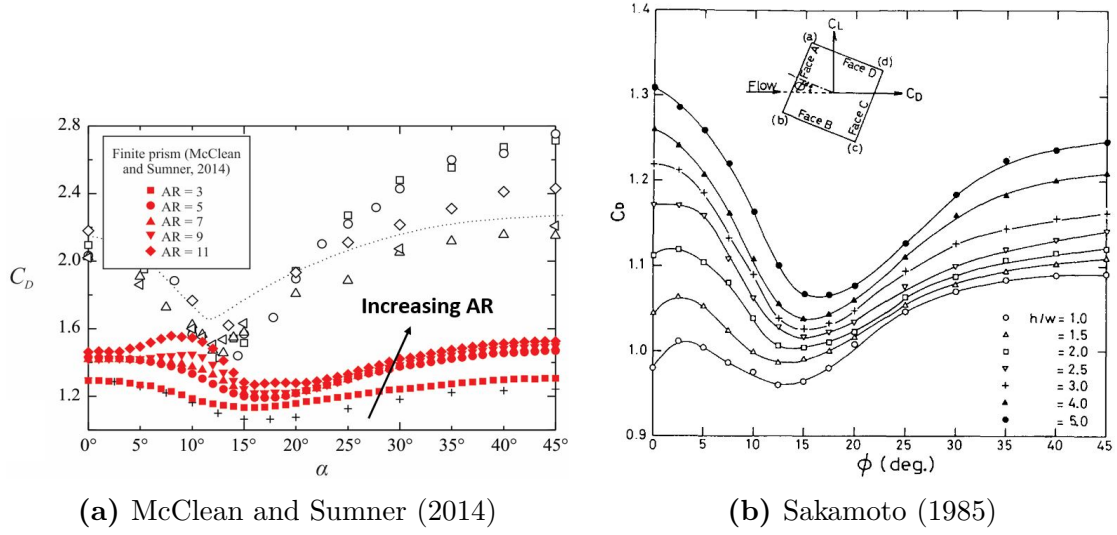


**Figure 2.20:** Mean drag force coefficient,  $C_D$  versus  $\alpha$  experimentally investigated by (a) McClean and Sumner (2014) ( $Re = 7.3 \times 10^4$ ,  $\delta/D = 1.5$ ) (used with permission of ASME) and (b) Sakamoto (1985) ( $Re = 3.3 \times 10^4$ ,  $\delta/H = 0.7$ ) (used with permission of Elsevier). The symbol  $\phi$  and  $h/w$  in the right diagram represent the incidence angle and aspect ratio, respectively, which are denoted by  $\alpha$  and AR in the present thesis. McClean and Sumner (2014) changed AR by varying  $H$ , while Sakamoto (1985) changed AR by varying  $D$ .

the sharp corner to the lower side of the prism, discussed in section 2.2. Recall from Table 2.1 that there was a critical angle, where the flow regime switched from the separation mode to reattachment mode, based on the studies of Igarashi (1984), Huang et al. (2010), and Yen and Yang (2011) for an infinite square prism. These studies also investigated the variation in  $C_D$  with  $\alpha$  for an infinite square prism, and the values were  $\alpha_c = 12^\circ$  for Igarashi (1984) and Yen and Yang (2011), and  $\alpha_c = 15^\circ$  for Huang et al. (2010). Table 2.3 summarizes different critical angles in different studies, and the estimated corresponding minimum  $C_D$  value. It appears that the critical angle for the infinite square prism was smaller than the finite-height prism. Moreover,  $\alpha_c$  for the finite-height square prism increased when a prism with higher AR was used.

The investigations of variation in  $C_D$  with  $\alpha$  by Sarode et al. (1981), Sakamoto (1985), and McClean and Sumner (2014) were performed at a single boundary layer thickness (Table 2.3). In the same study of Sakamoto (1985), the effect of boundary layer thickness was further investigated by adopting different combinations of the tripping rod diameter (installed upstream) and freestream velocity,  $U_\infty$  for four aspect ratios (AR = 2, 3, 4, and 5). For this

**Table 2.3:** Summary of critical angles,  $\alpha_c$  for different experimental investigations based on minimum  $C_D$ . The values shown are estimated by visually inspecting the  $C_D$  versus  $\alpha$  curve in the studies listed below.

Infinite Square Prism					
Study	Re	$\delta/D$	AR	$\alpha_c$	$C_{D,min}$
Igarashi (1984)	$3.7 \times 10^4$	$\sim 0$	(2D)	$12^\circ$	1.7
Huang et al. (2010)	$2.0 \times 10^4$	$\sim 0$	(2D)	$15^\circ$	not shown
Yen and Yang (2011)	$6.3 \times 10^3$	$\sim 0$	(2D)	$12^\circ$	1.3
Finite Square Prism					
Study	Re	$\delta/D$	AR	$\alpha_c$	$C_{D,min}$
Sarode et al. (1981)	$2.2 \times 10^4$	20	1.14	undefined	undefined
			2.27	undefined	undefined
			3.64	undefined	undefined
			6.36	$10^\circ - 25^\circ$	0.68
			10.00	$10^\circ - 25^\circ$	0.82
Sakamoto (1985)	$3.3 \times 10^4$	0.7 - 2.7 * ( $\delta/H = 0.7$ )	1.0	$13^\circ$	0.96
			1.5	$13^\circ$	0.98
			2.0	$15^\circ$	1.01
			2.5	$15^\circ$	1.02
			3.0	$15^\circ$	1.03
			4.0	$15^\circ$	1.04
			5.0	$17^\circ$	1.07
McClean and Summer (2014)	$7.3 \times 10^4$	1.5	3	$16^\circ$	1.13
			5	$16^\circ$	1.19
			7	$18^\circ$	1.20
			9	$16^\circ$	1.22
			11	$16^\circ$	1.27

\*Sakamoto (1985) varied the AR by changing  $D$  which resulted multiple values of  $\delta/D$ , despite only one single value of  $\delta$  was used for this investigation.

investigation of the effect of incoming flow condition, Sakamoto (1985) varied the AR by changing  $H$  (recall that Sakamoto (1985) varied  $D$  for the investigation about the effect  $\alpha$ ). The investigation for the effect of the boundary layer characteristics was also performed at  $\alpha = 0^\circ$  only. It was observed by Sakamoto (1985) that for all aspect ratios, the value of  $C_D$  increased linearly with the value of  $H/\delta$ , i.e. a thicker boundary layer (relative to the height of the prism) resulted in smaller drag force coefficient. In the similar study of Sakamoto and Oiwake (1984), where AR was varied by manipulating  $D$ , a similar observation was shown which illustrated the value of  $C_D$  increased rapidly with the value of  $H/\delta$ .

### 2.5.2 Lift force coefficient

Lift force is less commonly investigated compared to the drag force. For a square prism, the lift force coefficient is a strong function of  $\alpha$ . The mean lift force is zero at  $\alpha = 0^\circ$  and  $45^\circ$ . When the square prism is rotated at other  $\alpha$ , a mean lift force will be experienced by the prism. Based on the clockwise rotation of the prism as specified in Figure 2.1, the lift force is induced in the  $-y$  direction. The behavior of  $C_L$  was investigated by Akins and Paterka (1977), Sarode et al. (1981), Sakamoto (1985), and McClean and Sumner (2014).

The effect of the aspect ratio on the lift force coefficient was found similar to that of the drag force coefficient. It was observed by Sarode et al. (1981), Sakamoto (1985), and McClean and Sumner (2014) that the magnitude of  $C_L$  generally increased (became more negative) with an increase in AR. The difference in  $C_L$  at different aspect ratios was most pronounced close to the critical angles. McClean and Sumner (2014) observed that the  $C_L$  magnitude was generally greater for an infinite-height square prism in comparison to the finite square prism. For all the studies above-mentioned, it was evident that  $C_L$  was much more sensitive to the change of  $\alpha$  than that of the  $C_D$  for all aspect ratios investigated. Comparing the  $C_L$  versus  $\alpha$  curve at various aspect ratios, it was observed that when the aspect ratio decreased, the curve of  $C_L$  became relatively less sensitive to  $\alpha$ , and thus the peak shape of the curve is relatively less pronounced for the prism with the lowest aspect ratio.

The effect of  $\alpha$  was also investigated by Akins and Paterka (1977), Sarode et al. (1981), Sakamoto (1985), and McClean and Sumner (2014). Similar to the trend of  $C_D$ , only the study of Akins and Paterka (1977) showed that the magnitude of  $C_L$  generally increased (became more negative) with  $\alpha$ , while the other studies showed that the magnitude of  $C_L$  increased only until the critical angle. Sarode et al. (1981) found that, regardless of the aspect ratios used, the maximum magnitude of  $C_L$  was observed at  $\alpha_c \simeq 10^\circ$ . Sakamoto (1985) observed critical angles to be  $\alpha_c = 7^\circ$  (for smallest AR tested, AR = 1) to  $13^\circ$  (for largest AR tested, AR = 5). For McClean and Sumner (2014), the critical angles for the mean  $C_L$  were  $\alpha_c = 16^\circ$  for AR = 11, 9, 5, and 3;  $\alpha_c = 15^\circ$  for AR = 5;  $\alpha_c = 12^\circ$  for AR = 3. The  $\alpha_c$  identified by Sakamoto (1985) and McClean and Sumner (2014) tended to decrease with AR, while the  $\alpha_c$  observed by Sarode et al. (1981) were nearly independent

of AR. Figure 2.21 illustrates the  $C_L$  versus  $\alpha$  curves obtained experimentally by Sakamoto (1985) and McClean and Sumner (2014).

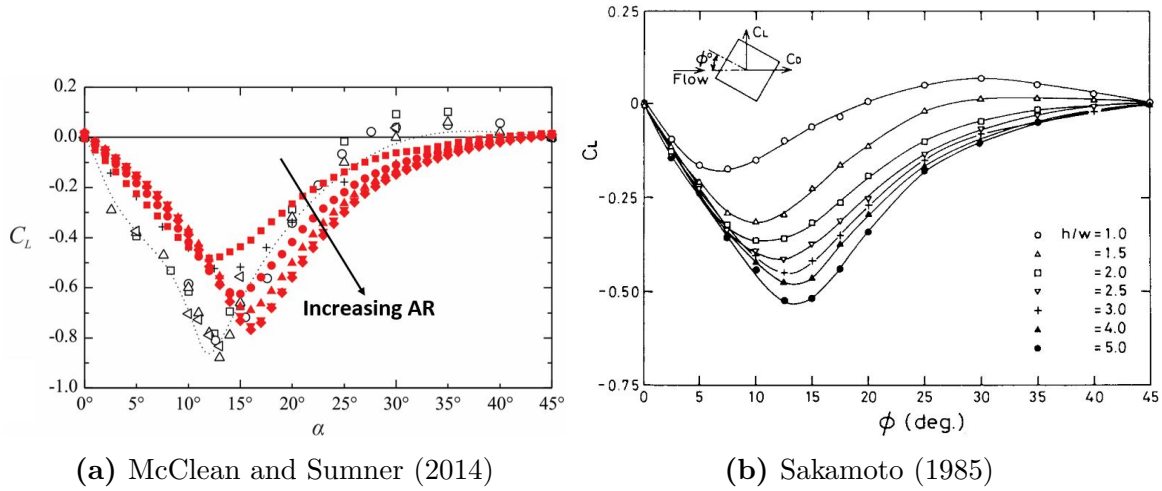


**Figure 2.21:** Mean lift force coefficient,  $C_L$  versus  $\alpha$  experimentally investigated by (a) McClean and Sumner (2014) ( $Re = 7.3 \times 10^4$ ,  $\delta/D = 1.5$ ) (used with permission of ASME) and (b) Sakamoto (1985) ( $Re = 3.3 \times 10^4$ ,  $\delta/H = 0.7$ ) (used with permission of Elsevier). The symbol  $\phi$  and  $h/w$  in the right diagram represent the incidence angle and aspect ratio, respectively, which are denoted by  $\alpha$  and AR in the present thesis. McClean and Sumner (2014) changed AR by varying  $H$ , while Sakamoto (1985) changed AR by varying  $D$ .

The studies of Igarashi (1984), Huang et al. (2010), and Yen and Yang (2011) revealed that the critical angle based on maximum magnitude of lift for an infinite prism were  $\alpha_c = 14^\circ$ ,  $15^\circ$ , and  $13^\circ$ , respectively. It is worth pointing out that these values were close to the critical angles where they observed the change of the flow regime from a perfect separation type to the reattachment mode. Also, Unnikrishnan et al. (2017) showed the highest asymmetrical wake profile at  $\alpha = 15^\circ$  (subsection 2.3.3), which is close to the critical angle based on the  $C_L$  versus  $\alpha$  curve as well. This observation infers that the greatest magnitude of lift is obtained at the occurrence of the highest asymmetrical wake profile, which is close to the region where the flow regimes switched from the perfect separation to the mode where shear layer reattached onto the bottom surface of the prism. The critical angles in different studies, and the estimated corresponding minimum  $C_L$  values are summarized in Table 2.4.

The effect of boundary layer thickness on  $C_L$  and  $\alpha_c$  based on the maximum magnitude of lift was not investigated further by Sarode et al. (1981), Sakamoto (1985), and McClean and

**Table 2.4:** Summary of critical angles,  $\alpha_c$  for different experimental investigations based on minimum  $C_L$ . The values shown are estimated by visually inspecting the  $C_L$  versus  $\alpha$  curve in the studies listed below.

Infinite Square Prism					
Study	Re	$\delta/D$	AR	$\alpha_c$	$ C_L _{max}$
Igarashi (1984)	$3.7 \times 10^4$	$\sim 0$	(2D)	$14^\circ$	0.8
Huang et al. (2010)	$2.0 \times 10^4$	$\sim 0$	(2D)	$15^\circ$	not shown
Yen and Yang (2011)	$6.3 \times 10^3$	$\sim 0$	(2D)	$13^\circ$	0.85
Finite Square Prism					
Study	Re	$\delta/D$	AR	$\alpha_c$	$ C_L _{max}$
Sarode et al. (1981)	$2.2 \times 10^4$	20	1.14	$10^\circ$	0.07
			2.27	$10^\circ$	0.13
			3.64	$10^\circ$	0.18
			6.36	$10^\circ$	0.26
			10.00	$10^\circ$	0.33
Sakamoto (1985)	$3.3 \times 10^4$	0.7 - 2.7 * ( $\delta/H = 0.7$ )	1.0	$7^\circ$	0.20
			1.5	$10^\circ$	0.28
			2.0	$10^\circ$	0.36
			2.5	$12^\circ$	0.42
			3.0	$12^\circ$	0.44
			4.0	$13^\circ$	0.48
McClean and Summer (2014)	$7.3 \times 10^4$	1.5	5.0	$13^\circ$	0.52
			3	$12^\circ$	0.48
			5	$15^\circ$	0.63
			7	$16^\circ$	0.69
			9	$16^\circ$	0.75
			11	$16^\circ$	0.77

\*Sakamoto (1985) varied the AR by changing  $D$  which resulted multiple values of  $\delta/D$ , despite only one single value of  $\delta$  was used for this investigation.

Sumner (2014). The result of Akins and Paterka (1977), however, somewhat illustrated the effect of boundary layer characteristic on the  $C_L$  values. Akins and Paterka (1977) adopted four boundary layers in their experiments with constant thickness, but with different wall shear stress or friction velocity. It was observed that the magnitude of  $C_L$  decreased slightly when the friction velocity at the wall increased, regardless of the aspect ratios used.

## 2.6 Strouhal number

The Strouhal number has been determined with various methods in different studies, such as through measuring the fluctuation in velocity (e.g: Wang and Zhou (2009), Bourgeois et al.

(2011), Kindree et al. (2018)), fluctuation in lift force (e.g: Sakamoto (1985), Wang et al. (2017)), and also fluctuation in pressure (Kindree et al. (2018)).

The Strouhal number at  $\alpha = 0^\circ$  for a single aspect ratio has been studied extensively by Wang and Zhou (2009), Bourgeois et al. (2011), Sattari et al. (2012), and Kindree et al. (2018). Wang and Zhou (2009), Bourgeois et al. (2011), and Sattari et al. (2012) used hotwire anemometry to measure the fluctuation in local streamwise velocity for a square prism with aspect ratios of  $AR = 7, 4$ , and  $4$ , respectively, at three to five different spanwise locations, and three streamwise locations within the wake region. Wang et al. (2017), also obtained power spectra at four different spanwise locations, but the Strouhal number was determined based on the fluctuation in lift force, which was calculated by integrating the surface pressure around the square prism's surface. The aspect ratio used by Wang et al. (2017) was  $AR = 5$ . On the other hand, Kindree et al. (2018) performed a variety of measurements of fluctuating of spanwise velocity, lateral velocity, surface pressure on the ground plane, and surface pressure on the bottom surface of the prism, to determine  $St$  for a square prism with  $AR = 4$ . Wang and Zhou (2009) and Wang et al. (2017) showed that the Strouhal number for a finite-height square prism was lower than that of the infinite square prism. Figure 2.22 illustrates the power spectral density obtained by Wang and Zhou (2009) at different spanwise and streamwise locations. Kindree et al. (2018) showed that the power spectral density (based on velocity fluctuation) obtained above the free-end surface did not show a remarkable peak, which suggests the vortex shedding was not dominant in the region closer to the free-end surface.

The effect of the aspect ratio on the Strouhal number has been experimentally investigated by Sakamoto and Oiwake (1984) and Porteous et al. (2017) at  $\alpha = 0^\circ$  only. Sakamoto and Oiwake (1984) varied the aspect ratio by changing  $D$ , and formed different rectangular prisms. The Strouhal number was calculated based on the fluctuation of lift (measured by strain-gauge balance) and vortex shedding frequency (measured by hot-film anemometer). There was a strong agreement between the Strouhal numbers obtained by both methods, and it was clearly illustrated by Sakamoto and Oiwake (1984) that the Strouhal number increased gradually with the aspect ratio. There were a total 18 of aspect ratios used by Sakamoto and Oiwake (1984) for a range of  $AR = 1$  to  $6$ .

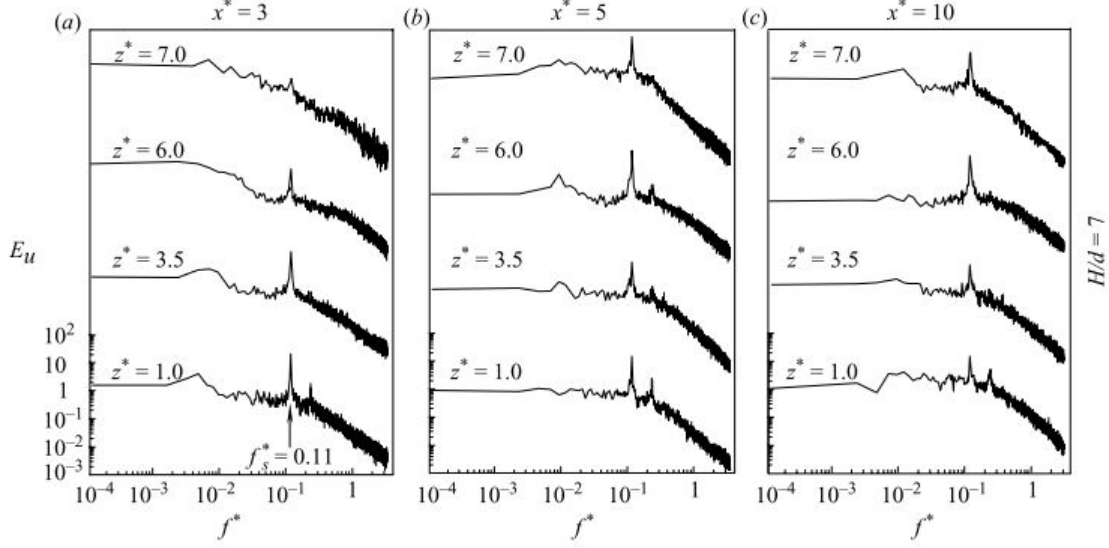


**Figure 2.22:** Power spectral density reproduced from Wang and Zhou (2009) at three streamwise location and four spanwise locations; used with permission of Cambridge University Press. The symbols  $x^*$  and  $z^*$  are denoted by  $x/D$  and  $z/D$  in the present thesis. The symbol of  $f^*$  is the dimensionless frequency, which is the Strouhal number,  $St$ . The notation  $E_u$  is the power spectral density, and the small letter  $d$  is the width of the prism and same as the capital letter  $D$  in the present thesis.

The other study of Porteous et al. (2017) on the effect of AR was much more comprehensive, with the adoption of 80 aspect ratios in total, for a wide range of  $0.29 \leq AR \leq 22.9$ . Porteous et al. (2017) identified four distinct shedding regimes based on the variation of  $St$  (using microphone measurement) with a wide range of AR as shown in Figure 2.23. The first regime occurred at a range of very low aspect ratio ( $AR < 2$ ), where the well-defined peak was not evident in the power spectral density. In the second shedding regime, Porteous et al. (2017) observed a single and relatively sharper peak around  $St = 0.1$ , for the aspect ratio range of  $2 \leq AR < 10$ . The values of  $St$  were slightly discernible for different AR at this regime. Porteous et al. (2017) showed that  $St \simeq 0.1$  for  $AR = 4.3$  and  $7.1$ , while the  $St$  value for higher aspect ratio of  $AR = 10$  was found slightly lower than  $0.1$  (Figure 2.23(b)). Notably, at this shedding regime, Porteous et al. (2017) observed the peak magnitude was the highest at  $AR = 4.3$ , but weaker at  $AR = 7.1$ . The aspect ratio range for the third shedding regime range was  $10 < AR < 18$ , as identified by Porteous et al. (2017). In this regime, it is interestingly observed the formation of two shedding peaks, with one occurring at  $St < 0.1$ , and the other at  $St > 0.1$ . For the final shedding regime ( $AR \geq 18$ ), there was an

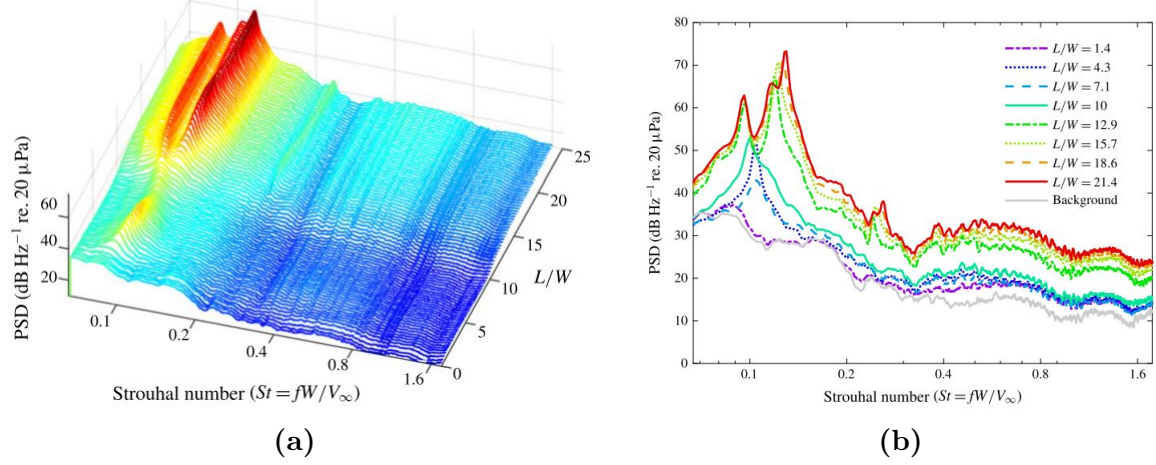


**Figure 2.23:** Power spectral density versus the  $St$  experimentally obtained by Porteous et al. (2017) for (a) waterfall diagram based on a wide range of aspect ratio ( $0.29 \leq AR \leq 22.9$ ), and (b) selected aspect ratios only. The symbols  $L$ ,  $W$ , and  $V_\infty$  in the diagram correspond to the symbols of  $H$ ,  $D$ , and  $U_\infty$  used in the present thesis. Used with permission of Cambridge University Press.

existence of the third peak (though it was relatively less remarkable). For the third and fourth shedding regime (where the aspect ratio lied between 10.0 to 22.9), the shedding frequency of the primary (most well-defined) peak shifted to the right (which led to an increase in  $St$ ) when the aspect ratio increased. The Strouhal numbers at the three identified peaks are summarized in Figure 2.24. Porteous et al. (2017) further explained that the generation of different peaks was related to the different characteristics in vortex filaments formation across various spanwise locations within the near-wake region, when  $AR$  varied.

The combined effects of the aspect ratio and incidence angle on  $St$  were further investigated by Sakamoto (1985) and McClean and Sumner (2014), with identical methodology as the investigation on  $C_D$  and  $C_L$  as described in subsection 2.5.1 and 2.5.2. Similarly, the presence of the critical angle was evident, where the Strouhal number obtained a maximum value, as shown in Figure 2.25. Sakamoto (1985) observed  $\alpha_c$ , where the Strouhal number was maximum, to be  $12^\circ$  (for smallest  $AR$  tested,  $AR = 1$ ) to  $15^\circ$  (for largest  $AR$  tested,  $AR = 5$ ), while McClean and Sumner (2014) obtained the Strouhal number at the mid-span location, and concluded  $\alpha_c = 17^\circ$  for  $AR = 11$ ;  $\alpha_c = 16^\circ$  for  $AR = 9$  and  $7$ ;  $\alpha_c = 15^\circ$  for  $AR = 5$  and  $3$ . Comparing with the data of an infinite prism, both studies showed that the  $\alpha_c$  was slightly higher for the finite-height prism, and McClean and Sumner (2014) explained

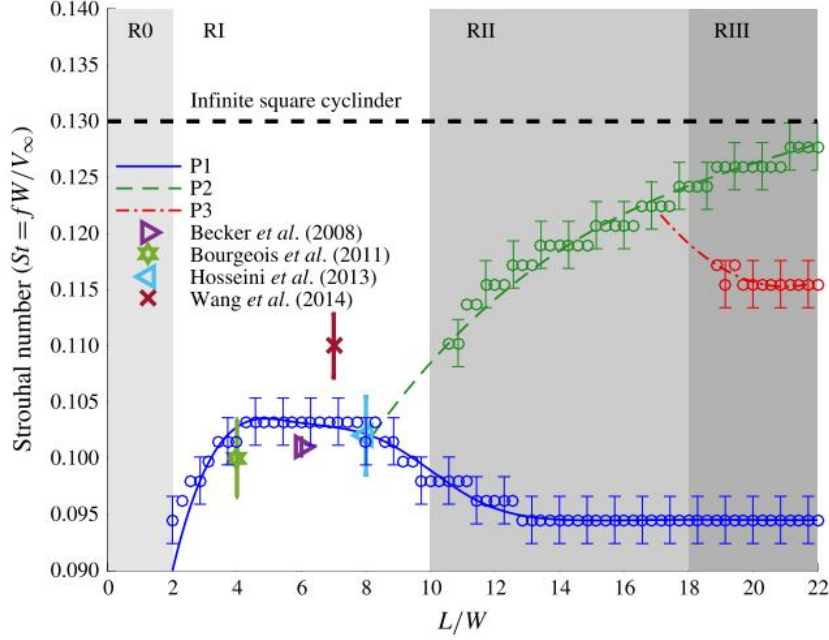


**Figure 2.24:** The variation of  $St$  with  $AR$  based on the peaks identified in different shedding regimes - reproduced from Porteous et al. (2017) with permission of Cambridge University Press. The symbols of R0, RI, RII and RIII denote different shedding regimes; the symbols P1, P2, P3 represent the different series of  $St$  based different peaks observed; the symbols  $L$ ,  $W$ , and  $V_\infty$  in the diagram correspond to the symbols of  $H$ ,  $D$ , and  $U_\infty$  used in the present thesis.

that the free-end effect delayed the reattachment process and separation bubble formation. Both studies also showed the Strouhal numbers for all aspect ratios tested were lower than an infinite square prism and decreased with the aspect ratio. Additionally, the trend of the Strouhal number behaved similarly to the infinite square prism, and the Strouhal number was sensitive to  $\alpha$ , but the increase trend in  $St$  was found less sensitive to  $AR$ , as compared to the increase trend of  $C_D$  and  $C_L$  with the change of  $AR$  as discussed in subsections 2.5.1 and 2.5.2. The critical angles based on maximum  $St$  were also similar to the critical angles where the minimum  $C_D$  and maximum magnitude of  $C_L$  were observed. Sakamoto (1985) further explained the maximum  $St$  at the critical angle corresponded to the smallest wake width and minimum vortex spacing, resulted in increase of vortex shedding frequency. The smallest wake width was also an indication of the occurrence of minimum drag force coefficient. Moreover,  $\alpha_c$  obtained by McClean and Sumner (2014) was  $16^\circ$  for  $C_D$ ,  $C_L$  and  $St$ , and this  $\alpha_c$  value is very close to  $\alpha_c = 15^\circ$  identified by Unnikrishnan et al. (2017) where highest wake asymmetry

and minimum length of recirculation zone were observed, as described in subsection 2.3.3. An obvious different behavior in the  $St$  versus  $\alpha$  curve can also be observed for  $AR = 3.0$ , where the curve became relatively more flat in shape (similar trend can be observed for  $C_D$  versus  $\alpha$  and  $C_L$  versus  $\alpha$  curves). This finding can also be related to the observation by Wang and Zhou (2009) and Unnikrishnan et al. (2017) (in subsection 2.3.2 and 2.3.3) where the wake profile changed abruptly with a double peak formation and vorticity contours switched from quadrupole to dipole type, when  $AR$  decreased from 7 to 3. McClean and Sumner (2014) also showed power spectra at different spanwise locations for  $\alpha = 0^\circ, 15^\circ, 30^\circ$ , and  $45^\circ$ . It was observed that the power spectra were more broad-banded at higher spanwise locations for those prisms with larger aspect ratio ( $AR = 9$  and  $11$ ). Generally, the broad-banded power spectra behaviour was also observed at higher incidence angle of  $\alpha = 30^\circ$  and  $45^\circ$ , as compared to those of  $\alpha = 0^\circ$  and  $15^\circ$ . This trend was also observed by Sakamoto (1985), where no  $St$  was identified when  $\alpha > 15^\circ$  for  $AR = 1.5$ ,  $\alpha > 20^\circ$  for  $AR = 2$ ,  $\alpha > 25^\circ$  for  $AR = 2.5$ , and  $\alpha > 30^\circ$  for  $AR = 3$ , due to the absence of strong fluctuating wakes and vortex shedding at this combination of  $AR$  and  $\alpha$ .

The other study which investigated the effect of incidence angle was performed by Sohankar et al. (2018), where various curves of  $St$  versus  $\alpha$  were plotted for different series of  $Re$  (instead of  $AR$  as the studies of Sakamoto (1985) and McClean and Sumner (2014)). The Reynolds number of the experimental investigation by Sohankar et al. (2018) was varied in a wide range, from  $Re = 6.5 - 28.5 \times 10^3$ , and a single aspect ratio of  $AR = 7$  was used. The experimental investigation of Sohankar et al. (2018) somewhat challenged the strong-standing belief of  $Re$  independency on the flow structure around a square prism. The critical angle identified by Sohankar et al. (2018) was  $\alpha_c = 15^\circ$ , regardless of the Reynolds number of the incoming flow. However, it was interestingly observed in their investigation that the  $St$  value decreased progressively as the  $Re$  increased, and the rate of decrease became insensitive once  $Re$  was sufficiently large ( $Re > 1.5 \times 10^4$ ). The critical angles for different studies at various  $AR$  and  $Re$  are summarized in Table 2.5. Similar to the data of  $C_D$  and  $C_L$  in previous Section 2.5, the critical angle for the infinite square prism is presented in this Table as well. Notably, despite at  $\alpha_c$ , where  $St$  showed the highest variation for different  $AR$  or  $Re$ , the value of  $St_{max}$  listed in Table 2.5 between different studies for finite-height square prism still did not

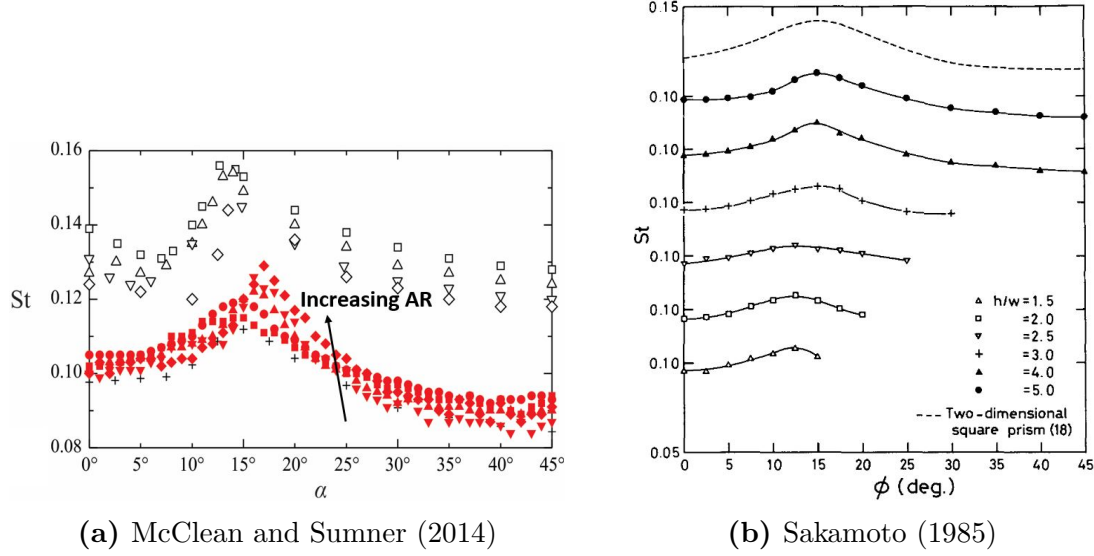


**Figure 2.25:** Strouhal number,  $St$  versus  $\alpha$  experimentally investigated by (a) McClean and Sumner (2014) ( $Re = 7.3 \times 10^4$ ,  $\delta/D = 1.5$ ) (used with permission of ASME) and (b) Sakamoto (1985) ( $Re = 3.3 \times 10^4$ ,  $\delta/H = 0.7$ ) (used with permission of Elsevier). The symbol  $\phi$  and  $h/w$  in the right diagram represent the incidence angle and aspect ratio, respectively, which are denoted by  $\alpha$  and  $AR$  in the present thesis. McClean and Sumner (2014) changed  $AR$  by varying  $H$ , while Sakamoto (1985) changed  $AR$  by varying  $D$ .

vary significantly. The variance of  $St$  at  $\alpha = 0$  (not shown) was even smaller. This is most likely due to the studies of Sakamoto (1985), McClean and Sumner (2014), and Sohankar et al. (2018) adopted the aspect ratio range which only lies within the first two (out of four) shedding regimes identified by Porteous et al. (2017).

The effect of the boundary layer on vortex shedding was relatively less popular to date, but was investigated by Sakamoto and Oiwake (1984), Wang et al. (2017) and Kindree et al. (2018). Sakamoto and Oiwake (1984) studied the relationship between  $St$  and  $H/\delta$  for a rectangular prism with  $AR = 3$ . It was observed that the value of  $St$  increased almost linearly from about 0.08 to 0.10 when the value of  $H/\delta$  increased from 0.5 to 2.5, which indicates that a thicker boundary layer (relative to the height) resulted in slightly smaller vortex shedding frequency. Recall that Wang et al. (2017) adopted two different boundary layer conditions,  $\delta/D = 1$  and 7, in their experimental investigations for a single square prism of  $AR = 5$ , and measured  $St$  based on fluctuating lift. For all the spanwise locations investigated, Wang et al. (2017) also observed that the  $St$  value decreased slightly from

**Table 2.5:** Summary of critical angles,  $\alpha_c$  for different experimental investigations based on maximum  $St$ . The values shown are estimated by visually inspecting the  $St$  versus  $\alpha$  curve in the studies listed below.

Infinite Square Prism					
Study	Re	$\delta/D$	AR	$\alpha_c$	$St_{\max}$
Igarashi (1984)	$3.7 \times 10^4$	$\sim 0$	(2D)	$14^\circ$	0.155
Huang et al. (2010)	$1.3 \times 10^4$	$\sim 0$	(2D)	$15^\circ$	0.192
Yen and Yang (2011)	$6.3 \times 10^3$	$\sim 0$	(2D)	$13^\circ$	0.190
Finite Square Prism					
Study	Re	$\delta/D$	AR	$\alpha_c$	$St_{\max}$
Sakamoto (1985)	$3.3 \times 10^4$	0.7 - 2.7 * ( $\delta/H = 0.7$ )	1.5	$12^\circ$	0.1
			2.0	$12^\circ$	0.1
			2.5	$12^\circ$	0.1
			3.0	$15^\circ$	0.1
			4.0	$15^\circ$	0.1
			5.0	$15^\circ$	0.1
McClean and Summer (2014)	$7.3 \times 10^4$	1.5	3	$15^\circ$	0.115
			5	$15^\circ$	0.120
			7	$16^\circ$	0.122
			9	$16^\circ$	0.126
			11	$17^\circ$	0.129
Study	AR	$\delta/D$	Re	$\alpha_c$	$St_{\max}$
Sohankar et al. (2018)	7	0.5	$6.5 \times 10^3$	$15^\circ$	0.142
			$1.1 \times 10^4$	$15^\circ$	0.135
			$1.4 \times 10^4$	$15^\circ$	0.126
			$1.9 \times 10^4$	$15^\circ$	0.120
			$2.9 \times 10^4$	$15^\circ$	0.115

\*Sakamoto (1985) varied the AR by changing  $D$  which resulted multiple values of  $\delta/D$ , despite only one single value of  $\delta$  was used for this investigation.

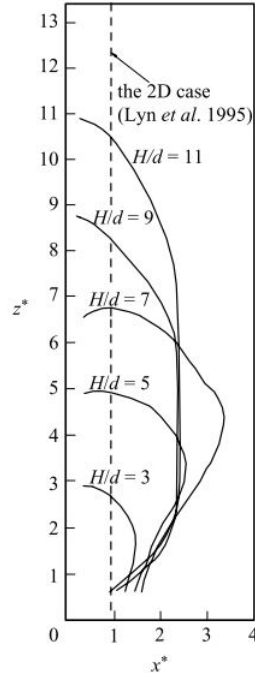
0.104 to 0.074, when the value of  $\delta/D$  was changed from 1 to 7. Additionally, the power spectra showed a more broad-banded peak when a thicker boundary layer was used. Kindree et al. (2018) performed a relatively more comprehensive study about the effect of boundary layer by using three different incoming flow conditions as follows: laminar, transitioning, and turbulent boundary layer. The results of Kindree et al. (2018), on the other hand, did not show an obvious shifting in the vortex shedding frequency for three conditions of boundary layer, but they observed a low-frequency signature (with a value about 10 times smaller than the shedding frequency) for the laminar and transitioning boundary layer ( $\delta/D = 0.21$  and  $0.22$ ;  $Re = 10,500$  and  $15,200$ , respectively), but this low-frequency signature disappeared for the case of turbulent boundary layer  $\delta/D = 1.02$ ,  $Re = 10,500$ ).

## 2.7 Vortex formation length

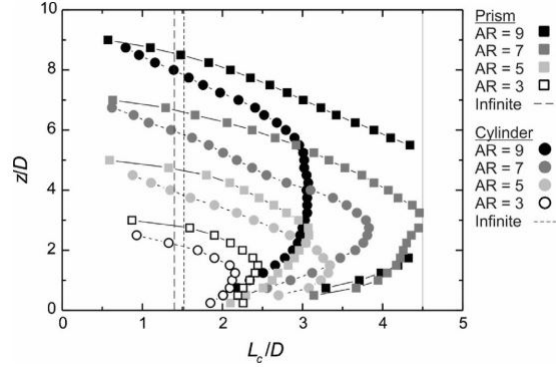
Vortex formation length,  $L_f$ , is defined as the longitudinal distance (parallel to the flow) from the centre of the prism until the dividing streamline which marks the end of the mean recirculation zone behind the body. In the literature, the formation length was determined by using several different methods, such as inspecting the velocity flow field vectors in PIV measurement (Wang and Zhou (2009) and Sumner et al. (2017)), using a seven-hole pressure probe to study the velocity flow field (Unnikrishnan et al. (2017)), or measuring the maximum velocity fluctuation or turbulence intensity with hotwire anemometry (Porteous et al. (2017)). The aspect ratio range for each study is different, but generally lied between the range of  $3 \leq \text{AR} \leq 11$  (Table 2.6), which was still within the first two (out of four) shedding regimes identified by Porteous et al. (2017).

There were some similarities observed between each studies above-mentioned. First, it was observed that the vortex formation length of a finite-square prism was found longer than that of the infinite square prism, regardless of the aspect ratios investigated. Second, it was found that the vortex formation length varied at different spanwise locations, and the shortest length was found at the region closer to the free end. These observations suggest that the downwash flow elongated the formation length, and also resulted in the dependency of the formation length on the spanwise location. However, some differences between each investigations are also observed, in terms of the shape of the curve of spanwise distance,  $z/D$ , versus dimensionless formation length,  $L_f/D$ , the spanwise location of the maximum formation length, and the critical aspect ratio based on the formation length. Wang and Zhou (2009) observed the curve of  $z/D$  versus  $L_f$  formed a flat plateau along the middle portion of the spanwise location, for the prism with higher aspect ratio ( $\text{AR} = 9$  and  $11$ ). For the intermediate aspect ratios ( $\text{AR} = 5$  and  $7$ ), there was a clear sharp peak can be identified in the curve of Wang and Zhou (2009) (Figure 2.7(a)). The result of Sumner et al. (2017), on the other hand, showed a well-defined peak in the  $z/D$  versus  $L_f$  curve for all square prisms from  $\text{AR} = 3$  to  $9$ , without an obvious flat plateau (Figure (b)). Unnikrishnan et al. (2017) proposed a dimensionless formation length of  $L_f/H$  instead of  $L_f/D$ . The result of Unnikrishnan et al. (2017) showed a flat plateau at the region below the mid-span location,

for  $AR = 5, 7$  and  $9$ . There was no decrease in  $L_f$  towards the spanwise location closer to the ground plane, as shown by Wang and Zhou (2009) and Sumner et al. (2017). The main reason for this difference was Unnikrishnan et al. (2017) used a seven-hole pressure probe which may have some limitation in capturing the reverse flow from certain angles. Comparing the differences in terms of the maximum formation length, Wang and Zhou (2009) observed that the  $L_{f,max}$  occurred slightly above the mid-span for  $AR = 3$  and  $5$  based on the location of peak in the  $L_f$  versus  $x/D$  curve. The spanwise locations of the maximum formation length for the prisms with higher aspect ratio ( $AR = 9$  and  $11$ ), however, were undefined due to the formation of the flat plateau (Figure 2.7(a)). On the other hand, Sumner et al. (2017), showed that the spanwise location for the maximum formation length was close to or slightly below the mid-span of the prism, for  $AR = 3, 5$ , and  $7$ . Wang and Zhou (2009) and Porteous et al. (2017) have identified the critical aspect ratio of  $AR = 7$  and  $7.1$ , respectively, based on the effect of  $AR$  on the variation in maximum formation length or the formation length at mid-span location. According to the result of Wang and Zhou (2009), the maximum formation length increased from  $1.4$  to  $3.4$ , when  $AR$  increased from  $3$  to  $7$ . When the formation length increased further to  $AR = 9$ , the maximum formation length dropped to  $2.5$ . The change in the maximum formation length was then became relatively less sensitive, when the aspect ratio further increased to  $11$ . The result of Porteous et al. (2017) complemented the observation of Wang and Zhou (2009), where the formation length was found increased from  $L_f/D \simeq 2.2$  to  $6.0$ , when the  $AR$  increased from  $1.4$  to  $7.1$ ; decreased from  $L_f/D \simeq 6.0$  to  $1.2$ , when the  $AR$  increased further from  $7.1$  to  $12.9$ . Porteous et al. (2017) further related the maximum formation length (at critical aspect ratio of  $7.1$ ) to the lower peak magnitude observed in the power spectral density (as described in Section 2.7). Conversely, the results of both Sumner et al. (2017) and Unnikrishnan et al. (2017), showed the maximum formation length increased with  $AR$ , and did not retreat to a lower value at higher aspect ratio. The results of different studies about the vortex formation length at different aspect ratios are summarized in Table 2.6. The vortex formation lengths shown are based on the measurement at mid-span location, which did not vary significantly with the maximum vortex formation length. It should be noted that the scope of the present thesis related to the vortex formation length is limited to the mid-span location only.



(a) Wang and Zhou (2009)



(b) Sumner et al. (2017)

**Figure 2.26:** Vortex formation length (based on PIV measurement) at different spanwise locations experimentally investigated by (a) Wang and Zhou (2009) and (b) Sumner et al. (2017). The symbols  $x^*$  and  $z^*$  in the left figure represents the dimensionless distances, which are denoted by  $x^*/D$  and  $z/D$  in the present thesis; the symbol  $d$  is the same as the notation  $D$  in the present thesis, which represents the width of the prism. Used with permissions of Cambridge University Press and Elsevier.

Unnikrishnan et al. (2017) and Sohankar et al. (2018) also conducted further investigation about the effect of incidence angle on the formation length and wake width, respectively. Unnikrishnan et al. (2017) observed that the formation length reached its maximum value for all aspect ratios investigated at  $\alpha = 45^\circ$ , while Sohankar et al. (2018) observed the occurrence of the maximum wake width at two downstream locations of  $x/D = 3$  and 5. These observations were similar to the experimental investigation of Ozgoren (2006) which studied the variation in formation length and wake width for infinite-height square prism at  $\alpha = 0^\circ$  and  $45^\circ$ . Ozgoren (2006) obtained a similar result that illustrated both the formation length and wake width at  $\alpha = 45^\circ$  was greater than those of at  $\alpha = 0^\circ$ . Notably, Unnikrishnan et al. (2017) and Sohankar et al. (2018) also concluded that the formation length and wake width was minimum at the critical incidence angle of  $\alpha_c = 15^\circ$ , which was very similar to

**Table 2.6:** Summary of the vortex formation length at the mid-span location of the prism, at  $\alpha = 0^\circ$ . The values shown are estimated based on visually inspecting on the  $z/D$  (or  $z/H$ ) versus  $L_f/D$  ( $L_f/H$ ) curve in the studies listed below.

Study	Re	$\delta/D$	AR	$L_f/D$ at mid-span
Wang and Zhou (2009)	$9.3 \times 10^3$	1.4	3	1.3
			5	2.4
			7	3.2
			9	2.5
			11	2.5
Porteous et al. (2017)	$1.4 \times 10^4$	1.3	1.4	2.2
			4.3	4.2
			7.1	6.0
			10.0	3.6
			12.9	1.2
			15.7	1.1
			18.6	1.1
			21.4	1.0
Sumner et al. (2017)	$4.2 \times 10^4$	1.5	3	2.5
			5	3.1
			7	4.5
			9	undefined*
Unnikrishnan et al. (2017)	$3.7 \times 10^4$	1.5	3	4.3
			5	5.9
			7	6.9
			9	7.4

\*The  $L_f$  at AR = 9 was longer than the velocity view plane in the PIV measurement

$\alpha_c$  for minimum  $C_D$ , maximum magnitude of  $C_L$ , and maximum St (Tables 2.3, 2.4, 2.5). Ozgoren (2006) and Bai and Alam (2018) have also studied the effect of Re on the formation length and wake width for an infinite-height square prism. However, it should be noted that the effect of  $\alpha$  and Re on the formation length is not the interest of the present thesis, as the scope of the current study intends to investigate the formation length at  $\alpha = 0^\circ$  only, with single Re, and focus more towards the effect of AR and  $\delta/D$ .

The experimental investigation about the effect of the boundary layer condition on the formation length is not abundantly available in the literature. Nevertheless, there are few recent numerical investigations to discuss this effect (Behera and Saha (2019) and Cao et al. (2019)). Behera and Saha (2019) adopted six different value of  $\delta/D$  (ranging from 0.0 to 0.3) in their numerical simulation at a single low Re value of 250, for a finite-height square prism of AR = 7. Although Behera and Saha (2019) did not specifically present the value of  $L_f$  at

different  $\delta/D$ , however, the result showed that the boundary layer had significant influence on the near-wake topology, which may be responsible to the change in the formation length. Cao et al. (2019), on the other hand, simulated the flow structure (including the formation length) for a prism with  $AR = 3$  at a much thicker boundary layer ( $\delta/D = 20.1$ ) than those studies listed in Table 2.6. The formation length identified by Cao et al. (2019) at  $Re = 5 \times 10^4$  was about  $L_f/D = 1.9$ . Comparing with some studies listed in Table 2.6 with the same order of  $Re$  at similar  $AR$ , the formation length identified by Cao et al. (2019) was significantly smaller than the studies of Porteous et al. (2017) ( $AR = 4.3$ ,  $L_f/D = 4.2$ ) and Sumner et al. (2017) ( $AR = 3.0$ ,  $L_f/D = 2.5$ ). This observation infers that the thicker boundary layer may induce some effect of shrinking the formation length.

## 2.8 Summary and identified gaps in the literature

A large number of studies in the literature from year of 1977 to 2019 were reviewed attentively. In Section 2.2, a general review about the flow around an infinite square prism is given. The flow regimes were classified by Igarashi (1984), Huang et al. (2010), and Yen and Yang (2011) based on different profiles of the shear layer separation and reattachment on the bottom surface, and the critical angle where the reattachment process began was investigated. Igarashi (1984) and Huang et al. (2010) identified  $\alpha_c = 15^\circ$  for a  $Re \sim 10^4$ ; Yen and Yang (2011) determined  $\alpha_c = 12^\circ$  for a  $Re \sim 10^3$ . Section 2.3 details the flow around a finite-height square prism. Comparing with Section 2.2, the review in Section 2.3 focuses more on the wake structure behind the prism body, where the free-end and ground plane effects are considered, instead of just the separated shear layer near to the prism surface. The interaction between the tip and base vortices, and Karman vortex street is also discussed. There were different flow models proposed in various studies (Wang and Zhou (2009), Bourgeois et al. (2011), and Rastan et al. (2017)). The effects of  $AR$  and  $\alpha$  on the wake structure (in the form of vorticity contours) are also reviewed in subsection 2.3.3 and 2.3.2. Undeniably, the wake is a strong function of both  $AR$  and  $\alpha$ . Although the reviews in Section 2.2 and 2.3 are not directly related to the main scopes of the present thesis, however, the reviews provide some preliminary understanding about the strong influence of  $AR$  and  $\alpha$  on the flow structure

and wake characteristic, so it can be inferred that both AR and  $\alpha$  would also result in some remarkable impact on other parameters including the mean  $C_P$  distribution at the free end.

In Section 2.4, the review on the flow structure is limited to the region above the free end only, which is more related to the main scope of the present thesis. Subsection 2.4.1 further supports the strong influence of AR (Sumner et al. (2017)) and  $\alpha$  (Okuda and Taniike (1993)) on the mean velocity flow field as well as the streamline profile above the free-end surface. Thus, it is most likely the surface pressure of the free end would be influenced significantly by those parameters as well. Unfortunately, the influence of  $\delta/D$  on the mean flow field above the free end is not commonly available to date. The review then focuses solely on the mean free-end pressure, which is the main measured variable in the present thesis, in subsection 2.4.2. There are only a few experimental studies to date which investigate extensively on the mean free-end pressure at the free end of an isolated square prism structure (Baines (1963), Castro and Robins (1977), Sitheeq et al. (1997), Nakamura et al. (2001), Nakamura et al. (2003), Lim and Ohba (2015), and Lee et al. (2016)). Most of these studies focused on the cube (AR = 1), and presented the centerline  $C_P$  profile. Also, out of these studies, it appears that only the studies of Baines (1963), Nakamura et al. (2001), and Nakamura et al. (2003) provided the full  $C_P$  contours at the free end. It should be noted that the main focus in the studies of Nakamura et al. (2001) and Nakamura et al. (2003) was the local heat transfer. Therefore, extensive details about the effect of AR and  $\delta/D$  on the full  $C_P$  contours is unavailable. Other studies have provided the details on the effect of AR (Baines (1963), Lim and Ohba (2015), and Lee et al. (2016)) and  $\alpha$  (Castro and Robins (1977) and Lim and Ohba (2015)), and some investigated the effect of  $\delta/D$  (Castro and Robins (1977) and Sitheeq et al. (1997)). Nevertheless, there are still several gaps in the literature:

- The study of Castro and Robins (1977), Lim and Ohba (2015), and Lee et al. (2016) only presented the centerline  $C_P$  profile instead of a full  $C_P$  contours. The full information about the free-end surface pressure at other non-centerline locations (such as near to the bottom surface) is therefore unknown.
- The range of AR used in those studies was markedly small ( $0.5 \leq \text{AR} \leq 2$ ), or the increment in AR adopted was large. The studies of Wang and Zhou (2009) and Sumner

et al. (2017) have shown significant changes in the wake structure and velocity field with the variation of AR. Hence, it is worth to adopt a wider range of AR to investigate if the mean surface pressure on the free end would undergo similar significant changes under the influence of AR.

- The aspect ratio in those studies was controlled by adjusting the width,  $D$  of the prism, instead of the height,  $H$ . The free end surface was therefore consistently exposing to a similar incoming flow velocity. It would be interesting to allow the free end surface exposes to different local velocity within the boundary layer by changing the height of the prism, so that the effect of AR can be studied more extensively from a different view point.
- The increment of  $\alpha$  in those studies were noticeably large, with up to  $45^\circ$  for Castro and Robins (1977) and  $10^\circ$  for Lim and Ohba (2015). With such a large increment in  $\alpha$ , it remains vague about the presence of any critical angle, where the pressure contour of the free end illustrates any discernible behaviour.
- The effect of  $\delta/D$  in the studies of Castro and Robins (1977) and Sitheeq et al. (1997) require further complementation from other experimental investigations. Castro and Robins (1977) adopted uniform incoming flow ( $\delta/D \simeq 0$ ) and atmospheric boundary layer ( $\delta/D > 1$ ). It would be better if there is an other experimental investigation which adopts the boundary layer thickness in between these two extremes. The result of Sitheeq et al. (1997), on the other hand, did not show a significant variation in  $C_P$  for different cases of the boundary layer thickness.

The identified gaps in the literature listed above support the objectives outlined in Section 1.3, where a much wider range of aspect ratio is used from  $AR = 1$  to 11, and with an increment of only  $AR = 0.5$ , and results in 21 different aspect ratios in total. The aspect ratio is varied by controlling the height of the prism,  $H$ , to allow the wake structure and downwash flow illustrate a more remarkable range of different characteristics. Similarly, the incidence angle increment is constrained to only  $1^\circ$  in a wide range of  $\alpha = 0^\circ$  to  $45^\circ$ . With a wider range and smaller increment in both AR and  $\alpha$ , the effect of those parameters on

the mean free-end pressure contour can be studied more extensively, with high possibility of the identification of any critical AR and  $\alpha$ , where the  $C_P$  contours demonstrate some unique behaviour. Furthermore, by using two different boundary layers of  $\delta/D = 0.7$  and 2.6, the effect of the boundary layer thickness on the surface pressure at free end can also be investigated. The  $C_P$  output is also presented in both full contours and centerline pressure profiles as mentioned in Section 1.4, so that the investigation can be conducted in a more effective and conclusive manner.

The strong influence of AR and  $\alpha$  on the aerodynamic forces, Strouhal number, and vortex formation length is also discussed in Section 2.5, 2.6, and 2.7 respectively. The studies of Sakamoto (1985) and McClean and Sumner (2014) appear to be the most comprehensive experimental investigations to date which illustrate the combined effect of AR and  $\alpha$  on  $C_D$ ,  $C_L$  and St. Based on their studies, there were three critical angles, based on the minimum  $C_D$ , and maximum magnitude of  $C_L$  and St. Notably, for both studies,  $\alpha_c$  based on the trend of  $C_D$ ,  $C_L$  and St were fairly similar, which lied within the range of  $15^\circ \pm 3^\circ$ , when  $AR \geq 3$ . The critical angles identified were also found very similar to the  $\alpha_c$  for infinite square prism identified by Igarashi (1984), Huang et al. (2010) and Yen and Yang (2011), where the shear layer reattachment process began along the bottom surface. Additionally, these critical angles also coincide with the experimental investigation of Unnikrishnan et al. (2017) and Sohankar et al. (2018) where the wake structure showed the highest asymmetrical profile, shortest formation length, and minimum wake width. This observation suggests a possible existence of strong correlation between the wake profile, aerodynamic force, vortex shedding frequency, and also the formation length. The variation of formation length with AR was also extensively investigated by Wang and Zhou (2009), Porteous et al. (2017), and Sumner et al. (2017). Although the current available studies have provided fairly sufficient information about  $C_D$ ,  $C_L$ , St and  $L_f$  for a finite-height square prism, these investigations can still be further enhanced and complemented due to the identified gaps in the literature listed below:

- The study of Sakamoto (1985) and McClean and Sumner (2014) was performed for 5 - 6 aspect ratios only, despite the increment of  $\alpha$  was sufficiently small (up to  $1^\circ$ ). It would be ideal to repeat the experiment in a wider range of aspect ratio, so that the

trend of  $\alpha_c$  with AR can be investigated in more detail, and the flow regimes may also be classified accordingly based on the trend of aerodynamic force and Strouhal number, as illustrated by Porteous et al. (2017) (for St only).

- The formation length was measured by Wang and Zhou (2009), Porteous et al. (2017), and Sumner et al. (2017) for a wide range of AR, but at a considerably large increment of  $AR = 2 - 3$ . Although there was critical aspect ratio of  $AR = 7$  identified by Wang and Zhou (2009), and Porteous et al. (2017) based on the longest  $L_f$ , the fairly large AR increment did not result in a more accurate prediction on the critical AR.
- The effect of  $\delta/D$  on  $C_D$ ,  $C_L$ , St was not investigated by Sakamoto (1985) and McClean and Sumner (2014). It is still questionable about the impact of the boundary layer on those parameters, which include the value of critical angles and the curve shape of  $C_D$ ,  $C_L$ , and St versus  $\alpha$ .
- The effect of  $\delta/D$  on  $L_f$  was not investigated by Wang and Zhou (2009), Porteous et al. (2017) and Sumner et al. (2017). Recent numerical simulation of Behera and Saha (2019) and Cao et al. (2019) seemed to suggest a non-negligible influence of the boundary layer thickness on the wake topology and so the formation length. Hence, more experimental investigation is needed to verify such statements.
- The information about the combined effect of AR,  $\alpha$  and  $\delta/D$  on  $C_N$ , which acts normally to the free end, is almost completely neglected in the literature to date.  $C_N$  quantifies the suction force experienced at the rooftop, and the investigation on this aerodynamic force would be beneficial in engineering applications.
- The relationship between the wake asymmetry, minimum  $L_f$ , minimum  $C_D$ , minimum  $C_L$ , and maximum St was evident from different studies above-mentioned. However, the correlation between the free-end pressure distribution with those features formerly mentioned was still not evident in the literature.

Therefore, the present thesis studies the combined effects of AR,  $\alpha$ , and  $\delta/D$  to further support the experimental investigation of Sakamoto (1985), McClean and Sumner (2014)

about the behaviour of  $C_D$ ,  $C_L$  and  $St$ . The selection of range and increment in both AR and  $\alpha$  is the same as those in the investigation of  $C_P$  distribution. With a smaller increment of AR, more data points can be obtained to illustrate the trend of  $\alpha_c$  versus AR. Similar trends can be plotted for  $C_D$ ,  $C_L$  and  $St$  at any interested  $\alpha$  to observe the variation of these parameters with AR. Based on these results, different flow regimes based on the characteristics of forces and shedding frequency may be classified for two different cases of boundary layer thickness. Similarly, with a smaller increment of AR, the present thesis complements the experimental investigations of Wang and Zhou (2009), Porteous et al. (2017), and Sumner et al. (2017) about the formation length behaviour, by determining the critical AR more accurately at two different conditions of boundary layer thickness. With the second set of objective in this research (outlined in Section 1.3) about the study of  $C_D$ ,  $C_L$ ,  $St$ ,  $L_f$ , the critical AR and  $\alpha_c$  can be determined more accurately, with the same wide range and small increment in AR and  $\alpha$  as the investigation of  $C_P$  distribution. This would complement many investigations which studied the flow field or wake structure at the most common increment of  $5^\circ$ . For instance, the wake structure investigated by Unnikrishnan et al. (2017) was performed at increment of  $5^\circ$ . Although  $\alpha_c = 15^\circ$  was identified, the existence of error with  $\pm 4^\circ$  in critical angle is still possible. With the new  $\alpha_c$  identified in this study, it perhaps could challenge future investigation to attempt the flow field measurement (such as using PIV) at other incidence angles not common in the current literature ( $\alpha$  which is not in the multiple of  $5^\circ$ ) to identify any interesting flow characteristics. The present study also presents the information of  $C_N$  based on the combined effect of AR,  $\alpha$ , and  $\delta/D$ , which is not ordinary available in the current literature. Additionally, the critical AR and  $\alpha$  identified in this research based on aerodynamic forces and vortex shedding can be used to relate the behaviour of free-end pressure distribution, which is a contribution not available in the current literature yet, to the author's knowledge.

# 3 METHODOLOGY AND EXPERIMENTAL SETUP

## 3.1 Introduction

This chapter provides further details about the instrumentation and experimental methods used to control the manipulated variables, set the fixed variables, and record the measured variables (Table 1.1). Section 3.2 details the wind tunnel that was used to perform the experimental investigation. Section 3.3 discusses the measurement of the freestream conditions. The boundary layer developed on the ground plane is discussed in Section 3.4. Section 3.5 describes the square prism models and the details of controlling the aspect ratio. Section 3.6 highlights the pressure transducer used to measure the surface pressure distribution at the free end. The force balance used to measure the aerodynamic forces is discussed in Section 3.7, while the hotwire anemometry used to measure the vortex shedding frequency and formation length is discussed in Section 3.8. The uncertainties associated with all the measured variables are discussed in Section 3.9.

## 3.2 Wind tunnel

All experiments were conducted in the wind tunnel lab at the University of Saskatchewan, which is managed by the Department of Mechanical Engineering. The wind tunnel facility is a closed-return system as shown in Figure 3.1. The wind velocity is supplied by a constant-speed and variable-pitch type fan, with a 100 hp motor. The starting current for the fan is about 150 A, which is about 10 times higher than its operating current ( $\sim 17$  A). Downstream of the fan, the air passes through two corners and turns  $180^\circ$ . The turning vanes at these corners reduce the minor loss due to the bent pathway. The air then passes

through a pair of turbulence reduction screens. The air continues flowing through a large nozzle section, located upstream of the test section, with a contraction ratio of 7:1. This contraction creates a higher speed in the test section. The dimensions of the test section (length, width, height) are  $1.8 \text{ m} \times 1.1 \text{ m} \times 0.9 \text{ m}$ , and the operating velocity range in the test section is about 5 - 45 m/s.

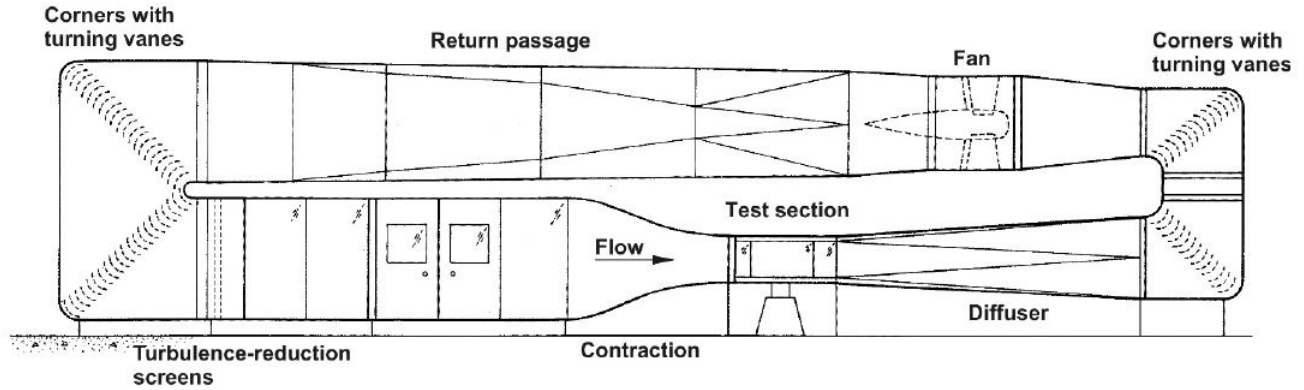


**Figure 3.1:** Schematic diagram of the low-speed, closed-return wind tunnel facility at the University of Saskatchewan.

There is a traversing wing located inside the test section, which was used to position the hotwire probe in the experiments. The traversing wing can be controlled to move the probe in  $x$ -,  $y$ -, and  $z$ -directions (Figure 1.3). The details of the hotwire anemometry system are discussed in Section 3.8. The movement of the traversing wing is controlled by three stepper motors (one for each direction), which are monitored by a desktop computer via LabVIEW Virtual Instruments (VI). Beneath the test section, there is a fourth stepper motor used to rotate the prism, which is also controlled by the LabVIEW program. The fourth stepper motor is located beside the force balance (discussed further in Section 3.7). The ground plane of the test section is flat and made of aluminum, with a rounded leading edge located 905 mm upstream of the prism.

### 3.3 Freestream conditions and Pitot-static probe

The freestream conditions are obtained with a Pitot-static probe (United Sensor, 3.2-mm diameter) mounted on the side wall of the test section. Some conditions of the freestream

are the static pressure ( $P_\infty$ ), dynamic pressure ( $q_\infty$ ), temperature ( $T_\infty$ ), density ( $\rho_\infty$ ), and velocity ( $U_\infty$ ). The Pitot-static probe is connected to a Datametrix Barocell (Type 600A) absolute pressure transducer and a Datametrix Barocell (Type 590D) differential pressure transducer. There is also a built-in thermocouple within the probe.  $P_\infty$  and  $T_\infty$  are directly measured by the absolute pressure transducer and thermocouple, respectively. Also, the static pressure,  $P_\infty$ , is used as a reference pressure for the differential pressure transducers. The ideal gas law was used to calculate the air density,  $\rho_\infty$ , using Equation 3.1.

$$\rho_\infty = \frac{P_\infty}{RT_\infty} \quad (3.1)$$

In this equation,  $R$  is the specific gas constant for air with value of  $287 \text{ Jkg}^{-1}\text{K}^{-1}$ . The freestream dynamic pressure,  $q_\infty$ , can be computed using Equation 3.2, through the input of the freestream static pressure,  $P_\infty$ , and stagnation pressure,  $P_0$ . The difference between  $P_0$  and  $P_\infty$  is directly measured by the differential pressure transducer. With the information of  $q_\infty$ , the freestream velocity,  $U_\infty$ , can be computed by Equation 3.2.

$$P_0 - P_\infty = \frac{1}{2}\rho_\infty U_\infty^2 = q_\infty \quad (3.2)$$

Another important freestream condition is dynamic viscosity,  $\mu_\infty$ , which is used to calculate the Reynolds number. Air viscosity varies with temperature. The temperature increased slowly during the experiment, due to heat transfer from the fan motor and friction on the wind tunnel walls. Hence, the value of  $\mu_\infty$  needs to be re-calculated timely based on the real-time temperature. Considering the temperature effect, the correlation used to compute the dynamic viscosity is the Sutherland Law (White (2011)) shown in Equation 3.3. In this equation,  $\mu_0 = 1.725 \times 10^{-5} \text{ kg/(ms)}$ , which is the air dynamic viscosity at the standard temperature of  $T_0 = 273 \text{ K}$ . The symbol  $S$  represents a temperature constant for air, with a value of  $S = 110.4 \text{ K}$ .

$$\mu_\infty = \mu_0 \frac{(T_\infty/T_0)^{3/2}(T_0 + S)}{T_\infty + S} \quad (3.3)$$

The Reynolds number can be determined by using Equation 3.4. In this equation,  $D$  is used as the reference length, and is fixed at a constant value of 48 mm in this experiment.

$$Re = \frac{\rho_{\infty} D U_{\infty}}{\mu_{\infty}} \quad (3.4)$$

Recall from Section 1.4 that, in this experiment, there are two different values for the freestream velocity:  $U_{\infty} = 22.5$  and  $40.0$  m/s. The higher freestream velocity,  $U_{\infty} = 40$  m/s was applied during the measurement of the aerodynamic forces to improve the accuracy by increasing the magnitude of the forces. Although this experiment intends to fix  $U_{\infty}$  (and  $Re$ ), however, it should be noted that  $Re$  is computed from  $\rho_{\infty}$  and  $\mu_{\infty}$ , which both are dependent on the surrounding temperature. Additionally,  $U_{\infty}$  was increased by manipulating the pitch angle of the fan blades via LabVIEW, until the desired value of  $U_{\infty}$  was reached. This process of setting the freestream velocity was manually controlled. Setting  $U_{\infty}$  to the exact desired values is difficult to achieve, and hence there was a 1% tolerance involved for  $U_{\infty}$ . Considering all these factors, the Reynolds number varied slightly in a range of  $6.4 \times 10^4 \leq Re \leq 6.6 \times 10^4$  when the freestream velocity was set at  $U_{\infty} = 22.5$  m/s  $\pm 1\%$ , and the range of  $1.0 \times 10^5 \leq Re \leq 1.2 \times 10^5$  was obtained when the value of  $U_{\infty}$  was set at  $40.0$  m/s  $\pm 1\%$ .

### 3.4 Boundary layer characteristics

The characteristics of the undisturbed boundary layer on the ground plane for different cases is discussed in this section. The boundary layer thickness,  $\delta$ , can be defined as the vertical distance from the ground plane to the first location where the local velocity reaches  $0.99U_{\infty}$ . In this experiment, a hotwire anemometer was used to measure the local velocity (to determine  $\delta$ ); the details of this instrument are discussed in Section 3.8.

The boundary layer was measured with the prism removed, for five different cases due to various combinations of the freestream velocity, measured variables, and scenarios where a boundary layer trip was installed upstream. As mentioned in Section 3.3, there were two freestream velocities in this experimental investigation,  $U_{\infty} = 22.5$  and  $40.0$  m/s. The latter

was used for the measurement of the aerodynamic forces to improve the accuracy by increasing the magnitude of the forces. For the case where no boundary layer trip was installed, the boundary layer originated from the leading edge of the ground plane (this case is herein after referred to as “the thin boundary layer”). To increase  $\delta$  to a higher value, a boundary layer trip in the form of a thin-vertical plate of 15-mm height was installed on the ground plane 795 mm upstream from the centre of the prism (this case is herein after referred to as “the thick boundary layer”). For  $U_\infty = 22.5$  m/s, the thin boundary layer was adopted for the measurement of  $C_P$ ,  $L_f$ , and  $St$  (herein after referred to as Case 1). With the same freestream condition, the boundary layer trip was installed to repeat the measurement of  $C_P$  and  $L_f$  (herein after referred to as Case 2), and also the measurement of  $St$  (herein after referred to as Case 3). It should be noted that the location of the trip did not change significantly for Case 2 and Case 3. Nevertheless, the values of  $\delta$  for both cases varied slightly on account of different measurement timings. The ground plane was shifted and this led to differences in initial conditions between Case 2 and Case 3. As the trip flow is particularly sensitive to the initial upstream conditions, the thick boundary layer values should be reported separately for each measurement at different experimental timings. For  $U_\infty = 40.0$  m/s, both cases of the thin and thick boundary layer were repeated for the measurement of aerodynamic forces (herein after referred as to Case 4 and Case 5, respectively). The velocity in the boundary layer was measured at an increment of 1 mm for the wall-normal (vertical) distance range of  $0 \text{ mm} < z \leq 20 \text{ mm}$ , 2 mm increment for  $20 \text{ mm} < z \leq 60 \text{ mm}$ , and 5 mm increment for  $60 \text{ mm} < z \leq 150 \text{ mm}$ . After determining  $\delta$  from the velocity profile, the displacement thickness ( $\delta^*$ ), momentum thickness ( $\theta$ ), and shape factor (the ratio of  $\delta^*$  to  $\theta$ ) were computed from Equations 3.5 and 3.6, respectively, as outlined in White (2011).

$$\delta^* = \int_0^\delta \left(1 - \frac{u}{U_\infty}\right) dz \quad (3.5)$$

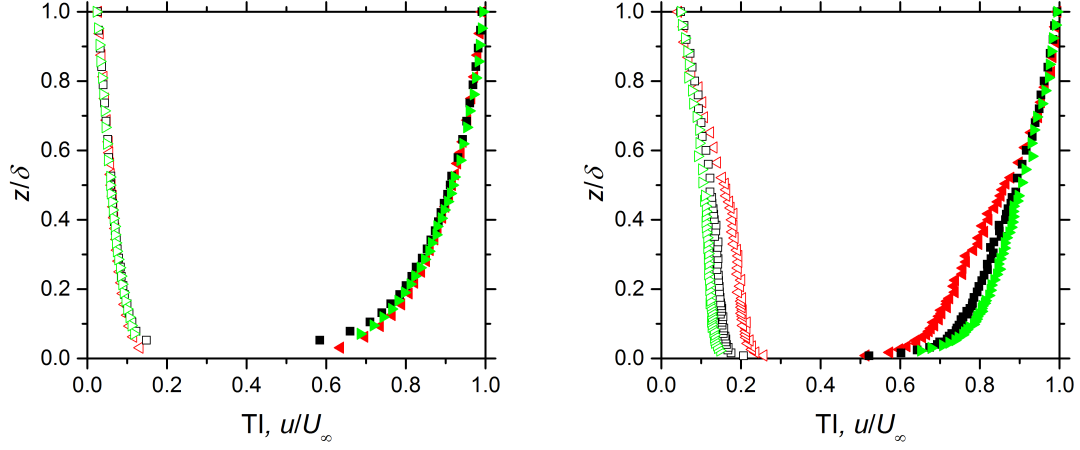
$$\theta = \int_0^\delta \left(\frac{u}{U_\infty}\right) \left(1 - \frac{u}{U_\infty}\right) dz \quad (3.6)$$

The trapezoidal rule was used to solve Equation 3.5 and 3.6 numerically using the velocity data. The values of  $\delta$ ,  $\delta^*$ ,  $\theta$ , and shape factor for the five cases previously discussed are

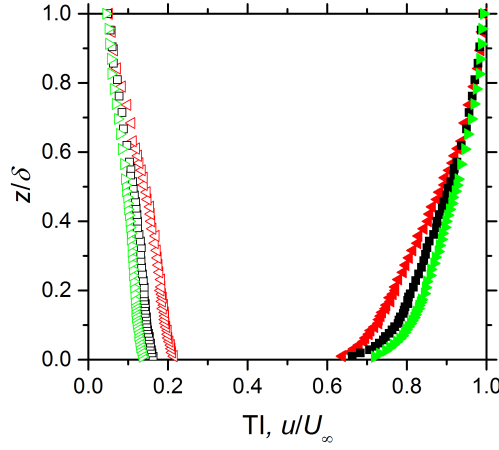
presented in Table 3.1, and Figure 3.2 illustrates the velocity and turbulence intensity profiles for each case, where  $u'$  is the local fluctuation of the velocity. Also, for each case, the velocity profile is presented at three streamwise locations:  $x/D = -5, 0$ , and  $+5$ , where  $x/D = 0$  is located at the centre of the prism.

The sampling frequency used for the local velocity and fluctuating velocity was 5 kHz for 50k samples for all the cases, except for Case 3. The sampling frequency of 5 kHz for 150k samples was used for Case 3. In the case of the thin boundary layers, both profiles of dimensionless velocity and turbulence intensity (TI) appear to collapse together for all three streamwise locations, regardless of the freestream velocity (Figure 3.2 (a)(d)). On the other hand, the profiles of the dimensionless velocity and TI show appreciable difference at three different streamwise locations, in the case of the thick boundary layer (Figure 3.2 (b)(c)(e)). The profiles for the thick boundary layer also have a higher turbulence intensity compared to the case of the thin boundary layer.

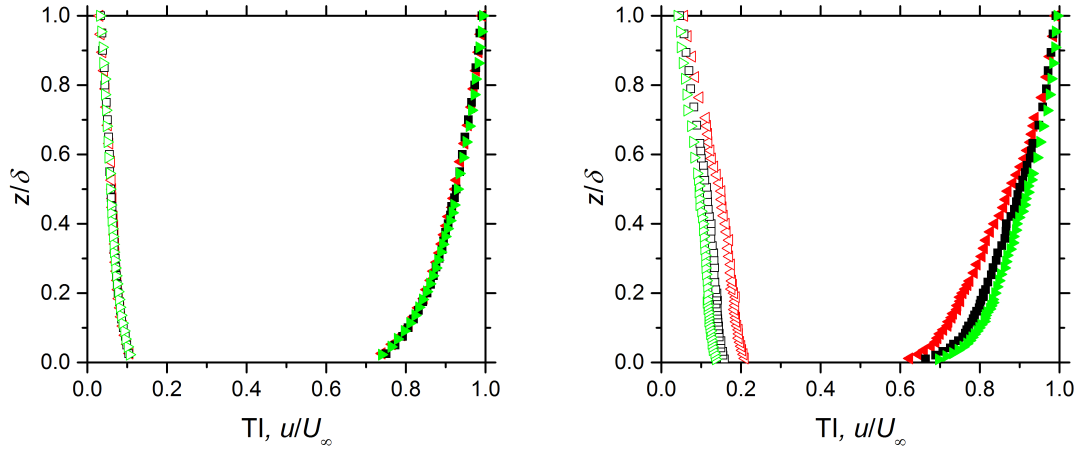
Reynolds number generally does not affect the velocity profiles qualitatively. However, from Table 3.1, it is observed that the values of  $\delta$ ,  $\delta^*$ , and  $\theta$  decrease when a higher value of  $U_\infty$  was used, for the case of the thick boundary layer (Case 2, 3, and 5). Conversely, for the case of the thin boundary layer, the values of  $\delta$ ,  $\delta^*$ , and  $\theta$  increase slightly when a higher  $U_\infty$  value was used (Case 1 and 4). It is worth pointing out that when  $U_\infty$  increases from 22.5 m/s to 40.0 m/s, the decrease rates of  $\delta$ ,  $\delta^*$ , and  $\theta$  for the case of the thick boundary layer is much higher (up to 24%), in comparison to the increase rate of those parameters (with  $\sim 5\%$ ) for the case of thin boundary layer. Hence, the effect of Re on the quantities of  $\delta$ ,  $\delta^*$ , and  $\theta$  is more remarkable for the case of the thick boundary layer.



(a) Case 1: Untripped,  $U_\infty = 22.5$  m/s    (b) Case 2: Tripped,  $U_\infty = 22.5$  m/s, Set A



(c) Case 3: Tripped,  $U_\infty = 22.5$  m/s, Set B



(d) Case 4: Untripped,  $U_\infty = 40.0$  m/s    (e) Case 5: Tripped,  $U_\infty = 40.0$  m/s

**Figure 3.2:** Normalized boundary layer profile for five different cases listed in Table 3.1. The closed symbols represent the velocity profile ( $u/U_\infty$ ), while the open symbols represent the turbulence intensity profile ( $u'/U_\infty$ ) denoted by abbreviation ‘TI’ on the  $x$ -axis. For each case, the profiles are presented in three streamwise locations:  $x/D = -5$  (red left triangle),  $0$  (black square), and  $+5$  (green right triangle).

**Table 3.1:** Characteristics of the undisturbed boundary layer developed from the ground plane (with the prism removed) for five different cases.

<sup>(1)</sup> Case 1: Thin Boundary Layer, $U_\infty = 22.5$ m/s				
Probe Location	$\delta$ [mm] ( $\delta/D$ )	$\delta^*$ [mm] ( $\delta^*/D$ )	$\theta$ [mm] ( $\theta/D$ )	$\delta^*/\theta$
-5D	32 (0.7)	3.2 (0.1)	2.7 (0.1)	1.2
0D	38 (0.8)	3.9 (0.1)	3.2 (0.1)	1.2
+5D	42 (0.9)	3.8 (0.1)	3.2 (0.1)	1.2
<sup>(2)</sup> Case 2: Thick Boundary Layer, $U_\infty = 22.5$ m/s, Set A				
Probe Location	$\delta$ [mm] ( $\delta/D$ )	$\delta^*$ [mm] ( $\delta^*/D$ )	$\theta$ [mm] ( $\theta/D$ )	$\delta^*/\theta$
-5D	115 (2.4)	17.0 (0.4)	13.0 (0.3)	1.3
0D	125 (2.6)	15.3 (0.3)	12.4 (0.3)	1.2
+5D	132 (2.8)	13.5 (0.3)	11.4 (0.2)	1.2
<sup>(3)</sup> Case 3: Thick Boundary Layer, $U_\infty = 22.5$ m/s, Set B				
Probe Location	$\delta$ [mm] ( $\delta/D$ )	$\delta^*$ [mm] ( $\delta^*/D$ )	$\theta$ [mm] ( $\theta/D$ )	$\delta^*/\theta$
-5D	95 (2.0)	12.1 (0.3)	9.6 (0.2)	1.3
0D	105 (2.2)	11.3 (0.2)	9.4 (0.2)	1.2
+5D	115 (2.4)	10.3 (0.2)	8.9 (0.2)	1.2
<sup>(4)</sup> Case 4: Thin Boundary Layer, $U_\infty = 40.0$ m/s				
Probe Location	$\delta$ [mm] ( $\delta/D$ )	$\delta^*$ [mm] ( $\delta^*/D$ )	$\theta$ [mm] ( $\theta/D$ )	$\delta^*/\theta$
-5D	38 (0.8)	3.2 (0.1)	2.8 (0.1)	1.2
0D	40 (0.8)	3.4 (0.1)	2.9 (0.1)	1.1
+5D	44 (0.9)	3.7 (0.1)	3.2 (0.1)	1.2
<sup>(5)</sup> Case 5: Thick Boundary Layer, $U_\infty = 40.0$ m/s				
Probe Location	$\delta$ [mm] ( $\delta/D$ )	$\delta^*$ [mm] ( $\delta^*/D$ )	$\theta$ [mm] ( $\theta/D$ )	$\delta^*/\theta$
-5D	85 (1.8)	11.5 (0.2)	9.1 (0.2)	1.3
0D	95 (2.0)	10.5 (0.2)	8.7 (0.2)	1.2
+5D	110 (2.3)	10.2 (0.2)	8.7 (0.2)	1.2

<sup>(1)</sup> Used for the measurement of  $C_P$ ,  $L_f$ , and St without the trip installed

<sup>(2)</sup> Used for the measurement of  $C_P$  and  $L_f$  with the trip installed

<sup>(3)</sup> Used for the measurement of St with the trip installed

<sup>(4)</sup> Used for the measurement of  $C_D$ ,  $C_L$ , and  $C_N$  without the trip installed

<sup>(5)</sup> Used for the measurement of  $C_D$ ,  $C_L$ , and  $C_N$  with the trip installed

### 3.5 Square prism models

Recall from Section 1.4, one of the fixed variables in this experimental investigation is the width,  $D$ , of the prism (where  $D = 48$  mm). Thus, in order to manipulate the aspect ratio, the height,  $H$ , of the square prism needs to be changed accordingly, similar to the works of McClean and Sumner (2014), Sumner et al. (2017), and Beitel (2017). Also, as highlighted in Section 1.3, the effect of AR is studied in a range of  $AR = 1$  to 11, in an increment of 0.5, which corresponds to 21 different aspect ratios in total. In other words, there are 21 different square prisms with various heights in this experiment, each tested separately to study the effect of aspect ratio.

A square prism model consists of a top cap, a prism body, and a bottom mounting collar. The top cap and bottom mounting collar are connected to the prism body with an exposed height of  $0.25D$  each ( $0.5D$  in total). This design indicates that 21 prism bodies with heights ranging from  $0.5D$  to  $10.5D$  (corresponds to 24 - 504 mm) are needed. With the highest aspect ratio, the distance between the free-end surface and the top ceiling of the test section is still considerably large (382 mm), which corresponds to the maximum blockage ratio of 2.6%. There is a mounting bracket located beneath the mounting collar, which is connected in between the mounting collar and the force balance (Section 3.7) to allow the force measurement. A turntable, which is parallel to the ground plane, is installed whose inner hole fits through the mounting collar and serves as a ground foundation of the prism model. Figure 3.3 illustrates the assembly of the square prism models in a front view and 3D view. All parts aforementioned are made with aluminum, and fabricated in Engineering Shops at the University of Saskatchewan. The design is almost the same as Beitel (2017), who studied the free-end pressure distribution for a finite-height circular cylinder and focused on the adoption of a wide AR range and a small AR increment.

There are 31 pressure taps in the free end of the top cap, and 1 pressure tap at the side surface of the cap. The pressure taps are connected to ZOC17 pressure scanner (Section 3.6) through urethane flexible tubing with an internal diameter of 0.7 mm. The pressure taps are concentrated in only one quadrant as shown in Figure 3.4 (a). The pressure taps have an equal spacing of  $0.09D$ , while the spacing between the edge and the nearest pressure tap is

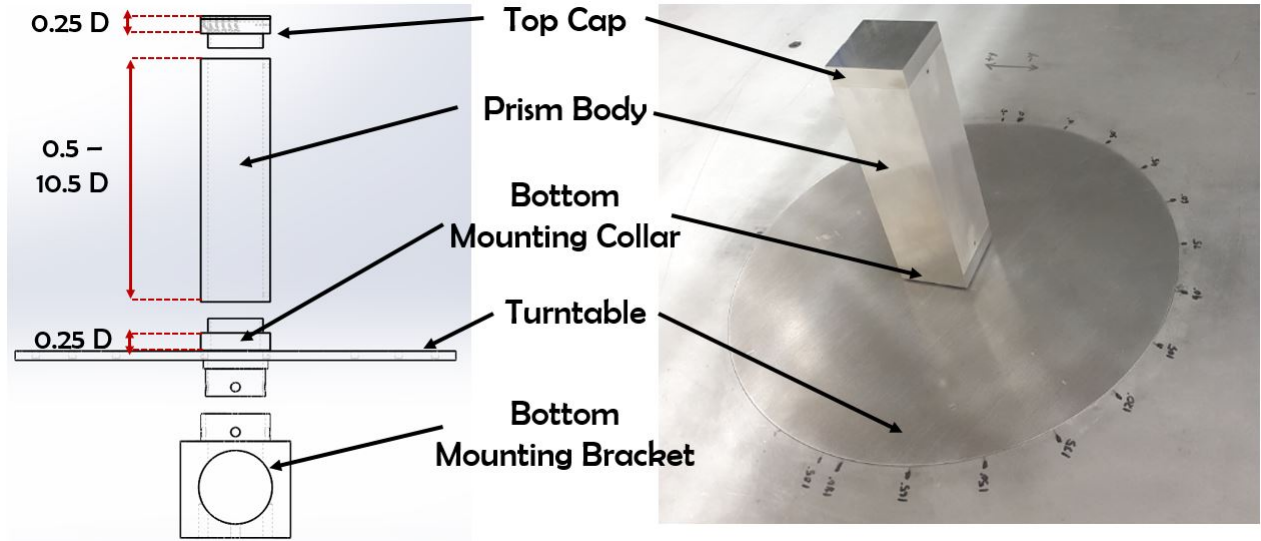
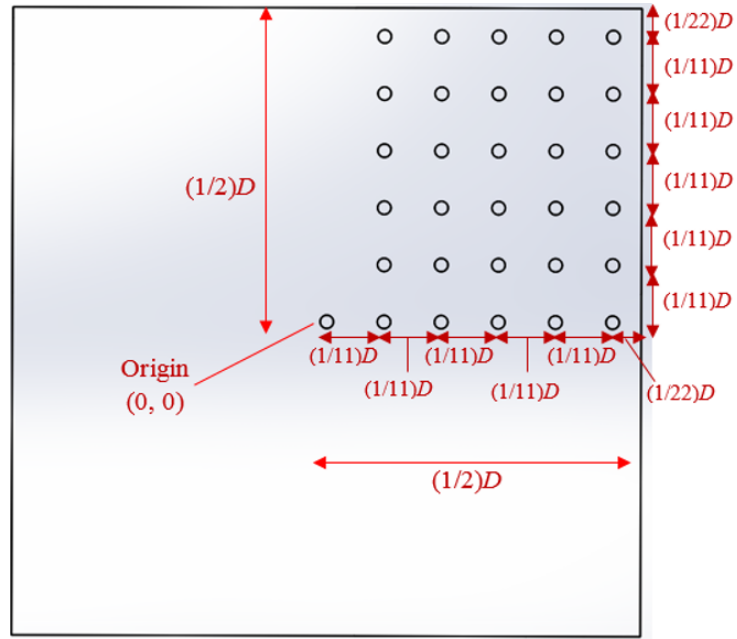
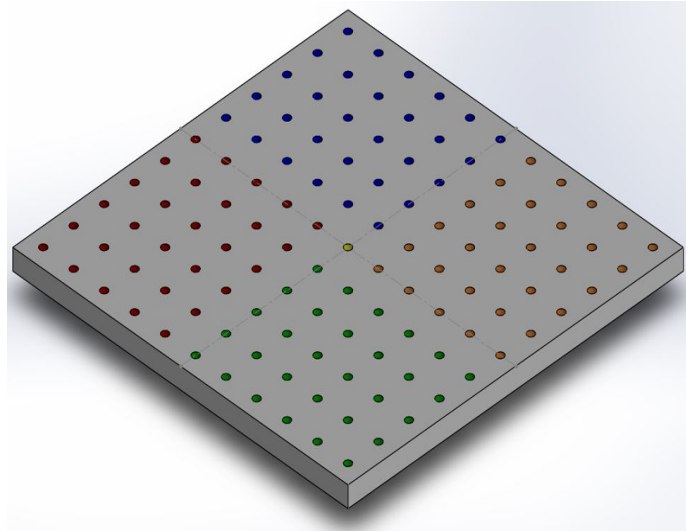


**Figure 3.3:** Square prism model of the experiment in (a) front view and (b) 3D view. The front view is shown in an exploded view, while the 3D view shows the full assembly. The mounting bracket (below the turntable) is not seen in the 3D view.

$0.045D$ . The smaller distance between the square edges and the pressure taps was designed to achieve better resolution on the surface pressure contours near the flow separation region and reattachment line (which might be very close to the leading and trailing edge) as described in the literature in Chapter 2. In order to measure the pressure distribution in other quadrants, the square prism needs to be rotated through  $360^\circ$ . The rotation of the prism model was done by a stepper motor, located next to the force balance, as described in Section 3.2. By rotating the prism models, the full pressure distribution for four different quadrants can be obtained as shown in Figure 3.4 (b). There was only one redundant location when the prism is rotated, which is the origin (colored with yellow in Figure 3.4 (b)). Hence, when the prism is rotated, a total of 121 measurement points is obtained on the free end. This design allows a relatively finer resolution for the pressure distribution as compared to other studies listed in Table 2.2.



(a)



(b)

**Figure 3.4:** (a) Pressure tap distribution at the free end with detailed dimensions ( $D$  is the width of the prism). (b) Surface pressure distribution in each quadrants. Holes in orange represent the surface distribution for quadrant 1, blue for quadrant 2, red for quadrant 3, green for quadrant 4, and yellow for origin.

### 3.6 Measurement of $C_P$ by ZOC17 pressure scanner

This section provides further information about the pressure scanner introduced briefly in Section 3.5, and also details some experimental strategies for the pressure measurements. The pressure scanner used in this experiment is a product of Scanivalve, with the model name of ZOC17IP/8Px (ZOC17), where ZOC stands for Zero-Operate-Calibrate, IP indicates that the model consists of Isolate-Purge Valve that allows on-line calibration, and 8Px means there are 8 available pressure sensors in this pressure scanner. This experiment used two pressure scanners, and hence this pressure measurement system can receive up to 16 pressure inputs in total at one time. These 16 pressure input lines are linked to a pneumatic connector, which is connected to the free-end pressure measurement locations via the urethane flexible tubing. Figure 3.5 shows part of the pressure measurement system which consists of pressure scanners, pressure lines, pneumatic connector, and flexible tubing. The full pressure measurement system is introduced later at the end of this subsection.

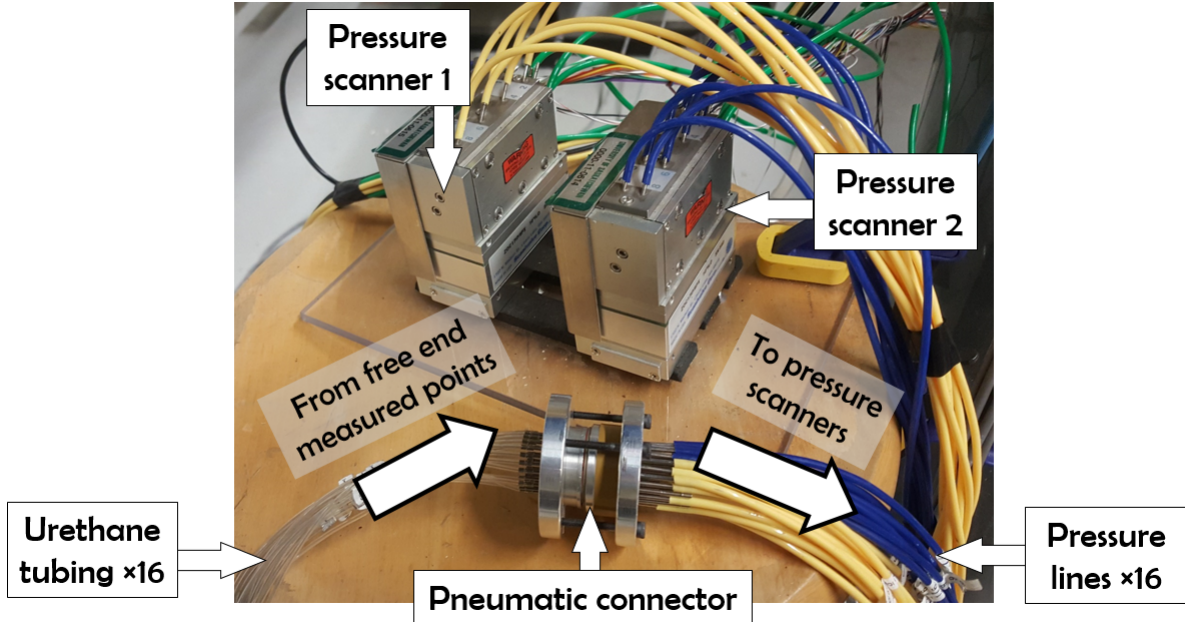


**Figure 3.5:** Pressure measurement system in the present experimental investigation. There are 8 yellow pressure lines connected to the pressure scanner 1, and 8 blue pressure lines connected to the pressure scanner 2.

Recall from Section 3.5 that there are 32 measurement locations on the free end. With the limitation of 16 available pressure inputs in the pressure scanners, two sets of pneumatic

connectors were used and they were connected to the system alternatively to allow pressure measurement for all the 32 pressure tap locations. Also, recall from Section 3.5, the prism needs to be rotated  $360^\circ$  in order to obtain the pressure distribution over the entire free end. There is another experimental limitation, where the stepper motor can only rotate the prism for about  $180^\circ$  due to the limited length of travel of the gear teeth around the force balance. Therefore, in order to allow the measurement on two quadrants which require a rotation for more than  $180^\circ$ , the wind tunnel was stopped and the top cap position was changed manually. Figure 3.6 details the experimental steps in obtaining the complete pressure distribution based on the two limitations above-mentioned.

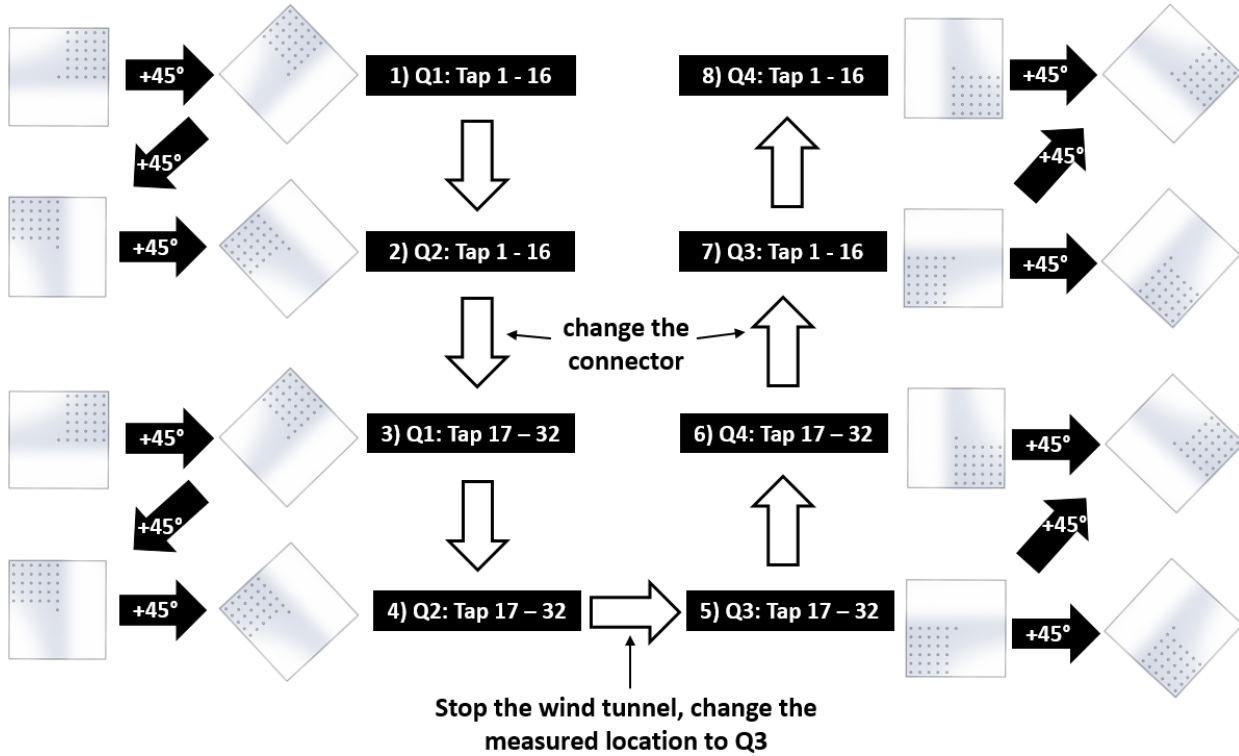


**Figure 3.6:** The experimental steps in the pressure measurement based on the limitation of available input of the pressure scanners and the maximum allowable rotation of the force balance of  $180^\circ$ . The abbreviation ‘Q’ indicates quadrant, and different lines of urethane flexible tubing are represented by the word ‘Tap’.

In this experiment, the surface pressure measurement was done by using a sampling frequency of 1 kHz for 20k samples. Based on the total samples obtained at the frequency aforementioned, the mean  $C_P$  value can be calculated by simply averaging all the samples. The ZOC17 pressure scanner is a differential pressure transducer, which uses the freestream

static pressure,  $P_\infty$ , measured by the Pitot-static tube (Section 3.3), as the reference pressure. It should also be noted that the pressure sensors are piezoresistive type, which means the sensor consists of a conductive element that undergoes a mechanical strain after experiencing the local pressure,  $P$ , at the free end. Based on the mechanical strain, an electrical resistance is produced, and the pressure can be measured based on the change in the electrical resistance.

Besides connecting to the free-end pressure measurement locations, the pressure scanners are also connected to two other pneumatic inputs: the control and calibration pressures. The control pressure is used to switch the calibration valve into purge, calibrate or isolate mode. The control pressure applied in this experiment was 90 psi (620.5 kPa), and was supplied by a compressor in the basement of the Engineering Building, and stepped down by a regulator. The control pressure was also further stepped down by a second regulator to about 5 inH<sub>2</sub>O (1.2 kPa), which was then directed to every individual pressure sensor and served as the calibration pressure. During the calibration process, the applied calibration pressure was measured by a highly-reliable transfer standard - the BOC Edwards differential pressure transducer, while the Datametrics Barocel differential pressure transducer was zeroed and calibrated for freestream dynamic pressure. The LabVIEW program was designed to allow the on-line calibration to be performed at the beginning of every step detailed in Figure 3.6, i.e. for 8 total steps, there were 8 on-line calibrations performed, with 1 calibration per 45 measurement points, in order to obtain the complete free-end pressure distribution. The number of calibrations is considered sufficient on account of the high reliability of the ZOC17 pressure scanner with a small pressure drift on the order of 0.1 Pa over a full day of measurements (Beitel (2017)), which involves about 1,000 measurement points. Additionally, the number of calibrations for the present thesis is greater than some previous investigations, such as Unnikrishnan et al. (2017) and Beitel (2017), who re-calibrated the ZOC17 pressure scanners once every 100 measurements. Figure 3.7 shows the schematic diagram of the full pressure measurement system in the present study, which includes the pressure scanners previously illustrated in Figure 3.5, the control and calibration pressures, as well as other pressure transducers discussed in Section 3.3.

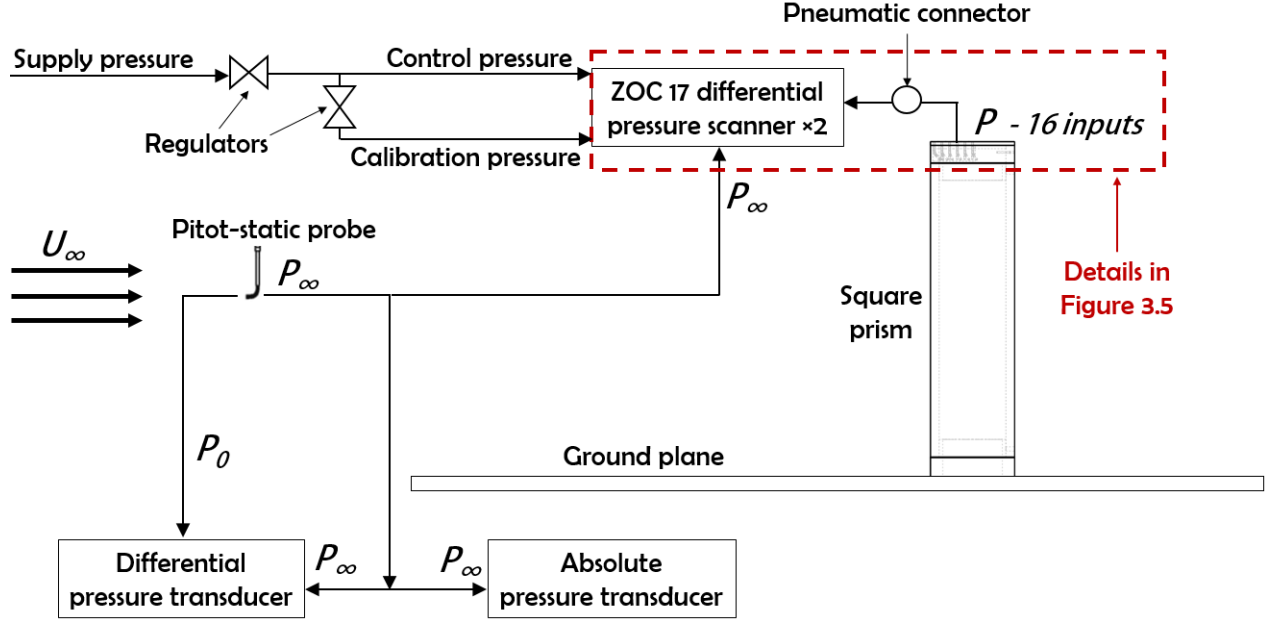


**Figure 3.7:** Schematic diagram of the full pressure measurement system in the present experimental investigation. The pictorial diagram of the instruments circled in the red dashed lines is provided in Figure 3.5.

### 3.7 Measurement of $C_D$ , $C_L$ , and $C_N$ by force balance

The aerodynamic forces were measured by a force balance, which consists of six single-point load cells. The square prism model was mounted on a T-bar, which is directly connected to the force balance, with the bottom mounting bracket as discussed in Section 3.5. The prism model can be rotated with a stepper motor located next to the load cells. Figure 3.8 shows the pictorial diagram of the force balance system, which includes the stepper motor, 4 load cells (out of 6), T-bar, and the mounting point for the prism model. The forces are measured in a form of electrical signals, where a voltage signal is generated based on the mechanical strain applied when the forces are experienced by the prism body. In this experimental investigation, the force balance system adopted the same calibration method as the work of Beitel (2017), where a calibration rig which consists of loads with known weights were used to generate voltage signals for different load cells. Based on the voltage signals generated and the magnitude of the known weights, a square matrix with a set of coefficients was determined. The forces acting on the square prism can then be measured by correlating the voltage signals generated during the experiment with the same matrix of coefficients obtained

during the calibration. Also, before each force measurement, the voltage signals from the load cells under the no-wind condition were measured. The voltage signals generated during the experiment were offset with the voltages obtained in the no-wind condition, so that only the forces due to the wind loading were measured.

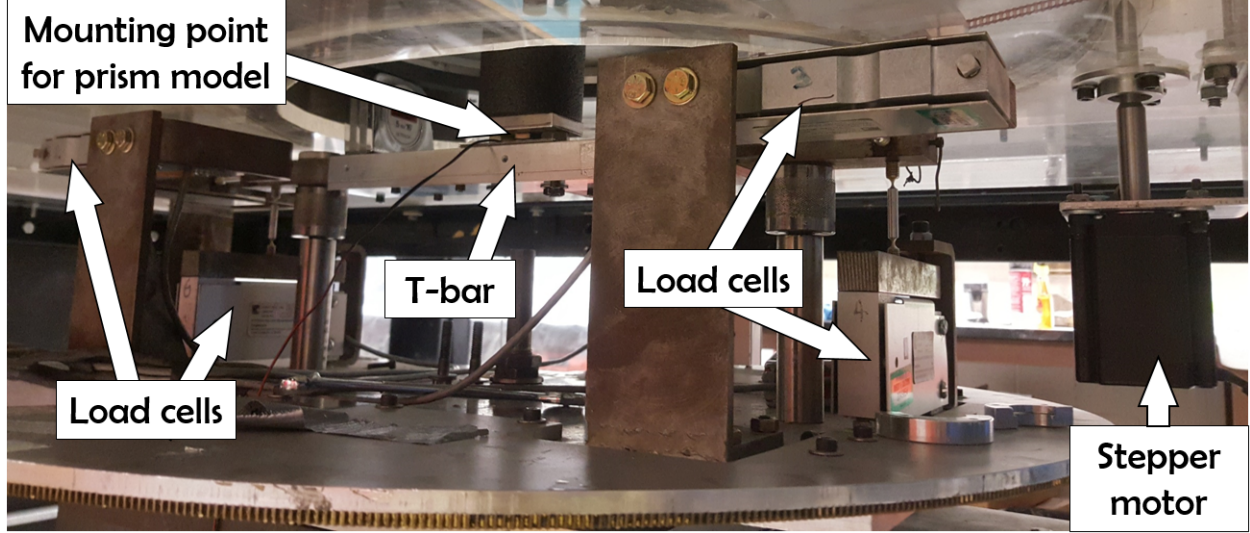


**Figure 3.8:** Force balance (located underneath of the ground plane) which is used for the measurement of the aerodynamic forces.

The force balance in the present study adopted the same coordinate system defined in Figure 1.3, i.e. a positive value is assigned if the aerodynamic force acts towards the same direction as the positive axes defined. In bluff-body aerodynamics, the drag force,  $F_D$ , experienced is often significant and its direction is always parallel to the flow and pointed towards the downstream; hence, the  $F_D$  is always positive. The lift force,  $F_L$ , and normal force,  $F_N$ , are perpendicular to the flow direction. As introduced in subsection 2.5.2, from many previous studies, it is customary that the lift force acts in the direction of  $-y$  based on the clockwise rotation of the prism, and resulted in a negative value of  $F_L$ . Also, from Section 2.4, it is evident that the free-end surface undergoes significant flow separation which lead to the negative suction differential pressure at the free end. Due to this suction pressure, the induced normal force acts in the upwards direction and results in positive  $F_N$  direction which indicates the prism is in tension. The aerodynamic moments which act along the axis of the drag force, lift force, and normal force are rolling moment ( $M_R$ ), pitching moment ( $M_P$ ), and yawing moment ( $M_Y$ ), respectively. However, it should be noted that the moment

measurement is not the main interest of the present study. Figure 3.9 shows the three aerodynamic forces and three moments defined, which are measured simultaneously by all six load cells of the force balance. The frequency of 1 kHz for 20k samples was used for the force measurements.

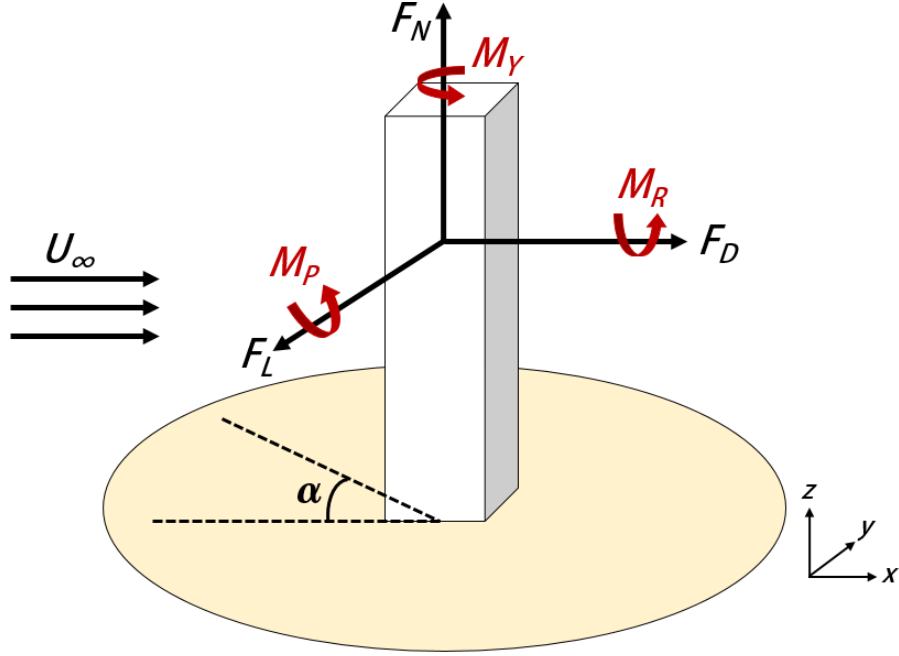


**Figure 3.9:** Definition of the aerodynamic forces and moments associated with the flow around a surface-mounted finite-height square prism in the present study.

It should be noted that when the prism is rotated with the stepper motor, the T-bar as well as the load cells are also rotated together with the prism body. The matrix of coefficients used calculates the forces in the direction parallel or perpendicular to the prism centerline, instead of the flow direction. The LabVIEW program was designed to apply the geometrical relation between the prism's orientation and the flow direction, and therefore  $C_D$  and  $C_L$  can still be determined at other non-zero  $\alpha$ . However, based on the calibration method used in this force balance system,  $C_N$  could not be determined at other non-symmetrical  $\alpha$ . Therefore, as highlighted in Section 1.4, the measurement of  $C_N$  by using the force balance is limited at two symmetrical incidence angles only:  $\alpha = 0^\circ$  and  $45^\circ$ . However, the normal force contributed solely by the suction pressure can be determined by integrating the pressure distribution at the free-end surface using Equation 3.7. In this equation,  $F_{N,p}$  is the normal force due to the suction pressure only,  $P_i$  is the local pressure measured at the individual

pressure tap location, the number of 121 in the upper limit of summation indicates that there is a total of 121 pressure measurement locations, and  $dA$  or  $\delta A_i$  is the individual small area which surrounds a pressure measurement location. The integration is done numerically, and Equation 3.8 is used to non-dimensionalize the value of  $F_{N,p}$ .

$$F_{N,p} = \int P \, dA \simeq \sum_{i=1}^{121} P_i \delta A_i \quad (3.7)$$

$$C_{N,p} = \frac{F_{N,p}}{\frac{1}{2}\rho_\infty D^2 U_\infty^2} \quad (3.8)$$

The pressure distribution is obtained at various  $\alpha$  from  $0^\circ$  to  $45^\circ$ . Hence, although the normal force could not be measured by the force balance at non-symmetrical  $\alpha$ , the normal force due to the suction pressure only can be calculated for all  $\alpha$  investigated, from  $0^\circ$  to  $45^\circ$ . Moreover, as mentioned in Section 3.5, the present study adopts a relatively finer grid to measure the free-end pressure distribution, compared to most of the previous studies. Therefore, the estimation of  $F_{N,p}$  by using Equation 3.8 is also appropriate with relatively smaller error introduced by the numerical method. With a similar numerical integration technique, the point of action of  $F_{N,p}$  can also be determined by using Equations 3.9 and 3.10. The notations  $X_{ac}$  and  $Y_{ac}$  indicate the  $X$  and  $Y$  coordinate of the point of action, while the symbols  $X_i$  and  $Y_i$  represent the individual  $X$  and  $Y$  coordinate system for each pressure measurement location. Note that the capital letter  $X$  and  $Y$  are the coordinates fixed to the free end, move together with the prism's rotation, and have their origin at the centre of the free end. These coordinates are different from the small letter  $x$  and  $y$ , defined in Figure 1.3, where the coordinate is fixed to the ground plane. Similar to  $F_{N,p}$ , the point of action can also be determined at various incidence angles,  $\alpha = 0^\circ$  to  $45^\circ$ , due to the available pressure distribution data at each  $\alpha$ .

$$X_{ac} = \int \frac{X P \, dA}{P \, dA} \simeq \sum_{i=1}^{121} \frac{X_i P_i \delta A_i}{P_i \delta A_i} \quad (3.9)$$

$$Y_{ac} = \int \frac{Y P \, dA}{P \, dA} \simeq \sum_{i=1}^{121} \frac{Y_i P_i \delta A_i}{P_i \delta A_i} \quad (3.10)$$

### 3.8 Measurement of $\delta$ , $St$ and $L_f$ by hotwire probe

A single normal wire hotwire probe was used in this experimental investigation to measure the velocity fluctuations in the wake of the prism. The model of the hotwire used in this experiment was Dantec 55P15 for the measurement of  $\delta$  and  $L_f$ , and Dantec 55P11 for the measurement of  $St$ . Both probes were mounted into the traversing wing and have a single platinum-plated tungsten wire with a diameter of  $5\text{ }\mu\text{m}$  and length of  $1.25\text{ mm}$ . The probes are operated using a Dantec Streamline constant temperature anemometer (CTA). When the wire is cooled by the forced convection due to the airflow, a current is supplied to keep the wire at a constant temperature at about  $250^\circ\text{C}$ . The voltage generated to keep the wire at constant temperature is correlated to the local velocity. These hotwire settings are coordinated by Dantec Streamware Pro software.

Based on the working principle described above, the velocity profile and turbulence intensity profiles were measured to investigate the boundary layer characteristics as highlighted in Section 3.4. Recall that the sampling frequency used for boundary layer measurement was  $5\text{ kHz}$  for  $50\text{k}$  samples for Case 1, 2, 4, and 5, and  $5\text{ kHz}$  for  $150\text{k}$  samples for Case 3. The voltage signal is dependent on the air temperature, and therefore a meticulous calibration needs to be done on the hotwire in order to measure the local velocity,  $u$ , at various temperatures,  $T_\infty$ , due to the wind tunnel system heating up throughout the experimental duration. Hence, before the measurement of the boundary layer was performed, the hotwire was calibrated over a wide range of temperature from  $T_\infty = 25.3^\circ\text{C}$  to  $35.3^\circ\text{C}$ . There were six calibration curves obtained at six different average operational temperatures of the hotwire during the calibration process as shown in Figure 3.10. A 4<sup>th</sup> order polynomial trendline is used to correlate the voltage output,  $E$ , and the known velocity,  $u$ , measured by the Pitot-static probe. These calibration curves were then incorporated into the LabVIEW program, so that  $u$  can be computed more accurately based on the input of both  $E$  and  $T_\infty$ . Linear interpolation was used to estimate the local velocity at any temperature lying between the available curves. From Figure 3.10, it can be observed that the voltage signals appear to be more sensitive to temperature at a higher velocity ( $u \geq 20\text{ m/s}$ ), and almost collapse together at a low range of velocity ( $5\text{ m/s} \leq u \leq 10\text{ m/s}$ ) regardless of the temperature.

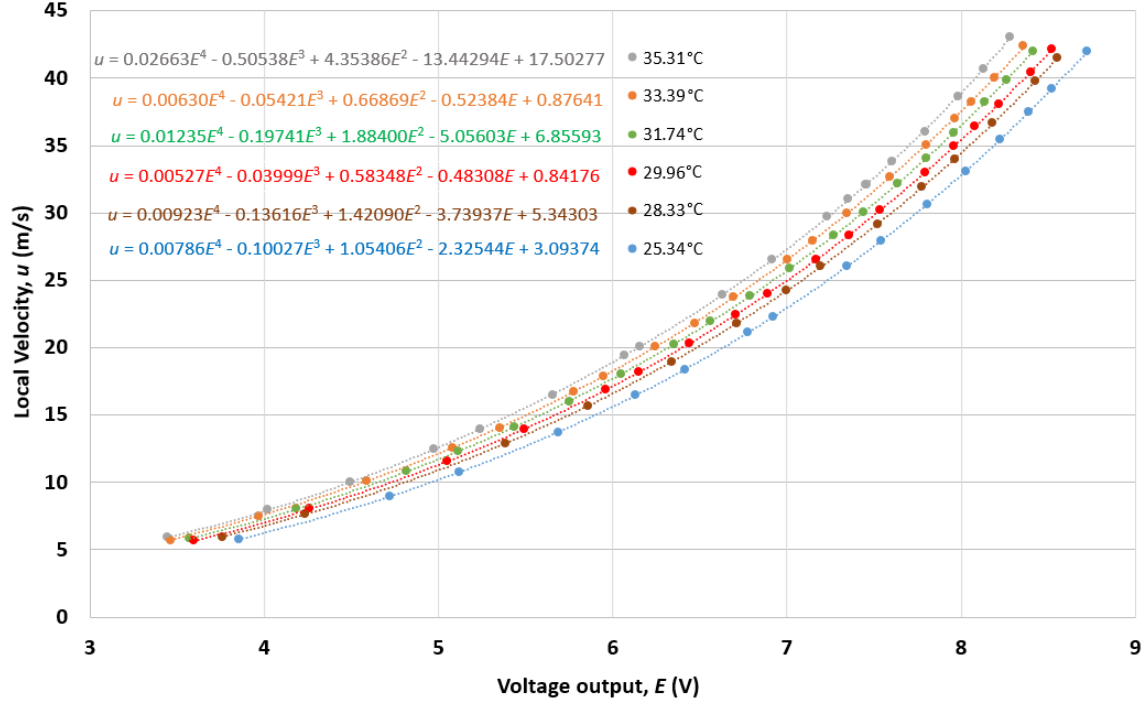


**Figure 3.10:** Calibration of the hotwire anemometer probe in the boundary layer measurement, where  $E$  is on the  $x$ -axis and  $u$  is on the  $y$ -axis in the curve fitting.

To measure the Strouhal number, the Dantec 55P11 hotwire was used to obtain a time series of voltage (and velocity) fluctuations. The voltage fluctuation signal was then separated into individual component frequencies by using a fast Fourier transform, and a power spectrum was obtained in LabVIEW to find the frequency content. The sampling frequency used to obtain a power spectrum was 1 kHz for 1k samples. To enhance the accuracy, 30 consecutive power spectra were averaged, i.e. the sampling time was 30 s to obtain the final power spectrum density output. The vortex shedding frequency corresponds to the location of the peak in the final power spectrum output; this frequency was then non-dimensionalized into  $St$  by using Equation 1.5. This hotwire was not calibrated before the  $St$  measurement, because only the fluctuating voltage is essential in determining the power spectrum, instead of the absolute magnitude of the velocity. The location of the hotwire probe for the  $St$  measurements was fixed at  $x/D = 6.0$ ,  $y/D = 2.5$ , and  $z/H = 0.5$  for all sets of the measurement. This method of fixed location is appropriate based on some previous studies that illustrated the vortex shedding frequency is independent of the spanwise and streamwise locations (Wang and Zhou (2009), Bourgeois et al. (2011), Sattari et al. (2012), Kindree et al.

(2018)). The selection of the  $+y$  location of the probe is based on the fact that the wake is shifted to the  $+y$  region when the prism is rotated clockwise (Unnikrishnan et al. (2017)). The mid-span location of the hotwire probe is considered suitable, because less discernible peaks are obtained if the probe is located higher than mid-span due to the influence of the downwash effect (Wang and Zhou (2009), McClean and Sumner (2014)).

In order to obtain the vortex formation length,  $L_f$ , the turbulence intensity (TI) profile was measured by the hotwire in the wake region at the rear side of the square prism. Noca et al. (1998) suggested that the vortex formation length can be obtained based on the maximum square of the velocity fluctuations  $\langle u'^2 \rangle$  measured along the centerline downstream of the prism. Therefore, for the measurement of  $L_f$ , the hotwire was located at  $y/D = 0$  and  $z/H = 0.5$  (mid-span), and traveled along downstream from a range of  $x/D = 1$  up to 7 (the range was further narrowed down into different smaller ranges based on different aspect ratios). The downstream location,  $x/D$  (measured from the prism centre) with the highest  $\langle u'^2 \rangle$  value is considered the formation length. The working principle of measuring the TI profile in identifying  $L_f$  was similar to the TI profile obtained in the boundary layer measurement (Figure 3.2), except the hotwire was only calibrated at a single temperature for the measurement of  $L_f$ . This is because only the maximum peak location of  $\langle u'^2 \rangle$  is of interest in identifying  $L_f$ , and it is assumed that the temperature does not vary significantly between the measurements of two consecutive downstream locations. The sampling frequency used in the  $L_f$  measurements was 1 kHz for 50k samples. The sampling duration for the  $L_f$  measurement was longer than other measured variables, in view of the high turbulence characteristics of the wake behind of the prism body.

### 3.9 Measurement uncertainty

The law of propagation of uncertainty is used to estimate the uncertainty of the pressure distribution. Recall from Equation 1.1 that the value of  $C_P$  depends on the dynamic pressure,  $q_\infty$ , and the measured differential pressure ( $P - P_\infty$ ). Therefore, the uncertainty of  $C_P$  should be related to the uncertainties of both  $q_\infty$  and ( $P - P_\infty$ ). Based on the propagation of uncertainty, the individual uncertainty contributions from both  $q_\infty$  and ( $P - P_\infty$ ) are

combined by taking the root-mean-square, and the final formula derived is shown in Equation 3.11. In this equation,  $\epsilon()$  refers to the uncertainty for the individual parameter written inside the bracket. This formula also assumes the individual errors  $\epsilon(q_\infty)$  and  $\epsilon(P - P_\infty)$  are uncorrelated.

$$\epsilon(C_P) = \sqrt{\left(\frac{\epsilon(P - P_\infty)}{q_\infty}\right)^2 + \left((P - P_\infty)\frac{\epsilon(q_\infty)}{q_\infty^2}\right)^2} \quad (3.11)$$

From the given service manual of the ZOC17 pressure scanner, the uncertainty of the scanner is reported to be 0.2% FS for 10 inH<sub>2</sub>O (2.5 kPa) which includes both systematic and random error, such as linearity, hysteresis and repeatability. This reported accuracy corresponds to the uncertainty of 5 Pa resulted from the pressure scanner itself. Chue (1975) suggested another source of the systematic error due to the presence of the hole in retaining wall (free-end surface in the case of this study), and this error can be correlated with the hole diameter. Based on the hole diameter of 0.7 mm in this experiment, the induced uncertainty on the local static pressure,  $P - P_\infty$  is estimated to be 0.9% of the dynamic pressure,  $q_\infty$ . Based on the freestream velocity of  $U_\infty = 22.5 \text{ m/s} \pm 1\%$  in  $C_P$  measurement, and also the highest air density (occurred at the lowest temperature) recorded throughout the experiment, the maximum dynamic pressure is equivalent to 288 Pa. The maximum uncertainty in the static pressure due to the wall hole suggested by Chue (1975) is therefore 2.6 Pa. Thus, the combined uncertainty of  $\epsilon(P - P_\infty)$  by taking the root-mean-square of the individual contributions of the pressure scanners and the wall hole is 5.6 Pa. For the dynamic pressure, the reported uncertainty of the differential pressure transducer, Datametrix Barocel Type 590D, is 0.05% for linearity, 0.015% for hysteresis, and 0.01% for repeatability, which is corresponding to the combined uncertainty of 0.053%, or about 0.15 Pa.

Equation 3.11 suggests that the uncertainty is dependent on the value of  $P - P_\infty$ . Unlike  $q_\infty$ , the value of  $P - P_\infty$  changed significantly throughout the experiment based on different measured locations and other manipulated variables of the experiment. The maximum recorded magnitude of the  $P - P_\infty$  in this experiment was 1036 Pa. Based on the maximum magnitude of  $P - P_\infty$ , the maximum uncertainty of  $C_P$  calculated by Equation 3.11 is  $\epsilon(C_P)_{\max} = 0.02$  (absolute uncertainty), or 0.6% FS. It should be noted that there are also

some other systematic errors, such as the head loss inside the flexible tubing, uncertainty of the calibration pressure, and uncertainty of the reference pressure measured by the absolute pressure transducer. These factors are, however, considerably small and not accounted for in the uncertainty analysis. Moreover, the present thesis is mainly qualitative research and is focused on the data trend (instead of the absolute value), so it would be tedious to consider insignificant systematic errors which do not remarkably affect the trend of the results.

The main uncertainty in the force measurements resulted from the temperature drift. Although the voltage offset was measured before each experiment, there was still some challenge faced since the temperature slowly increased throughout the experiment due to the forced convection from the heated motor to the supplied wind, and resulted in measured voltage drift for the force balance. Some experiments were conducted to quantify the voltage drift effect, and it was found that for a  $5^\circ$  increase in the temperature (maximum temperature increment for all the experiments), the maximum voltage drifts recorded were 0.07 mV (LC1), 0.02 mV (LC2, LC5, LC6), 0.03 mV (LC3), and 0.04 (LC4), where ‘LC’ stands for load cell. It was observed that load cell 1 was most sensitive to the temperature drift. The maximum voltage drift of 0.07 mV in load cell 1 corresponds to 2.1% change in voltage affected by the temperature, which was similar to the previous studies of Beitel (2017) and Reitenbach (2018), who were still able to obtain sufficiently accurate force data. These uncertainties in voltage are then converted to forces by multiplying the maximum voltage drift with the matrix of coefficients obtained during the force balance calibration process. The maximum uncertainties for  $F_D$ ,  $F_L$ , and  $F_N$  calculated are therefore 0.36 N (1.0%), 0.19 N (1.0%), and 0.26N (0.7%), respectively. The maximum uncertainty of  $C_D$  varies from 0.02 to 0.18, and for  $C_L$  varies from 0.01 to 0.09 (both from largest to smallest AR). The variation of the uncertainty is because both  $C_D$  and  $C_L$  are dependent on the frontal area, and this area changes with AR. The value of  $C_N$ , however, uses the same reference area for all the aspect ratios, and has the maximum uncertainty of 0.13, or 7.3%. The uncertainty percentage is fairly large due to the small measured values of the force coefficients.

The uncertainty in St measurement is more straight forward because this measurement is not strongly affected by the uncertainty in the velocity magnitude. It should be noted that the minimum uncertainty of St in all sets of the experiment is 0.002, because the minimum

frequency increment used in the power spectra was 1 Hz. Some additional experiments were also conducted for few aspect ratios to observe the change in the dominated frequency, and it was found that the dominant frequency did not vary significantly, with difference in only 1-2 Hz (corresponds to the uncertainty of 0.004 in St). The fairly small uncertainty in St can also be related to the fact that most of the power spectra show well-defined peaks or less appreciable broad-banded peaks, on account of the measurement was taken at the mid-span location. Some of the remarkable broad-banded peaks, however, were obtained for some prisms with low aspect ratio (details to be given in Section 4.4). The uncertainties for these aspect ratios are not analyzed and St is considered undefined for the case where a very broad-banded peak is obtained. The method in quantifying the uncertainty of  $L_f$  is similar to that of St, where the characteristics of the peak is studied, i.e. higher uncertainty when a more broad-banded peak in the Reynolds stress profile  $\langle u' \rangle^2$  is obtained (details to be given in Section 4.5).

For the boundary layer, it should also be noted that the maximum increment used for the thin and thick boundary layer case are 2 mm and 5 mm, respectively. These increments corresponds to the maximum uncertainty in  $\delta/D$  of close to zero for the thin boundary layer, and  $\pm 0.1$  for the thick boundary layer. Table 3.2 summarizes the maximum uncertainties for all the measured variables discussed in this section.

**Table 3.2:** Maximum experimental uncertainties for the measured variables.

<b>Variables</b>	<b>Associated Uncertainty</b>
Pressure coefficient, $C_P$	$-3.6 \pm 0.6\%$ FS
Drag force coefficient, $C_D$	$\pm 0.02$ to $\pm 0.18$ (from highest to lowest AR)
Lift force coefficient, $C_L$	$\pm 0.01$ to $\pm 0.09$ (from highest to lowest AR)
Normal force coefficient, $C_N$	$1.7 \pm 7.3\%$ FS
Strouhal number, St	$0.132 \pm 1.5\%$ FS
Boundary layer thickness, $\delta/D$	Case 1: $0.8 \pm \simeq 0.0$ Case 2: $2.6 \pm 0.1$ Case 3: $2.2 \pm 0.1$ Case 4: $0.8 \pm \simeq 0.0$ Case 5: $2.0 \pm 0.1$

## 4 RESULTS AND DISCUSSION

In this chapter, the results of the present experimental investigation are discussed in detail. Section 4.1 presents the results of the main scope of this thesis, which is the mean free-end surface pressure distribution, and the effects of the three manipulated variables previously specified on this distribution. In Section 4.2, the pressure distribution of the present thesis is compared with the thesis of Beitel (2017) for the finite circular cylinder. Then, the results of other measured variables are discussed in Sections 4.3, 4.4, and 4.5, for the aerodynamic forces, Strouhal number, and vortex formation length, respectively.

### 4.1 Mean free-end surface pressure distribution

This section illustrates the results of the main measured variable of the present thesis, which is the free-end surface pressure distribution, and the effect of the three manipulated variables in this study: the aspect ratio (AR), incidence angle ( $\alpha$ ), and boundary layer thickness ( $\delta/D$ ). Subsection 4.1.1 discusses the effect of the incidence angle, subsection 4.1.2 highlights the effect of the aspect ratio, and subsection 4.1.3 compares the pressure distributions for the two boundary layer conditions. Recall that the Reynolds number adopted in obtaining the pressure distribution data was  $Re = 6.5 \times 10^4$ . Regardless of the values of AR,  $\alpha$ , and  $\delta/D$ , the  $C_P$  values on the free end are negative due to significant flow separation above the free end of the prism. The negative  $C_P$  results in a vertically upwards mean normal pressure force experienced by the prism. The results in this section are presented in the form of both full pressure contour plots and centerline pressure profiles. However, only selected contour plots or centerline profiles are presented throughout this section. The complete data sets are found in Appendix A and B, for the  $C_P$  contour plots and  $C_P$  centerline profiles, respectively.

### 4.1.1 The effect of incidence angle

Figure 4.1 illustrates the mean free-end pressure distribution at six selected incidence angles for the cube ( $AR = 1$ ). All the  $C_P$  results shown in this subsection are for the thin boundary layer ( $\delta/D = 0.8$ ). As shown in Figure 4.1, as  $\alpha$  increases, the minimum values of  $C_P$  become more negative. Notably, the location of the minimum  $C_P$  is generally close to the windward corner (Corner A in Figure 2.1), for most of the incidence angles ( $\alpha > 5^\circ$ ). The minimum  $C_P$  may be related to the conical vortices emerging from the windward corner, and rolling above the free end, as identified by Okuda and Taniike (1993) for all non-zero  $\alpha$  (subsection 2.4.1). At  $\alpha = 10^\circ$  to  $20^\circ$  (Figure 4.1(b)-(d)), a small higher-pressure region can be observed near to the bottom-right corner (Corner B in Figure 2.1) of the trailing edge. When  $\alpha$  is further increased, this higher-pressure region expands and moves towards the centre. For all of the aspect ratios tested, at  $\alpha = 25^\circ$  to  $35^\circ$  (Figure 4.1(e)), the contour line pattern is relatively dense (which indicates a stronger pressure gradient), and the surface pressure is relatively lower near to the bottom-oblique leading edge, compared to other regions. The pressure contours slowly regain their symmetry when the incidence angle is further increased to  $\alpha = 45^\circ$ .

Figure 4.2 illustrates the effect of  $\alpha$  on the pressure distribution for one of the intermediate aspect ratios ( $AR = 6$ ), while Figure 4.3 presents a similar pressure distribution for the highest aspect ratio tested ( $AR = 11$ ). Note that the effect of the incidence angle for those aspect ratios has been rarely reported in the literature. From Figures 4.2 and 4.3, it can be observed that the variation in the  $C_P$  contours with  $\alpha$  for the prisms with higher  $AR$  is somewhat similar to the cube ( $AR = 1$ ), where the contour pattern is much more complex at a higher  $\alpha$ , as compared to that at  $\alpha = 0^\circ$ . For a given  $\alpha$ , the complexity of the  $C_P$  contours for various  $AR$ , however, is different and will be discussed further in subsection 4.1.2. The higher complexity of the  $C_P$  contours at higher  $\alpha$  is related to a more complicated flow structure above the free end through the formation of the conical vortices. There is no evidence for the existence of the conical vortices at  $\alpha = 0^\circ$ , as many experimental investigations have shown a significant flow separation above the free end at this angle (Nakamura et al. (2001), McClean and Sumner (2014), Sumner et al. (2017)). Recall from subsection 2.4.1 that for a

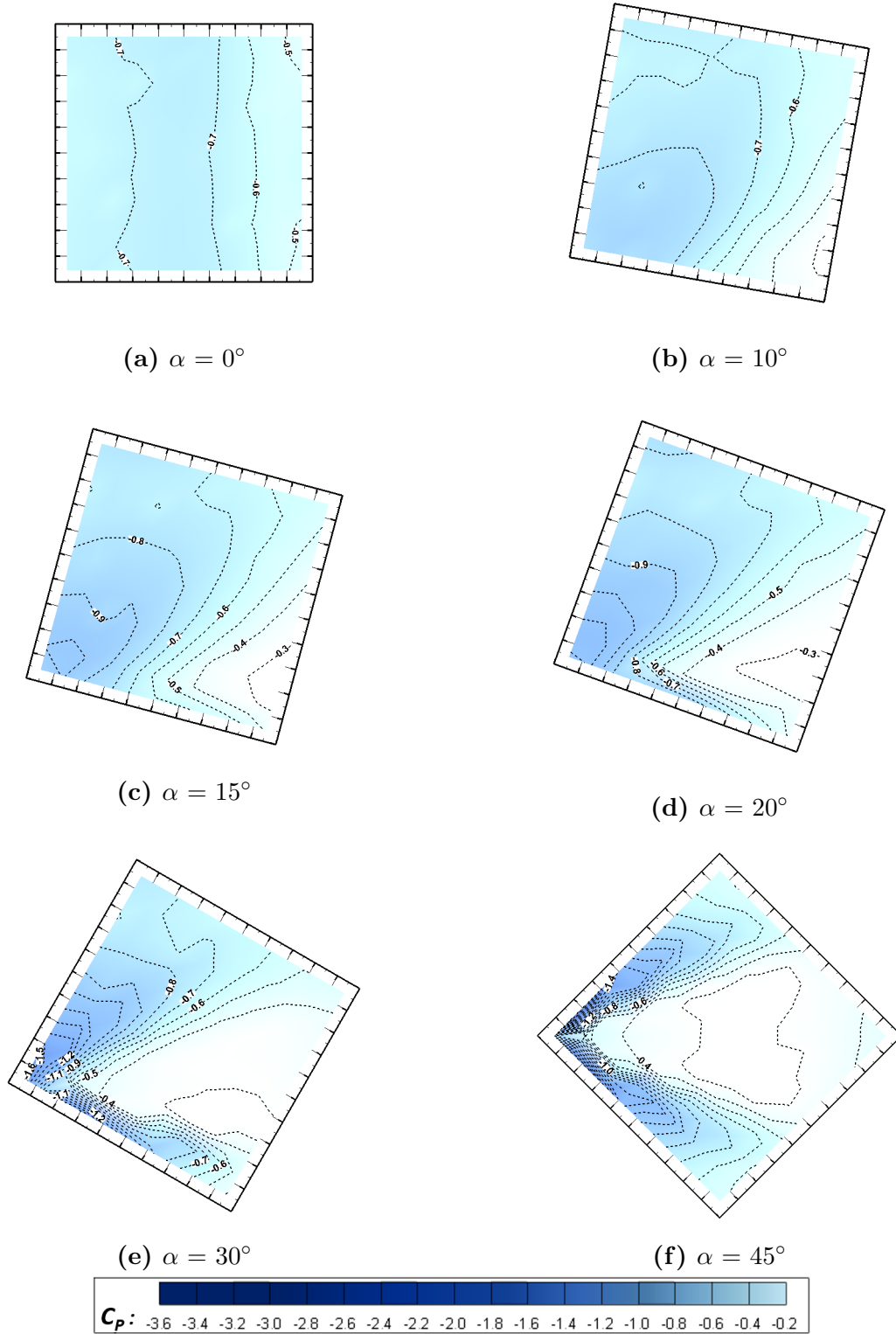


**Figure 4.1:** Free-end mean pressure distribution (contour lines of constant  $C_p$ ) for a prism of AR = 1 (cube): (a)  $\alpha = 0^\circ$ , (b)  $\alpha = 10^\circ$ , (c)  $\alpha = 15^\circ$ , (d)  $\alpha = 20^\circ$ , (e)  $\alpha = 30^\circ$ , and (f)  $\alpha = 45^\circ$ . The flow is from left to right.

finite square prism of  $AR = 4$ , Okuda and Taniike (1993) identified a single conical vortex emerging from the windward corner for intermediate incidence angles of  $\alpha = 10^\circ$  to  $15^\circ$ , and a pair of conical vortices are formed above the free end at higher incidence angles of  $\alpha = 20^\circ$  to  $45^\circ$ . For a square prism with relatively higher aspect ratio ( $AR = 9$ ), the PIV measurements of McClean and Sumner (2014) showed that the flow above the free end (on the centerline) was mostly attached to the free-end surface at  $\alpha = 45^\circ$ . Additionally, significantly higher vorticities were observed close to the free-end surface at  $\alpha = 45^\circ$ , compared to the flow field at  $\alpha = 0^\circ$ . Therefore, the complexity of the contours and the pressure gradients generally increase with  $\alpha$ , for a wide range of the tested aspect ratios, due to the formation of the conical vortices and the increased proportion of flow reattachment at a higher  $\alpha$ . It is also worth pointing out that the minimum locations of  $C_P$  for  $\alpha > 5^\circ$  are generally close to the windward corner for higher aspect ratios, although the locations of the minimum  $C_P$  for  $20^\circ \leq \alpha \leq 35^\circ$  are slightly further downstream of the windward corner for the prisms with  $AR > 2$ . This observation also supports the existence of the conical vortices above the free end (as identified by Okuda and Taniike (1993) for a prism with  $AR = 4$ ) for a wide range of aspect ratios at non-zero  $\alpha$ . Moreover, the  $C_P$  distribution is strongly asymmetric for  $\alpha$  between  $0^\circ$  (Figure 2.1(a)) and  $45^\circ$  (Figure 2.1(f)) for all the tested aspect ratios, owing to the different orientations of the two leading edges, and the different strengths and sizes of the conical vortices. Also, the  $C_P$  contour line pattern at  $\alpha = 15^\circ$  at Figure 4.2(b) for  $AR = 6$  is similar to that of  $AR = 3$  (shown in Appendix A), and the pattern somewhat coincides with the profile of reattachment lines above the free end identified by Cao et al. (2019) (Figure 2.15).

The centerline  $C_P$  profiles in Figure 4.4 show the extent of variation in the mean  $C_P$  distribution with  $\alpha$ , at six selected aspect ratios. The profiles complement the contour plots in Figures 4.1 - 4.3, further illustrating how  $\alpha$  significantly affects the variation in the mean pressure distribution on the free-end surface, and that the pressure variation appears to be greater at higher  $\alpha$ , for a wide range of  $AR$ . At the smallest incidence angle of  $\alpha = 0^\circ$ , there is almost no pressure gradient observed for most of the tested aspect ratios (black squares in Figure 4.4(a)-(f)). The centerline  $C_P$  profiles at  $\alpha = 15^\circ$  are qualitatively similar to that at  $\alpha = 0^\circ$  for the locations closer to the oblique leading edge ( $X/D < 0$ ). However, the profiles for  $\alpha = 15^\circ$  show a slightly higher pressure recovery trend towards the trailing edge ( $X/D$

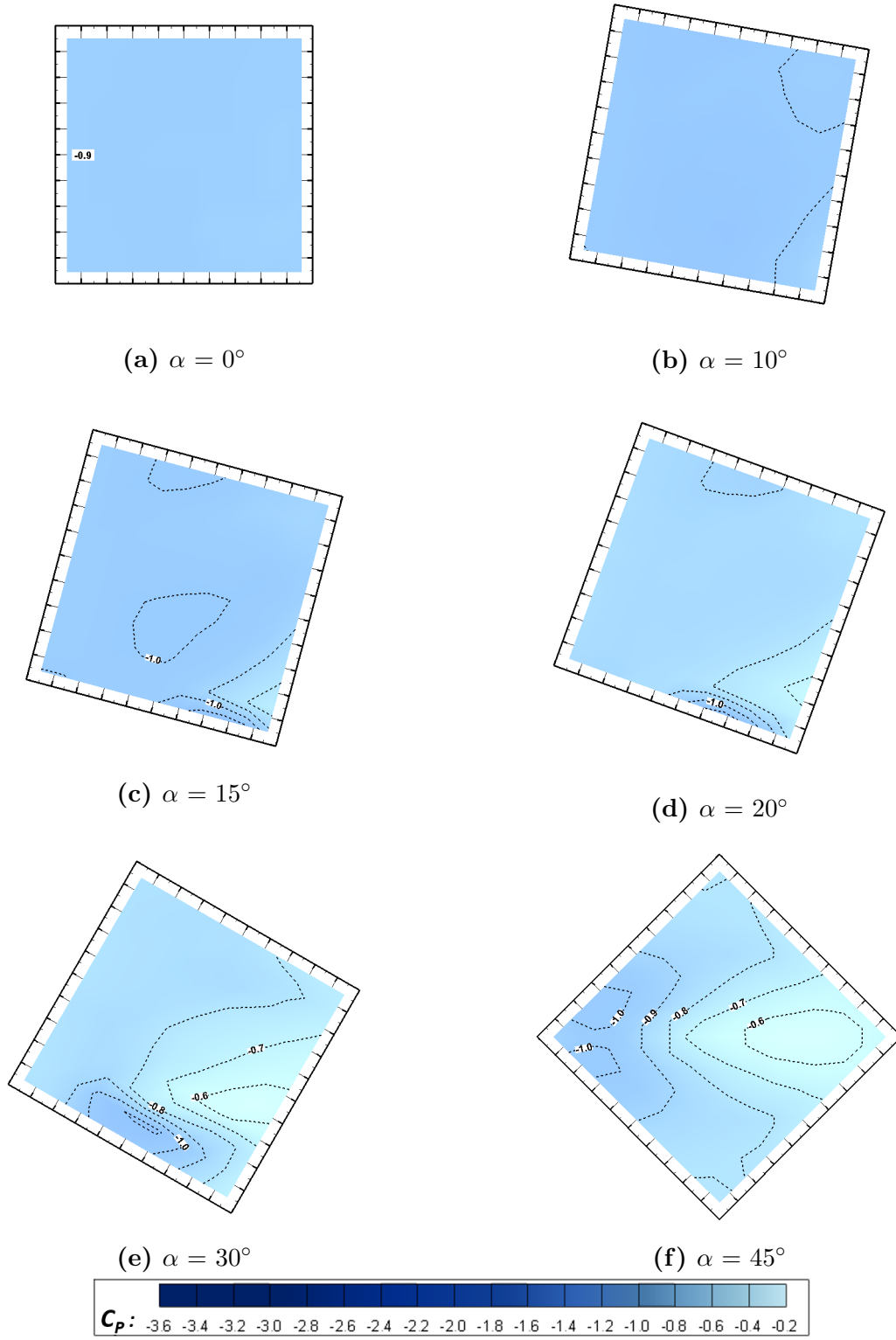


**Figure 4.2:** Free-end mean pressure distribution (contour lines of constant  $C_P$ ) for a prism of  $AR = 6$ : (a)  $\alpha = 0^\circ$ , (b)  $\alpha = 10^\circ$ , (c)  $\alpha = 15^\circ$ , (d)  $\alpha = 20^\circ$ , (e)  $\alpha = 30^\circ$ , and (f)  $\alpha = 45^\circ$ . The flow is from left to right.

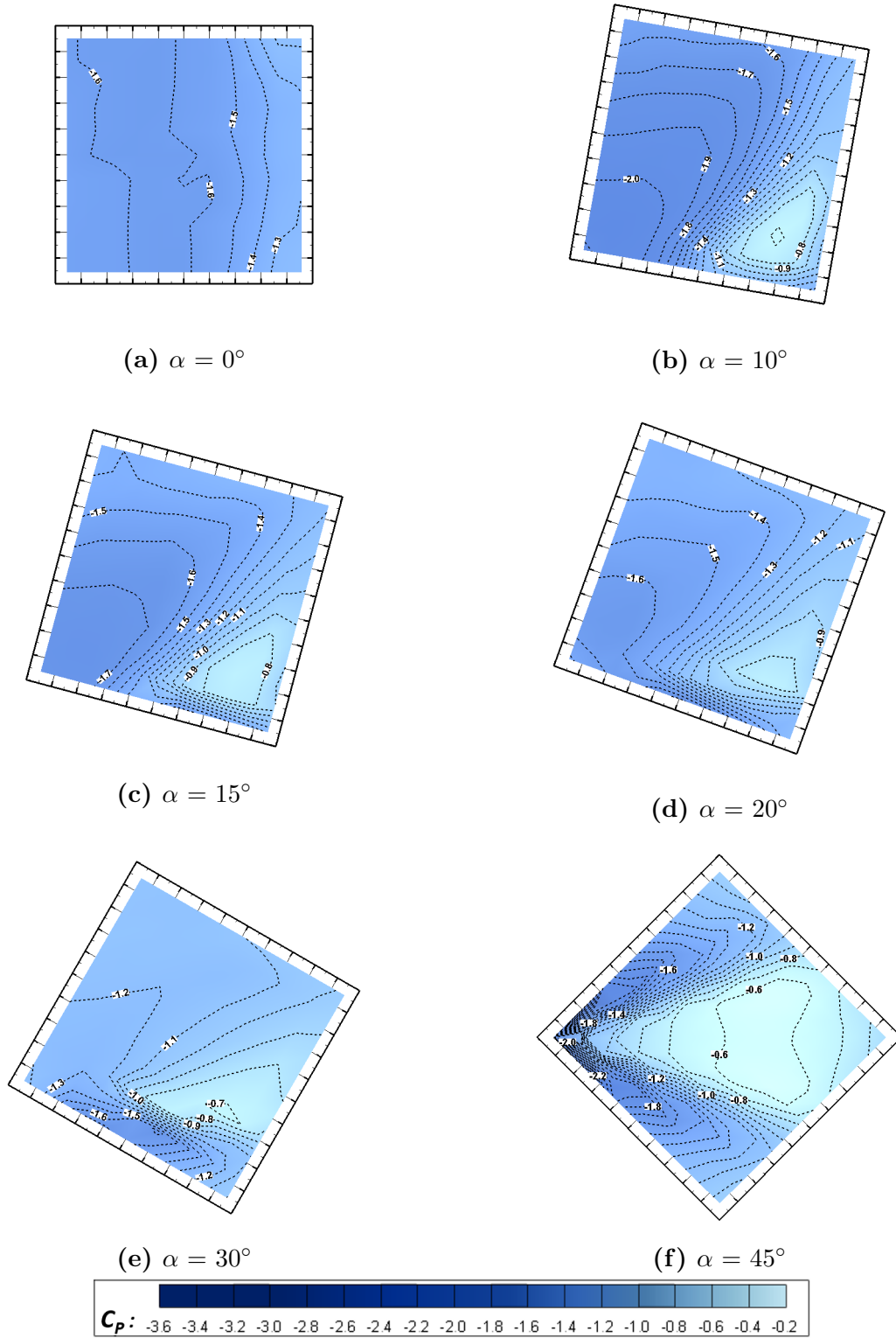
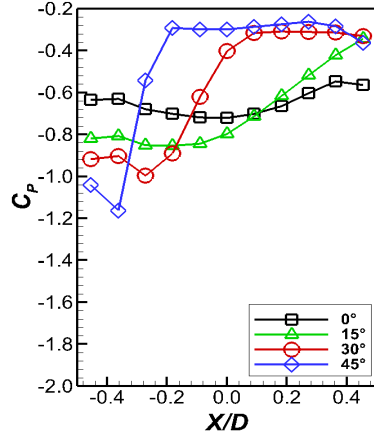


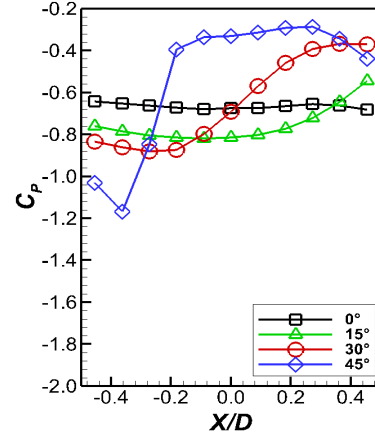
**Figure 4.3:** Free-end mean pressure distribution (contour lines of constant  $C_p$ ) for a prism of AR = 11: (a)  $\alpha = 0^\circ$ , (b)  $\alpha = 10^\circ$ , (c)  $\alpha = 15^\circ$ , (d)  $\alpha = 20^\circ$ , (e)  $\alpha = 30^\circ$ , and (f)  $\alpha = 45^\circ$ . The flow is from left to right.

$> 0$ ) (green triangles in Figure 4.4(a)-(f)), in comparison to the profiles of  $\alpha = 0^\circ$ . The pressure gradient at  $\alpha = 30^\circ$  is relatively more appreciable (red circles in Figure 4.4(a)-(f)) as compared to that at  $\alpha = 0^\circ$  and  $15^\circ$ . It should be noted that the pressure gradients at  $\alpha = 30^\circ$  are more significant at the location closer to the bottom-oblique leading edge, based on the full  $C_P$  contours shown in Figures 4.1(e), 4.2(e), and 4.3(e). Therefore, the centerline profiles at  $\alpha = 30^\circ$  shown in Figure 4.4 should not be used solely to justify the complexity of the contours and pressure variation at this angle. At  $\alpha = 45^\circ$ , an extremely sharp pressure gradient is identified starting from about  $X/D = -0.4$ , and the pressure gradient is remarkable for all the tested aspect ratios (blue diamonds in Figure 4.4(a)-(f)), for most of the tested aspect ratios.

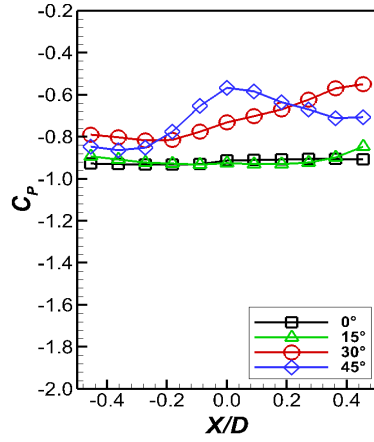
The profiles in Figure 4.4 show relatively smaller pressure gradients for a lower incidence angle, (generally  $\alpha < 20^\circ$ , based on the full experimental results). However, from Figure 4.4, it appears that the pressure variation is also strongly affected by the aspect ratio. The profiles of lowest and highest aspect ratios ( $AR = 1$  and  $11$  in Figures 4.4(a)(f)) show a slight pressure recovery trend despite at a small incidence angle of  $\alpha = 0^\circ$ . The behaviour of the insensitive pressure variation at the small incidence angle of  $0^\circ \leq \alpha \leq 15^\circ$  remains evident for the intermediate aspect ratios (Figures 4.4(c)(d)).



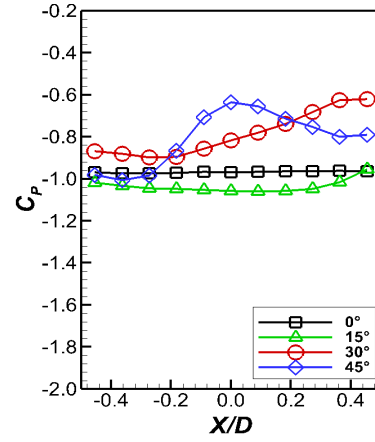
(a)  $AR = 1$



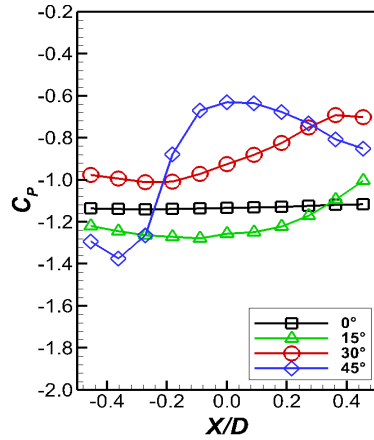
(b)  $AR = 1.5$



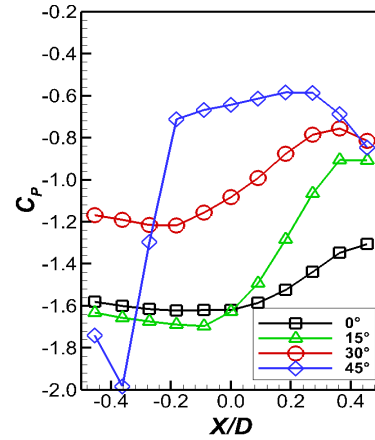
(c)  $AR = 4.5$



(d)  $AR = 7$



(e)  $AR = 9$



(f)  $AR = 11$

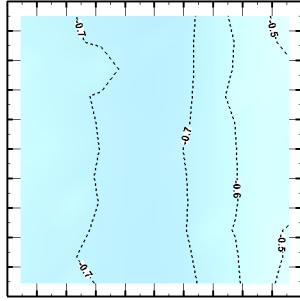
**Figure 4.4:** Centerline mean  $C_P$  profiles (where  $X$  is a coordinate fixed to the prism free-end surface, and rotates with the prism) at (a)  $AR = 1$ , (b)  $AR = 1.5$ , (c)  $AR = 4.5$ , (d)  $AR = 7$ , (e)  $AR = 9$ , and (f)  $AR = 11$  at selected  $\alpha = 0^\circ, 15^\circ, 30^\circ$  and  $45^\circ$ .

### 4.1.2 The effect of aspect ratio

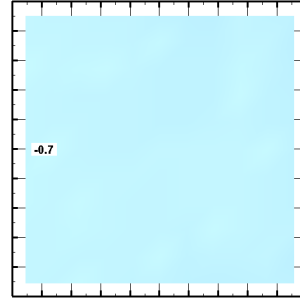
Similar to the previous subsection, all the pressure contours and centerline profiles presented in this subsection are for the thin boundary layer ( $\delta/D = 0.8$ ). This subsection discusses the effect of AR at four selected incidence angles,  $\alpha = 0^\circ$ ,  $15^\circ$ ,  $30^\circ$ , and  $45^\circ$ .

The variation of the pressure distribution at  $\alpha = 0^\circ$  with six selected AR is shown in Figure 4.5. The  $C_P$  values decrease (become more negative) with increasing AR and results in higher suction forces for the prisms with higher AR. The decrease rate in  $C_P$  is found most insensitive for  $4 \leq \text{AR} \leq 8.5$ , with the range of  $C_P$  lying between -1.1 to -0.9. This result somewhat corresponds to the study of Sumner et al. (2017), where the mean velocity vector field is very close to the free-end surface was found qualitatively and quantitatively similar for  $\text{AR} = 5, 7$  and  $9$ . Comparing the pressure variation for different AR, there is little pressure variation for the prisms with  $\text{AR} = 1.5$  to  $10$  at  $\alpha = 0^\circ$  (Figure 4.5(b)-(e)). On the other hand, for the lowest and highest tested aspect ratios ( $\text{AR} = 1$  and  $11$ ), there is a slightly appreciable pressure recovery trend towards the downstream direction (Figure 4.5(a)(f)). The  $C_P$  contours for the cube ( $\text{AR} = 1$ ) in the present study are somewhat similar to the  $C_P$  contour pattern obtained by Nakamura et al. (2001) (Figure 2.16(a)). Hence, the slight pressure recovery trend observed for  $\text{AR} = 1$  in the present study may indicate the occurrence of flow reattachment, with the reattachment line located very close to the trailing edge. For other prisms with higher AR, the study of Sumner et al. (2017) has shown that the location of vortex centre and saddle point moved closer to the free-end surface and towards upstream (subsection 2.4.1), when AR increased from  $3$  to  $9$ . Moreover, for  $\text{AR} = 9$ , Sumner et al. (2017) also observed the vertical distance between the free end to the separated shear layer decreased slightly and the mean streamline profile above the free end is relatively more complicated (Figure 2.13). These flow features may be responsible for the slight pressure recovery trend observed for  $\text{AR} = 10.5$  (not shown here) and  $\text{AR} = 11$  (Figure 4.5(f)).

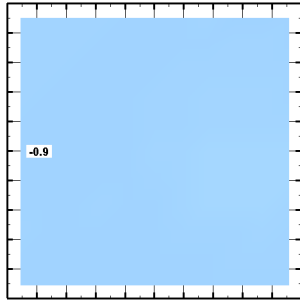
Figure 4.6 illustrates the free-end  $C_P$  contours for various aspect ratios at  $\alpha = 15^\circ$ , an incidence angle close to the critical incidence angle for square prisms (Sakamoto (1985); McClean and Sumner (2014); Unnikrishnan et al. (2017)). Similar to  $\alpha = 0^\circ$ , the  $C_P$  values generally decrease with increasing AR. However, at  $\alpha = 15^\circ$ , the variation of the pressure



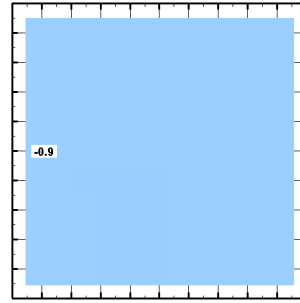
(a)  $AR = 1$



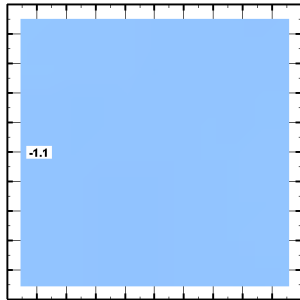
(b)  $AR = 2$



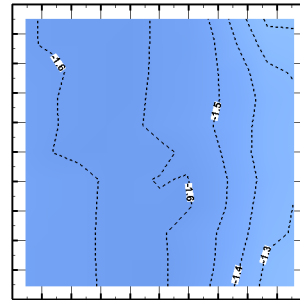
(c)  $AR = 4.5$



(d)  $AR = 7$



(e)  $AR = 9$



(f)  $AR = 11$

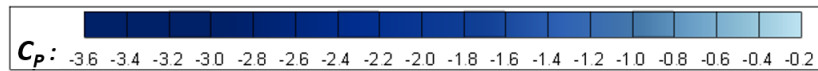
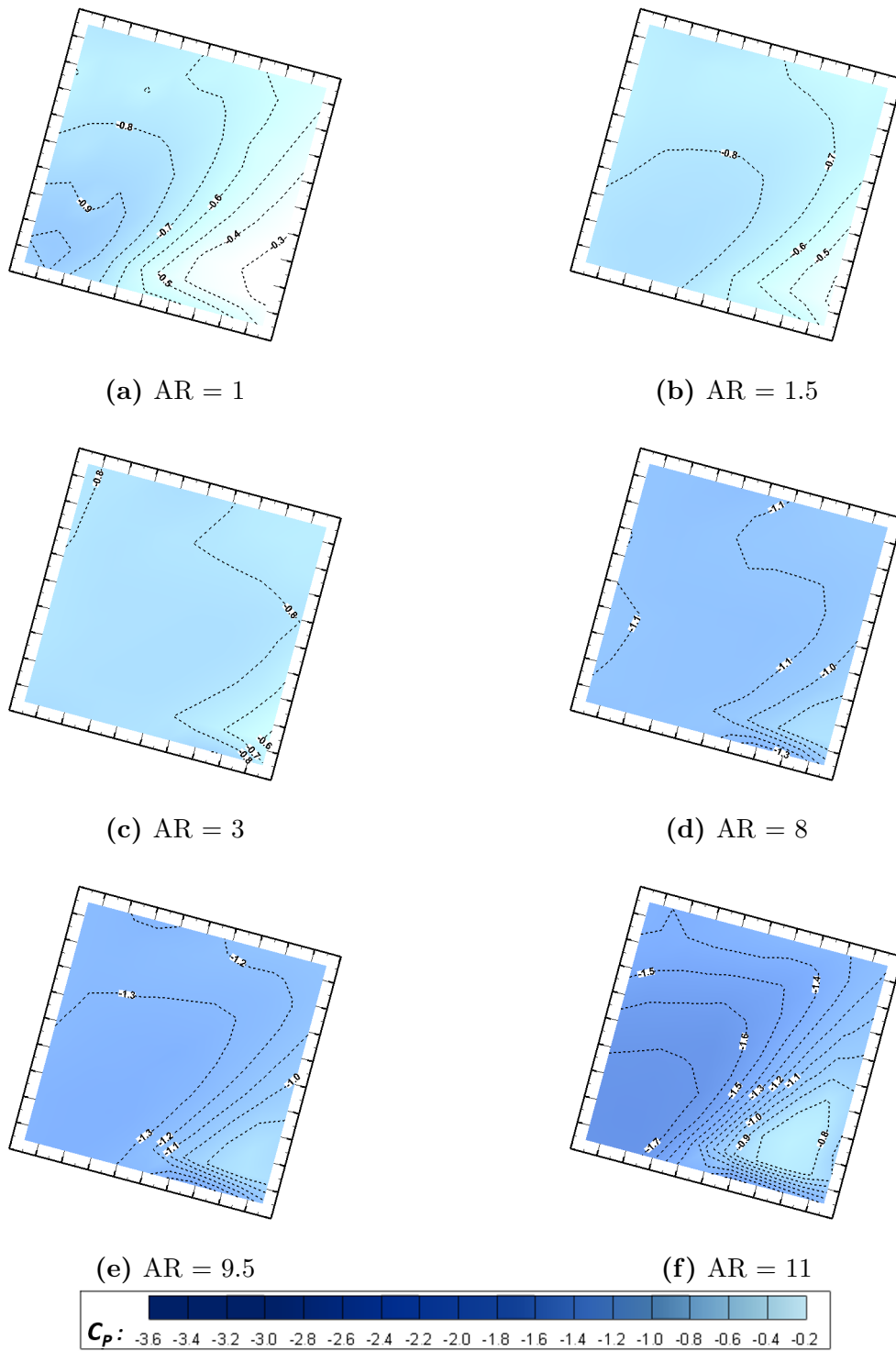


**Figure 4.5:** Free-end mean pressure distribution (contour lines of constant  $C_P$ ) at  $\alpha = 0^\circ$ : (a)  $AR = 1$ , (b)  $AR = 2$ , (c)  $AR = 4.5$ , (d)  $AR = 7$ , (e)  $AR = 9$ , and (f)  $AR = 11$ . The flow is from left to right.

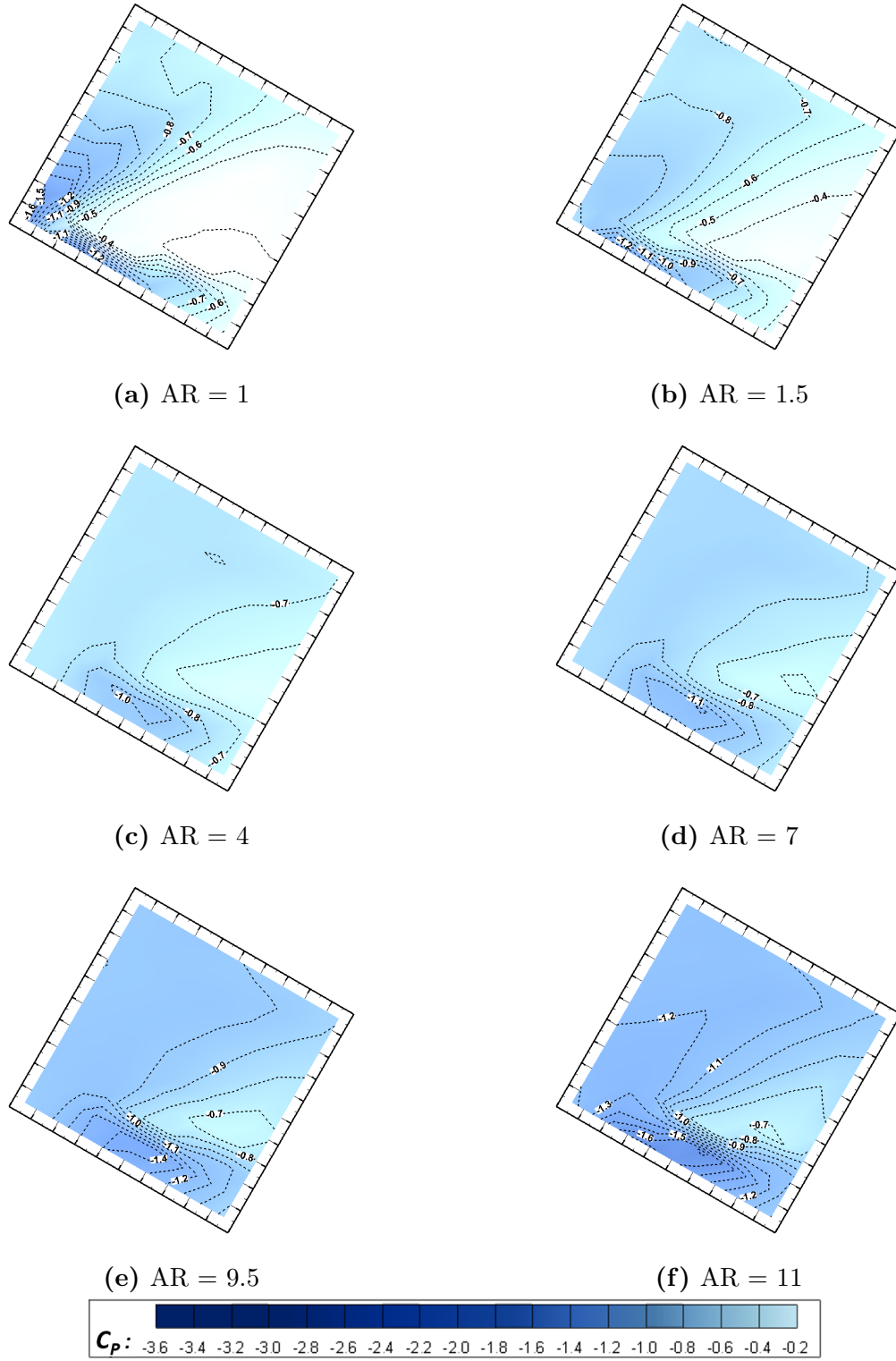
distribution is noticeably sensitive to the change of AR. For the low-aspect-ratio prisms ( $AR = 1$  and  $1.5$ ), some pressure variations can be observed from the contour line patterns (Figure 4.6 (a)(b)). For the prisms with intermediate aspect ratio ( $AR = 2$  to  $7.5$ ), the  $C_P$  values become more negative but the pressure variation was found to be very minimal (Figure 4.6(c)). At  $AR = 8$ , more complicated pressure contours can again be observed (Figure 4.6(d)). The contour lines become more complex with a further increase in AR, with those of the high aspect ratio prisms ( $AR = 9.5$  to  $11$ ) (Figure 4.6(e)(f)) more complex than those of the prisms with low aspect ratio ( $AR = 1$  and  $1.5$ ) (Figure 4.6(a)(b)). Notably, a circular higher pressure region can also be observed at the bottom-right region of the surface, starting from  $AR = 10.5$  (Figure 4.6(f)). It is worth mentioning that the variation in the  $C_P$  contours for various AR at  $\alpha = 10^\circ$  is qualitatively similar to that at  $\alpha = 15^\circ$ . However, comparing the  $C_P$  contours between these two incidence angles, the  $C_P$  contours at  $\alpha = 10^\circ$  are relatively more dynamic, where the value of  $C_P$  decreases with AR relatively more rapidly. Moreover, at  $\alpha = 10^\circ$ , the circular higher pressure region can be observed starting from  $AR = 8.5$ , compared to  $AR = 10.5$  for the  $C_P$  contours observed at  $\alpha = 15^\circ$ .

Figure 4.7 presents the variation of the free-end surface pressure distribution contours with aspect ratio at  $\alpha = 30^\circ$ . These profiles are somewhat similar to the profiles at other incidence angles between  $\alpha = 25^\circ$  to  $35^\circ$  (shown in Appendix A), where contour lines near the bottom-oblique leading edge are found to be relatively dense (closely spaced). For the prisms with  $AR \leq 1.5$  (Figure 4.7(a)(b)), significant pressure variations can be noticed from the  $C_P$  contours. The pressure variation becomes relatively less obvious for the intermediate aspect ratios ( $3 \leq AR \leq 7$ ) (Figure 4.7(c)(d)), though a small lower pressure region can still be observed near the centre location of the bottom-oblique leading edge. This lower pressure region expands, and the value of the  $C_P$  in this region further drops, when the aspect ratio is further increased. When  $AR \geq 9.5$  (Figure 4.7(e)(f)), the pressure variation becomes distinct, although it is somewhat similar to the prisms with low AR.

It is also worth comparing the  $C_P$  distributions at  $\alpha = 45^\circ$  (shown in Figure 4.8) for different aspect ratios, since the  $C_P$  contour lines at this incidence angle show substantial variation. At  $\alpha = 45^\circ$ , the most negative  $C_P$  is located close to the leading edge for all AR tested, while the region for the least negative  $C_P$  is wider and located close to the region



**Figure 4.6:** Free-end mean pressure distribution (contour lines of constant  $C_p$ ) at  $\alpha = 15^\circ$ : (a) AR = 1, (b) AR = 1.5, (c) AR = 3, (d) AR = 8, (e) AR = 9.5, and (f) AR = 11. The flow is from left to right.



**Figure 4.7:** Free-end mean pressure distribution (contour lines of constant  $C_P$ ) at  $\alpha = 30^\circ$ : (a) AR = 1, (b) AR = 1.5, (c) AR = 4, (d) AR = 7, (e) AR = 9.5, and (f) AR = 11. The flow is from left to right.

between the centre and the trailing edge. The  $C_P$  contour lines at  $\alpha = 45^\circ$  are generally denser (more closely spaced, indicating stronger pressure gradients) along both leading edges, which is evidence of the roll-up of the separated shear layers into the pair of conical vortices (Okuda and Taniike (1993)). An interesting trend is observed where the  $C_P$  sensitivity to AR was found to be significant for low-AR prisms ( $AR \leq 2$ ) (Figure 4.8(a)(b)), which lie below the critical aspect ratio (McClellan and Sumner (2014); Unnikrishnan et al. (2017)). For these prisms, small changes in AR result in marked changes to the  $C_P$  values and distributions. For prisms of  $4.5 \leq AR \leq 7$  (Figure 4.8(c)(d)), the contour levels and pressure gradients associated with the conical vortices are found to be weaker and less complex. More complex  $C_P$  distributions are again observed for  $AR = 9$  to  $11$  (Figure 4.8(e)(f)). These findings were similar to the results for other incidence angles such as  $\alpha = 0^\circ$ ,  $15^\circ$ , and  $30^\circ$  presented in Figures 4.5, 4.6, 4.7, respectively, where the  $C_P$  variations were found to be minimal for the intermediate AR, while more complicated  $C_P$  contour line patterns were seen when the prism was approaching the lowest and highest aspect ratios tested.

The value of AR where the pressure variation was found to be minimal and the pressure distribution started to be insensitive to the change of AR is, however, different at various  $\alpha$ . Table 4.1 summarizes the behaviour of the pressure distributions based on two characteristics: whether the pressure distribution shows “evident pressure variation”, or whether the pressure variation was “minimal” or relatively insensitive to the change of AR. For a wide range of AR investigated, there are three flow regimes identified in the present study based on the pressure distribution. The first flow regime shows the characteristics of “evident pressure variation” and occurs for the prisms with lower aspect ratios. The second flow regime is observed for the intermediate aspect ratios and demonstrates the characteristics of “minimal pressure variation”. The third flow regime shows similar characteristics as the first regime (“evident pressure variation”) and occurs for the high-aspect-ratio prisms, but perhaps the third flow regime shows even a higher pressure variation and a more complicated  $C_P$  contour pattern compared to the first flow regime. With the small increment of AR adopted, the boundaries between the different flow regimes can be identified more accurately and are presented in Table 4.1. The results also show how flow separation from the oblique leading edges, the conical vortex pair that forms (Unnikrishnan et al. (2017)), and the “pressure signature” of

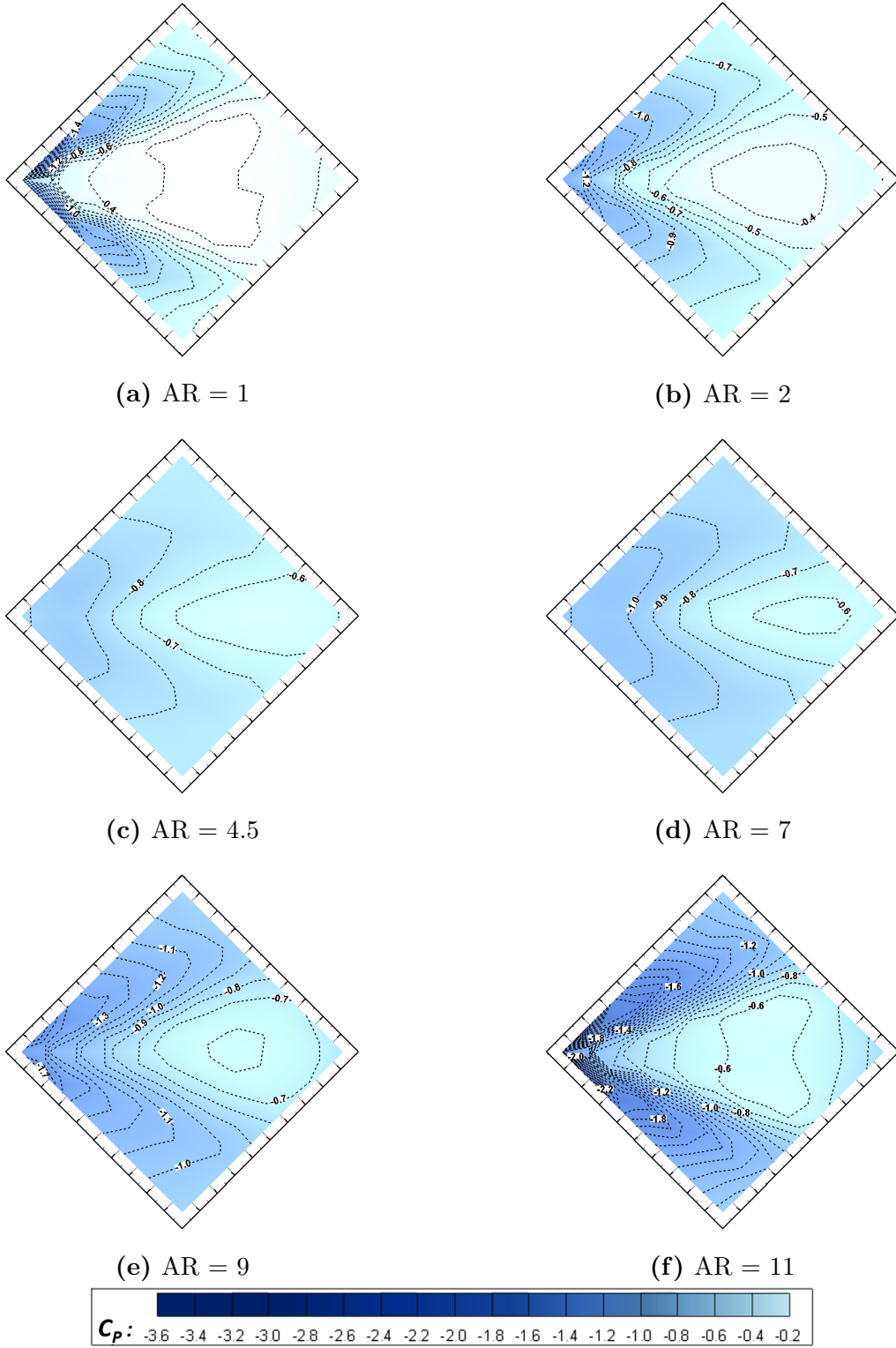


**Figure 4.8:** Free-end mean pressure distribution (contour lines of constant  $C_P$ ) at  $\alpha = 45^\circ$ : (a) AR = 1, (b) AR = 2, (c) AR = 4.5, (d) AR = 7, (e) AR = 9, and (f) AR = 11. The flow is from left to right.

the vortex pair on the free end, are all influenced by AR at various  $\alpha$ . It is worth mentioning that this sensitivity to AR has not been extensively reported in previous studies to date.

**Table 4.1:** The ranges of AR for two characteristics and three regimes of the free-end mean  $C_P$  distribution at four selected incidence angles:  $\alpha = 0^\circ, 15^\circ, 30^\circ$  and  $45^\circ$ .

$\alpha$	<b>First flow regime</b> Evident pressure variation	<b>Second flow regime</b> Minimal pressure variation	<b>Third flow regime</b> Evident pressure variation
$0^\circ$	AR = 1	$1.5 \leq \text{AR} \leq 10$	AR $\geq 10.5$
$15^\circ$	AR $\leq 1.5$	$2 \leq \text{AR} \leq 8$	AR $\geq 10$
$30^\circ$	AR $\leq 1.5$	$3 \leq \text{AR} \leq 7$	AR $\geq 9.5$
$45^\circ$	AR $\leq 2$	$4.5 \leq \text{AR} \leq 7$	AR $\geq 9$

The centerline  $C_P$  profiles for AR = 1 to 11, with the increment of 1, are presented in Figure 4.9, for the four selected  $\alpha$  discussed before. Comparing the centerline profile for the cube (AR = 1) at  $\alpha = 0^\circ$ , a small pressure recovery trend can be observed along downstream after  $X/D = \sim 0$  (Figure 4.9(a)). This trend is similar to the studies of Lim and Ohba (2015) and Lee et al. (2016), although the pressure recovery trend in their investigations can be observed starting from the leading edge, mainly due to different boundary layer conditions (discussed further in subsection 4.1.3). The centerline profiles complement the range of the intermediate aspect ratios presented in Table 4.1 for the flow regime of minimal pressure variation, and further illustrate that the pressure variation is more noticeable for the lowest and highest AR tested. At  $\alpha = 0^\circ$ , the pressure recovery trend diminishes and the pressure gradient is less noticeable starting from AR = 1.5, but a significant substantial pressure recovery trend occurs towards the downstream after about  $X/D = 0$ , when AR increases further and approaches the highest tested aspect ratio (AR = 10.5 and 11) (Figure 4.9(a)). At  $\alpha = 15^\circ$ , the pressure gradient is less remarkable for intermediate aspect ratios ( $2 \leq \text{AR} \leq 8$ ), but an obvious pressure recovery trend is seen for the prisms with low aspect ratio (AR  $\leq 1.5$ ) and high aspect ratio (AR  $\geq 10$ ), after about  $X/D = 0$  (Figure 4.9(b)). The centerline  $C_P$  profiles for  $\alpha = 30^\circ$  appear to be qualitatively and quantitatively similar between each subsequent aspect ratio (except for AR = 1) (Figure 4.9(c)). However, it should be noted that for  $\alpha = 30^\circ$ , the region where the highest pressure variation was experienced is close to the bottom-oblique leading edge, when the aspect ratio is varied. The region near the centerline does not undergo any significant change as can be seen from the full  $C_P$  contour

results in Figure 4.7. For  $\alpha = 45^\circ$ , significant changes in behaviour and magnitude are most pronounced, and the pressure gradient can be observed starting from about  $X/D = -0.4$ , close to the leading edge, for all the tested aspect ratios. Moreover, an extremely sharp pressure gradient is observed between about  $X/D = -0.4$  to  $-0.2$ , for the prisms with low aspect ratio ( $AR \leq 1.5$ ), and high aspect ratio ( $AR \geq 9$ ) (Figure 4.9(d)). Based on the centerline mean pressure profiles presented in Figures 4.4 and 4.9, the strong influences of both  $\alpha$  and  $AR$  are apparent on the mean  $C_P$  distribution. Furthermore, it appears that the pressure variation is more remarkable at a higher incidence angle (generally for  $\alpha > 20^\circ$ ) and for a non-intermediate  $AR$  (listed in Table 4.1).

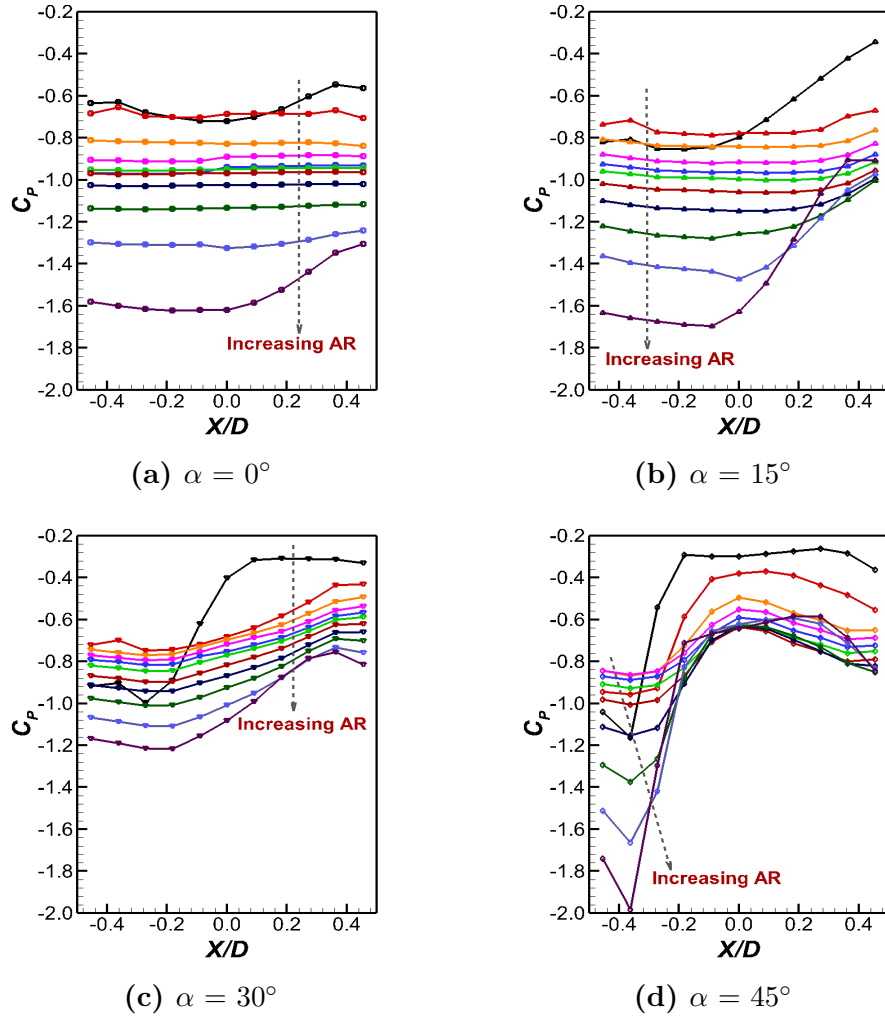


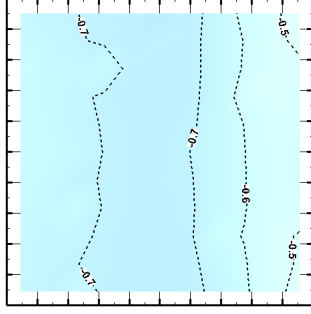
**Figure 4.9:** Centerline mean  $C_P$  profiles (where  $X$  is a coordinate fixed to the prism free-end surface, and rotates with the prism) at (a)  $\alpha = 0^\circ$ , (b)  $\alpha = 15^\circ$ , (c)  $\alpha = 30^\circ$ , and (d)  $\alpha = 45^\circ$  for  $AR = 1$  to  $11$ , with increment of  $1$ .

### 4.1.3 The effect of boundary layer thickness

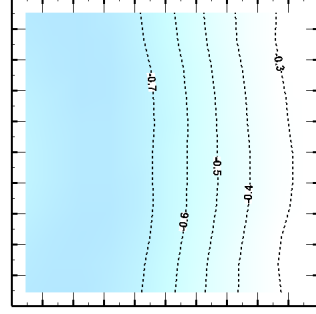
This section specifically discusses the effect of the boundary layer by comparing the previously presented  $C_P$  distributions with those for the thick boundary layer. Recall from Section 3.4 that for the  $C_P$  measurements, the boundary layer thicknesses are  $\delta/D = 0.8$  and  $2.6$  for the thin and thick boundary layers, respectively.

Figure 4.10 shows the pressure distribution for the cube ( $AR = 1$ ) at  $\alpha = 0^\circ$ . It is evident that the trend of the substantial downstream pressure recovery becomes more obvious for the thick boundary layer. The pressure recovers to a value of  $C_P = -0.3$  at streamwise locations closer to the trailing edge, as compared to the maximum pressure of  $C_P = -0.5$  observed for the thin boundary layer. Notably, the contour line of the maximum value ( $C_P = -0.5$ ) only forms a small region, which is close to both corners of the trailing edge (Figure 4.10(a)). On the other hand, the contour line of the maximum value of  $C_P = -0.3$  forms a full line without separation for the thick boundary layer (Figure 4.10(b)). Comparing both  $C_P$  contours for the thin and thick boundary layers, the pressure contours for the thick boundary layer appear to be more qualitatively similar to that obtained by Nakamura et al. (2001) (Figure 4.10(c)) and Chen et al. (2018) (Figure 4.10(d)) (details in subsection 2.4.2), where the substantial pressure recovery is more remarkable, indicating the possibility of the flow reattachment on the free end (Figure 2.10). The rate of the pressure recovery in the present study is also quantitatively similar to Nakamura et al. (2001), but somewhat quantitatively different from the study of Chen et al. (2018). For the thick boundary layer in the present study, the pressure recovers from  $C_P = -0.7$  to  $-0.3$ , from the leading to trailing edge, while the pressure was observed to recover from  $C_P = -0.95$  to  $-0.2$  in the study of Chen et al. (2018). It is noted that Chen et al. (2018) used an atmospheric boundary layer, however, which is much thicker than the “thick boundary layer” in the present study, and the aspect ratio used by Chen et al. (2018) was also slightly lower ( $AR = 0.5$ ).

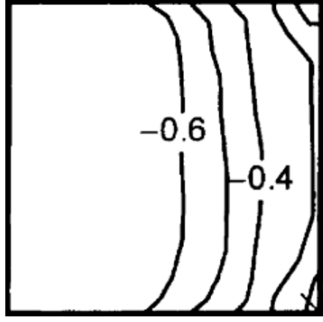
The pressure contours for other prisms with higher aspect ratios are shown in Figure 4.11 for  $\alpha = 0^\circ$ . The same trend of substantial pressure recovery towards downstream is still observed for the prism of  $AR = 1.5$  when a thicker boundary layer is adopted Figure 4.11(b). However, this recovery trend becomes insignificant when the aspect ratio is further increased



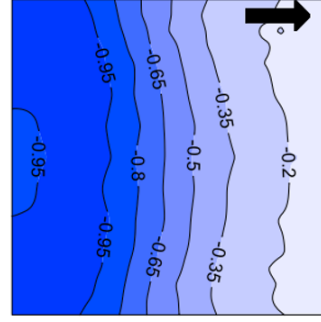
(a) Present study,  $\delta/D = 0.8$



(b) Present study,  $\delta/D = 2.6$



(c) Nakamura et al. (2001),  $\delta/D = 1.5 - 1.83$



(d) Chen et al. (2018),  $\delta/D \gg 1$

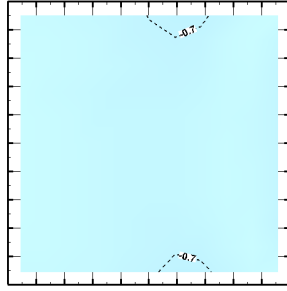
**Figure 4.10:** Free-end mean pressure distribution (contour lines of constant  $C_P$ ) at  $\alpha = 0^\circ$ : (a) present study ( $AR = 1$ ,  $\delta/D = 0.8$ ,  $Re = 6.5 \times 10^4$ ), (b) present study ( $AR = 1$ ,  $\delta/D = 2.6$ ,  $Re = 6.5 \times 10^4$ ), (c) Nakamura et al. (2001) ( $AR = 1$ ,  $\delta/D = 1.5 - 1.83$ ,  $Re = 3.1 \times 10^4$ ), and (d) Chen et al. (2018) ( $AR = 0.5$ ,  $\delta/D \gg 1$ ,  $Re = 8.4 \times 10^4$ ). The flow is from left to right. The reproduced figures are used with permission of Elsevier.

to  $AR = 2$  (not shown here). When  $AR \geq 2$ , no pressure variation can be observed for the thick boundary layer, similar to the contours observed for the thin boundary layer. However, the value of  $C_P$  is higher (less suction effect) when a thicker boundary layer is used. Figure 4.11(c)(d)) shows one of the intermediate aspect ratios of  $AR = 4.5$  that explains this trend, which can also be observed for other prisms with  $AR \geq 2$ . Recall from subsection 4.1.2 that the pressure recovery trend can again be observed when the aspect ratio is further increased to  $AR = 10.5$  (Figure 4.11(e)) and 11, for the thin boundary layer. However, this recovery trend could not be observed for the thick boundary layer, despite the aspect ratio is increased

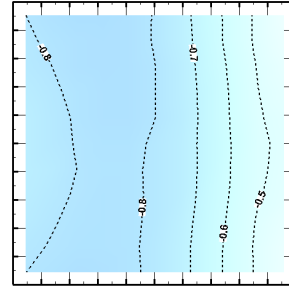
further to  $AR = 10.5$  (Figure 4.11(f)) and the highest tested aspect ratio of  $AR = 11$  (not shown here).

The effect of the boundary layer is not remarkable for the intermediate incidence angles of  $\alpha = 10^\circ$  to  $35^\circ$ . At these intermediate angles, the minimum value of  $C_P$  generally does not vary significantly, and the  $C_P$  contour patterns are qualitatively similar between both cases of boundary layer, for most of the tested aspect ratios (not shown here). This finding is similar to the study of Okuda and Taniike (1993), where the flow visualization above the free end for a prism with  $AR = 4$  at the intermediate angles did not show significant variation for two cases of boundary layer with  $\delta/H < 1$ . The flow visualization model for  $\delta/H > 1$ , at non-zero  $\alpha$ , is unfortunately unavailable in the study of Okuda and Taniike (1993). However, with a wider range of  $AR$  in the present study, some exceptions are observed for the prisms with  $AR \leq 2$ , where the boundary layer effect is found slightly evident. For  $AR \leq 2$ , the  $C_P$  contours are found relatively more complex for the thick boundary layer. Also, the maximum pressure region located close to the trailing edge is slightly larger for the thick boundary layer. Figure 4.12 shows an example for  $AR = 2$  which demonstrate these exceptions, where the difference in the pressure contours can still be observed at intermediate incidence angles of  $\alpha = 15^\circ$  to  $35^\circ$ . These exceptions are most probably due to the free-end surface of the prisms with  $AR \leq 2$  being located below the thickness of the thick boundary layer ( $\delta/H > 1$ ). Therefore, the effect of the boundary layer is more dominant for this aspect ratio range, despite the effect of  $\alpha$  not being significant at the intermediate angles.

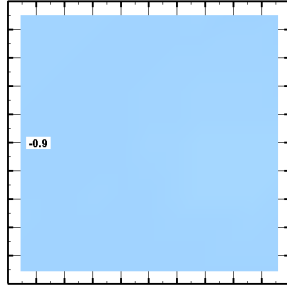
The effect of the boundary layer is most pronounced at  $\alpha = 45^\circ$ . For the lowest tested aspect ratio ( $AR = 1$ ) at this angle, the maximum pressure region is significantly larger at the center of the free end for the case of the thick boundary layer (Figure 4.13(a)(b)). Recall from subsection 4.1.2 that minimal pressure variation is observed for the intermediate aspect ratio range of  $4.5 \leq AR \leq 7$ . However, this trend of minimal pressure variation is not appreciable for the case of the thick boundary layer. Figure 4.13(c)-(f) illustrates the pressure contours for  $AR = 4$  and  $7$ , where the pressure variation for the case of the thick boundary layer is more pronounced than the case of the thin boundary layer. For the prisms with higher aspect ratio ( $AR \geq 8$ ), the  $C_P$  contours do not show significant differences for the two boundary layers. Nevertheless, it should be noted that at this high range of aspect



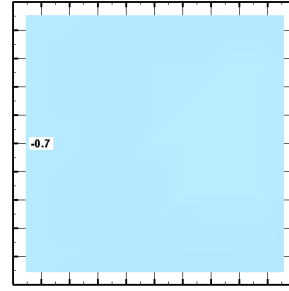
(a)  $AR = 1.5, \delta/D = 0.8$



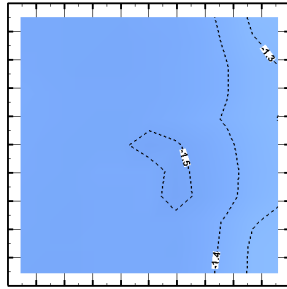
(b)  $AR = 1.5, \delta/D = 2.6$



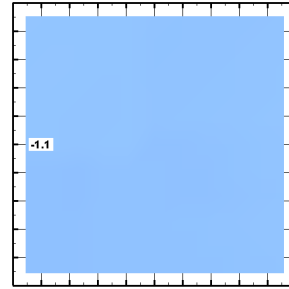
(c)  $AR = 4.5, \delta/D = 0.8$



(d)  $AR = 4.5, \delta/D = 2.6$



(e)  $AR = 10.5, \delta/D = 0.8$



(f)  $AR = 10.5, \delta/D = 2.6$

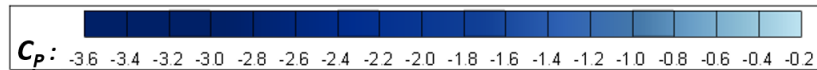


**Figure 4.11:** Free-end mean pressure distribution (contour lines of constant  $C_P$ ) at  $\alpha = 0^\circ$ : (a)(b)  $AR = 1.5$ , (c)(d)  $AR = 4.5$ , (e)(f)  $AR = 10.5$ .  $\delta/D = 0.8$  and  $2.6$  for the diagrams on the left and right, respectively. The flow is from left to right.

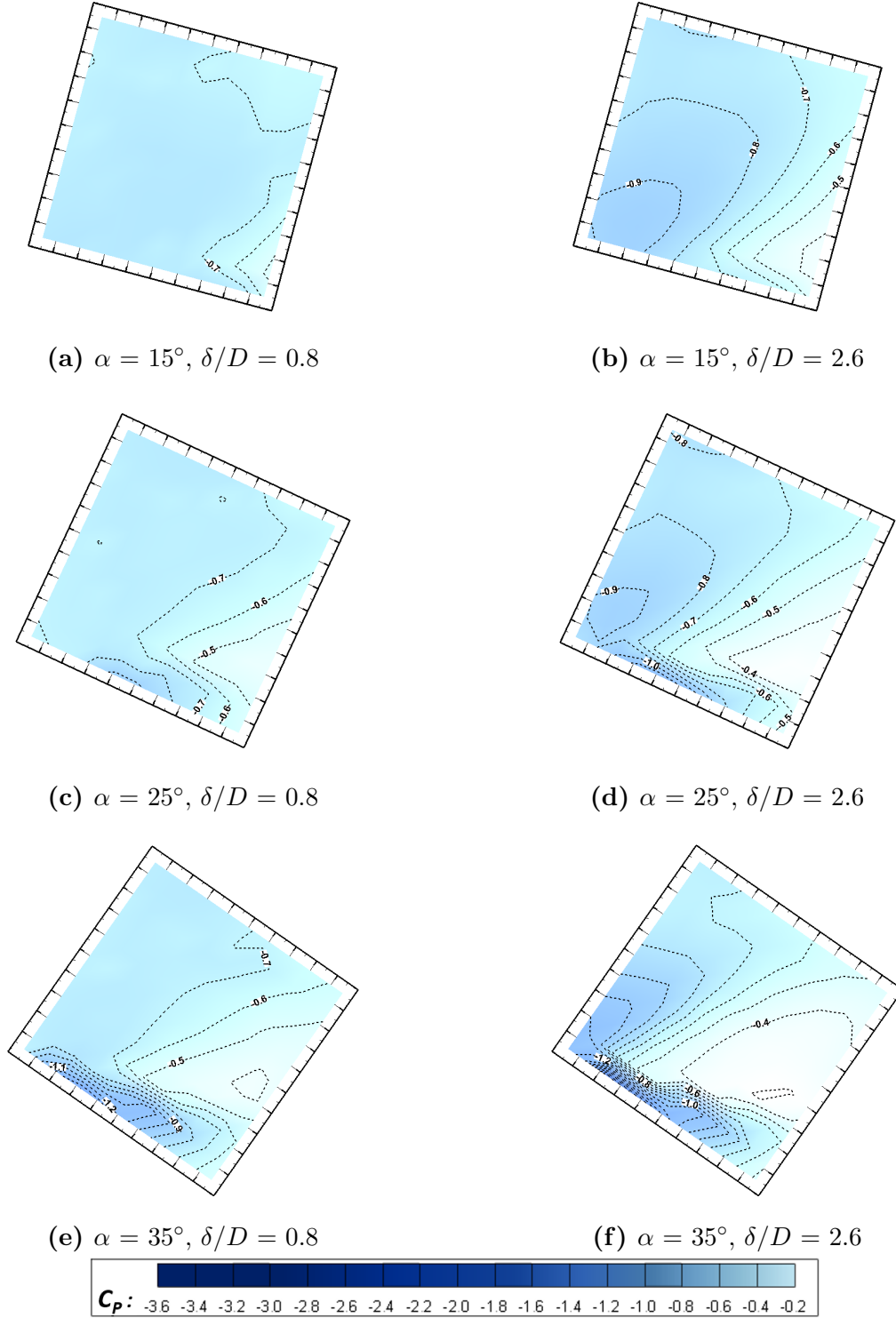


**Figure 4.12:** Free-end mean pressure distribution (contour lines of constant  $C_p$ ) for  $AR = 2$ : (a)(b)  $\alpha = 15^\circ$ , (c)(d)  $\alpha = 25^\circ$ , and (e)(f)  $\alpha = 35^\circ$ .  $\delta/D = 0.8$  and  $2.6$  for the diagrams on the left and right, respectively. The flow is from left to right.

ratio, the maximum pressure region at the centre of the free end is found slightly larger for the thick boundary layer, similar to the observation for the prisms with low aspect ratio. Notably, at  $\alpha = 45^\circ$ , the minimum  $C_P$  value is found lower (more suction) for the prisms with high and low aspect ratio ( $AR \leq 1.5$ ;  $AR \geq 10$ ) for the case of the thin boundary layer; for the intermediate aspect ratios ( $2 \leq AR \leq 9.5$ ), the minimum  $C_P$  value is found lower for the case of the thick boundary layer, mainly because of the higher pressure variation. The locations of the minimum  $C_P$  value, however, do not vary between both cases of boundary layer, with both located near the leading edge apex.

Apparently, the three flow regimes of the thin boundary layer presented in Table 4.1 are still valid for the thick boundary layer at  $\alpha = 15^\circ$  and  $\alpha = 30^\circ$ , because the boundary layer does not generally affect the flow characteristics at these incidence angles. For  $\alpha = 0^\circ$ , there are only two flow regimes can be identified for the thick boundary layer due to the absence of the “evident pressure variation” for the highest tested AR. On the other hand, the flow regimes at  $\alpha = 45^\circ$  are somewhat difficult to classify because the existence of the “minimal pressure variation” is ambiguous, mainly due to the contour line patterns for the intermediate AR becoming much more complicated for the thick boundary layer, and there is less variation in the  $C_P$  contours between each subsequent aspect ratio.

The  $C_P$  centerline profiles for the cube ( $AR = 1$ ) at four selected incidence angles are shown in Figure 4.14(a) and 4.14(b) for the thin and thick boundary layers, respectively. The results are also compared with the study of Lim and Ohba (2015) which illustrates the  $C_P$  centerline profile at various incidence angles (Figure 4.14(c)). By using an atmospheric boundary layer ( $\delta/D \gg 1$ ), Lim and Ohba (2015) have showed that  $C_P$  generally increases with  $\alpha$  from the centerline profile, and the pressure recovery trend can be observed starting from the leading edge, regardless of  $\alpha$ . On the other hand, the present study, where  $\delta/D = 0.8$  and  $2.6$ , demonstrates that the trends of  $C_P$  at various  $\alpha$  cannot be generalized because those trends vary at different locations. For those locations which are nearer to the leading edge ( $X/D < -0.3$ ), the value of  $C_P$  decreases with  $\alpha$  for both cases of  $\delta/D = 0.8$  and  $2.6$ . However, the variation in the value of  $C_P$  is relatively smaller for the thick boundary layer, at the locations of  $X/D < -0.3$ . The increase trend of  $C_P$  with  $\alpha$  (as observed by Lim and Ohba (2015)) can be observed in the present study at the locations further downstream,

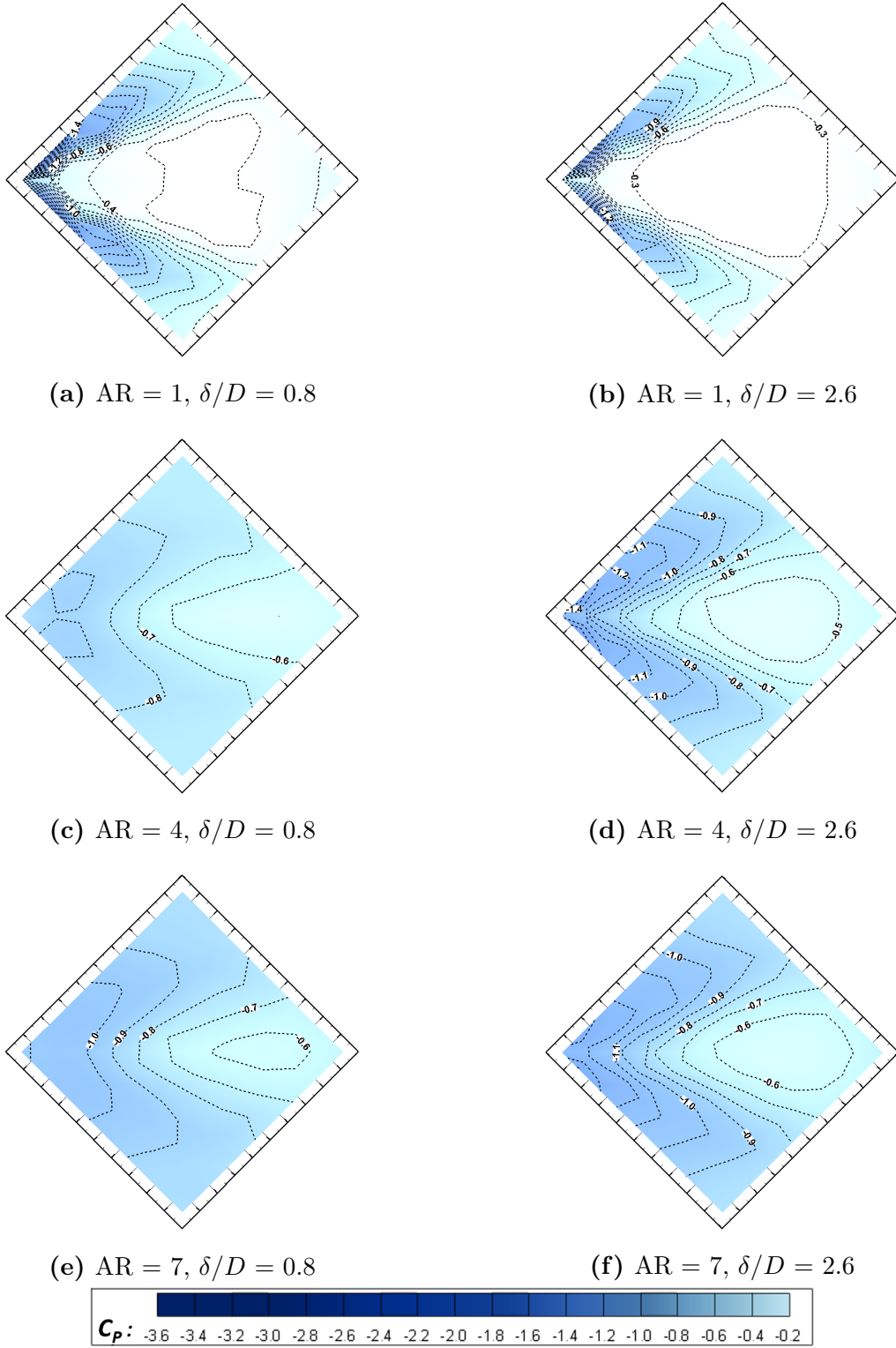


**Figure 4.13:** Free-end mean pressure distribution (contour lines of constant  $C_P$ ) at  $\alpha = 45^\circ$ : (a)(b)  $AR = 1$ , (c)(d)  $AR = 4$ , (e)(f)  $AR = 7$ .  $\delta/D = 0.8$  and  $2.6$  for the diagrams on the left and right, respectively. The flow is from left to right.

which are  $X/D \geq 0.2$  and  $X/D \geq -0.1$ , for the thin and thick boundary layers, respectively. The centerline profiles presented in Figure 4.14 also show the effect of the boundary layer on the trend of the pressure recovery at various incidence angles for the cube ( $AR = 1$ ). The centerline  $C_P$  profiles for other aspect ratios for both cases of boundary layer are presented in Appendix B. These profiles again justify the effect of the boundary layer previously discussed, where the highest profile variation between both cases is observed at  $\alpha = 45^\circ$ , while the minimal profile variation can be seen for the intermediate angles and the prisms with  $AR > 2$ .

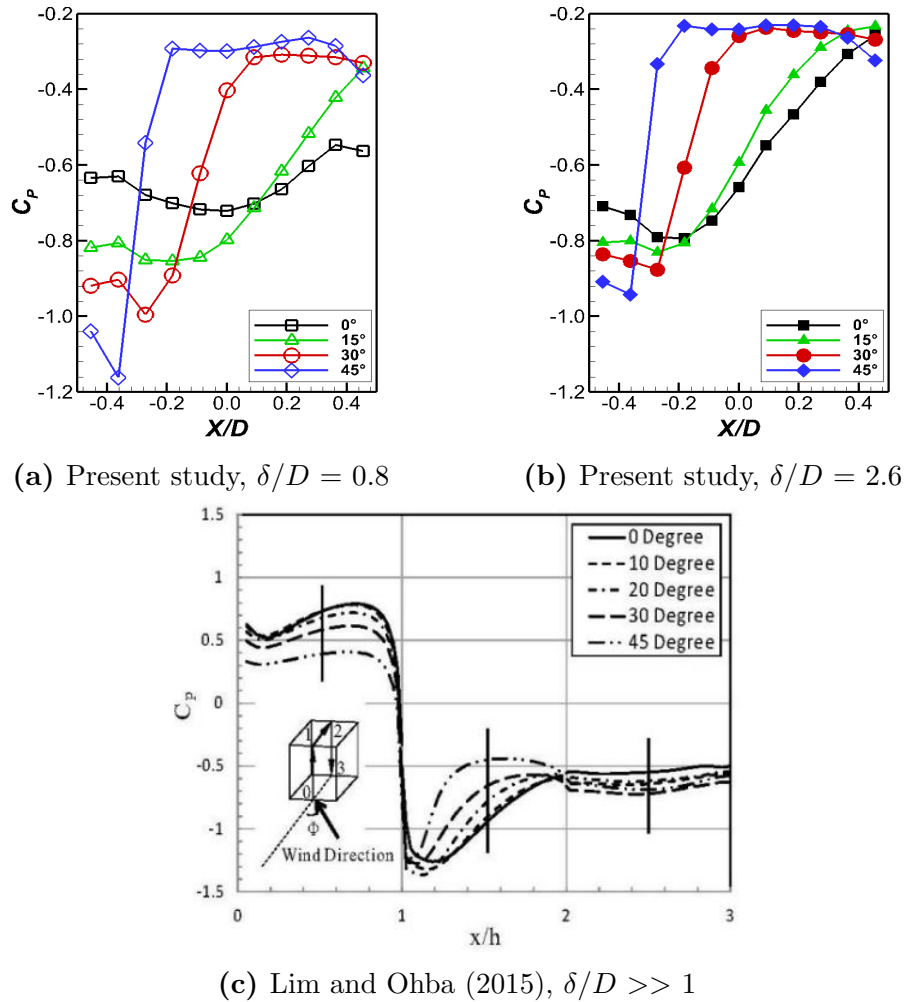


**Figure 4.14:** Centerline mean  $C_P$  profiles (where  $X$  is a coordinate fixed to the prism free-end surface, and rotates with the prism) for (a) present study ( $AR = 1$ ,  $\delta/D = 0.8$ ,  $Re = 6.5 \times 10^4$ ), (b) present study ( $AR = 1$ ,  $\delta/D = 2.6$ ,  $Re = 6.5 \times 10^4$ ), and (c) Lim and Ohba (2015) ( $AR = 1$ ,  $\delta/D \gg 1$ ,  $Re = 4.6 \times 10^4$ ) - used with permission of Techno-Press, refer to Figure 2.18 for the full caption.

## 4.2 Comparison of $C_P$ distribution between cylinder and square prism

In this section, the free-end  $C_P$  distributions of the square prisms studied are compared with those of the cylinders investigated by Beitel (2017). The comparison is performed for various aspect ratios, but is limited to the  $C_P$  centerline profile only. Also, two incidence angles of the square prism are selected for the comparison:  $\alpha = 0^\circ$  and  $45^\circ$ . The centerline profiles are plotted along the streamwise ( $x$ -coordinate) and cross-stream ( $y$ -coordinate) directions. The distances of  $x$  and  $y$  are normalized with the width of the prism (for  $\alpha = 0^\circ$ ) and diameter of the cylinder (both with  $D = 48$  mm). For the square prism at  $\alpha = 45^\circ$ , the distances of  $x$  and  $y$  are normalized with the projected width,  $D'$ , which is the distance between the leading edge apex and trailing edge apex. Note that the centerline profiles along  $x/D'$  for the prism at  $\alpha = 45^\circ$  in this section are different from those profiles previously presented in Section 4.1. The previous section presented the centerline profiles along  $X/D$ , where the distance  $X$  is fixed to the free-end surface and rotated with the prism, while the distance  $x/D'$  used in this section is fixed to the coordinate system of the wind tunnel defined in Figure 1.3. Note that the distance of  $x/D'$  used in this section for the prism at  $\alpha = 45^\circ$  is parallel to the distances of  $x/D$  used for both the cylinder and square prism at  $\alpha = 0^\circ$ .

The  $C_P$  centerline profiles along the  $x$ -axis of the three shapes above-mentioned are presented in Figure 4.15 for six selected aspect ratios. The full profiles for all the aspect ratios are presented in Appendix C. Comparing the profiles between the cylinder and prism at  $\alpha = 0^\circ$ , the cylinder profiles show higher pressure variation for all the tested aspect ratios. The downstream pressure recovery trend of the cylinder is more pronounced, and it appears that the pressure gradients of the cylinder increase with AR. Conversely, there is no pressure gradient observed for the square prism at  $\alpha = 0^\circ$  except for the lowest and highest tested aspect ratios (AR = 1, 10.5, and 11), as mentioned in subsection 4.1.2. The rapid pressure recovery trend observed for the cylinder is related to the flow reattachment characteristics above the free end. In the experimental investigation of Rostamy et al. (2012) and Sumner et al. (2015) for four cylinders with AR = 3, 5, 7, and 9, the occurrence of the

flow reattachment above the free end was evident for all the tested aspect ratios. Rostamy et al. (2012) also observed that the reattachment point to be  $x/D = 0.21$  to  $\sim 0.29$  when the aspect ratio decreased from  $AR = 9$  to  $3$ . The closer location of the reattachment point to the leading edge with increasing  $AR$  may explain the higher pressure recovery trend for the more slender cylinders (Figure 4.15(e)(f)). In comparison to the study of Sumner et al. (2017) (subsection 2.4.1) for square prisms, the shear layer above the free end separated from the leading edge was found directly entering the near-wake region without reattachment on the free-end surface. This finding may explain the flat pressure profiles observed in all of the intermediate aspect ratios of the square prism at  $\alpha = 0^\circ$  (Figure 4.15(b)-(e)).

In term of the values of  $C_P$ , the suction effect for the cylinders is generally higher (with lower  $C_P$ ) than the square prism at  $\alpha = 0^\circ$  at the region closer to the leading edge ( $x/D < 0$ ). Conversely, at the region closer to the trailing edge ( $x/D > 0.2$ ), the values of  $C_P$  for the cylinders exceed those of the square prism at  $\alpha = 0^\circ$  on account of the more rapid pressure recovery trend due to the flow reattachment as identified for the cylinders. However, at  $AR = 10.5$ , the values of  $C_P$  for the square prism at  $\alpha = 0^\circ$  start becoming lower (higher suction) than those of the cylinder, even at the region closer to the leading edge. This is the same  $AR$  based on the  $C_P$  contours where the pressure recovery trend begins to be observed (Figure 4.5(f)).

For the square prism at  $\alpha = 45^\circ$ , the centerline profiles begin at a low  $C_P$  value, and the pressure recovery trend towards downstream can also be seen, similar to the cylinder. However, the pressure recovery trend of the square prism at  $\alpha = 45^\circ$  is more rapid at the upstream location of the free end ( $x/D' < -0.2$ ), and the rate of recovery is comparable to, or even higher than, the cylinder at these locations. Conversely, the pressure recovery trend at the downstream location ( $x/D' > 0$ ) for the square prism at  $\alpha = 45^\circ$  is generally insensitive to the streamwise distance. The pressure contours at  $\alpha = 45^\circ$  presented in the subsection 4.1.2 illustrate that the high pressure region begins at the centre of the free end, which explains the insensitive pressure recovery trend after the centre location, while the low  $C_P$  value close to the leading edge corresponds to the starting point of the conical vortices emerging from the leading edge apex. Similar to the cylinder, the pressure recovery trend observed for the square prism at  $\alpha = 45^\circ$  can be related to the flow attachment above the

free end, as observed in the PIV result of McClean and Sumner (2014) (Figure 2.12).

For the boundary layer effect, it is notable from Figure 4.15 that the value of  $C_P$  is higher (lower suction) for the thick boundary layer. For the square prism at  $\alpha = 0^\circ$  and the cylinder, the profiles for the two cases of boundary layer are found qualitatively similar for the intermediate aspect ratios ( $3 \leq \text{AR} \leq 9$ ) (Figure 4.15(c)-(e)). For the low-aspect-ratio square prisms ( $\text{AR} = 1$  and  $1.5$ ) at  $\alpha = 0^\circ$ , it is observed that the pressure recovery trend is more noticeable for the thick boundary layer (Figure 4.15(a)). However, for the highest tested aspect ratios ( $\text{AR} = 10.5$  and  $11$ ), the pressure recovery trend is relatively more appreciable for the thin boundary layer (Figure 4.15(f)). On the other hand, for the cylinders with low aspect ratio ( $\text{AR} \leq 2.5$ ), it appears that the region of the higher suction (close to the leading edge) becomes narrower for the thick boundary layer. The boundary layer seems to have lesser influence on the profiles of the cylinders with high aspect ratio ( $\text{AR} > 9$ ), where the profiles of both cases of the boundary layer almost collapse together. This behavior is different from the square prism at  $\alpha = 0^\circ$ , where the influence of the boundary layer is found to be more significant on the highest tested aspect ratios, both qualitatively and quantitatively.

Similar to the cylinder and prism at  $\alpha = 0^\circ$ , the centerline  $C_P$  is also lower for the square prism at  $\alpha = 45^\circ$ , for the thin boundary layer. However, the effect of the boundary layer for the square prism at  $\alpha = 45^\circ$  is relatively not noticeable, as compared to the cylinder and the square prism at  $\alpha = 0^\circ$ , except close to the leading edge. At  $x/D' < -0.4$ , it can be observed that the suction effect is higher (lower  $C_P$ ) for the thick boundary layer, for the square prism at  $\alpha = 45^\circ$  with intermediate aspect ratios ( $2.5 \leq \text{AR} \leq 9$ ). This behavior is different from the cylinder and square prism at  $\alpha = 0^\circ$ , where the value of  $C_P$  is found increasing with the boundary layer thickness for the same aspect ratios. Other than the location close to the leading edge, the profiles of the square prism at  $\alpha = 45^\circ$  for both cases of boundary layer almost collapse together for most of the tested aspect ratios. This observation is similar to the experimental investigation of Castro and Robins (1977) for the cube ( $\text{AR} = 1$ ), where the centerline profiles obtained for  $\alpha = 45^\circ$  did not vary significantly for two cases of boundary layer ( $\delta/D \simeq 0$  and  $\delta/D \simeq 10$ ). However, recall that the pressure contours presented in the subsection 4.1.3 showed that the boundary layer effect is most pronounced for the square prism at  $\alpha = 45^\circ$ . If the data of both the  $C_P$  full contours and  $C_P$  centerline profiles

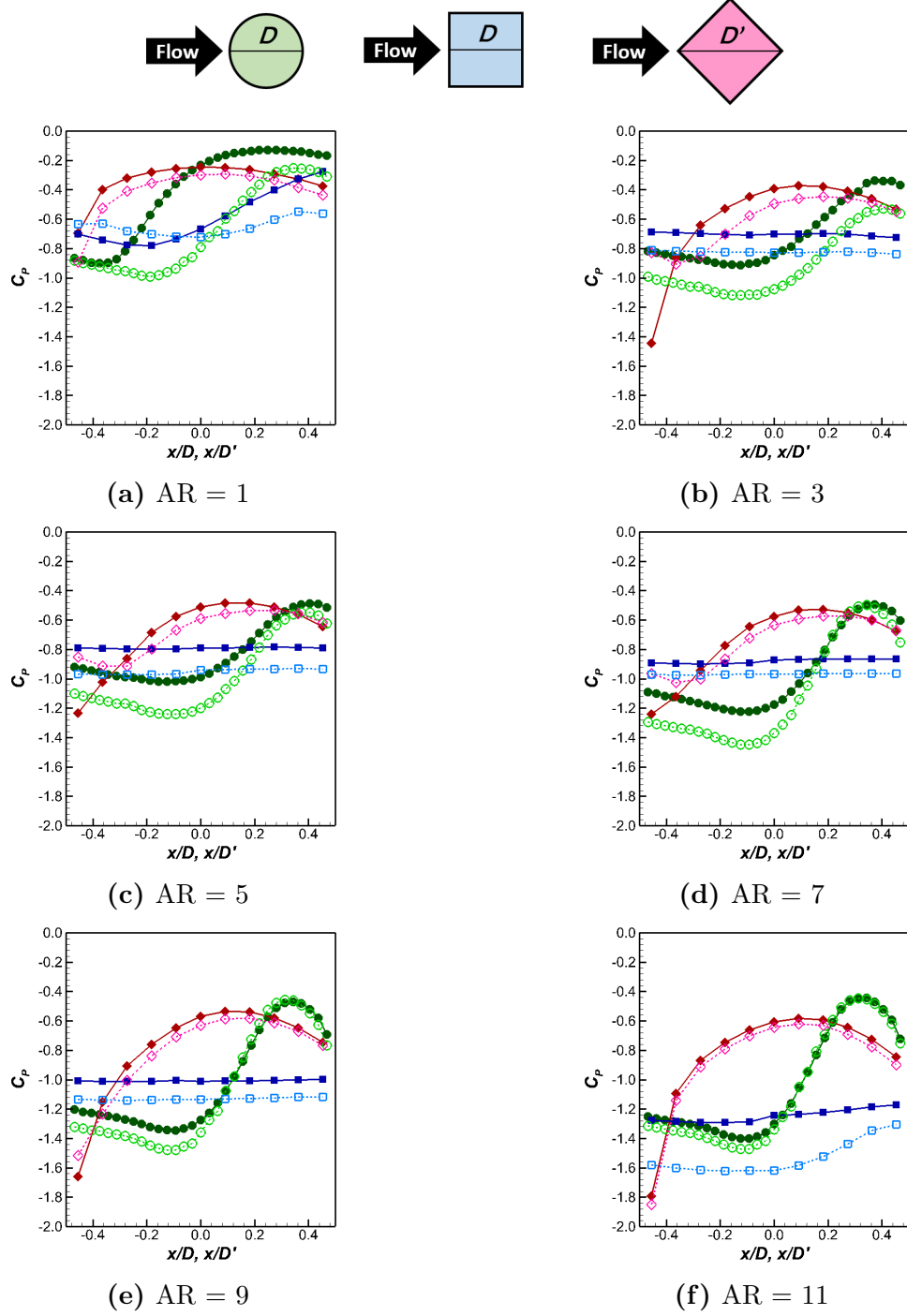


**Figure 4.15:** Comparison of  $x$ -axis centerline  $C_P$  profile between square prisms in the present study at  $\alpha = 0^\circ$  (blue square) and  $\alpha = 45^\circ$  (normalized with projected width,  $D'$ ) (red diamond), and circular cylinder studied by Beitel (2017) (green circle): (a) AR = 1, (b) AR = 3, (c) AR = 5, (d) AR = 7, (e) AR = 9, and (f) AR = 11.  $Re = 6.5 \times 10^4$  for both studies. Open symbol and dashed line represent the thin boundary layer ( $\delta/D = 0.8$  (present) and 0.6 (Beitel (2017))), while solid symbol and solid line represent the thick boundary layer ( $\delta/D = 2.6$  (present) and 1.9 (Beitel (2017))).

are compared more meticulously at this angle, it can be observed that the variation in the boundary layer remarkably affects the pressure distribution along both oblique leading edges (region where the conical vortices are dominant), but has insignificant impact on the profiles along the centerline (attached flow region).

Figure 4.16 presents the centerline  $C_P$  profiles along the  $y$ -axis for the same six selected aspect ratios. The profiles shown in Figure 4.16 are all symmetric along  $y/D$  or  $y/D' = 0$ . For the cylinder and prism at  $\alpha = 0^\circ$ , it can be observed that there is a very minimal pressure gradient on the profiles presented, except for the profiles of low-aspect-ratio cylinders ( $AR \leq 1.5$ ) for the thick boundary layer which form a semi-circle shape (Figure 4.16(a)). Moreover, the values of  $C_P$  for the cylinder are consistently lower than those of the prism at  $\alpha = 0^\circ$  for all the intermediate aspect ratios ( $2 < AR \leq 10.5$ ). The higher suction effect (with lower  $C_P$ ) along the  $y$ -axis centerline observed for the cylinder may be related to the proximity of the vortex centre to the free-end surface. Comparing the vortex centre above the free end for both studies of Rostamy et al. (2012) and Sumner et al. (2017), the location of the vortex centre and the separated shear layer for the cylinders appear to be closer to the free end, as compared to the prism at  $\alpha = 0^\circ$ . In addition, the vortex centre observed for the cylinder by Rostamy et al. (2012) was slightly upstream or close to the  $y$ -axis centerline. Conversely, the locations of the vortex centre observed by Sumner et al. (2017) for the prism were all downstream of the  $y$ -axis centerline ( $x/D > 0$ ). This may be the reason for the lower  $C_P$  values observed for the cylinders along the  $y$ -axis centerline. Some exceptions were, however, observed for low-aspect-ratio cylinders ( $AR \leq 2$ ) for the thick boundary layer (Figure 4.16(a)), and also the high-aspect-ratio cylinders ( $AR \geq 10.5$ ) for the thin boundary layer (Figure 4.16(f)). The exception observed for the low-aspect-ratio cylinders ( $AR \leq 2$ ) may be related to the boundary layer effect, as the values of  $\delta/H$  are more than unity for these aspect ratios. The exception where the  $C_P$  values of the prism at  $\alpha = 0^\circ$  is lower than the cylinder may be related to the study of Sumner et al. (2017), which has shown that the separated shear layer above the free end was somehow thinner for the most slender prism of  $AR = 9$ , and the location of the vortex centre moves upstream with increasing  $AR$ . The location of the vortex centre at  $AR = 11$  for the prism may move closer to the  $y$ -axis centerline (perhaps is further upstream than that of the cylinder at  $AR = 11$ ). However,

additional data for both prism and cylinder at high aspect ratio are needed to make this statement more conclusive.

For the cylinders, the variation in the boundary layer may influence the reattachment point above the free end. Rostamy et al. (2012) and Sumner et al. (2015) compared the reattachment point above the free end with other studies with a much thinner boundary layer thickness but at similar aspect ratios, and found that the reattachment point was slightly closer to the leading edge with a thicker boundary layer. This observation may be used to explain the effect of the boundary layer on the  $y$ -axis centerline profile of the cylinder, where the values of  $C_P$  are found higher for the thick boundary layer, which may be due to the further upstream location of the reattachment point. On the other hand, for the low-aspect-ratio prisms at  $\alpha = 0^\circ$ , the effect of the boundary layer along the  $y$ -axis centerline profile is relatively less pronounced, as compared to the cylinder (Figure 4.16(a)). For the low-aspect-ratio prisms at  $\alpha = 0^\circ$ , the lesser influence of the boundary layer on the  $y$ -axis centerline profiles may be due to a farther reattachment location from the  $y$ -axis centerline for the prism. From the  $C_P$  contours observed in Figure 4.10, it appears that the possibility of the flow reattachment on the free end increases with a thicker boundary layer. However, in the present study, it is most likely the reattachment point of the prism for the thick boundary layer is much further downstream, perhaps still very close to the trailing edge, despite the increase in  $\delta/D$  from 0.8 to 2.6. A much thicker boundary layer may be needed, perhaps with an atmospheric boundary layer (similar to Chen et al. (2018)), in order to observe the influence of the boundary layer in increasing the values of  $C_P$  along the  $y$ -axis, by changing the reattachment point to further upstream, closer to the  $y$ -axis centerline.

The centerline profiles along the  $y$ -axis for the square prism at  $\alpha = 45^\circ$  show the highest pressure variation for all the tested aspect ratios, in comparison to the cylinder and prism at  $\alpha = 0^\circ$ . The profiles of the prism at  $\alpha = 45^\circ$  show a plateau formation at the centre location of about  $-0.3 \leq y/D' \leq 0.3$ . The lower values of  $C_P$  at the locations of  $y/D' \leq -0.3$  and  $y/D' \geq 0.3$  indicates the location of the conical vortices which roll along both oblique leading edges. The behavior of the pressure gradient at these non-centre locations varies with AR, which indicates the size and strength of the conical vortices above the free end are influenced by the aspect ratio. Similar to the profiles along the  $x$ -axis, there is minimal influence of the

boundary layer on the centerline profile along the  $y$ -axis for the prism at  $\alpha = 45^\circ$ .

From the centerline profiles along both the  $x$ -axis and  $y$ -axis, it is evident that the boundary layer effect could not be generalized as this behaviour varies with AR and the bluff-body shape. The influence of the boundary layer for three different shapes previously mentioned at various aspect ratios is classified in Table 4.2. In this table, the notation ‘Low’ is used when the profiles of both cases of the boundary layer almost collapse together; the notation ‘Medium’ is used when the boundary layer generally influences the profile quantitatively only, and the profiles for both cases of boundary layer are still qualitatively similar; the notation ‘High’ is used when both profiles are qualitatively and quantitatively different. The full results of the comparison between the centerline  $C_P$  profiles of the cylinder and prisms are shown in Appendix C.

**Table 4.2:** The influence of the boundary layer on the cylinder, and square prism at  $\alpha = 0^\circ$  and  $45^\circ$  based on the centerline  $C_P$  profiles along  $x$ -axis and  $y$ -axis.

Shape	Low	Medium	High
Cylinder	$AR \geq 9.5$	$3 \leq AR \leq 9$	$AR \leq 2.5$
Prism at $\alpha = 0^\circ$	$2 \leq AR \leq 2.5$	$3 \leq AR \leq 10$	$AR \leq 1.5; AR \geq 10.5$
Prism at $\alpha = 45^\circ$	$AR \geq 8$	$1 \leq AR \leq 7.5$	Only at $x/D' < -0.4$ for $2.5 \leq AR \leq 7.5$

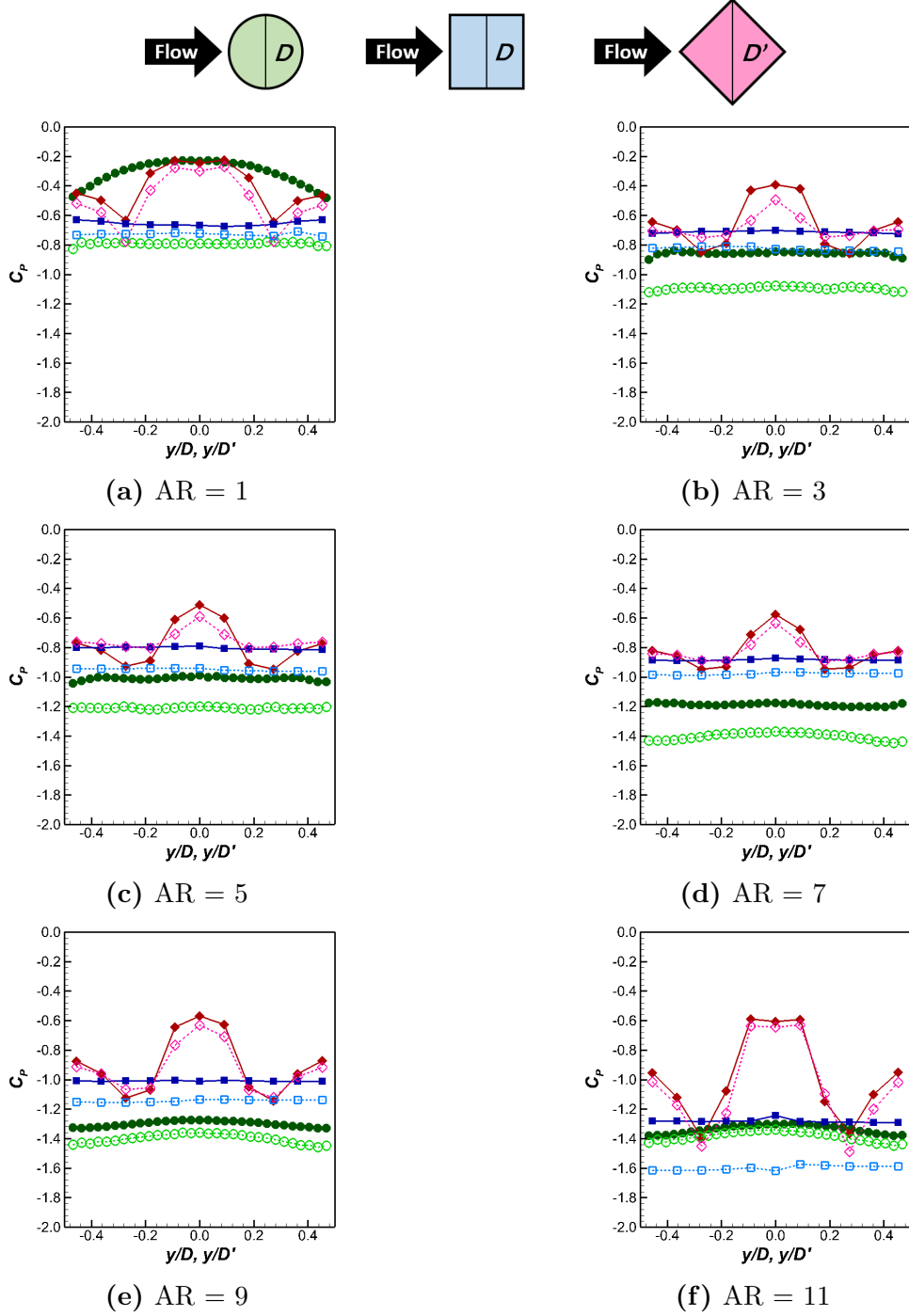


**Figure 4.16:** Comparison of  $y$ -axis centerline  $C_p$  profile between square prisms in the present study at  $\alpha = 0^\circ$  (blue square) and  $\alpha = 45^\circ$  (normalized with projected width,  $D'$ ) (red diamond), and circular cylinder studied by Beitel (2017) (green circle): (a) AR = 1, (b) AR = 3, (c) AR = 5, (d) AR = 7, (e) AR = 9, and (f) AR = 11.  $Re = 6.5 \times 10^4$  for both studies. Open symbol and dashed line represent the thin boundary layer ( $\delta/D = 0.8$  (present) and 0.6 (Beitel (2017))), while solid symbol and solid line represent the thick boundary layer ( $\delta/D = 2.6$  (present) and 1.9 (Beitel (2017))).

## 4.3 Aerodynamic forces

In this section, the results of the mean aerodynamic force coefficients are discussed. The mean drag force coefficient,  $C_D$ , mean lift force coefficient,  $C_L$ , and mean normal force coefficient,  $C_N$  are discussed in subsections 4.3.1, 4.3.2, and 4.3.3, respectively. In addition, subsection 4.3.3 also compares  $C_N$  measured by the force balance and  $C_{N,p}$  resulted from the free-end pressure distributions. The point of action of  $C_{N,p}$  on the free end at various AR and  $\alpha$  is further discussed in subsection 4.3.4. Recall from Section 3.4 that the freestream velocity used in the measurement of forces was  $U_\infty = 40$  m/s, which corresponds to the Reynolds number of  $Re = 1.1 \times 10^5$ . The higher freestream velocity was used with the intention of reducing the measurement uncertainty by increasing the magnitude of the forces. Additional experiments were carried out to perform the force measurements at  $U_\infty = 22.5$  m/s. It was found that the force coefficients measured did not differ significantly, and the data were still qualitatively similar for both freestream velocities. However, by adopting  $U_\infty = 40$  m/s, the fluctuation in data points was reduced and therefore the results obtained were much smoother. The freestream velocity of  $U_\infty = 40$  m/s corresponds to  $\delta/D = 0.8$  and  $2.0$  for the thin and thick boundary layer (Case 4 and 5 in Section 3.4).

### 4.3.1 Drag force coefficient

The mean drag force coefficient,  $C_D$ , data for all the tested aspect ratios (AR = 1 to 11) are presented in waterfall diagrams as shown in Figure 4.17 for two cases of the boundary layer. The figures show that  $C_D$  is generally higher when  $\alpha$  approaches  $\alpha = 0^\circ$  or  $45^\circ$ . The minimum value of  $C_D$  occurs at intermediate angles between  $9^\circ$  to  $21^\circ$  (varies with AR), which corresponds to the critical incidence angle similar to the studies of Sakamoto (1985) and McClean and Sumner (2014). The critical angles,  $\alpha_c$ , based on the minimum  $C_D$  obtained by Sakamoto (1985) and McClean and Sumner (2014) are slightly lower than, but still comparable to,  $\alpha_c$  of the present study.

With a wider range of AR in the present study, the sensitivity of  $\alpha_c$  with AR can be better understood. The value of  $\alpha_c$  based on the minimum  $C_D$  is found most sensitive to AR for those prisms with  $AR \leq 1.5$  and  $AR \leq 2.5$ , for the thin and thick boundary layers,

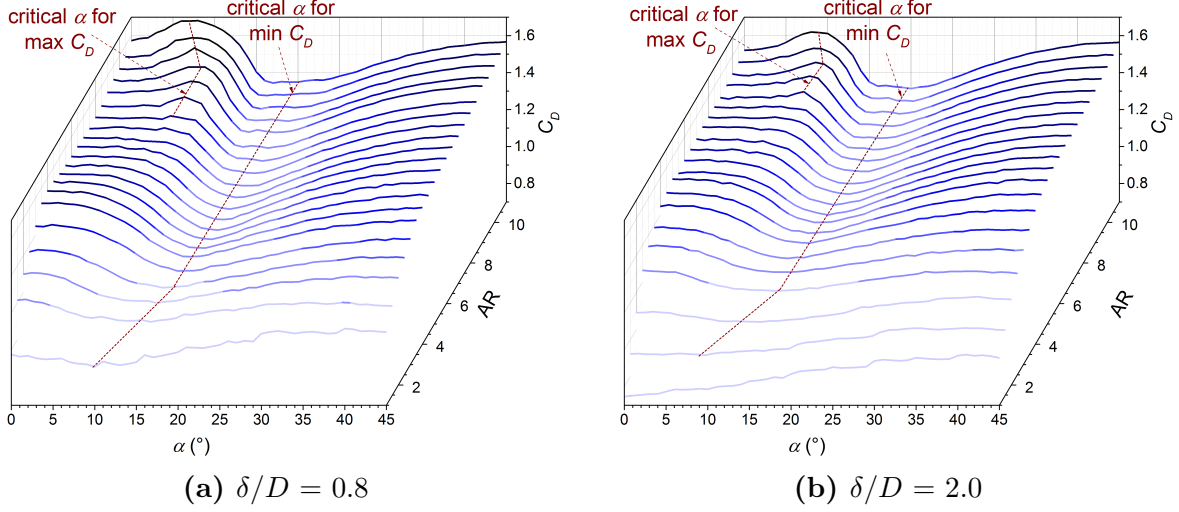


**Figure 4.17:** Mean drag force coefficient,  $C_D$ , versus  $\alpha$  (colored by the magnitude of  $C_D$ ) for all the tested aspect ratios in two boundary layers conditions: (a)  $\delta/D = 0.8$  and (b)  $\delta/D = 2.0$  at  $Re = 1.1 \times 10^5$ .

respectively. The value of  $\alpha_c$  for the thin boundary layer increases from  $10^\circ$  to  $16^\circ$  from  $AR = 1$  to  $1.5$ , while the for the thick boundary layer,  $\alpha_c$  increases from  $9^\circ$  to  $15^\circ$  when  $AR$  increases from  $1$  to  $2.5$ . This sensitivity is due to the dominant effect of the boundary layer as the value of  $\delta/H$  is less than unity for these prisms. The value of  $\alpha_c$  increases slowly ( $16^\circ$  to  $19^\circ$ ) for the aspect ratio range of  $1.5 \leq AR \leq 4$  and  $2.5 \leq AR \leq 5$ , for the thin and thick boundary layers, respectively. The value of  $\alpha_c$  almost remains constant ( $19^\circ$  to  $21^\circ$ ) for  $AR \geq 4$  for the thin boundary layer; however, there is a sharp drop in the value of  $\alpha_c$  from  $21^\circ$  to  $17^\circ$  at  $AR = 10$ . For the thick boundary layer, there is no sudden reduction in  $\alpha_c$  for  $AR \geq 5$ , and  $\alpha_c$  remains fairly constant within the range of  $18^\circ$  to  $19^\circ$ , and increases slightly further from  $20^\circ$  to  $21^\circ$  for the prism with high aspect ratio ( $AR \geq 9.5$ ).

The waterfall diagrams in Figures 4.17(a) and 4.17(b) also show a plateau formation with a fairly well-defined peak for the prisms with high aspect ratio. This plateau formation is observed for the prisms starting from the critical aspect ratio of  $AR = 8$  and  $AR = 9$  for the thin and thick boundary layers, respectively. The adoption of a wider range of aspect ratio in the present study allows the determination of this second critical angle, which corresponds to the maximum value of  $C_D$  at this plateau formation region. For boundary layers, the values of the second  $\alpha_c$  decrease slowly from  $10^\circ$  to  $8^\circ$ , when the aspect ratio increases from  $AR = 9$  to  $11$ . Figure 4.18 illustrates both values of  $\alpha_c$  based on the minimum  $C_D$  and maximum

$C_D$  at the region of the plateau formation. The results are also compared with the studies of Sakamoto (1985) and McClean and Sumner (2014). The plateau formation was also observed by McClean and Sumner (2014) for  $AR = 7$  and  $9$ ; however, the critical aspect ratio was difficult to locate because they used a large increment in  $AR$ . The investigation of Sakamoto (1985), on the other hand, did not show the second  $\alpha_c$  due to the low range of the tested aspect ratios from  $AR = 1$  to  $5$ .

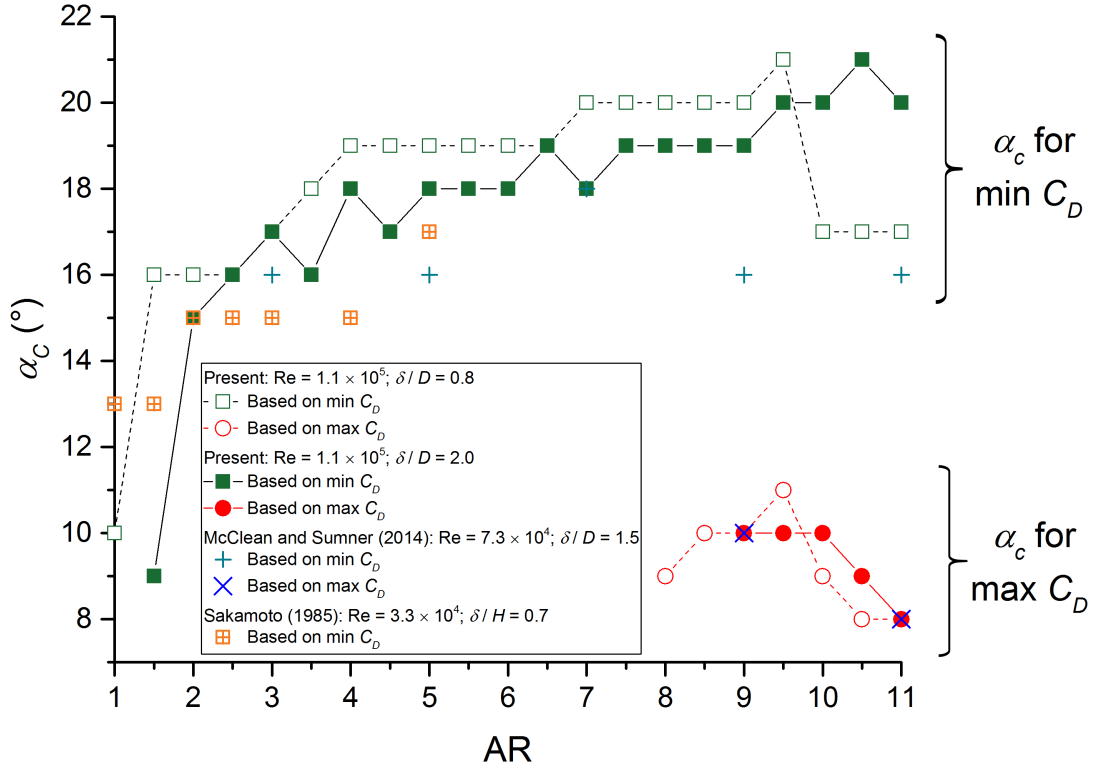


**Figure 4.18:** Critical incidence angles,  $\alpha_c$  based on the minimum  $C_D$  and maximum  $C_D$  at the region of the plateau formation for all the tested aspect ratios in both cases of boundary layers ( $\delta/D = 0.8$  and  $2.0$ ) at  $Re = 1.1 \times 10^5$ . The results are also compared with previous studies of Sakamoto (1985) ( $\delta/H = 0.7$ ;  $Re = 3.3 \times 10^4$ ) and McClean and Sumner (2014) ( $\delta/D = 1.5$ ;  $Re = 7.3 \times 10^4$ ).

Looking further at the effect of the aspect ratio,  $C_D$  becomes less sensitive to  $\alpha$  at lower aspect ratios. The waterfall diagrams in Figures 4.17(a) and 4.17(b) do not illustrate any plateau formation for the low-aspect-ratio prisms. Additionally, the curve flattens out when  $AR$  decreases. The color map in the waterfall diagrams also demonstrates that  $C_D$  increases with  $AR$ .

Figure 4.19 also illustrates the effect of the boundary layer, where the values of  $C_D$  are generally lower for the thick boundary layer, which is most likely due to the prism being immersed in a higher portion of the low-momentum-fluid. This effect is much more obvious for the low aspect ratio prisms where  $\delta/H > 1$ , and also at the plateau formation region for the high-aspect-ratio prisms. The boundary layer does not influence the values and trends of  $C_D$  significantly for intermediate aspect ratios. From Figure 4.18, it also appears that the boundary layer generally reduces slightly the value of the first  $\alpha_c$  based on the minimum  $C_D$ . Moreover, the investigation of Sakamoto (1985) with  $\delta/H = 0.7$  (greater than most prisms in the present study) shows a lower value of  $\alpha_c$ , which is additional evidence of the influence the thick boundary layer in reducing  $\alpha_c$ . On the other hand, the thicker boundary layer appears to increase slightly the second  $\alpha_c$  based on the maximum  $C_D$  at the region of the plateau formation. The values of the second  $\alpha_c$  for the thick boundary layer ( $\delta/D = 2.0$ ) in the present study, are the same with the investigation of McClean and Sumner (2014) which adopted a similar value of the boundary layer ( $\delta/D = 1.5$ ).

Figure 4.20 presents  $C_D$  at six selected  $\alpha$  for all the tested aspect ratios. The results are comparable to the investigation of McClean and Sumner (2014). The values of  $C_D$  obtained from the study of Sakamoto (1985) (compared at the same  $\alpha$  and AR), are found lower than those of the present study, which again underlines the significant impact of the boundary layer. With the wide range and small increment in AR, the flow can be classified into two distinct flow regimes based on the  $C_D$  data at various aspect ratios. The first flow regime lies within the aspect ratio range of  $1 \leq \text{AR} \leq 4$ , where the values of  $C_D$  at all selected  $\alpha$  demonstrate a significant increase. The second flow regime ( $\text{AR} > 4$ ) shows that  $C_D$  is insensitive to the change of AR, but increases slowly with AR. It appears that there is a third flow regime, although it is not too appreciable, where the increasing trend of  $C_D$  becomes more obvious when the aspect ratio is increased further ( $\text{AR} \geq 9$ ). It should be noted that the third flow regime is not evident for most of the incidence angles. Apparently, the existence of the third flow regime is most pronounced at  $\alpha = 10^\circ$  for both boundary layer thicknesses. Recall that this incidence angle also corresponds to the second  $\alpha_c$  (Figure 4.18) which is responsible for the plateau formation in the curve of  $C_D$  versus  $\alpha$ . Comparing this result with the pressure contours previously discussed, Section 4.1 highlighted that the  $C_P$

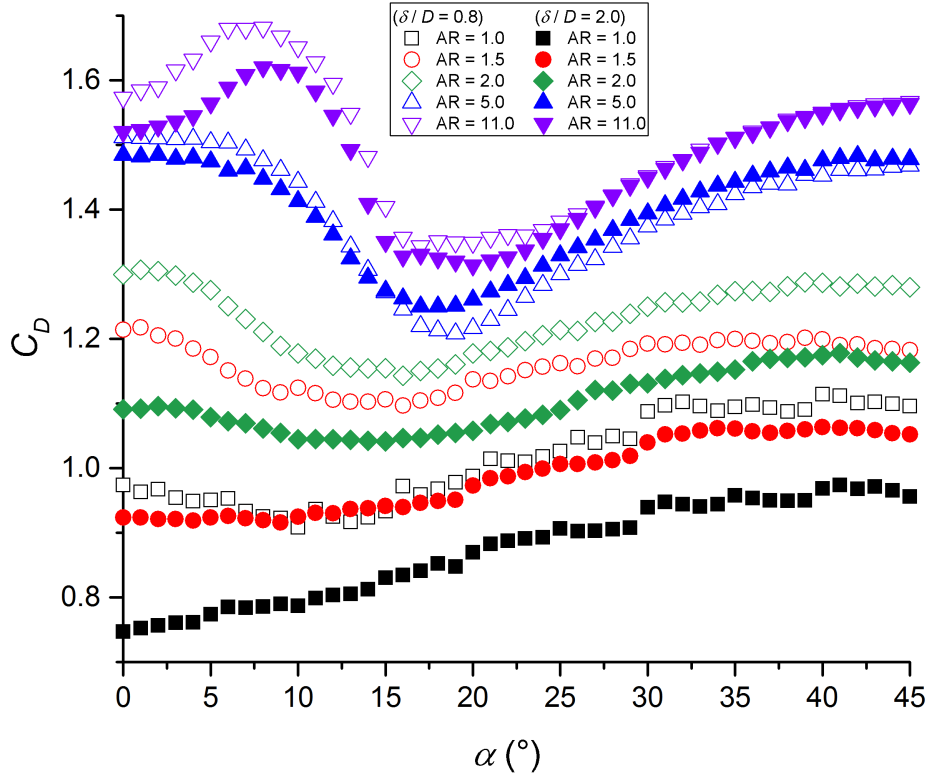


**Figure 4.19:** Mean drag force coefficient,  $C_D$ , versus  $\alpha$  for selected aspect ratios and both boundary layers ( $\delta/D = 0.8$  and  $2.0$ ) at  $\text{Re} = 1.1 \times 10^5$ .

contours undergo the most significant change with AR at the same incidence angle of  $\alpha = 10^\circ$ . At this angle, the values of  $C_P$  significantly drop (with more suction) with the increasing AR. Moreover, the complexity of the pressure contours increases dramatically, after  $\text{AR} = 8.5$  and  $9.5$  (which is close to the critical AR for the plateau formation), for the thin and thick boundary layers, respectively. After the critical aspect ratio, the formation of a circular higher pressure region near to the bottom-right region on the free end can also be observed. This observation may imprint the relationship between the free-end  $C_P$  distribution, the plateau formation, and the existence of the third flow regime. The full  $C_P$  contours at  $\alpha = 10^\circ$  for six selected aspect ratios are shown in Figure 4.21; the full results for all the tested aspect ratios can be found in Appendix A.

The sensitivity of  $C_D$  with AR is compared with the results of the finite cylinder data of Beitel et al. (2019) in Figure 4.22. The comparison is performed for the square prisms at two incidence angles,  $\alpha = 0^\circ$  and  $45^\circ$ . It is found that the values of  $C_D$  for the prisms at both

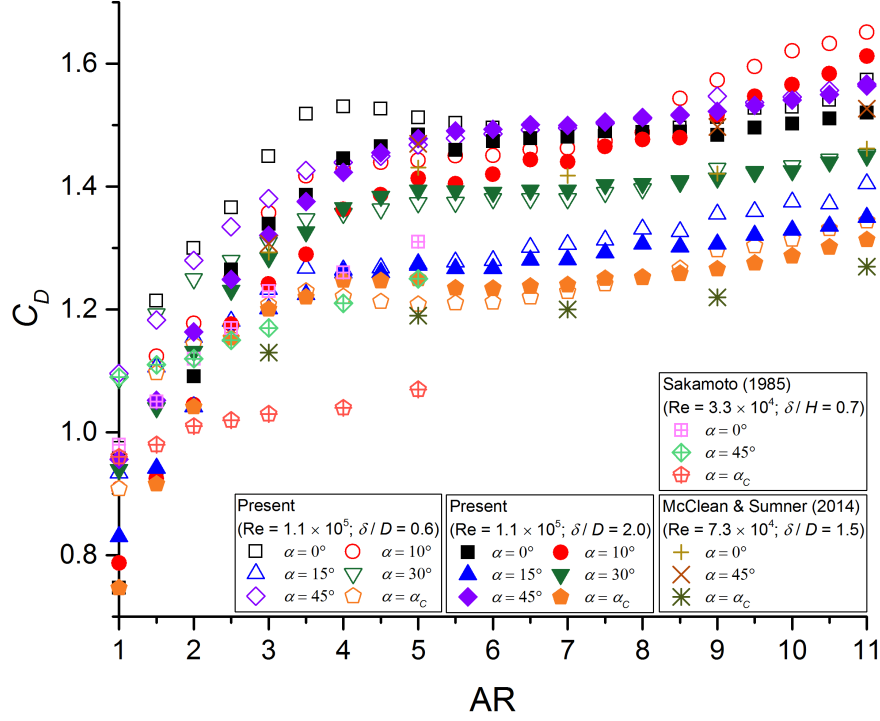
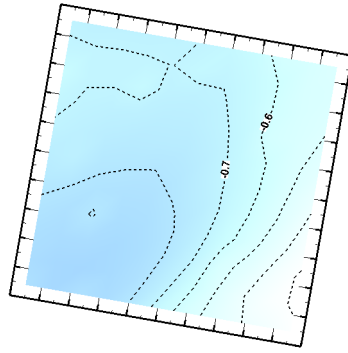
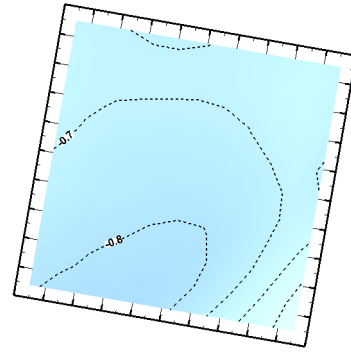


**Figure 4.20:** Mean drag force coefficient,  $C_D$ , at various  $\alpha$  for all the tested aspect ratios in both cases of boundary layers ( $\delta/D = 0.8$  and  $2.0$ ) at  $Re = 1.1 \times 10^5$ . The results are also compared with previous studies of Sakamoto (1985) ( $\delta/H = 0.7$ ;  $Re = 3.3 \times 10^4$ ) and McClean and Sumner (2014) ( $\delta/D = 1.5$ ;  $Re = 7.3 \times 10^4$ ).

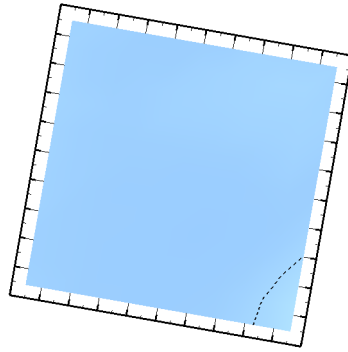
angles are significantly higher than the cylinder, regardless of the aspect ratio. Moreover, the minimum values of  $C_D$  of the prisms at  $\alpha_c$  (not shown in Figure 4.22) are also higher than the  $C_D$  of the cylinder. This is due to a much wider wake width and longer formation length (discussed in Section 4.5) of the square prism compared to the cylinder. The  $C_D$  results of Beitel et al. (2019) demonstrate three flow regimes previously mentioned, with critical aspect ratios of  $AR = \sim 3$  and  $\sim 5$ . Notably, the third flow regime of the cylinder is more appreciable as compared to the prisms. In addition, the effect of the boundary layer in reducing  $C_D$  is less significant for the prism at both angles, as compared to the cylinder.



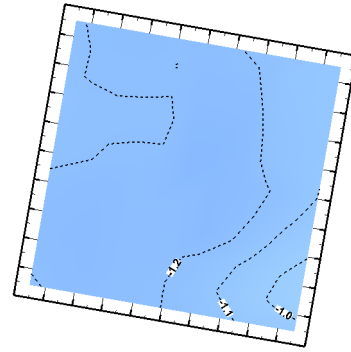
(a)  $AR = 1$



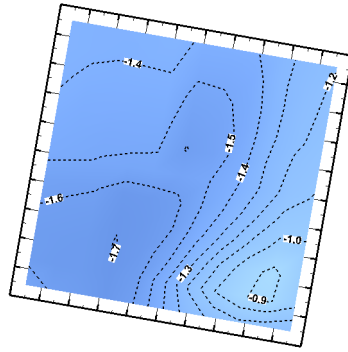
(b)  $AR = 1.5$



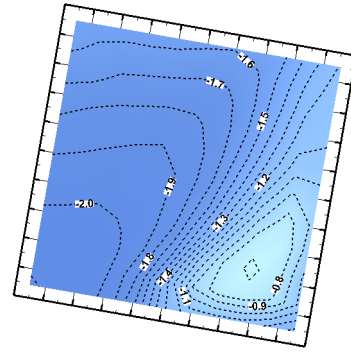
(c)  $AR = 4.5$



(d)  $AR = 7.5$



(e)  $AR = 8.5$



(f)  $AR = 11$

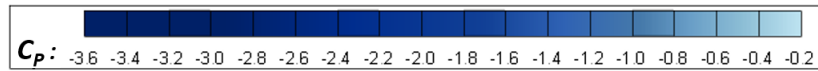


**Figure 4.21:** Free-end mean pressure distribution (contour lines of constant  $C_P$ ) at  $\alpha = 10^\circ$ : (a)  $AR = 1$ , (b)  $AR = 1.5$ , (c)  $AR = 4.5$ , (d)  $AR = 7.5$ , (e)  $AR = 8.5$ , and (f)  $AR = 11$ . The flow is from left to right.

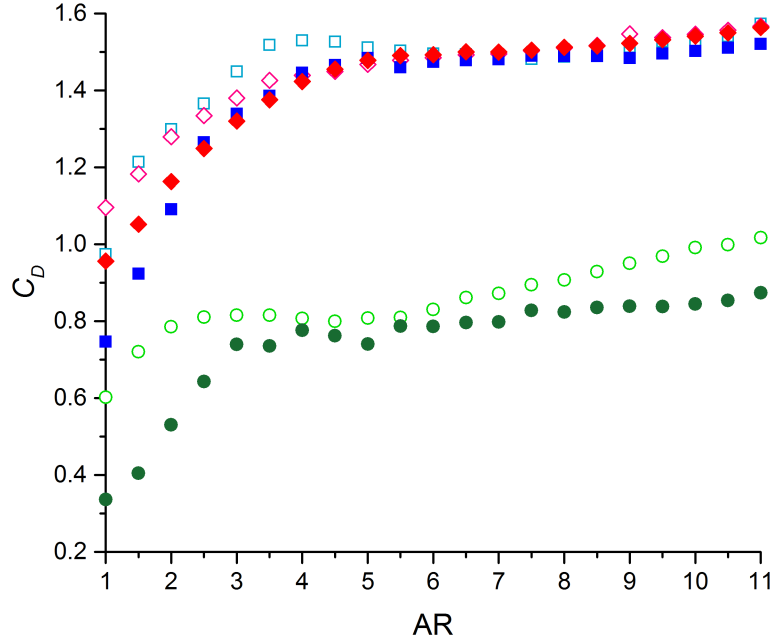


**Figure 4.22:** Comparison of  $C_D$  between cylinder (Beitel et al. (2019) - green circle), and square prisms at  $\alpha = 0^\circ$  (blue square) and  $\alpha = 45^\circ$  (red diamond) of  $AR = 1$  to 11 in two boundary layers conditions:  $\delta/D = 0.8$  (present) and 0.6 (Beitel et al. (2019));  $\delta/D = 2.0$  (present) and 1.9 (Beitel et al. (2019)).  $Re = 1.1 \times 10^5$  and  $6.5 \times 10^4$ , for the present study and the study of Beitel et al. (2019), respectively.

### 4.3.2 Lift force coefficient

Compared to the  $C_D$  data, the  $C_L$  data are more sensitive to the incidence angle. Figure 4.23 illustrates the  $C_L$  versus  $\alpha$  waterfall diagrams.

From Figure 4.23, critical angles can also be identified based on the highest magnitude of  $C_L$ ; these  $\alpha_c$  are similar to those obtained based on the minimum  $C_D$ . Figure 4.24 shows the critical angles based on the highest magnitude of  $C_L$  for all the tested aspect ratios. Similar to the  $C_D$  data, the critical angles for  $C_L$  increase rapidly for the prisms with smaller aspect ratio. For the thin boundary layer, the values of  $\alpha_c$  based on the maximum magnitude of  $C_L$  increase from  $8^\circ$  to  $15^\circ$  when the aspect ratio increases from  $AR = 1$  to 3, while  $\alpha_c$  increases from  $7^\circ$  to  $15^\circ$  when the aspect ratio increases from  $AR = 1$  to 4.5 for the thick boundary layer. The aspect ratio range which shows the high sensitivity of  $\alpha_c$  with  $AR$  is found to occur over a wider range for  $C_L$  compared to  $C_D$ . After this regime with high sensitivity, the value of  $\alpha_c$  based on the  $C_L$  data increases very slowly from  $15^\circ$  to  $17^\circ$  for the thin boundary

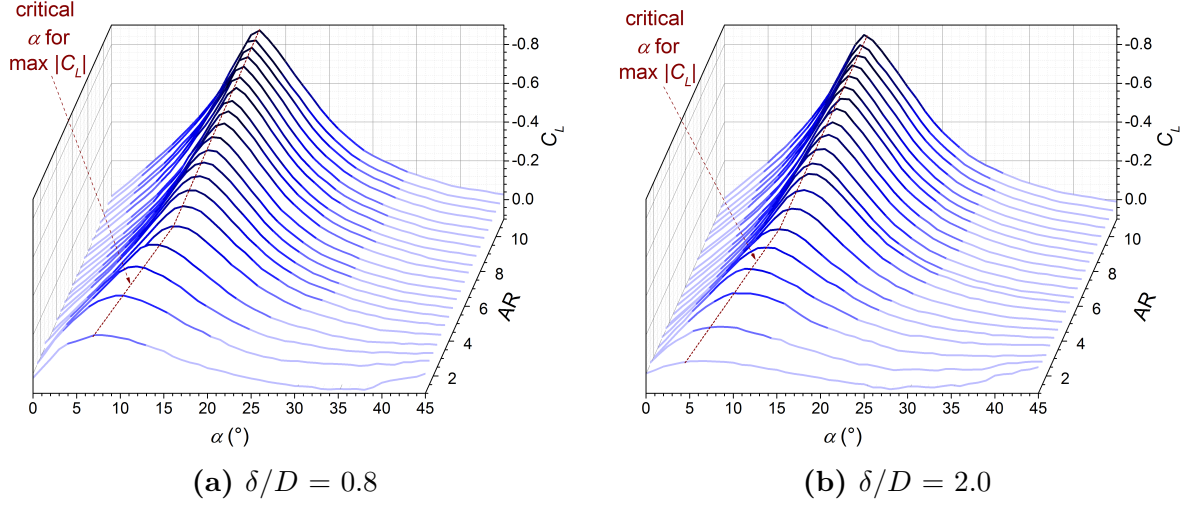


**Figure 4.23:** Mean lift force coefficient,  $C_L$ , versus  $\alpha$  (colored by the magnitude of  $C_L$ ) for all the tested aspect ratios in two boundary layers conditions: (a)  $\delta/D = 0.8$  and (b)  $\delta/D = 2.0$ .

layer, and  $15^\circ$  to  $16^\circ$  for the thick boundary layer. The increased rate of  $\alpha_c$  based on  $C_L$  for the prisms with higher aspect ratio appears to be slower compared to those  $\alpha_c$  based on the minimum  $C_D$ .

The effect of the aspect ratio on  $C_L$  is similar to that of  $C_D$ , where the magnitude of the coefficient is observed to increase with the aspect ratio. Moreover, the  $C_L$  data illustrate two flow regimes, where the first regime demonstrates the high sensitivity of  $C_L$  with AR, while the second regime shows that  $C_L$  is insensitive to AR. The aspect ratio range for the first flow regime is  $1 \leq AR \leq 3.5$  for the thin boundary layer, and  $1 \leq AR \leq 4.5$  for the thick boundary layer, and the second flow regime lies within all the aspect ratios which exceed the upper limits of the first flow regime. Figure 4.25 illustrates this sensitivity by presenting the  $C_L$  data for three selected prisms with low aspect ratio ( $AR = 1, 2$ , and  $3$ ), one intermediate aspect ratio ( $AR = 6$ ), and the highest aspect ratio ( $AR = 11$ ), for both boundary layer conditions. Comparing the data with the same boundary layer thickness, a remarkable gap can be observed between the data of the low range aspect ratios ( $AR = 1, 2, 3$ ), and an insignificant difference between the data of  $AR = 6$  and  $11$ . Another interesting observation from Figure 4.25 about the effect of AR is the observed positive value of  $C_L$  for the prisms with significantly low aspect ratio. For the thin boundary layer,  $C_L$  is found to become positive starting from  $\alpha = 23^\circ$  (indicating the second critical angle based on the  $C_L$  data)

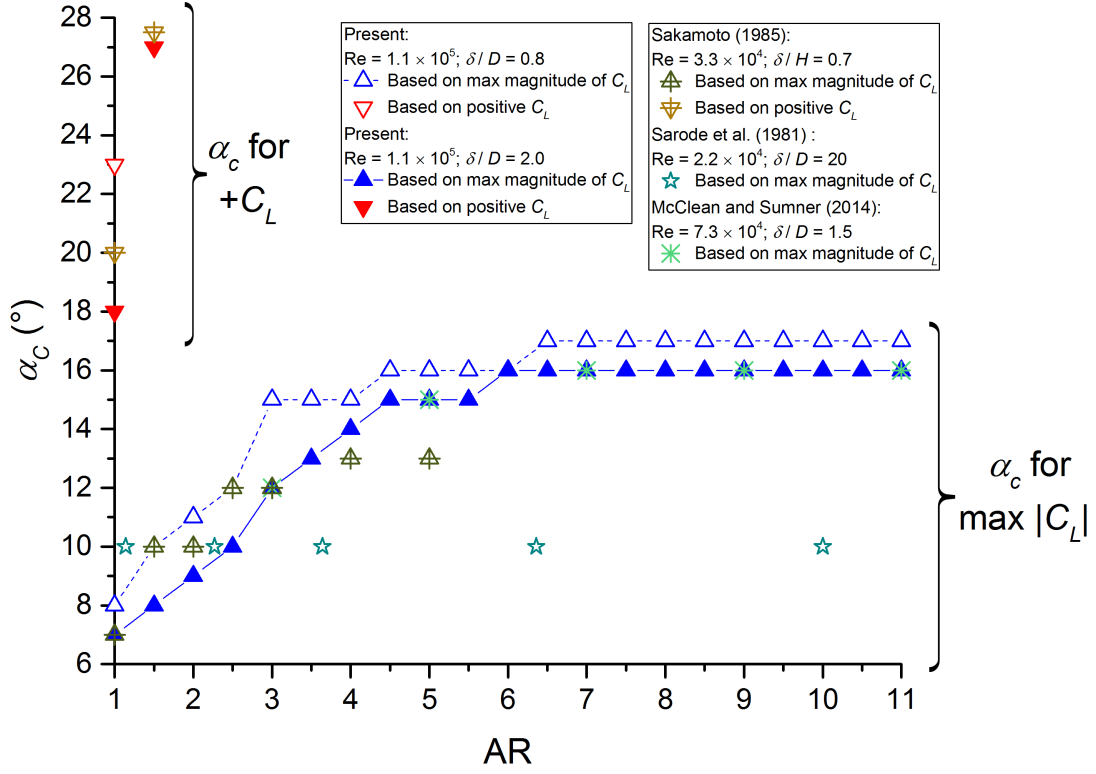


**Figure 4.24:** Critical incidence angles,  $\alpha_c$  based on the maximum magnitude of  $C_L$  for all the tested aspect ratios in both cases of boundary layers ( $\delta/D = 0.8$  and  $2.0$ ) at  $Re = 1.1 \times 10^5$ . The results are also compared with previous studies of Sarode et al. (1981) ( $\delta/D = 20$ ;  $Re = 2.2 \times 10^4$ ), Sakamoto (1985) ( $\delta/H = 0.7$ ;  $Re = 3.3 \times 10^4$ ), and McClean and Sumner (2014) ( $\delta/D = 1.5$ ;  $Re = 7.3 \times 10^4$ ).

for  $AR = 1$ . For the thick boundary layer, the second critical angle based on the positive value of  $C_L$  is  $\alpha = 18^\circ$  and  $27^\circ$  for  $AR = 1$  and  $1.5$ , respectively. These values of the second  $\alpha_c$  based on the positive lift are comparable to the investigation of Sakamoto (1985) which identified  $\alpha = 20^\circ$  and  $27.5^\circ$  for the low-aspect-ratio prisms of  $AR = 1$  and  $1.5$ , respectively. The second  $\alpha_c$  of the present study and Sakamoto (1985) based on the positive lift is also presented in Figure 4.24. It should be noted that  $\alpha_c$  data from Sakamoto (1985) are obtained by interpolation, due to the increment of  $5^\circ$  in  $\alpha$ . Similar to the study of Sakamoto (1985), no positive lift was observed in the present study for  $AR > 1.5$  for the thick boundary layer. The occurrence of the positive lift indicates that the low-aspect-ratio prisms undergo a significant change in the wake structure and separation bubble characteristics, owing to the fact that the flow around the least slender prism is strongly three-dimensional.

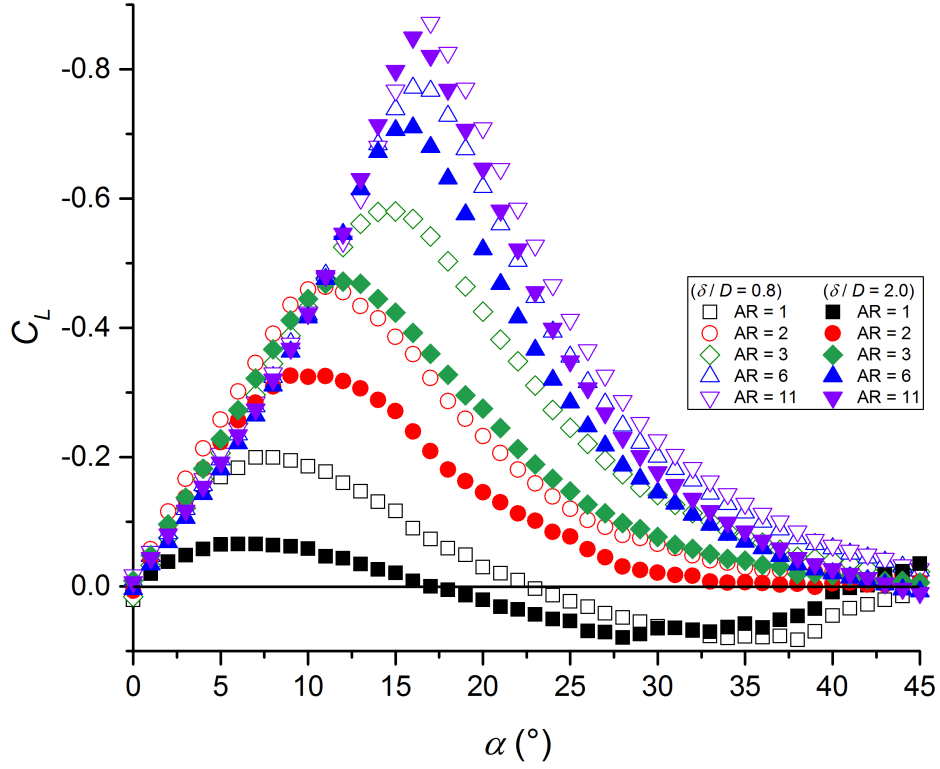


**Figure 4.25:** Mean lift force coefficient,  $C_L$ , versus  $\alpha$  for selected aspect ratios and both boundary layers ( $\delta/D = 0.8$  and  $2.0$ ) at  $\text{Re} = 1.1 \times 10^5$ .

The effect of the boundary layer on  $C_L$  is also similar to that on  $C_D$ . From Figure 4.24, both critical angles tend to decrease slightly for the thick boundary layer. Notably, significant reduction in the second  $\alpha_c$  based on the positive lift for  $\text{AR} = 1$  is also observed for the thick boundary layer. The results are comparable to Sakamoto (1985) and McClean and Sumner (2014). However, the critical angles obtained in the present study are remarkably higher than those in the study of Sarode et al. (1981), which adopted a significantly thicker boundary layer of  $\delta/D = 20$ . This observation further implies the effect of the boundary layer in altering the flow structures around the prism, and therefore also the critical angles. From Figure 4.25, the magnitude of  $C_L$  is slightly lower for the case of the thick boundary layer. Similar to  $C_D$ , the effect of the boundary layer in reducing the magnitude of  $C_L$  is most obvious for the low-aspect-ratio prisms which lie within the first flow regime, which are the prisms with  $\delta/H > 1$  and  $\text{AR}$  less than the critical value.

### 4.3.3 Normal force coefficient

The present study investigates the normal force, in view of these data are not commonly available in the literature. Recall from Section 3.7 that the force balance can only measure  $C_N$  at the symmetrical angles of  $\alpha = 0^\circ$  and  $45^\circ$ . However, Equation 3.8 allows the computation of the normal force coefficient resulted from the free-end suction effect only ( $C_{N,p}$ ) at all tested  $\alpha$ . It should be noted that the  $C_{N,p}$  data are obtained based on the integration of the pressure data on the free-end surface. Therefore, the boundary layer thicknesses of  $\delta/D = 0.8$  and  $2.6$  (refer to Case 1 and 2 in Section 3.4) are used for the data of  $C_{N,p}$ , while the value of  $\delta/D = 0.8$  and  $2.0$  (refer to Case 4 and 5 in Section 3.4) are used for the data of  $C_N$ . Similarly, the Reynolds numbers adopted are different, with  $Re = 6.5 \times 10^4$  for  $C_{N,p}$ , and  $Re = 1.1 \times 10^5$  for  $C_N$ . Complementary experiments were carried out to measure  $C_N$  at  $Re = 6.5 \times 10^4$ , and it was observed that  $C_N$  is qualitatively similar for both values of  $Re$ , but a slight reduction in  $C_N$  was observed when higher  $Re$  was used. The  $C_{N,p}$  data at various  $\alpha$  for all tested aspect ratios are presented in Figure 4.26 as waterfall diagrams, for both cases of boundary layer.

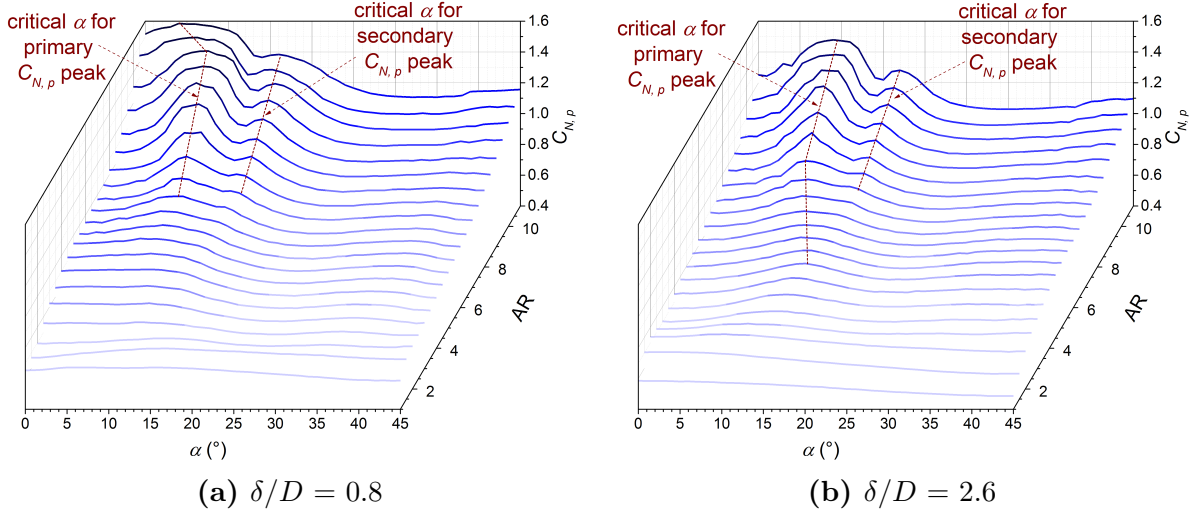


**Figure 4.26:** Mean normal suction force coefficient,  $C_{N,p}$ , versus  $\alpha$  (colored by the magnitude of  $C_{N,p}$ ) for all the tested aspect ratios in two boundary layers conditions: (a)  $\delta/D = 0.8$  and (b)  $\delta/D = 2.6$ .

Comparing  $C_{N,p}$  (Figure 4.26) with  $C_D$  (Figure 4.17), the effect of  $\alpha$  is somewhat similar. However, the formation of the minimum peak is not too apparent in the waterfall diagrams of

$C_{N,p}$ , and hence the critical angles based on the minimum  $C_{N,p}$  could not be clearly defined. Conversely, the critical angles based on the maximum peak formation in  $C_{N,p}$  is evident for the high-aspect-ratio prisms. Similar plateau formation with a maximum peak is observed in  $C_{N,p}$  data, with the critical angles close to those  $\alpha_c$  obtained from  $C_D$  data based on the maximum peak formation. The plateau formation is observed starting at the critical aspect ratio of  $AR = 6$  for the thin boundary layer and  $AR = 4$  for the thick boundary layer. The critical angles based on this plateau formation are found to be  $\alpha_c = 9^\circ$  to  $11^\circ$  (with one outlier of  $\alpha_c = 4^\circ$  for  $AR = 11$ ) for the thin boundary layer, and  $9^\circ$  to  $15^\circ$  for the thick boundary layer. The value of  $\alpha_c$  generally decreases with the aspect ratio. Interestingly, there is a secondary maximum peak observed (which is absent in the  $C_D$  data) for the high-aspect-ratio prisms, starting from  $AR = 7.5$  and  $AR = 8.5$  for the thin and thick boundary layer, respectively. The range of  $\alpha_c$  based on the secondary peak is very small, which lies within  $16^\circ$  to  $17^\circ$ , for both cases of boundary layer. Notably, the critical angles based on the secondary peak are very close to the critical angles obtained based on the maximum magnitude of  $C_L$  (Figure 4.24). The critical angles based on the primary and secondary peak in the  $C_{N,p}$  data are presented in Figure 4.27.

The effect of the aspect ratio on  $C_{N,p}$  is also somewhat similar to that of  $C_D$ , where the value increases with  $AR$  as illustrated in the waterfall diagrams in Figure 4.26. However, the rates of increase are different. Recall that after the flow first regime (with  $\delta/H > 1$ ), the values of  $C_D$  exhibit lesser sensitivity to the change of  $AR$ . However,  $C_{N,p}$  from the present study appears to increase with  $AR$  relatively linearly, in comparison to  $C_D$ . This sensitivity is illustrated in Figure 4.28 for four selected aspect ratios with a similar increment ( $AR = 1, 4, 8$ , and  $11$ ) for both cases of boundary layer thickness. Comparing the data with the same boundary layer condition, it can be shown in Figure 4.28 that the gaps between the data of subsequent aspect ratios are fairly similar, unlike the data of  $C_D$  and  $C_L$  that demonstrate a sharp increase for the less slender prisms, and insensitive increase for the prisms with intermediate to high aspect ratios (Figures 4.19 and 4.25). Also, the values of  $C_{N,p}$  at  $0^\circ$  and  $45^\circ$  are similar for the less slender prisms; however, for the prisms with high aspect ratio, a significant difference can be observed with  $C_{N,p}$  at  $0^\circ$  remarkably higher than that at  $45^\circ$ .

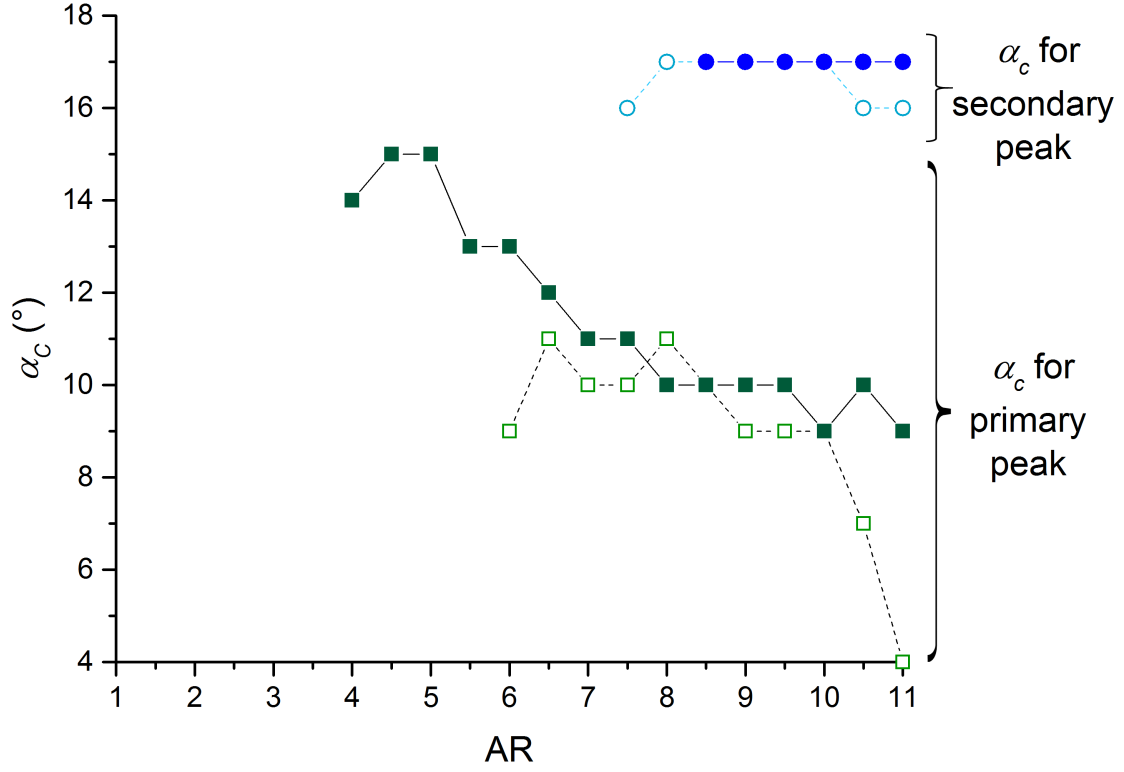


**Figure 4.27:** Critical incidence angles,  $\alpha_c$  based on the maximum magnitudes of  $C_{N,p}$  at two regions of the plateau formation. The black squares represent  $\alpha_c$  based on the primary peak formation, while the blue circles represent  $\alpha_c$  based the secondary peak. The data are presented for all the tested aspect ratios in both cases of boundary layers ( $\delta/D = 0.8$  (open symbol) and  $2.6$  (solid symbol)) at  $Re = 6.5 \times 10^4$ .

Recall that the thick boundary layer slightly reduces the critical angles obtained from  $C_D$  and  $C_L$  data (Figure 4.27). The  $C_{N,p}$  data, on the other hand, show that the critical angles based on the primary peak appear to increase slightly for the thick boundary layer. The critical angles obtained from the secondary peak of the  $C_{N,p}$  data are generally not influenced by the boundary layer. In terms of the values of  $C_{N,p}$ , the thick boundary layer generally decreases  $C_{N,p}$  (indicating lesser suction effect) as shown in Figure 4.28, which is similar to the observations made from the  $C_D$  and  $C_L$  data.

The  $C_{N,p}$  data are compared with the  $C_N$  data in Figure 4.29 for three bluff-body shapes: the cylinder (from Beitel et al. (2019)), the prism at  $\alpha = 0^\circ$ , and the prism at  $\alpha = 45^\circ$ . The data for boundary layers are shown; however, it appears that the boundary layer does not influence these data qualitatively. From Figure 4.29, it can be observed that  $C_{N,p}$

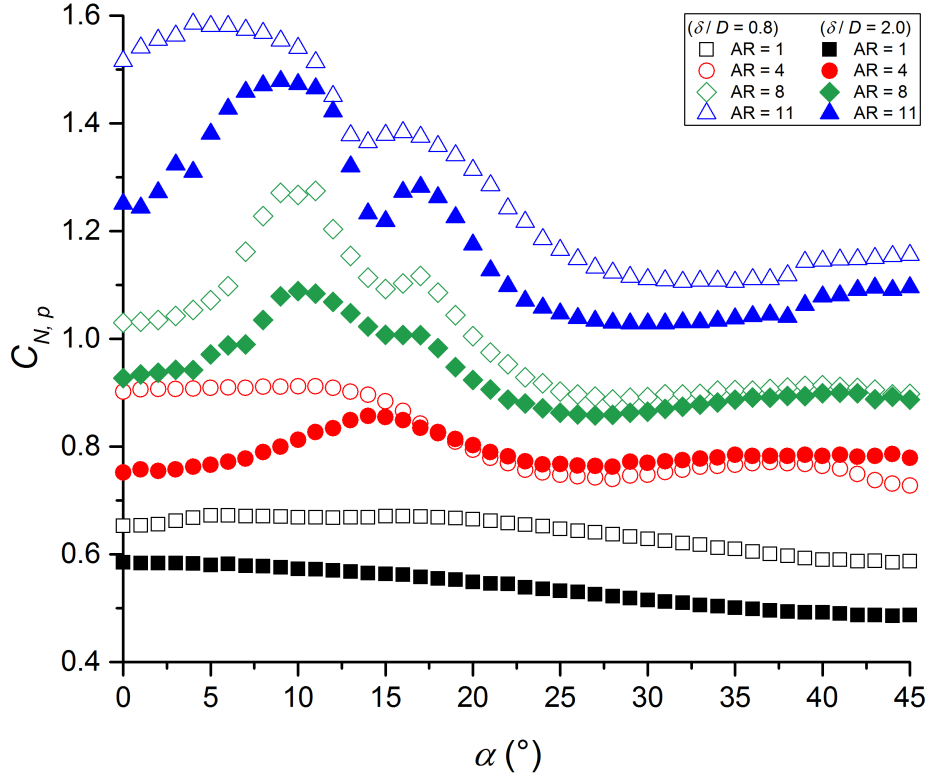


**Figure 4.28:** Mean normal suction force coefficient,  $C_{N,p}$ , versus  $\alpha$  for selected aspect ratios and both boundary layers ( $\delta/D = 0.8$  and  $2.6$ ) at  $\text{Re} = 6.5 \times 10^4$ .

increases with aspect ratio for all the three shapes investigated. This increase corresponds to the reduction in  $C_P$  (with higher suction) observed (in Section 4.2), when the aspect ratio increases. The  $C_N$  data, however, do not exhibit a simple increasing trend for the cylinder and prism at  $\alpha = 0^\circ$ . For the cylinder, the  $C_N$  data increase slowly or remain constant below the critical aspect ratio of  $\text{AR} \simeq 7$ , as identified by Beitel et al. (2019). After this critical aspect ratio,  $C_N$  reduces rapidly with the increase of the aspect ratio. On the other hand,  $C_N$  data for the prism at  $\alpha = 0^\circ$  show a decreasing trend starting from the least slender prism ( $\text{AR} = 1$ ). However, the rate of decrease is not constant throughout the change in aspect ratio. For both boundary layers, it appears that the decreasing rate is more rapid for the prisms with  $\text{AR} < 3$ . The decreasing trend observed for the cylinders and prisms at  $\alpha = 0^\circ$  indicates the dominant effect of the wall shear stress. Referring again to the experimental investigation by Rostamy et al. (2012) and Sumner et al. (2017), due to the downward-directed flow, there was a vortex  $N_w$  observed that is located near the ground

plane and the wall of the test model. This vortex structure was found to be absent for the lowest tested aspect ratio ( $AR = 3$ ) in both studies. Also, based on the PIV results, the proportion of the downwash-directed flow next to the wall appears to increase with the aspect ratio. These findings may indicate the increasing wall shear stress on the side-wall of the prism with  $AR$ , and explain the reduction in  $C_N$  data for both cylinder and prism at  $\alpha = 0^\circ$ . However, for the prism at  $\alpha = 0^\circ$ , the values of  $C_N$  are consistently smaller than  $C_{N,p}$ , regardless of the aspect ratio. This observation suggests that there is another flow structure (other than vortex  $N_w$ ) with the downward-directed flow and responsible for the reduction in  $C_N$  for the prisms at  $\alpha = 0^\circ$ .

The  $C_N$  data for the prism at  $\alpha = 45^\circ$  show a fairly linearly increasing trend, which is a completely different trend compared to the cylinder and prism at  $\alpha = 0^\circ$ . For the prism at  $\alpha = 45^\circ$ , the critical aspect ratios of  $AR = 4$  and  $AR = 4.5$  can be identified, for the thin and thick boundary layers, respectively. Below this critical aspect ratio,  $C_N$  is lower than  $C_{N,p}$  which suggests the dominant effect of the downward-directed flow and wall shear stress. Conversely, above this critical aspect ratio,  $C_N$  is found higher than  $C_{N,p}$ , which may be due to the existence of some flow structure with significant portion of upward-directed flow. With different downwash characteristics and a significant portion of the attached flow at  $\alpha = 45^\circ$ , the formation of the vortex  $N_w$  still remains questionable. The different complexity of the  $C_P$  contours presented in Section 4.1 and PIV measurement of McClean and Sumner (2014) have suggested completely different flow characteristics for the prisms at  $\alpha = 0^\circ$  and  $45^\circ$ . Comparing the data between the prism at  $\alpha = 45^\circ$  (with critical  $AR \simeq 4$ ) and the cylinder (critical  $AR \simeq 7$ ), it is interesting to find that the prism data at  $\alpha = 45^\circ$  show higher  $C_N$  compared to  $C_{N,p}$  when exceeding the critical aspect ratio. This trend is different from the data of the cylinder that show lower  $C_N$  compared to  $C_{N,p}$  above the critical aspect ratio, which again suggest a possible significant difference in the flow structures between the two shapes. In addition, from Figures 4.29(a) and 4.29(b), the  $C_N$  data of the prisms at both angles appear to be less sensitive to the boundary layer effect in comparison to the cylinder.

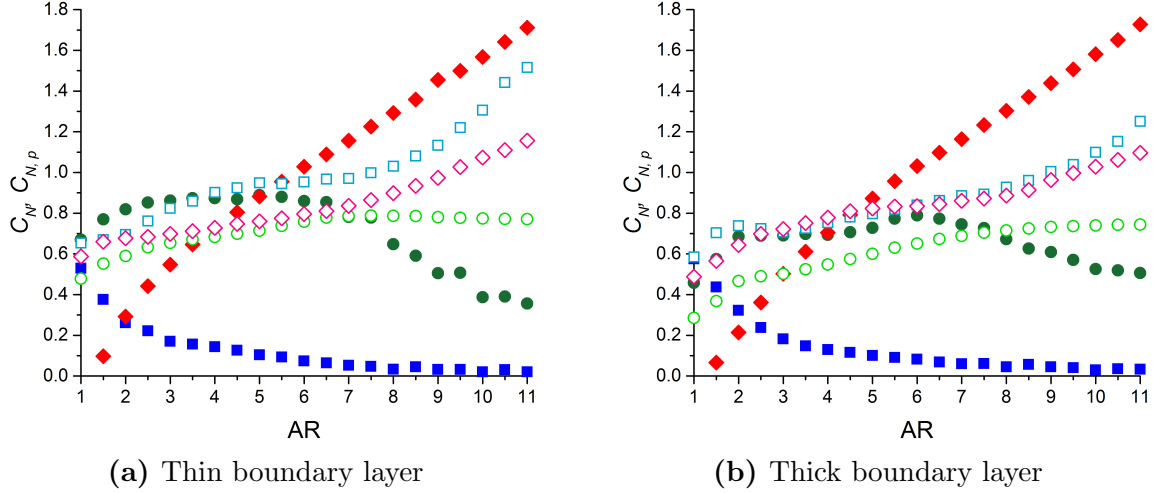


**Figure 4.29:** Comparison between the mean normal suction force coefficient computed by integration ( $C_{N,p}$  - open symbol) and resultant normal force measured by force balance ( $C_N$  - solid symbol) for the cylinder (Beitel et al. (2019) - green circle), and square prisms at  $\alpha = 0^\circ$  (blue square), and  $\alpha = 45^\circ$  (red diamond) of  $AR = 1$  to  $11$  in two boundary layers conditions: (a)  $\delta/D = 0.8$  (present) and  $0.6$  (Beitel et al. (2019)) (b)  $\delta/D = 2.0$  (present - force balance),  $2.6$  (present - integration), and  $1.9$  (Beitel et al. (2019)).  $Re = 1.1 \times 10^5$  for the  $C_N$  data of the prisms, and  $Re = 6.5 \times 10^4$  for the remaining data.

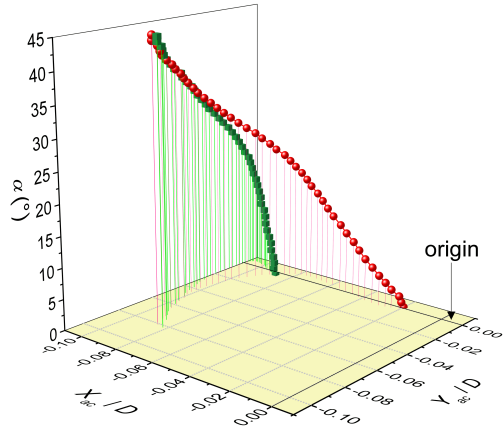
#### 4.3.4 Point of action

The point of action of  $C_{N,p}$  on the free-end surface is presented as a coordinate of  $(X_{ac}, Y_{ac})$ . The location of  $X_{ac}$  and  $Y_{ac}$  are computed by Equations 3.9 and 3.10, respectively. It should be again noted that the  $X_{ac}$  and  $Y_{ac}$  coordinates defined in this subsection are the locations fixed to the free-end surface. The values of  $X_{ac}$  and  $Y_{ac}$  are normalized with the width of the prism,  $D$ . Similar to the  $C_{N,p}$  data, the boundary layer thicknesses are  $\delta/D = 0.8$  and  $2.6$  (refer to Case 1 and 2 in Section 3.4) with  $Re = 6.5 \times 10^4$ .

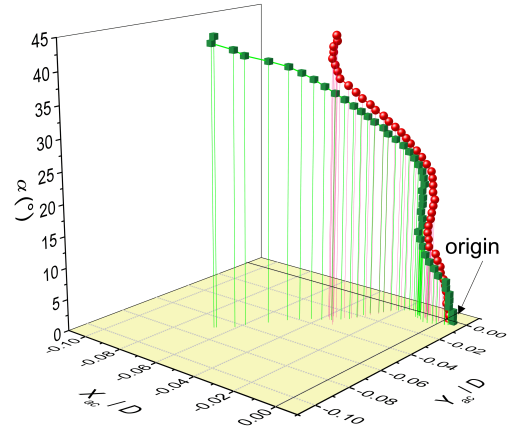
Figure 4.30 shows the points of action at all incidence angles for six selected aspect ratios. The data are plotted in three-dimensional trajectory view, where towards the positive  $z$ -axis direction indicates increasing  $\alpha$ . Most of the points of action are found to be located in the upstream-bottom region (with negative values in both  $X_{ac}/D$  and  $Y_{ac}/D$ ). However, the magnitudes of  $X_{ac}/D$  and  $Y_{ac}/D$  are significantly small, with both values between  $-0.1D$  to  $\sim 0D$ . These small magnitudes indicate that the points of action for all  $AR$  and  $\alpha$  are close to the origin. For a wide range of aspect ratio, the point of action generally moves relatively

further away from the origin with the increase of  $\alpha$ . This effect is more apparent for the prisms with lower and higher aspect ratios (Figures 4.30(a)(b), 4.30(f)). For the prisms with intermediate aspect ratios, the point of action is less sensitive to  $\alpha$  (Figure 4.30(c)-(d)). For the least slender prism studied ( $AR = 1$ ), the points of action do not fluctuate significantly between subsequent incidence angles (Figure 4.30(a)). On the other hand, there is an obvious fluctuation observed in the points of action for  $10^\circ \leq \alpha \leq 20^\circ$ , for the high-aspect-ratio prisms (Figure 4.30(e)-(f)). This region of the high fluctuation interestingly coincides with the maximum plateau formation in the data of  $C_D$  and  $C_{N,p}$ , which are highlighted previously in the subsections 4.3.1 and 4.3.3.

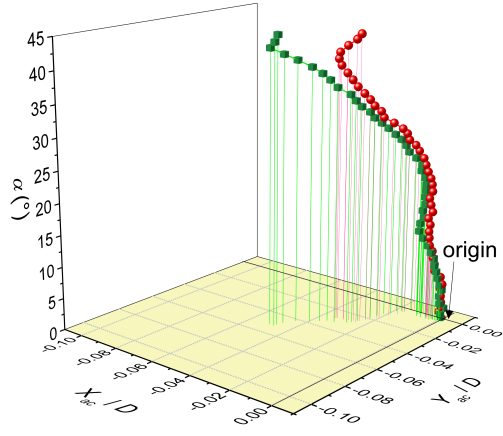
The points of action for all the tested aspect ratios at six selected incidence angles are presented in Figure 4.31. At  $\alpha = 0^\circ$ , the points of action lie very close on the  $X$ -axis ( $Y = 0$ ) due to the symmetrical arrangement (Figure 4.31(a)). For the intermediate incidence angles of  $\alpha = 10^\circ$  to  $20^\circ$ , the locations of  $Y_{ac}/D$  remain close to the  $X$ -axis, but appreciable variation in  $X_{ac}/D$  with  $AR$  can be observed, especially for the prisms with low and high aspect ratios (Figure 4.31(b)-(d)). The sensitivity of  $X_{ac}/D$  with  $AR$  for the high-aspect-ratio prisms becomes less evident at  $\alpha = 30^\circ$ , but the high sensitivity of the data for the least slender prisms can still be observed at this angle (Figure 4.31(e)). The effect of  $AR$  on the point of action is most pronounced at  $\alpha = 45^\circ$ , where the data show the highest sensitivity (Figure 4.31(f)). This high sensitivity also corresponds to the highest variation in the  $C_P$  contours with  $AR$  presented in Figure 4.8. The values of  $X_{ac}/D$  and  $Y_{ac}/D$  are similar at  $\alpha = 45^\circ$ , and therefore the points of action at this angle lie closely on the straight line that joins the origin and leading edge apex. The results presented in Figure 4.31 seem to suggest the existence of three flow regimes based on the sensitivity of the points of action with  $AR$ , similar to the  $C_P$  data in Table 4.1. Comparing Figures 4.30 and 4.31, the thicker boundary layer moves the point of action farther from the centre. This effect is more appreciable at low incidence angles for  $AR = 1$  (Figure 4.30(a)) and at  $\alpha = 45^\circ$  for the intermediate aspect ratios (Figure 4.31(f)).



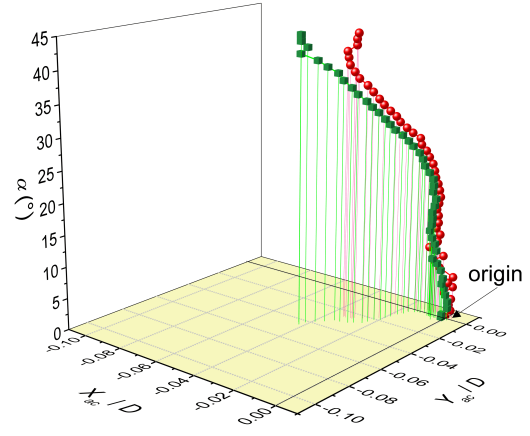
(a) AR = 1



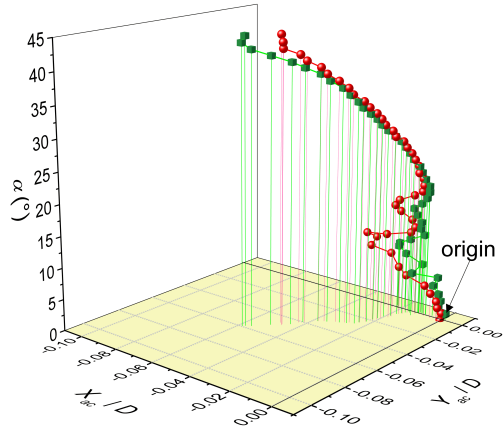
(b) AR = 3



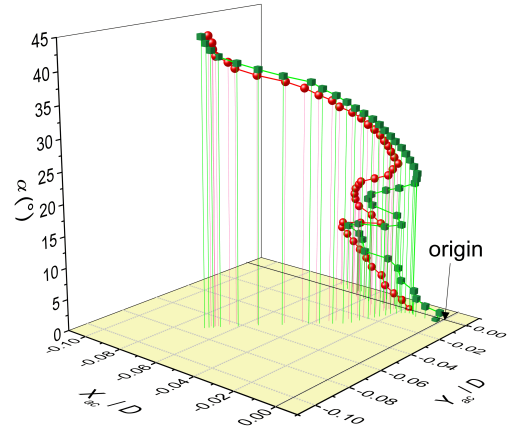
(c) AR = 5



(d) AR = 7

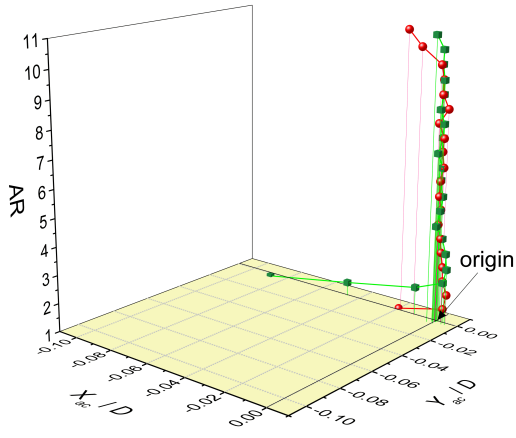


(e) AR = 9

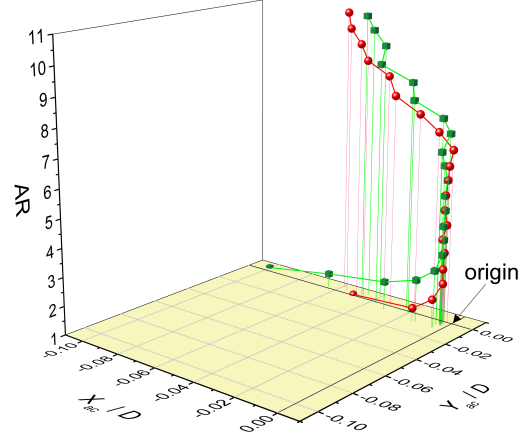


(f) AR = 11

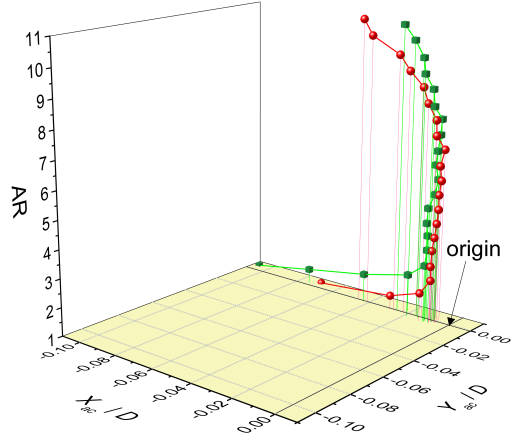
**Figure 4.30:** Point of action of  $C_{N,p}$  for selected aspect ratios: (a) AR = 1, (b) AR = 3, (c) AR = 5, (d) AR = 7, (e) AR = 9, and (f) AR = 11 at  $\alpha = 0^\circ$  to  $45^\circ$  (represented by  $z$ -axis) in both cases of boundary layer ( $\delta/D = 0.8$  (red sphere) and  $2.6$  (green cube);  $Re = 6.5 \times 10^4$ ).



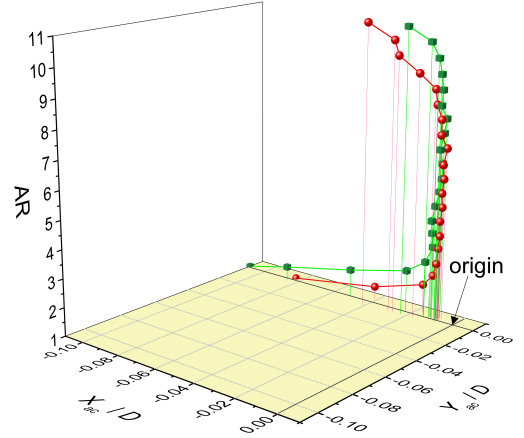
(a)  $\alpha = 0^\circ$



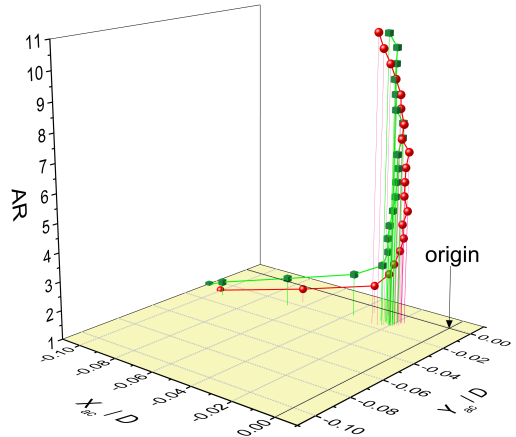
(b)  $\alpha = 10^\circ$



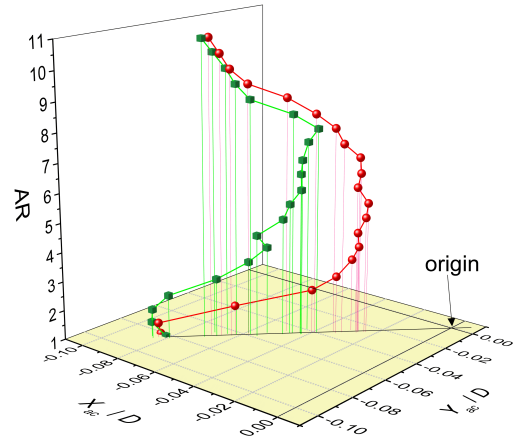
(c)  $\alpha = 15^\circ$



(d)  $\alpha = 20^\circ$



(e)  $\alpha = 30^\circ$



(f)  $\alpha = 45^\circ$

**Figure 4.31:** Point of action of  $C_{N,p}$  for selected incidence angles: (a)  $\alpha = 0^\circ$ , (b)  $\alpha = 10^\circ$ , (c)  $\alpha = 15^\circ$ , (d)  $\alpha = 20^\circ$ , (e)  $\alpha = 30^\circ$ , and (f)  $\alpha = 45^\circ$  for  $AR = 1$  to  $11$  (represented by  $z$ -axis) in both cases of boundary layer ( $\delta/D = 0.8$  (red sphere) and  $2.6$  (green cube);  $Re = 1.1 \times 10^5$ ).

## 4.4 Strouhal number

Figure 4.32 shows the Strouhal number as a function of AR and  $\alpha$  in both boundary layer conditions. The aspect ratio range shown in Figure 4.32 is from AR = 3 to 11 for both cases of the boundary layer. In the present study, due to an undefined peak in the power spectrum, the Strouhal number for the thin boundary layer could not be identified for the prisms of AR = 1 at  $\alpha = 0^\circ$  to  $45^\circ$ , AR = 1.5 at  $\alpha = 10^\circ$  to  $45^\circ$ , and AR = 2 at  $\alpha = 30^\circ$  to  $45^\circ$ . For the thick boundary layer, the peaks were absent for prisms with AR  $\leq 2$  at  $\alpha = 0^\circ$  to  $45^\circ$ , and AR = 2.5 at  $\alpha = 20^\circ$  to  $45^\circ$ . This result is similar to the study of Sakamoto (1985) that could not identify vortex shedding frequencies for prisms with AR  $\leq 3$ , especially at a higher incidence angle.

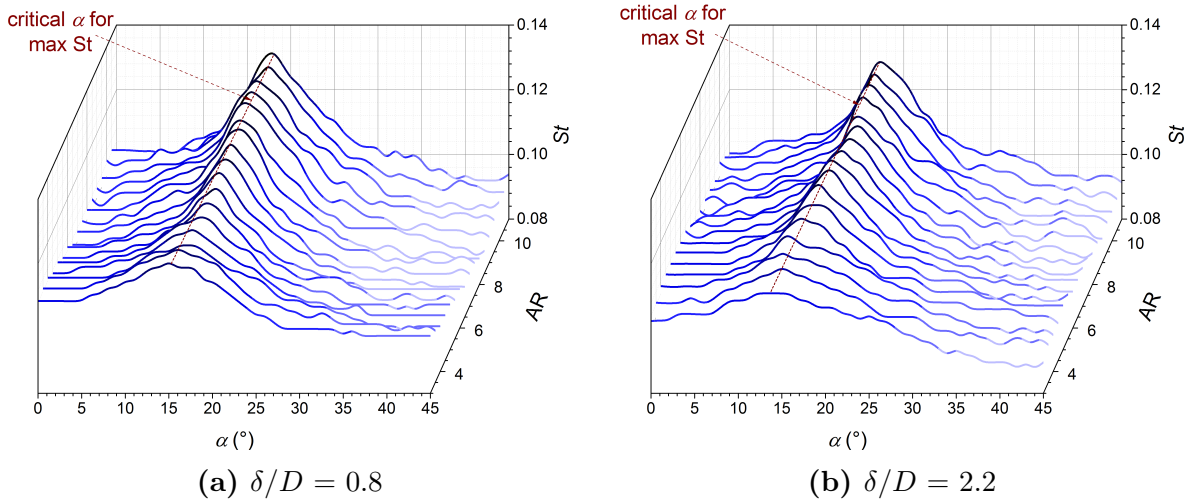


**Figure 4.32:** Strouhal number,  $St$ , versus  $\alpha$  (colored by the magnitude of  $St$ ) for all the tested aspect ratios in two boundary layers conditions: (a)  $\delta/D = 0.8$  and (b)  $\delta/D = 2.2$  at  $Re = 6.5 \times 10^4$ .

Recall that  $St$  calculated in the present study is based on the fixed width as defined in Equation 1.5. Also note that the  $St$  was obtained at  $Re = 6.5 \times 10^4$ , and  $\delta/D = 0.8$  and  $2.2$  (refer to Case 1 and 3 in Section 3.4), for the thin and thick boundary layer, respectively. Comparing to the data of  $C_D$  and  $C_L$ , the  $St$  data show relatively higher fluctuation between each data points of  $\alpha$ , mainly due to the minimum measurement uncertainty of 0.002 discussed in Section 3.9. It can be observed that  $St$  is close to the minimum value when  $\alpha$  is approaching  $45^\circ$ , with remarkably lower value than  $St$  at  $\alpha = 0^\circ$ . This trend is different than the  $C_D$  and

$C_L$  data which show the force coefficients of the prism are similar at  $\alpha = 0^\circ$  and  $45^\circ$ . The presence of a critical angle, based on the maximum St, is evident as similar to the studies of Sakamoto (1985), McClean and Sumner (2014), and Sohankar et al. (2018). The comparison of  $\alpha_c$  based on the maximum St between different studies is illustrated in Figure 4.33. In the present study, the values of  $\alpha_c$  based on the maximum St increase more steadily with the aspect ratio, in comparison to the  $C_D$  and  $C_L$  data. For  $AR > 2.5$ ,  $\alpha_c$  increases slowly with AR from  $15^\circ$  to  $18^\circ$  for the thin boundary layer, and from  $13^\circ$  to  $17^\circ$  for the thick boundary layer. The values of  $\alpha_c$  are very similar to the investigation of McClean and Sumner (2014).

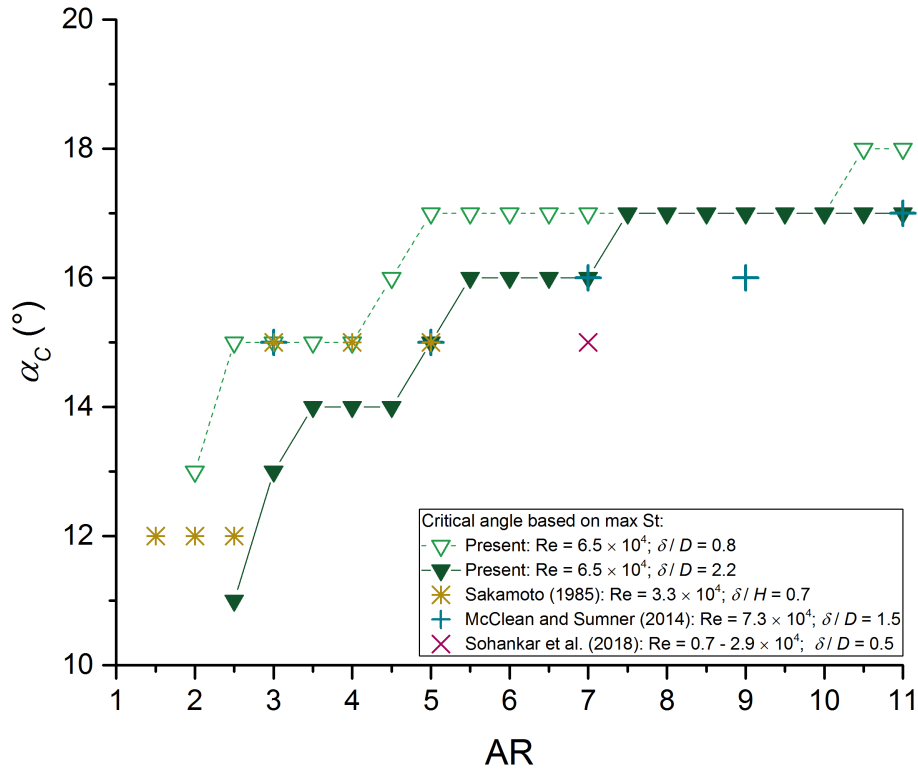


**Figure 4.33:** Critical incidence angles,  $\alpha_c$  based on the maximum St for all the tested aspect ratios in both cases of boundary layers ( $\delta/D = 0.8$  and  $2.2$ ) at  $Re = 6.5 \times 10^4$ . The results are also compared with previous studies of Sakamoto (1985) ( $\delta/H = 0.7$ ;  $Re = 3.3 \times 10^4$ ) and McClean and Sumner (2014) ( $\delta/D = 1.5$ ;  $Re = 7.3 \times 10^4$ ).

The effect of AR on St is very similar to that on  $C_D$  and  $C_L$ , where St increases with AR. However, in comparison to the  $C_D$  and  $C_L$  data, the St data are observed to be relatively insensitive to the change of AR, at most of the incidence angles. For both cases of boundary layer, the most sensitive trend of St with AR is observed near the critical angle, where the

prisms with lower aspect ratios show a relatively broad-banded peak. The maximum peak of the  $St$  versus  $\alpha$  at the critical angle appears to become more well-defined with the increase of the aspect ratio. This sensitivity of  $St$  with  $AR$  is demonstrated in Figure 4.34 for both boundary layer conditions. A similar sensitivity was also observed by McClean and Sumner (2014), and a critical aspect ratio of  $AR = 3$  was identified in their study due to a distinct behaviour of the curve of  $St$  versus  $\alpha$  at this aspect ratio. With a smaller increment in  $AR$ , the present study suggests a critical aspect ratio of  $AR = 4$  for both boundary layer conditions, where the maximum peak of the  $St$  curve appears to be more well-defined after this critical aspect ratio.

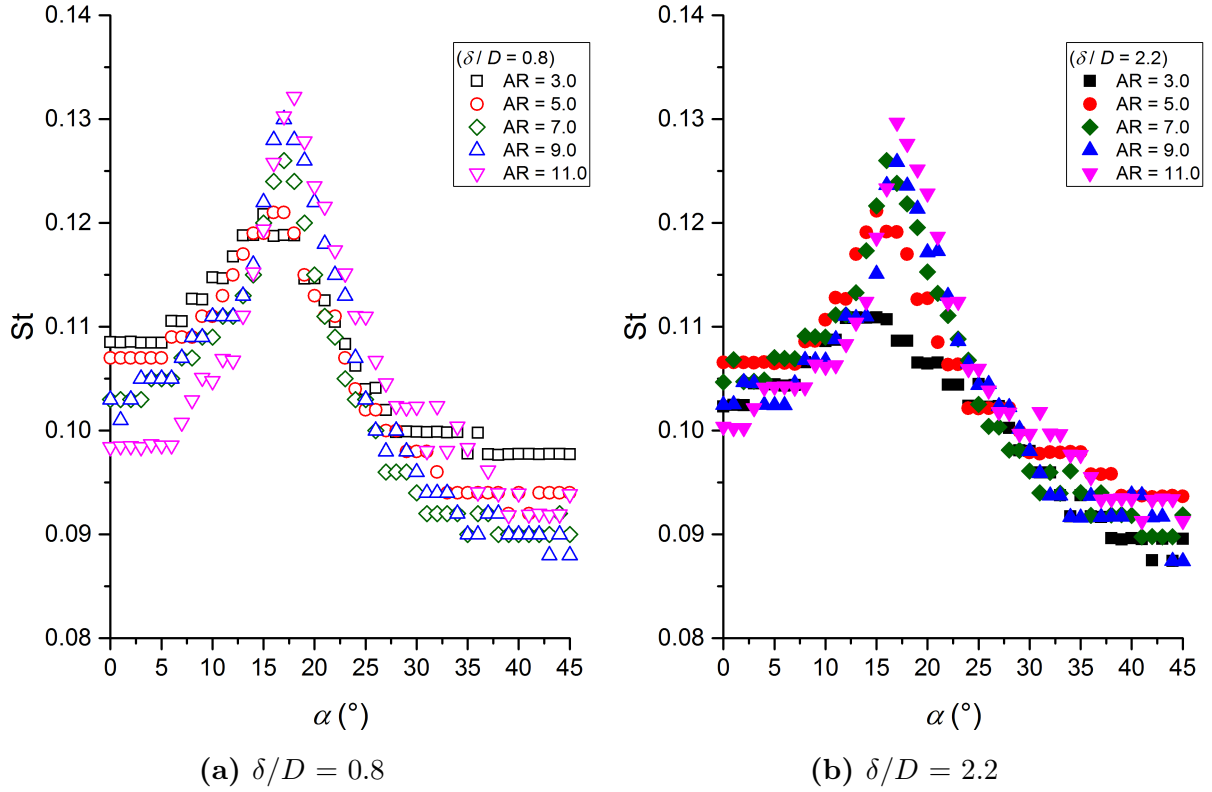


**Figure 4.34:** Strouhal number,  $St$ , versus  $\alpha$  for selected aspect ratios and both boundary layers: (a)  $\delta/D = 0.8$  and (b)  $\delta/D = 2.2$  at  $Re = 6.5 \times 10^4$ .

From Figure 4.33, it can be seen that the critical angles reduce slightly when a thick boundary layer is used. This effect of the thick boundary layer in decreasing the critical angle is similar to the  $C_D$  and  $C_L$  data. This observation again supports the claim about the shear layer reattachment on the bottom surface is influenced by the boundary layer thickness.

In term of the value of  $St$ , the thick boundary layer reduces  $St$  slightly for the low-aspect-ratio prisms which lie below the critical aspect ratio of  $AR = 4$ . Above this critical  $AR$ , the values of  $St$  are generally not influenced by  $\delta/D$ . This trend is found similar to  $C_D$  and  $C_L$ , where the impact of the thick boundary layer is most pronounced for the prisms with low aspect ratio ( $\delta/H > 1$ ).

The  $St$  data at  $\alpha = 0^\circ$  and  $45^\circ$  are compared with the finite cylinder data of Beitel et al. (2019) in Figure 4.35. The  $St$  data of the prisms at both angles are remarkably lower than the cylinder, regardless of the aspect ratio. The  $St$  data for the three shapes are consistent with Ozgoren (2006) who adopted the same three shapes and studied the effect of those shapes on the the wake width. Recall from Section 2.7 that Ozgoren (2006) identified the largest wake width for the prism at  $\alpha = 45^\circ$ , followed by the prism at  $\alpha = 0^\circ$ , and the smallest wake width for the cylinder. Due to the larger wake width, there is a reduced possibility for the shear layers separated from the prisms' sides to interact together (especially for the prism at  $\alpha = 45^\circ$  with larger projected width), and results in lower  $St$ . Another interesting observation from Figure 4.35 is the  $St$  data for the cylinder are greatly influenced by the boundary layer thickness, where the higher  $St$  values are obtained for the thick boundary layer. On the other hand, the impact of the boundary layer is not too apparent for the prisms at  $\alpha = 0^\circ$  and  $45^\circ$ , except for the prisms which lie above the critical aspect ratio of  $AR = 4$  previously mentioned. This trend is very similar to  $C_D$  (Figure 4.22), where the prisms at both orientations exhibit lesser sensitivity with the change in both  $AR$  and boundary layer, and the distinct three flow regimes are more apparent for the cylinder (with critical  $AR = \sim 2$  and  $\sim 6$ ). Based on the  $St$  data shown in Figure 4.35, it appears there are only two  $St$  flow regimes for the prisms. The first flow regime, although it is not too apparent, shows  $St$  at  $\alpha = 0^\circ$  increases slightly with  $AR$ , while the second flow regime shows that  $St$  is almost independent of  $AR$ . The critical aspect ratio of  $AR = 4$  marks the boundary between two flow regimes. This flow regime is also somewhat similar to that identified from  $C_D$ , but  $C_D$  shows a relatively more sensitive trend with  $AR$ .

Compared to Porteous et al. (2017), the present study could not identify up to four distinct flow regimes. Porteous et al. (2017) suggested that the third flow regime occurred at sufficiently slender aspect ratio of  $AR > 10$ , which is just slightly below the upper limit of

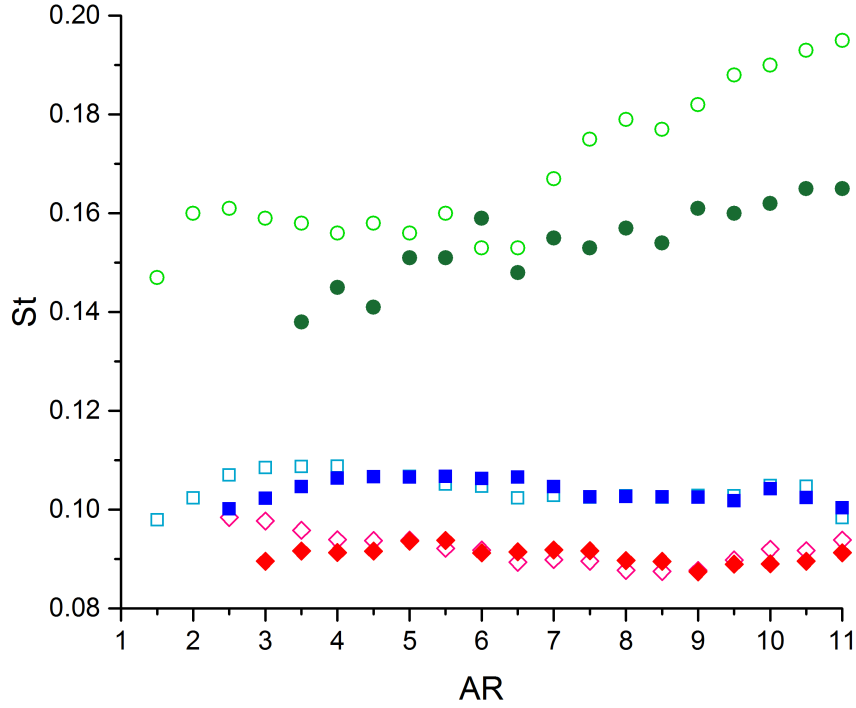


**Figure 4.35:** Comparison of  $St$  between cylinder (Beitel et al. (2019) - green circle), and square prisms at  $\alpha = 0^\circ$  (blue square) and  $\alpha = 45^\circ$  (red diamond) of  $AR = 1$  to  $11$  in two boundary layers conditions:  $\delta/D = 0.8$  (present) and  $0.6$  (Beitel et al. (2019)), and  $\delta/D = 2.2$  (present) and  $1.9$  (Beitel et al. (2019)).  $Re = 6.5 \times 10^4$  for both studies.

AR in the present study. However, from Figure 4.35, at  $\alpha = 0^\circ$ , a slight decrease in  $St$  can still be observed for the aspect ratio range of  $10 \leq AR \leq 11$ , which may mark the beginning of the third flow regime. This decreasing trend in  $St$  is found similar to the  $St$  data obtained by Porteous et al. (2017) for  $8 \leq AR \leq 13$ , as shown in Figure 2.25. For the  $St$  data at  $\alpha = 45^\circ$  (which was not investigated by Porteous et al. (2017)), the two flow regimes are similar to the data of  $\alpha = 0^\circ$ . However, the prisms at  $\alpha = 45^\circ$  exhibit a different trend, where the values of  $St$  for the thin boundary layer decrease with AR in the first flow regime, and increase slightly towards the possible beginning of the third flow regime identified by Porteous et al. (2017). The first flow regime is not evident for the thick boundary layer at  $\alpha = 45^\circ$  because no well-defined peak was identified for the low-aspect-ratio prisms.

The power spectra obtained at mid-height measured by the hotwire are presented in Figure 4.36 as a function of  $\alpha$ , for six selected aspect ratios. Unlike the experimental investigation of Porteous et al. (2017), the present study focuses mainly on the trend of the spectra and

does not specifically quantify the magnitude of the power spectrum density. Therefore, the vertical scale plotted in Figure 4.36 is arbitrary, but with the same scale used for all the sub-figures. As mentioned before, for the least slender prism, no peak can be identified as illustrated in Figures 4.36(a)(i) and 4.36(b)(i). For the thin boundary layer, when  $AR \geq 2.5$ , a well-defined peak can be observed for  $\alpha = 0^\circ$  to  $15^\circ$ , and the peak is relatively broad-banded at  $\alpha = 20^\circ$  to  $30^\circ$ . The behaviour of the peak at  $\alpha = 30^\circ$  to  $45^\circ$  varies with AR. For  $3 \leq AR \leq 7$ , the peaks at these angles can still be identified, although they are slightly broad-banded compared to those at lower  $\alpha$  (Figures 4.36(a)(ii)-(a)(iv)). On the other hand, when  $AR \geq 9$ , the peak at high incidence angles become significantly broad-banded, and this effect is most pronounced at  $\alpha = 45^\circ$  (Figures 4.36(a)(v)-(a)(vi)). This finding is similar to McClean and Sumner (2014) who observed a much more broad-banded peak for the prisms with both high AR and  $\alpha$ . McClean and Sumner (2014) predicted the downwash effect is more dominant at high incidence angle from their PIV result presented in Figure 2.12. The increasing effect of the downwash with increasing AR was also observed by Unnikrishnan et al. (2017). In addition, the present study provides additional data on the free-end  $C_P$  contours which show a significant portion of the attached flow at  $\alpha = 45^\circ$  (from a remarkable higher pressure region between the free-end centre to trailing edge apex), and the possible increasing downwash effect based on the observation of decreasing minimum value of  $C_P$  (with higher suction) with increasing AR. By integrating all these observations from different studies, the broad-banded peaks observed for the prisms with high AR and  $\alpha$  may be explained with the increasing downwash effect. A higher AR increases the magnitude of the downwash, while the proximity of the downward-directed shear layer (separated from the free end) to the mid-span reduces with the attached flow at  $\alpha = 45^\circ$ .

The present study complements the investigation of McClean and Sumner (2014) by providing the power spectra at two different boundary layer conditions. The effect of  $\alpha$  on both cases of the boundary layer is somewhat similar, where a relatively more broad-banded peak is observed at the prisms with higher AR and  $\alpha$ . However, comparing the power spectra of the prisms with high AR and  $\alpha$  for both cases of boundary layer, the thick boundary layer shows a more well-defined peak especially at a higher  $\alpha$  (Figure 4.36(b)(v)-(b)(vi)), in comparison to the thin boundary layer (Figure 4.36(a)(v)-(a)(vi)). Based on this finding, an

inference can be made where the downwash effect reduces with the increasing thickness of the boundary layer due to a higher proportion of the low-momentum incoming flow.

The effect of the boundary layer is also found pronounced for the prisms which lie slightly below the critical aspect ratio of  $AR = 4$ , where the power spectra at all incidence angles become less well-defined for the thick boundary layer (Figure 4.36(b)(ii)). This effect can also be seen in Figure 4.37 that presents the power spectra at the mid-span as a function of the aspect ratio, at four incidence angles. The power spectra for  $AR = 2$  to  $3.5$  for the thin boundary layer have a relatively well-defined peak (Figure 4.37(a)), in comparison to the thick boundary layer (Figure 4.37(b)). The peak shapes for  $AR = 1$  and  $1.5$  are generally not influenced by the boundary layer, as the shedding frequencies of these prisms are extremely weak, regardless of the presence of the boundary layer. For all the power spectra illustrated in Figures 4.36 and 4.37, there is no secondary or tertiary peak observed as identified in the study of Porteous et al. (2017) for the prisms with  $AR \geq 10.6$ , which again suggests the possible absence of the third or fourth flow regime in the present study.

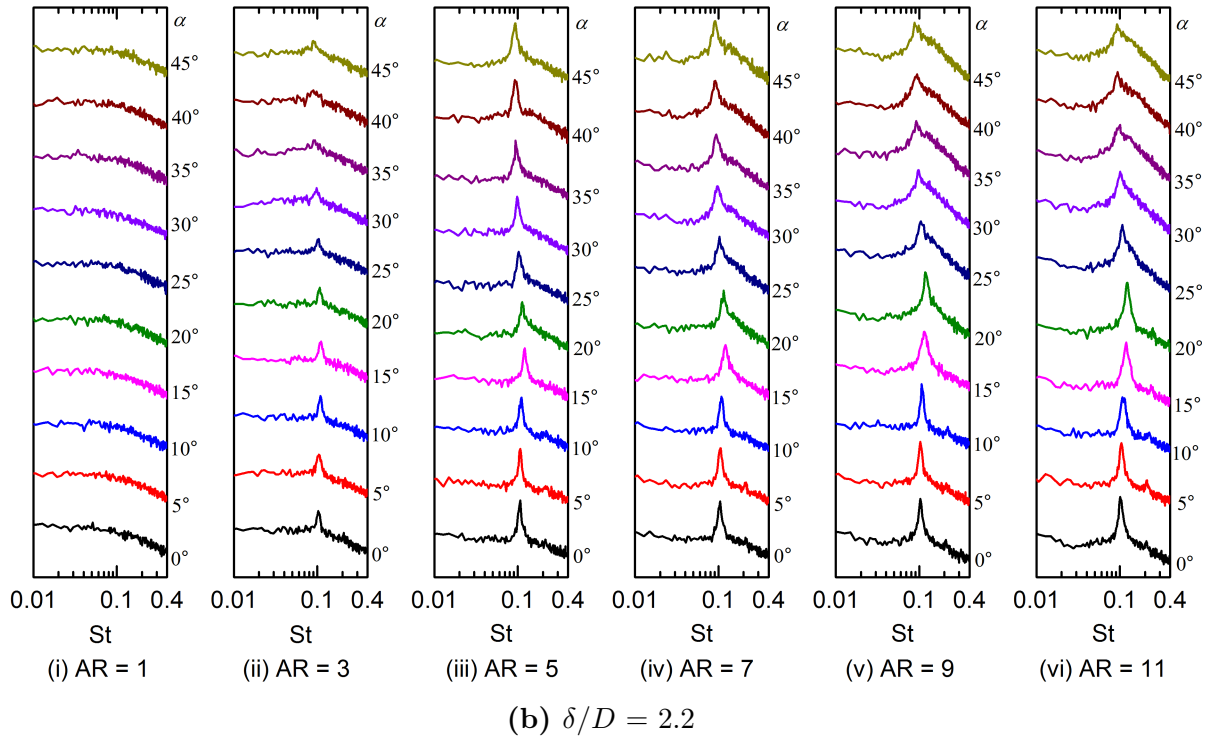
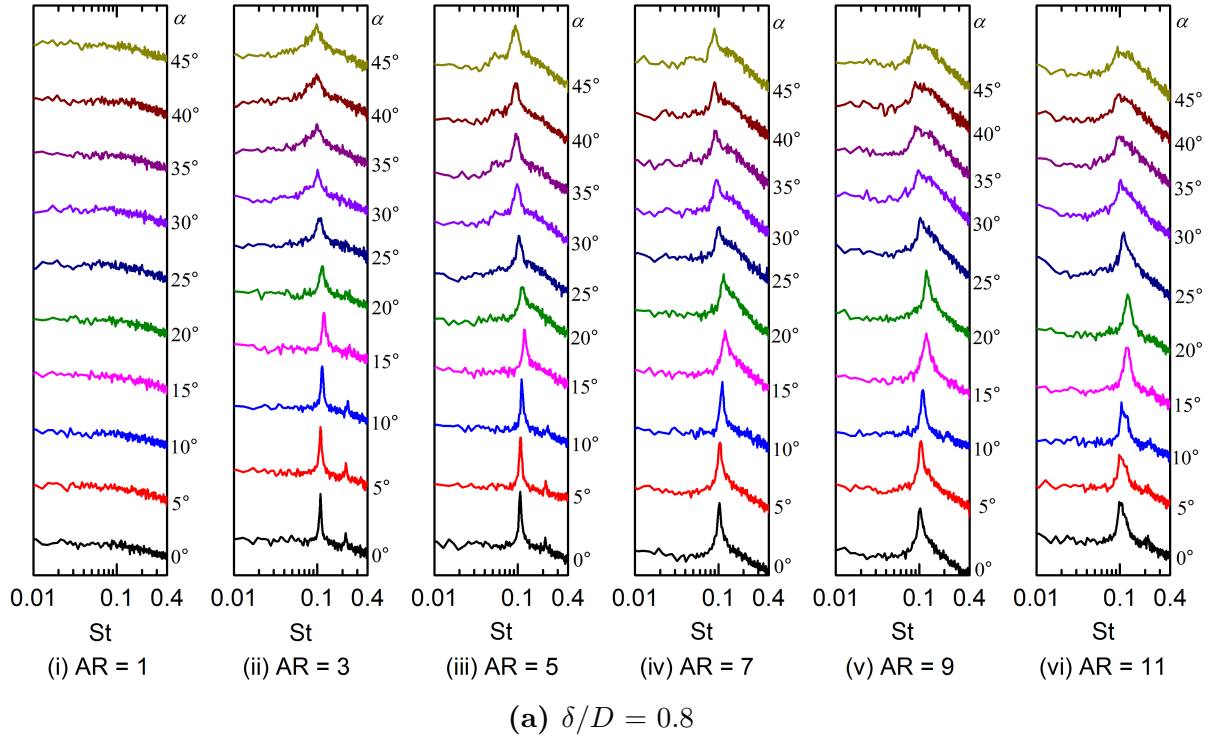


**Figure 4.36:** Power spectra of the velocity fluctuations at the mid-span as a function of incidence angle for selected aspect ratios ( $AR = 1$  to  $11$ , with increment of  $2$ ): (a)  $\delta/D = 0.8$  and (b)  $\delta/D = 2.2$  at  $Re = 6.5 \times 10^4$ .

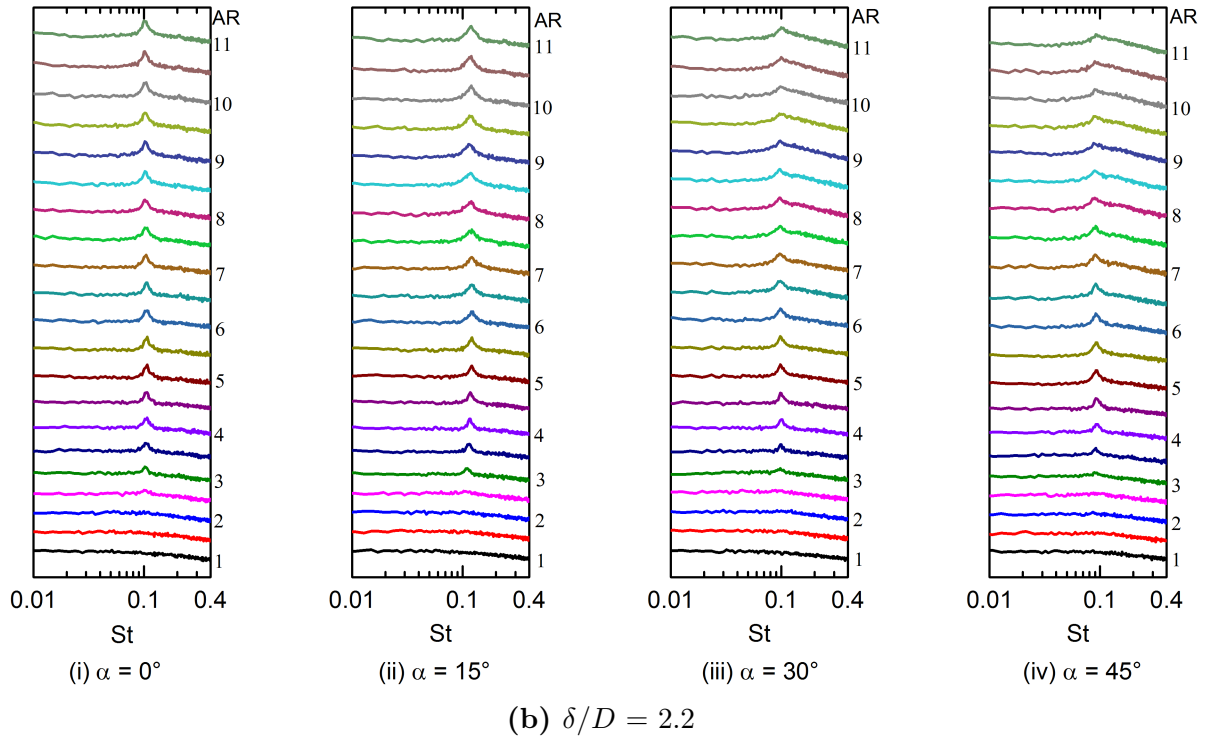
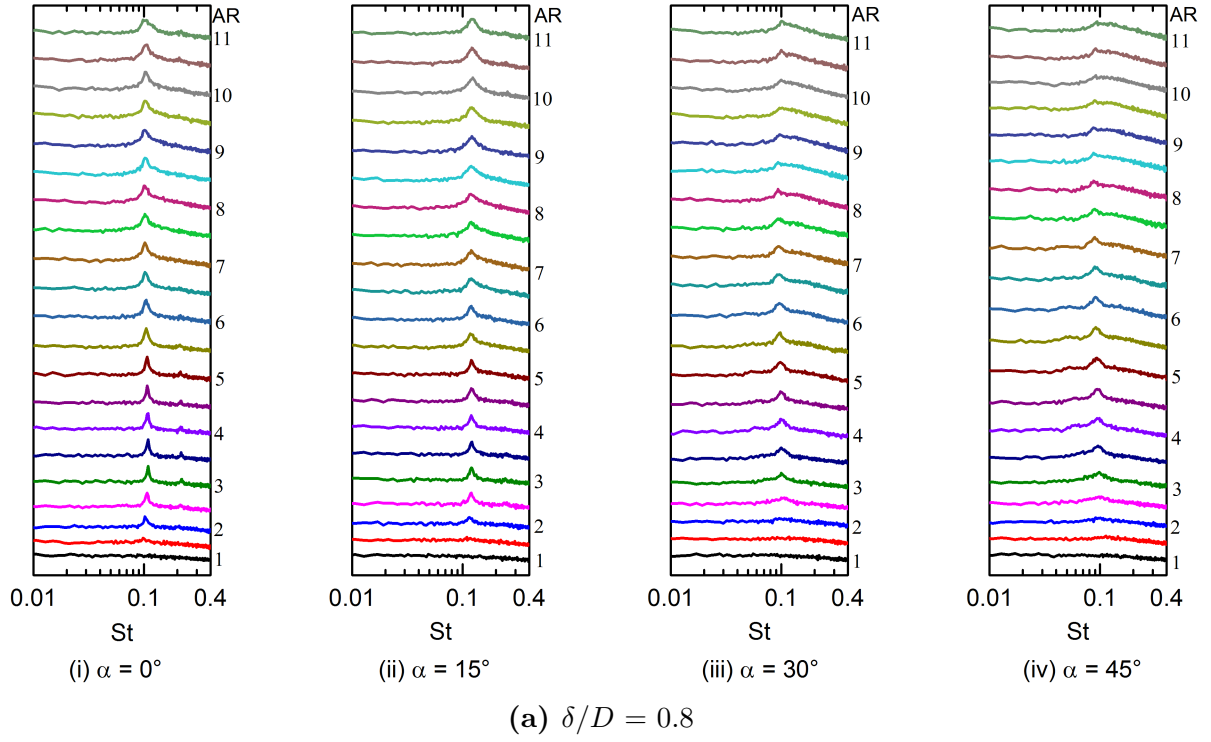


**Figure 4.37:** Power spectra of the velocity fluctuations at the mid-span as a function of aspect ratio for selected incidence angles ( $\alpha = 0^\circ$  to  $45^\circ$ , with increment of  $15^\circ$ ): (a)  $\delta/D = 0.8$  and (b)  $\delta/D = 2.2$  at  $\text{Re} = 6.5 \times 10^4$ .

## 4.5 Vortex formation length

The vortex formation length measured at the mid-span was investigated to further observe the effect of the aspect ratio. Recall that the formation length was obtained at  $Re = 6.5 \times 10^4$  for  $\delta/D = 0.8$  and  $2.6$  (refer to Case 1 and 2 in Section 3.4). The formation length was obtained based on the location of the maximum streamwise Reynolds stress  $\langle u' \rangle^2$  on the wake centerline at  $z = H/2$ , measured by the hotwire. The graph of  $\langle u' \rangle^2$  versus  $x/D$  was plotted and the streamwise location corresponding to the maximum  $\langle u' \rangle^2$  represents the formation length. However, manual inspection on the  $\langle u' \rangle^2$  versus  $x/D$  was performed to filter outliers observed in the data, and ensure the formation length obtained show a reasonable continuity between subsequent aspect ratios. However, this method still introduces a significant measurement uncertainty, especially when the curves of  $\langle u' \rangle^2$  versus  $x/D$  show a broad-banded peak. The measurement uncertainty is calculated by identifying the streamwise location range which corresponds to the range of  $\langle u' \rangle^2_{max} \pm 1$ , where  $\langle u' \rangle^2_{max}$  is the maximum Reynolds stress based on the streamwise velocity fluctuation. This method allows a lower predicted measurement uncertainty in the formation length for a well-defined peak.

Figure 4.38 shows the formation length,  $L_f$ , for the prism at  $\alpha = 0^\circ$  as a function of AR for both boundary layers, and the results are compared with the finite cylinder investigated by Beitel et al. (2019). The measurement uncertainty of the square prism data is generally higher than the cylinder data, due to the wider wake; the wider wake leads to some difficulty in measuring appreciable velocity fluctuation along the centerline downstream, due to the reduced possibility for shear layer interaction along the centerline location. The formation lengths for some prisms could not be measured using the definition of Noca et al. (1998) since there was no clear peak in the curve of  $\langle u' \rangle^2$  versus  $x/D$ .

It can be observed from Figure 4.38 that for a given boundary layer thickness, the formation length of the prism is remarkably longer than that of the cylinder. This observation is different from the investigation of Ozgoren (2006) who showed the formation length of an infinite cylinder to be longer than that of an infinite square prism at  $\alpha = 0^\circ$ . This difference highlights that the flow structures between the infinite and finite bluff bodies are dissimilar,

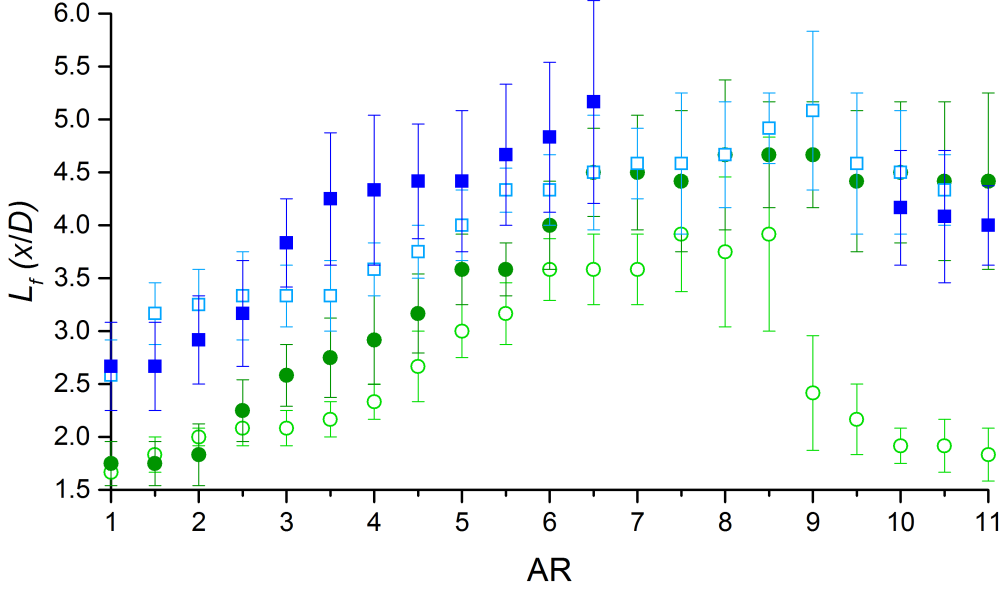


**Figure 4.38:** Comparison of vortex formation length at the mid-span between cylinder (Beitel et al. (2019) - green circle) and square prisms at  $\alpha = 0^\circ$  (blue square) of AR = 1 to 11 in two boundary layers conditions:  $\delta/D = 0.8$  (both studies), and  $\delta/D = 2.6$  (present) and 3.0 (Beitel et al. (2019)).  $Re = 6.5 \times 10^4$  for both studies. Open and solid symbols represent the thin and thick boundary layer, respectively.

and the downwash effect of the finite bodies influences the wake structure significantly. In fact, the studies of Wang and Zhou (2009) and Porteous et al. (2017) showed that  $L_f$  of a finite square prism at the mid-span is significantly longer than that of an infinite prism, where the downwash flow elongates the formation length (Section 2.7). The  $L_f$  data of the cylinder show that the formation length increases steadily with AR until a critical aspect ratio. The behaviour of  $L_f$  after the critical aspect ratio varies with two cases of boundary layer for the cylinder. For the thin boundary layer, the values of  $L_f$  of the cylinder drop significantly after the critical aspect ratio of AR = 7. On the other hand,  $L_f$  of the cylinder for the thick boundary layer does not show appreciable decrease after the critical aspect ratio of AR = 8 - 9. For the square prism, a similar trend can be observed as the cylinder, with a critical aspect ratio of AR = 9 for the thin boundary layer. The critical aspect ratio for the thick boundary layer is undetermined due to the undefined  $L_f$  previously explained. The critical aspect ratio of AR = 9 for the thin boundary layer determined in the present study is higher than the studies of Wang and Zhou (2009) and Porteous et al. (2017) (with both AR

$\simeq 7$ ). This finding suggests that a thicker boundary layer reduces the critical aspect ratio, in view of Wang and Zhou (2009) and Porteous et al. (2017) adopted a larger value of  $\delta/D$  than the thin boundary layer in the present study. Table 4.3 shows the value of the critical AR obtained from different experimental investigations, and the experiment parameters for each studies.

**Table 4.3:** Summary of the critical aspect ratio based on the maximum vortex formation length at the mid-span location for cylinder and square prism at  $\alpha = 0^\circ$ .

<b>Square Prism at <math>\alpha = 0^\circ</math></b>			
<b>Study</b>	<b>Re</b>	<b><math>\delta/D</math></b>	<b>Critical AR</b>
Present	$6.5 \times 10^4$	0.8	9.0
Wang and Zhou (2009)	$9.3 \times 10^3$	1.4	7.0
Porteous et al. (2017)	$1.4 \times 10^4$	1.3	7.1
Sumner et al. (2017)	$4.2 \times 10^4$	1.5	undefined*
Unnikrishnan et al. (2017)	$3.7 \times 10^4$	1.5	undefined*
<b>Cylinder</b>			
<b>Study</b>	<b>Re</b>	<b><math>\delta/D</math></b>	<b>Critical AR</b>
Beitel et al. (2019)	$6.5 \times 10^4$	0.8	7.5
Beitel et al. (2019)	$6.5 \times 10^4$	3.0	8.0 - 9.0
Rostamy (2012)	$4.2 \times 10^4$	1.6	7.0

\*The curve of  $L_f$  as the function of AR does not form a maximum peak.

From both Figure 4.38 and Table 4.3, it can be seen that the effect of the boundary layer varies for the two different shapes studied. The cylinder data show that the thick boundary layer increases  $L_f$  significantly after the critical AR. Conversely, the values of  $L_f$  for the three most slender prisms appear to decrease slightly for the thick boundary layer, after the critical AR (determined from the thin boundary layer). For the thick boundary layer, the rate of decrease in  $L_f$  of the square prism is much smaller than the increase rate of  $L_f$  observed in the cylinder. This trend of the boundary layer effect is somewhat different from the  $C_P$  centerline profiles presented in Figures 4.15 and 4.16 that show the influence of the boundary layer is more pronounced for the square prisms at  $\alpha = 0^\circ$  with high aspect ratio of  $AR \geq 10$ , while the boundary layer has no significant impact on the high-aspect-ratio cylinders ( $AR > 9$ ). Nonetheless, the dynamic effect of the boundary layer for two different shapes remains standing in both  $C_P$  (Table 4.2) and  $L_f$ .

The high critical aspect ratio of the square prism, based on the maximum  $L_f$  observed in the thin boundary layer, may suggest that the aspect ratio of the square prism needs to be

increased beyond  $AR = 11$ , in order to identify a new flow regime. This would be consistent with the  $C_D$  and  $St$  data which do not show any evident third flow regime, which is most likely due to the limited tested range of  $AR$ . In comparison to the cylinder data which show a lower critical aspect ratio, the third flow regime of the cylinder is much more pronounced, as observed in the  $C_D$  and  $St$  data (Figures 4.22 and 4.35).

# 5 CONCLUSIONS, CONTRIBUTIONS, AND RECOMMENDATIONS

This chapter concludes the present experimental investigations in Section 5.1, reiterates the contributions of the present study in Section 5.2, and also provides some recommendations to complement the current research in Section 5.3.

## 5.1 Conclusions

The current research is an experimental investigation of the effect of incidence angle, aspect ratio, and boundary layer thickness on the mean free-end surface pressure distribution for a surface-mounted finite-height square prism. The minimum value of  $C_P$  is generally lower (indicating higher suction) with increasing  $\alpha$  and AR. The complexity of the  $C_P$  contours at  $\alpha = 45^\circ$  is much greater than at  $\alpha = 0^\circ$ . At  $\alpha = 0^\circ$ , there is no pressure variation in the  $C_P$  contours for the intermediate aspect ratios from  $1.5 \leq \text{AR} \leq 10.5$ . Although the  $C_P$  contours at  $\alpha = 45^\circ$  are more complex, the  $C_P$  contours between each subsequent aspect ratio do not vary significantly for the intermediate aspect ratios from  $4.5 \leq \text{AR} \leq 7$ . The sensitivity of the  $C_P$  contours with AR is most pronounced at  $\alpha = 10^\circ$ . The thick boundary layer generally increases the value of  $C_P$  (lower suction). In term of the contour pattern, the effect of the boundary layer is strongest at  $\alpha = 0^\circ$  and  $45^\circ$ . For the thick boundary layer, at  $\alpha = 0^\circ$ , the downstream pressure recovery trend is not observed for the high-aspect-ratio prisms, while the pressure recovery trend is much more significant for the low-aspect-ratio prisms.

Based on the results of the  $C_P$  contours, three distinct flow regimes can be classified for different ranges of the aspect ratio. The first flow regime lies below the critical aspect ratio with  $\delta/H > 1$ , and shows a complicated  $C_P$  contour pattern. The second flow regime represents the intermediate aspect ratios that show an uncomplicated  $C_P$  contour pattern,

or an insensitive behavior of the  $C_P$  contours with the change of the aspect ratio. The aspect ratio range of the second flow regime varies at different incidence angles, with the widest range observed at  $\alpha = 0^\circ$  and narrowest range observed at  $\alpha = 45^\circ$ . The third flow regime is observed for the high-aspect-ratio prisms, where the  $C_P$  contours are more complex than the second flow regime, and in some cases more complex than the first flow regime.

Based on the results of aerodynamic forces and Strouhal number, seven different critical angles can be identified. For a given AR and boundary layer, the critical angles based on the minimum  $C_D$ , maximum magnitude of  $C_L$ , and maximum St do not vary significantly. These critical angles generally increase with AR, and decrease for the thick boundary layer. These critical angles correspond to flow reattachment on the prism's bottom surface (McClellan and Sumner (2014)), highest wake asymmetry, maximum downwash, and minimum formation length (Unnikrishnan et al. (2017)). The critical angle based on the primary peak of the  $C_{N,p}$  data, on the other hand, generally decreases with AR and increases for the thick boundary layer. The critical angles based on the secondary peak of the  $C_{N,p}$  data are similar to the critical angles obtained based on the plateau formation observed in the  $C_D$  data. These critical angles can only be observed for the high-aspect-ratio prisms, and are insensitive to aspect ratio and boundary layer thickness. The critical angles at the plateau formation region in the  $C_D$  data also correspond to the sudden change in the complexity of the  $C_P$  contours observed at  $\alpha = 10^\circ$ . The critical angle based on the positive lift, on the other hand, is only observed for the low-aspect-ratio prisms. This critical angle is significantly higher than other critical angles, but the value significantly reduces for the thick boundary layer.

There are also various critical aspect ratios can be determined based on the results of the aerodynamic forces and Strouhal number. The  $C_D$  data show the critical aspect ratios of AR  $\simeq 4$  for both boundary layer thicknesses, where the values of  $C_D$  below these critical aspect ratios at  $\alpha = 0^\circ$  and  $45^\circ$  exhibit a high sensitivity to the change of the aspect ratio. The  $C_L$  data, at various  $\alpha$  in general, show similar trends with critical aspect ratios of AR = 3.5 and 4.5, for the thin and thick boundary layers, respectively. Based on the St data, a critical aspect ratio of AR  $\simeq 4$  is also identified for both boundary layers, where the data above this critical aspect ratio demonstrate a more well-defined peak at the critical angle. The critical aspect ratio based on the data of  $C_N$  at  $\alpha = 0^\circ$  is AR  $\simeq 3$  for both boundary layers, where

the data above this critical value are generally insensitive to the change of the aspect ratio. For the  $C_N$  data at  $\alpha = 45^\circ$ , the critical aspect ratios are observed to be  $AR = 4$  and  $4.5$  for the thin and thick boundary layers, respectively, where the value of  $C_N$  exceeds  $C_{N,p}$  for the prisms above these critical aspect ratios. These considerably lower critical values observed are similar to each other, and are most likely due to the dominant effect of the boundary layer, where  $\delta/H > 1$ . In the present study, some critical aspect ratios with higher values are also identified. Based on the plateau formation observed in the  $C_D$  data, the critical aspect ratios are observed to be  $AR = 8$  and  $AR = 9$ , for the thin and thick boundary layers, respectively; the critical aspect ratio based on the primary peak formation from the  $C_{N,p}$  data are  $AR = 6$  and  $AR = 4$ , for the thin and thick boundary layers, respectively; the critical aspect ratio based on the secondary peak formation from the  $C_{N,p}$  data are  $AR = 7.5$  and  $AR = 8.5$ , for the thin and thick boundary layers, respectively. It should be noted that these higher critical aspect ratios are mainly based on the peak formation, and therefore is only observed at certain critical angles. The effect of boundary layer is generally to increase the values of the critical aspect ratio slightly, except for the critical aspect ratio based on the primary peak in the  $C_{N,p}$  data.

The aerodynamic forces and Strouhal number of three bluff-body shapes as follows were compared: cylinder (Beitel et al. (2019)), square prism at  $\alpha = 0^\circ$ , and square prism at  $\alpha = 45^\circ$ . With the same aspect ratio range of  $AR = 1$  to  $11$ , it was found that the square prism exhibits significantly higher insensitivity with the aspect ratio compared to the cylinder. The force coefficients and Strouhal number data of the square prisms only show two flow regimes (instead of three regimes as based on the  $C_P$  distribution). The first flow regime shows the appreciable increasing trend (but decreasing trend for  $St$  at  $\alpha = 45^\circ$ ) on the data with the aspect ratio due to the reducing dominant effect of the boundary layer (reducing  $\delta/H$  with  $AR$ ), and the second flow regime shows the insensitive behaviour of the data with  $AR$ . The present study proposed a critical aspect ratio of  $AR \simeq 4$  that marks the beginning of the second flow regime based on the forces and Strouhal data previously summarized. On the other hand, the cylinder data show three distinct flow regimes. The first two regimes of the cylinder are similar as the square prism, while the third flow regime of the cylinder demonstrates a more discernible increasing trend on the data with  $AR$ , as compared to the

second flow regime. The critical aspect ratios based on the study Beitel et al. (2019) are generally close to  $AR = 2$  and  $AR = 6$ , which mark the beginning of the second and third flow regimes. Table 5.1 provides the comparison for different critical aspect ratios in the present study and the study of Beitel et al. (2019). From all these observations, it is most likely that the critical aspect ratio of the square prism, which marks the beginning of the third flow regime, is considerably higher than the cylinder. This inference can be supported by the study of Porteous et al. (2017), which suggests the aspect ratio range of  $10 \leq AR \leq 18$  for the third flow regime of square prism. Moreover, the critical aspect ratio, based on the data of the vortex formation length, for the square prism ( $AR = 9$ ) is also found higher than that of the cylinder ( $AR = 7.5$ ). In addition, the critical aspect ratio that symbolizes the commencement of the second flow regime for the square prism are also higher ( $AR \simeq 4$ ), in comparison to the cylinder ( $AR \simeq 2$ ).

**Table 5.1:** Summary of critical aspect ratios based on different observations in the present study and the study of Beitel et al. (2019).

<b>Critical AR between the first and second flow regime</b>		
Shape	Critical AR*	Observations after the critical AR
Prism at various $\alpha$	3.5 - 4.5	Less sensitivity on $C_D$ , $C_L$ , and $\alpha_c$
Prism at various $\alpha$	$\simeq 4.0$	Sharper peak for St versus $\alpha$ curve; less sensitivity on St
Prism at $0^\circ$	3.0	Less sensitivity on $C_N$
Prism at $45^\circ$	4.0 - 4.5	Higher $C_N$ values compared to $C_{N,p}$
Cylinder	2.0	Less sensitivity on $C_D$ and $C_N$
<b>Critical AR between the second and third flow regime</b>		
Shape	Critical AR*	Observations after the critical AR
Prism at $0^\circ$ and $45^\circ$	not observed	Not applicable
Cylinder	5.0	$C_D$ data again show appreciable increasing trend with AR
Cylinder	6.0	St data show appreciable increasing trend with AR
Cylinder	7.0	Lower $C_N$ values compared to $C_{N,p}$
<b>Critical AR based on the formation length</b>		
Shape	Critical AR*	Observations after the critical AR
Prism at $0^\circ$	9.0	Formation length begins to decrease (thin boundary layer)
Cylinder	7.5	Formation length begins to decrease (thin boundary layer)
<b>Critical AR based on the plateau formation</b>		
Shape	Critical AR*	Observations after the critical AR
Prism at $10^\circ$ to $15^\circ$	4.0 - 6.0	Formation of primary peak in the $C_{N,p}$ data
Prism at $\sim 17^\circ$	7.5 - 8.5	Formation of secondary peak in the $C_{N,p}$ data
Prism at $\sim 10^\circ$	8.0 - 9.0	Plateau formation in the $C_D$ data

\* The critical values are presented in a range to represent the values for both boundary layers.

Comparing the boundary layer effect on the force coefficients and Strouhal number between the cylinder and square prism, it is observed that the boundary layer has much stronger influence on the cylinder in reducing the forces and vortex shedding frequency, especially on the first and the third flow regimes. The boundary layer effect on the square prism is only appreciable in the first flow regime.

## 5.2 Contributions of the present work

The present study fills the identified gaps in the literature written in Section 2.8 as follows:

- The present study provides both full  $C_P$  contours and centerline  $C_P$  profiles and complements the experimental investigations of Castro and Robins (1977), Lim and Ohba (2015), and Lee et al. (2016) that provided the centerline  $C_P$  profiles only. The results in Sections 4.1 and 4.2 show that the centerline profile may not be used solely to generalize the free-end pressure distribution behaviour, especially at higher incidence angles of  $\alpha = 30^\circ$  and  $45^\circ$ .
- The aspect ratio and incidence angle ranges used in the present study are considerably wide, with a sufficiently small increment, compared to previous investigations which studied the free-end pressure distribution. While most of the previous studies adopted the aspect ratio of  $AR \leq 2$ , the wide range of the aspect ratio in the present study allows the identification of the three flow regimes based on the  $C_P$  distribution which shows different pressure variation and the sensitivity of the  $C_P$  contours with  $AR$ , at various  $\alpha$ . This classification has not been reported extensively in the literature.
- Previous studies of Castro and Robins (1977) and Sitheeq et al. (1997) about the effect of the boundary layer on the pressure distribution are also complemented by the present study. The present study adopted two boundary layers which lie between the extremes of  $\delta/D \simeq 0$  and  $\delta/D \gg 1$ , and able to identify the effect of the boundary layer in varying the value of  $C_P$  and the complexity of the contour patterns, for a wide range of aspect ratio.

- The present study provides additional data about the aerodynamic forces and Strouhal number that complement the studies of Sakamoto (1985) and McClean and Sumner (2014). There are up to seven critical incidence angles determined in the present study. Sakamoto (1985) and McClean and Sumner (2014) only shows three critical angles based on the minimum  $C_D$ , maximum magnitude of  $C_L$ , and maximum  $St$ , while the present study provides four additional critical angles based on the criteria as follows: the plateau formation in the  $C_D$  data, the positive lift in the  $C_L$  data, and the primary and secondary peaks in the  $C_{N,p}$  data. The former two incidence angles were also briefly reported by McClean and Sumner (2014) and Sakamoto (1985), respectively; however, the present study illustrates a relatively more extensive result which includes the effect of the aspect ratio and boundary layer.
- The critical incidence angle based on the plateau formation in the  $C_D$  data for the high-aspect-ratio prism at around  $\alpha = 10^\circ$  is found related to the  $C_P$  contours observed at the same incidence angle, where the contours become more complex with increasing AR. The present study relates this critical angle with the free-end pressure distribution, which is a contribution not commonly observed in the literature yet.
- The  $C_N$  data and point of action of  $C_{N,p}$  have not been extensively reported in the literature. The present study compares  $C_N$  and  $C_{N,p}$  at  $\alpha = 0^\circ$  and  $45^\circ$ , for a wide range of the aspect ratio.
- The experimental investigations of Wang and Zhou (2009) and Porteous et al. (2017) about the vortex formation length are complemented by the present study which includes a relatively wider range of, and smaller increment in, aspect ratio. The present study also provides additional details about the effect of the boundary layer on  $L_f$ .
- The results of the force coefficients and Strouhal number of the square prisms at  $\alpha = 0^\circ$  and  $45^\circ$  are also compared with the cylinder data of Beitel (2017) and Beitel et al. (2019). Two flow regimes are classified for the square prisms based on these results, and the present study proposes a high value of the critical aspect ratio, compared to the cylinder, in order to observe the third flow regimes.

### 5.3 Recommendations for future work

To enhance the physical explanations for some fascinating observations in the present study, the following recommendations are proposed:

- As the present study proposes a higher critical aspect ratio that marks the beginning of the third flow regime for the square prisms as compared to the cylinder, it is highly recommended that the experiments of the force coefficients and Strouhal number be extended to higher aspect ratios,  $AR > 11$ .
- The higher critical aspect ratio of the square prism compared to the cylinder is also worth discovering by integrating more studies with the flow visualization between these shapes. It is suspected that the sharp edges of the square prism resulted in a relatively insensitive flow structure with AR due to the reduced possibility of the reattachment. This argument can be at least supported by the studies of Rostamy et al. (2012) and Sumner et al. (2017) that illustrate a reattachment point on the free end for the cylinder, but no reattachment point observed at the free end for the square prism at  $\alpha = 0^\circ$ . More studies which integrate the flow visualization between these two shapes are required to make the statement above more conclusive.
- At  $\alpha = 0^\circ$ , many interesting observations can be made from the present study for the high-aspect-ratio prism ( $AR \geq 10.5$ ), such as the reappearance of the substantial pressure recovery trend along downstream, the increasing effect of the boundary layer, the lower centerline  $C_P$  values (with higher suction) as compared to the cylinder, and slight decrease in the St data. It is suspected in the present study that the flow structure above the free end, which includes the separated shear layer and vortex center, undergoes a significant change. Therefore, additional PIV measurements on the flow structure above the free end for prisms with  $AR \geq 11$  are recommended.
- More PIV measurements are required to explain the flow structure for the square prism at  $\alpha = 45^\circ$ . The present study observes some interesting features for this prism such as a smaller aspect ratio range for the second flow regime based on the pressure distribution,

the significant increase in the complexity of the contours for the thick boundary layer, the higher values in  $C_N$  than  $C_{N,p}$  above the critical AR (different trend than the cylinder), and a more discernible peak in the power spectra for the high-aspect-ratio prisms in the thick boundary layer.

- For the intermediate angles, although the present study relates the  $C_P$  contours at  $\alpha = 10^\circ$  with the plateau formation observed in the  $C_D$  data for the high-aspect-ratio prisms, additional flow visualization investigation by using PIV at this angle is recommended to explain further the flow structure. Some smoke flow visualization was performed by Okuda and Taniike (1993) for a single aspect ratio of  $AR = 4$  at  $\alpha = 10^\circ$  to  $15^\circ$ , where standing conical vortex on the side, and a pair of conical vortices on the top were observed (subsection 2.4.1). Similar studies for square prisms at higher aspect ratio at  $\alpha = 10^\circ$  are required to observe any behavioural changes in the standing conical vortex and the conical vortices on the top, and perhaps these behavioural changes could be related to the plateau formation in the  $C_D$  and complicated  $C_P$  contour patterns around  $\alpha = 10^\circ$  observed in the present study.
- The positive lift observed for the low-aspect-ratio prism has not been extensively investigated in the literature. PIV measurements for prisms with  $AR = 1$  and  $1.5$  are recommended to explain the positive lift after the identified critical incidence angle in the present study, and perhaps to provide the reason why such positive lift only exists for the low-aspect-ratio prisms at high incidence angles.

## REFERENCES

- Adaramola, M. S. (2008). *The Wake of an Exhaust Stack in a Crossflow*. PhD thesis, Mechanical Engineering, University of Saskatchewan, Saskatoon, SK, Canada.
- Akins, R. E. and Paterka, J. A. (1977). Mean force and moment coefficients for buildings in turbulent boundary layers. *Journal of Wind Engineering and Industrial Aerodynamics*, 2(3):195–209.
- Bai, H. and Alam, M. M. (2018). Dependence of square cylinder wake on Reynolds number. *Physics of Fluids*, 30(1):015102.
- Baines, W. (1963). Effects of velocity distributions on wind loads and flow patterns on buildings. In *International Conference on Wind Effects on Building and Structures*, June 26-28, 1963, Teddington, UK, pp. 197-225.
- Banks, D., Meroney, R. N., Sarkar, P. P., Zhao, Z., and Wu, F. (2000). Flow visualization of conical vortices on flat roofs with simultaneous surface pressure measurement. *Journal of Wind Engineering and Industrial Aerodynamics*, 84(1):65–85.
- Behera, S. and Saha, A. K. (2019). Characteristics of the flow past a wall-mounted finite-length square cylinder at low Reynolds number with varying boundary layer thickness. *Journal of Fluids Engineering*, 141(6):061204–061204–17.
- Beitel, A. (2017). *The Effect of Aspect Ratio on the Aerodynamic Forces and Free End Pressure Distribution for a Surface-Mounted Finite Height Cylinder*. Master’s thesis, Mechanical Engineering, University of Saskatchewan, Saskatoon, SK, Canada.
- Beitel, A., Heng, H., and Sumner, D. (2019). The effect of aspect ratio on the aerodynamic forces and bending moment for a surface-mounted finite-height cylinder. *Journal of Wind Engineering and Industrial Aerodynamics*, 186:204–213.
- Bourgeois, J. A., Sattari, P., and Martinuzzi, R. J. (2011). Alternating half-loop shedding in the turbulent wake of a finite surface-mounted square cylinder with a thin boundary layer. *Physics of Fluids*, 23(9):095101.
- Cao, Y., Tamura, T., and Kawai, H. (2019). Investigation of wall pressures and surface flow patterns on a wall-mounted square cylinder using very high-resolution Cartesian mesh. *Journal of Wind Engineering and Industrial Aerodynamics*, 188:1–18.
- Castro, I. P. and Robins, A. G. (1977). The flow around a surface-mounted cube in uniform and turbulent streams. *Journal of Fluid Mechanics*, 79(2):307–335.

- Chakravarty, R. (2018). *Turbulent Flow Visualization over Surface-Mounted Finite-Height Cylinders and Square Prisms*. PhD thesis, Mechanical Engineering, University of Saskatchewan, Saskatoon, SK, Canada.
- Chen, B., Shang, L., Qin, M., Chen, X., and Yang, Q. (2018). Wind interference effects of high-rise building on low-rise building with flat roof. *Journal of Wind Engineering and Industrial Aerodynamics*, 183:88–113.
- Chue, S. H. (1975). Pressure probes for fluid mechanics. *Progress in Aerospace Sciences*, 16(2):147–223.
- Dutta, S., Muralidhar, K., and Panigrahi, P. K. (2003). Influence of the orientation of a square cylinder on the wake properties. *Experiments in Fluids*, 34(1):16–23.
- Einian, M. (2012). *Large Eddy Simulation of Flow Around a Finite Square Cylinder*. PhD thesis, Mechanical Engineering, University of Saskatchewan, Saskatoon, SK, Canada.
- Heseltine, J. L. (2003). *Flow Around a Circular Cylinder with a Free End*. Master’s thesis, Mechanical Engineering, University of Saskatchewan, Saskatoon, SK, Canada.
- Huang, R. F., Lin, B. H., and Yen, S. C. (2010). Time-averaged topological flow patterns and their influence on vortex shedding of a square cylinder in crossflow at incidence. *Journal of Fluids and Structures*, 26(3):406–429.
- Igarashi, T. (1984). Characteristics of the flow around a square prism. *Bulletin of JSME*, 27(231):1858–1865.
- Igbalajobi, A. (2011). *The Effect of a Splitter Plate on the Flow Around a Surface-Mounted Finite-Height Circular Cylinder*. Master’s thesis, Mechanical Engineering, University of Saskatchewan, Saskatoon, SK, Canada.
- Kindree, M. G., Shahroodi, M., and Martinuzzi, R. J. (2018). Low-frequency dynamics in the turbulent wake of cantilevered square and circular cylinders protruding a thin laminar boundary layer. *Experiments in Fluids*, 59:186.
- Lee, Y. T., Boo, S., Lim, H. C., and Misutani, K. (2016). Pressure distribution on rectangular buildings with changes in aspect ratio and wind direction. *Wind and Structures*, 23(5):465–483.
- Lim, H. C. and Ohba, M. (2015). Detached eddy simulation of flow around rectangular bodies with different aspect ratios. *Wind and Structures*, 20(1):37–58.
- Lim, H. C., Thomas, T. G., and Castro, I. P. (2009). Flow around a cube in a turbulent boundary layer: LES and experiment. *Journal of Wind Engineering and Industrial Aerodynamics*, 97(2):96–109.
- Lim, H. C., Tsukamoto, K., Ohba, M., and Mizutani, K. (2014). Study on the surface pressure distribution of cubes in cross-wind arrays. *Journal of Wind Engineering and Industrial Aerodynamics*, 133:18–26.

- McClean, J. F. and Sumner, D. (2014). An experimental investigation of aspect ratio and incidence angle effects for the flow around surface-mounted finite-height square prisms. *Journal of Fluids Engineering*, 136(8):081206–081206–10.
- Nakamura, H., Igarashi, T., and Tsutsui, T. (2001). Local heat transfer around a wall-mounted cube in the turbulent boundary layer. *International Journal of Heat and Mass Transfer*, 44(18):3385–3395.
- Nakamura, H., Igarashi, T., and Tsutsui, T. (2003). Local heat transfer around a wall-mounted cube at 45 deg to flow in a turbulent boundary layer. *International Journal of Heat and Fluid Flow*, 24(6):807–815.
- Noca, F., Park, H. G., and Gharib, M. (1998). Vortex formation length of a circular cylinder ( $300 < Re < 4,000$ ) using DPIV. In *ASME Fluids Engineering Division Summer Meeting*, June 21-25, 1998, Washington, DC, FEDSM98-5149.
- Ogunremi, A. R. (2014). *The Effect of a Wake-Mounted Splitter Plate on the Flow Around a Surface-Mounted Finite-Height Square Prism*. Master’s thesis, Mechanical Engineering, University of Saskatchewan, Saskatoon, SK, Canada.
- Okuda, Y. and Taniike, Y. (1993). Conical vortices over side face of a three-dimensional square prism. *Journal of Wind Engineering and Industrial Aerodynamics*, 50:163–172.
- Ozgoren, M. (2006). Flow structure in the downstream of square and circular cylinders. *Flow Measurement and Instrumentation*, 17(4):225–235.
- Porteous, R., Moreau, D. J., and Doolan, C. J. (2017). The aeroacoustics of finite wall-mounted square cylinders. *Journal of Fluid Mechanics*, 832:287–328.
- Rastan, M. R., Sohankar, A., and Alam, M. M. (2017). Low-Reynolds-number flow around a wall-mounted square cylinder: Flow structures and onset of vortex shedding. *Physics of Fluids*, 29(10):103601.
- Reitenbach, H. (2018). *Two Staggered Surface-Mounted Finite-Height Cylinders in a Cross-Flow*. Master’s thesis, Mechanical Engineering, University of Saskatchewan, Saskatoon, SK, Canada.
- Rostamy, N. (2012). *Fundamental Studies of the Wake Structure for Surface-mounted Finite-height Cylinders and Prisms*. PhD thesis, Mechanical Engineering, University of Saskatchewan, Saskatoon, SK, Canada.
- Rostamy, N., Sumner, D., Bergstrom, D., and Bugg, J. (2012). Local flow field of a surface-mounted finite circular cylinder. *Journal of Fluids and Structures*, 34:105–122.
- Saha, A. K. (2013). Unsteady flow past a finite square cylinder mounted on a wall at low Reynolds number. *Computers and Fluids*, 88:599–615.
- Sakamoto, H. (1985). Aerodynamic forces acting on a rectangular prism placed vertically in a turbulent boundary layer. *Journal of Wind Engineering and Industrial Aerodynamics*, 18(2):131–151.

- Sakamoto, H. and Oiwake, S. (1984). Fluctuating forces on a rectangular prism and a circular cylinder placed vertically in a turbulent boundary layer. *Journal of Fluids Engineering*, 106(2):160–166.
- Sarode, R. S., Gai, S. L., and Ramesh, C. K. (1981). Flow around circular- and square-section models of finite height in a turbulent shear flow. *Journal of Wind Engineering and Industrial Aerodynamics*, 8(3):223–230.
- Sattari, P., Bourgeois, J. A., and Martinuzzi, R. J. (2012). On the vortex dynamics in the wake of a finite surface-mounted square cylinder. *Experiments in Fluids*, 52(5):1149–1167.
- Sitheeq, M. M., Iyengar, A. K., and Farell, C. (1997). Effect of turbulence and its scales on the pressure field on the surface of a three-dimensional square prism. *Journal of Wind Engineering and Industrial Aerodynamics*, 69-71:461–471.
- Sohankar, A., Esfeh, M., Pourjafari, H., Alam, M. M., and Wang, L. (2018). Features of the flow over a finite length square prism on a wall at various incidence angles. *Wind and Structures*, 26(5):317–329.
- Sumner, D., Rostamy, N., Bergstrom, D. J., and Bugg, J. D. (2015). Influence of aspect ratio on the flow above the free end of a surface-mounted finite cylinder. *International Journal of Heat and Fluid Flow*, 56:290–304.
- Sumner, D., Rostamy, N., Bergstrom, D. J., and Bugg, J. D. (2017). Influence of aspect ratio on the mean flow field of a surface-mounted finite-height square prism. *International Journal of Heat and Fluid Flow*, 65:1–20.
- Unnikrishnan, S. (2016). *An Experimental Investigation of Aspect Ratio and Incidence Angle Effects on the Mean Wake of a Surface-Mounted Finite-Height Square Prism*. Master’s thesis, Mechanical Engineering, University of Saskatchewan, Saskatoon, SK, Canada.
- Unnikrishnan, S., Ogunremi, A., and Sumner, D. (2017). The effect of incidence angle on the mean wake of surface-mounted finite-height square prisms. *International Journal of Heat and Fluid Flow*, 66:137–156.
- Wang, H., Zhao, X., He, X., and Zhou, Y. (2017). Effects of oncoming flow conditions on the aerodynamic forces on a cantilevered square cylinder. *Journal of Fluids and Structures*, 75:140–157.
- Wang, H. F. and Zhou, Y. (2009). The finite-length square cylinder near wake. *Journal of Fluid Mechanics*, 638:453–490.
- White, F. M. (2011). *Fluid Mechanics*. McGraw-Hill, New York, 7th edition.
- Yen, S. C. and Yang, C. W. (2011). Flow patterns and vortex shedding behavior behind a square cylinder. *Journal of Wind Engineering and Industrial Aerodynamics*, 99(8):868–878.
- Zhang, D., Cheng, L., An, H., and Zhao, M. (2017). Direct numerical simulation of flow around a surface-mounted finite square cylinder at low Reynolds numbers. *Physics of Fluids*, 29(4):045101.

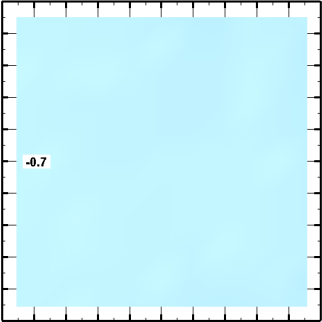
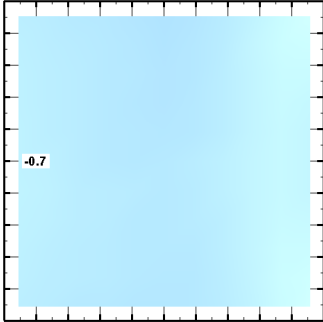
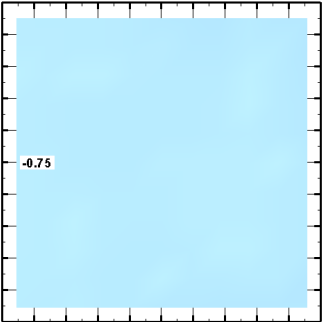
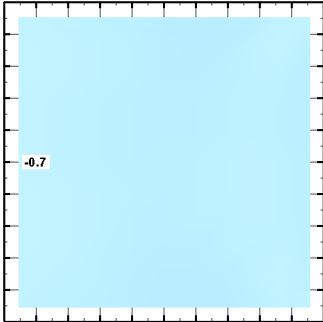
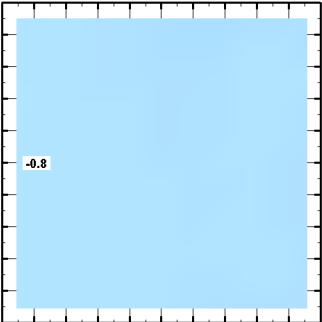
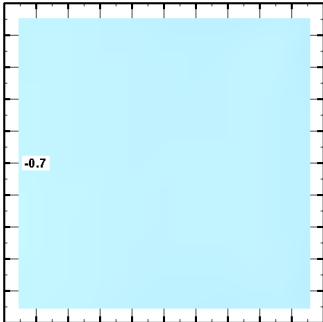
# APPENDIX A

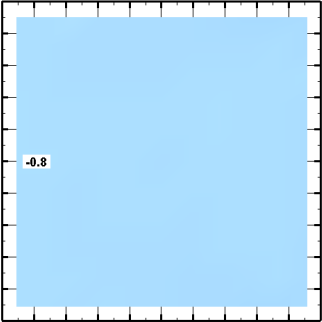
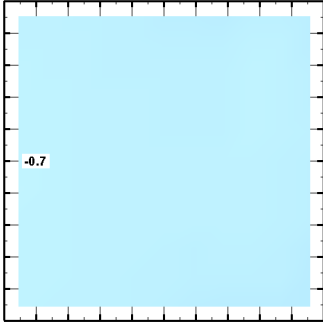
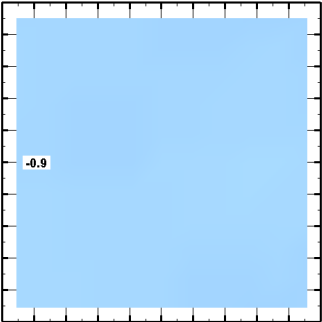
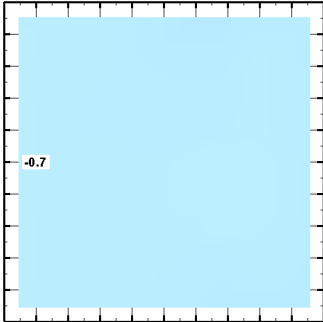
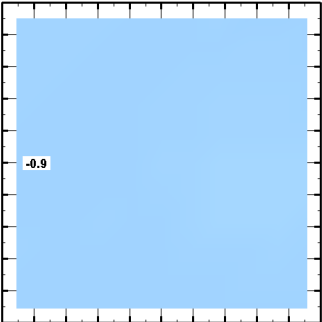
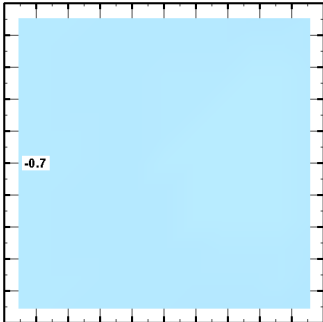
## MEAN FREE-END $C_P$ DISTRIBUTION

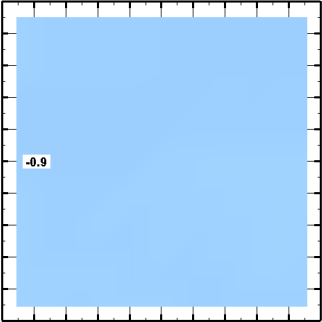
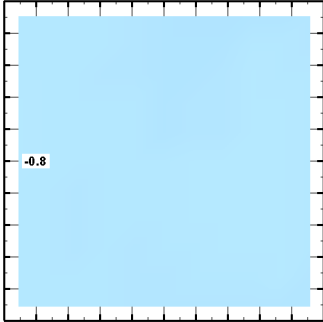
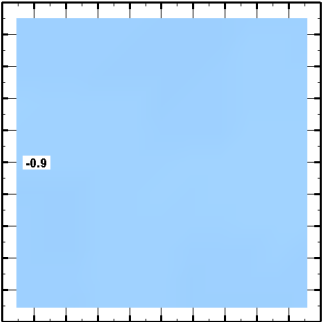
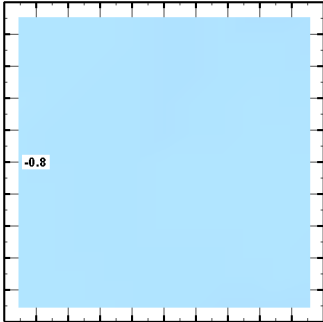
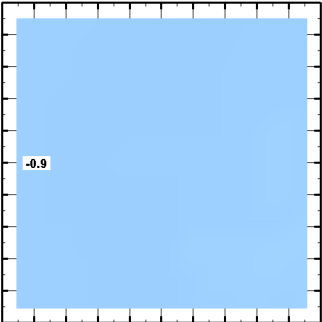
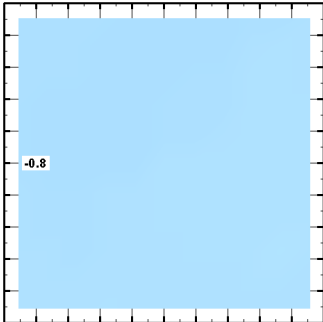
This appendix contains the mean free-end pressure distribution for five selected incidence angles of  $\alpha = 0^\circ, 10^\circ, 15^\circ, 30^\circ$ , and  $45^\circ$ . The contours are colored with the value of  $C_P$ , with the higher intensity represents the lower  $C_P$  value (indicating higher suction). All the tested aspect ratios from  $AR = 1$  to  $11$  at the five selected incidence angles are presented for both boundary layers. The results of the thin and thick boundary layers are shown in the left and right, respectively.

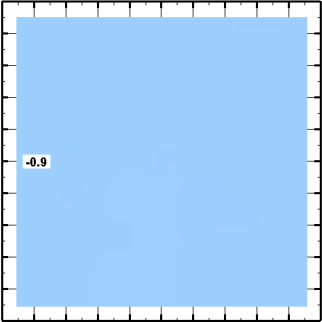
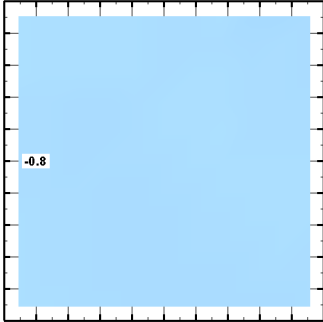
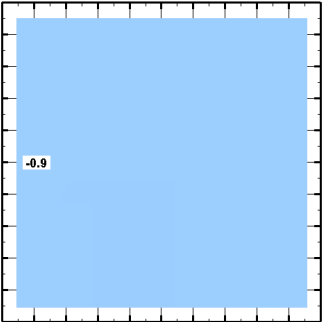
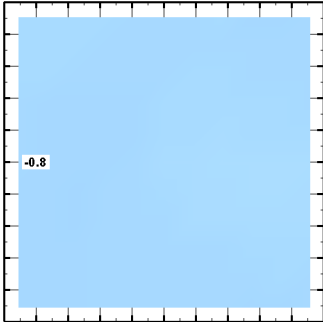
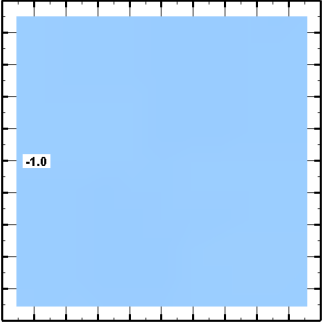
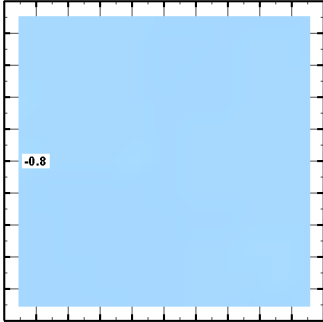
**Table A.1:** Free-end mean pressure distribution (contour lines of constant  $C_P$ ) at  $\alpha = 0^\circ$  for  $AR = 1$  to  $11$ . The flow is from left to right. See page 173 for the scale.

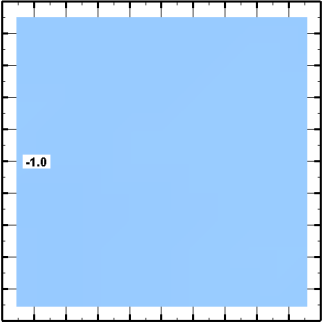
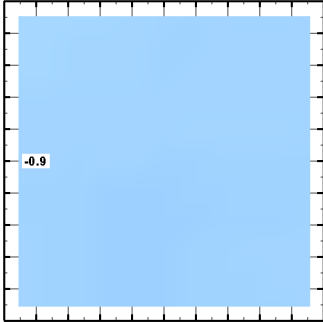
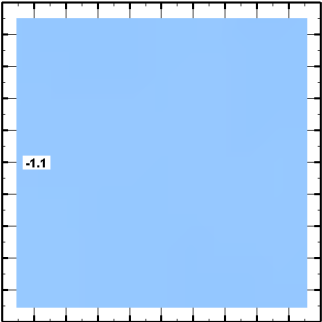
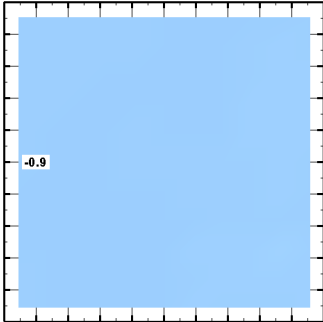
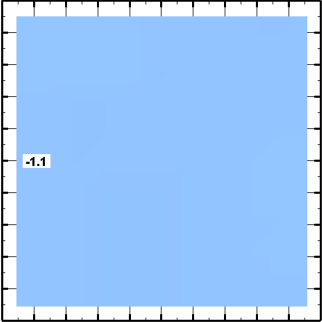
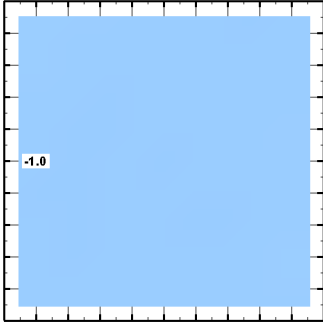
AR	$\delta/D = 0.8$	$\delta/D = 2.6$
1.0		
1.5		

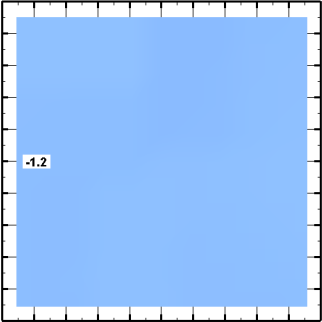
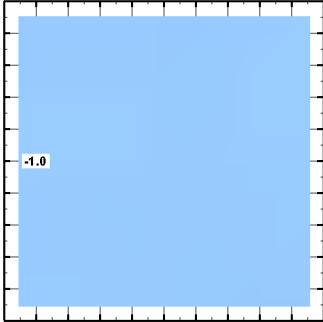
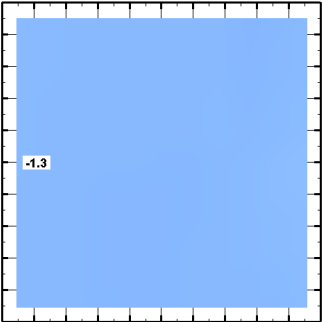
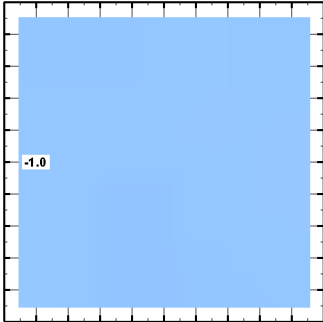
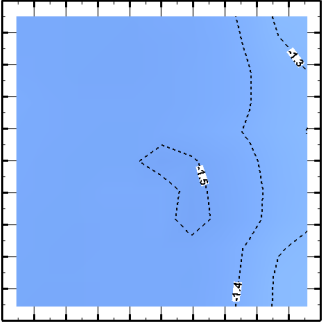
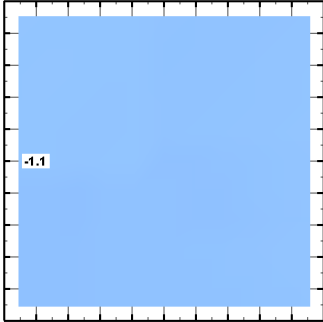
2.0		
2.5		
3.0		

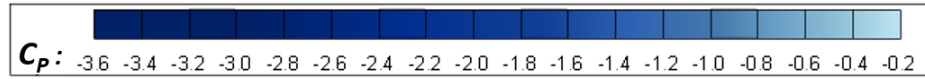
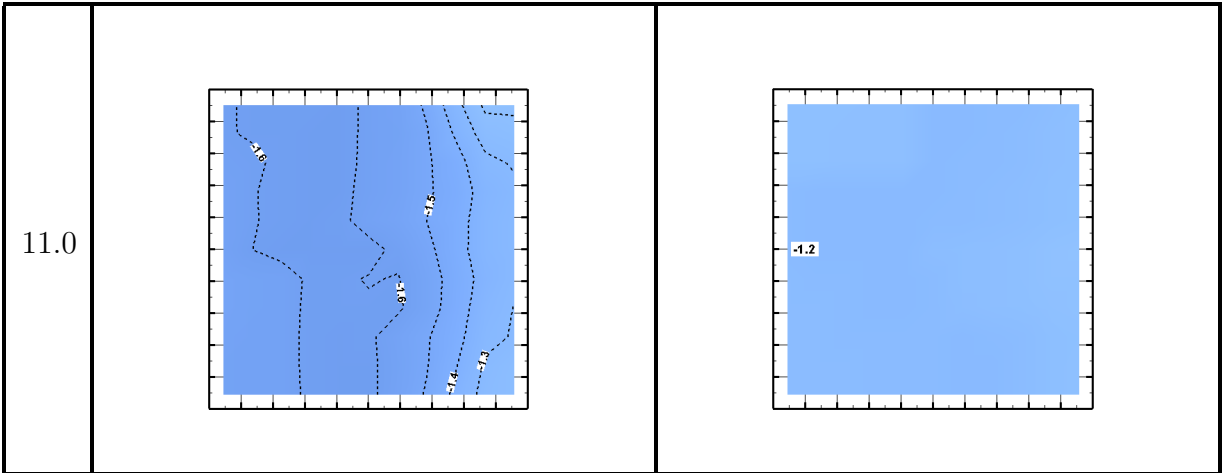
3.5		
4.0		
4.5		

5.0		
5.5		
6.0		

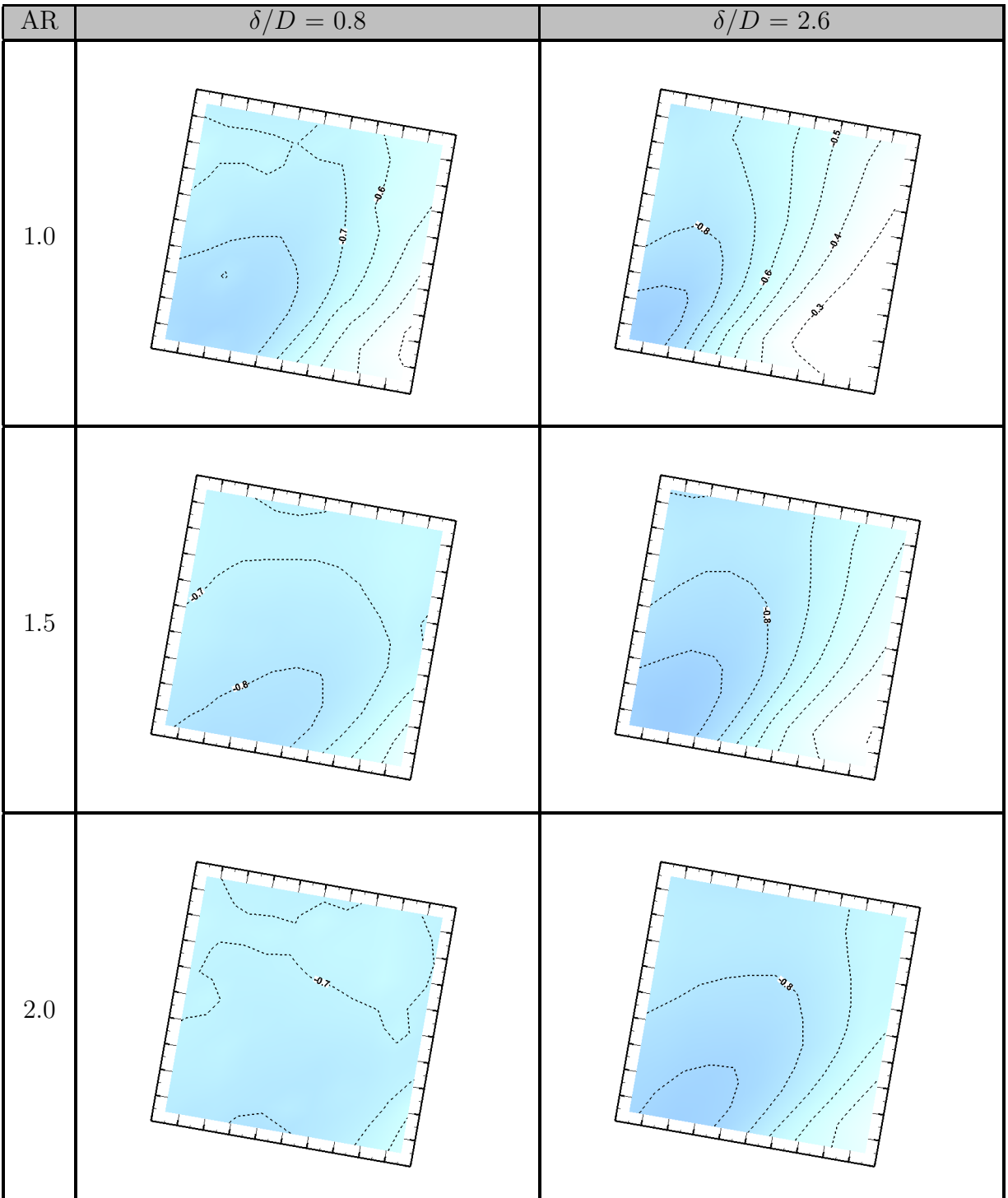
6.5		
7.0		
7.5		

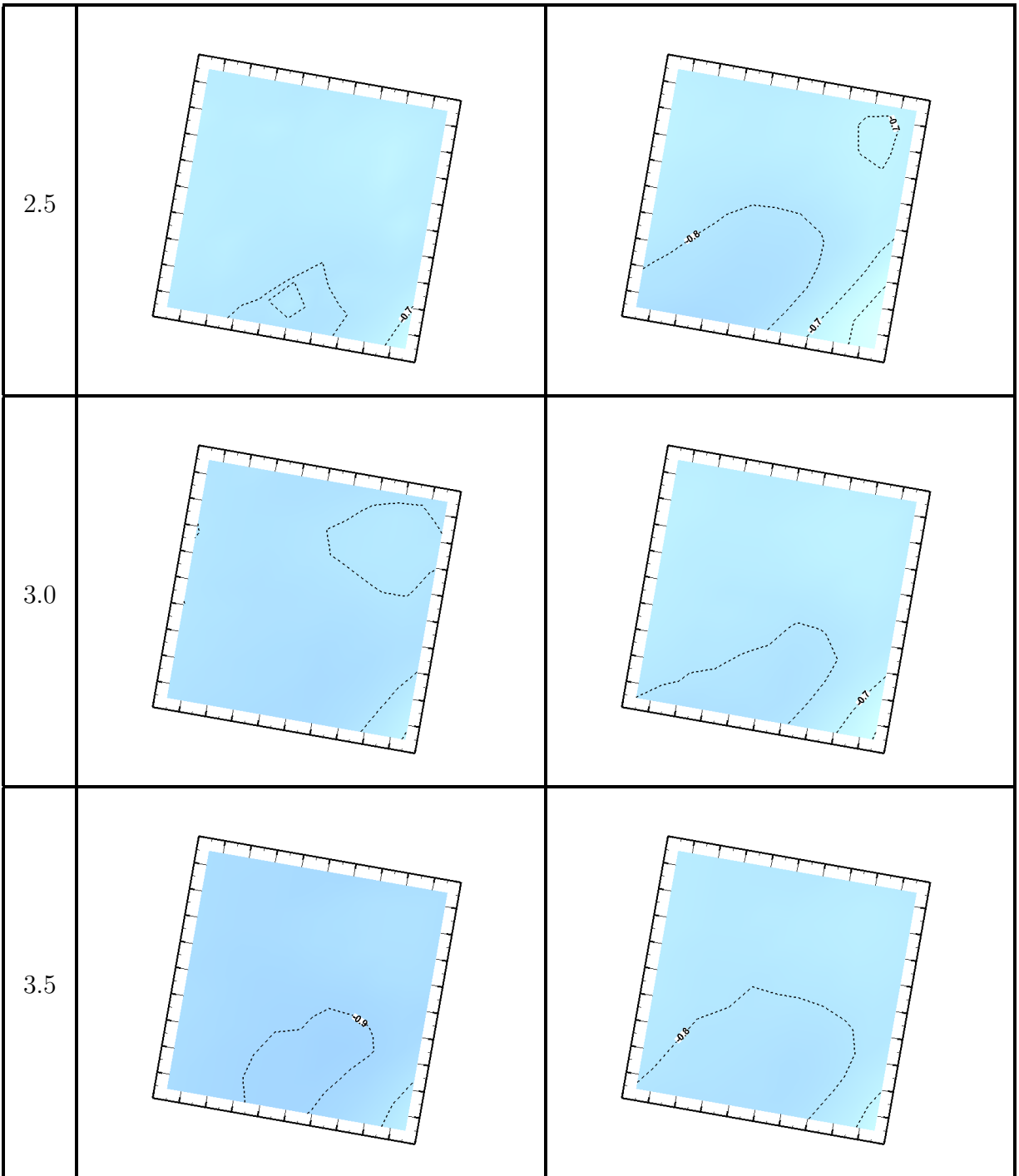
8.0		
8.5		
9.0		

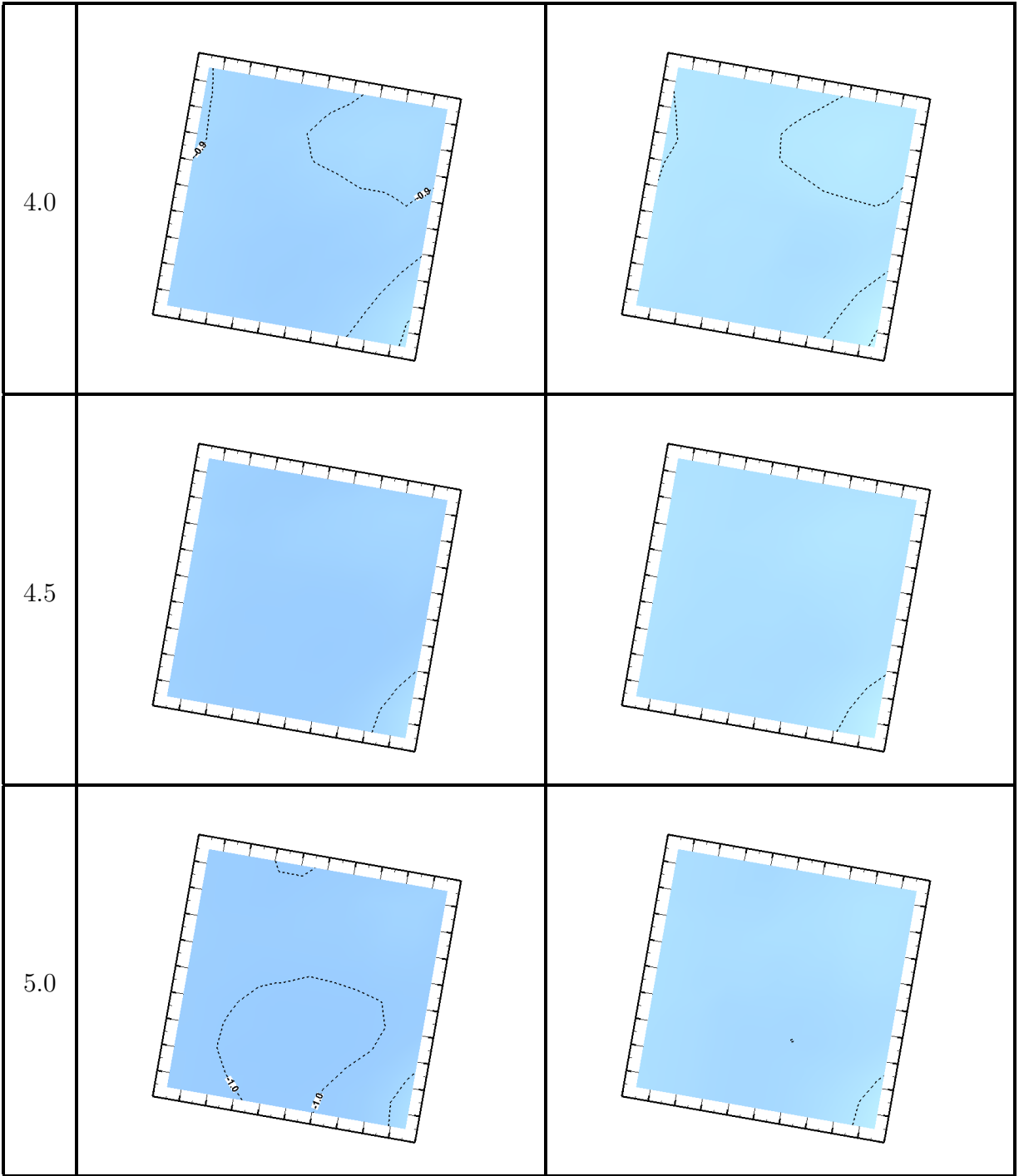
9.5		
10.0		
10.5		

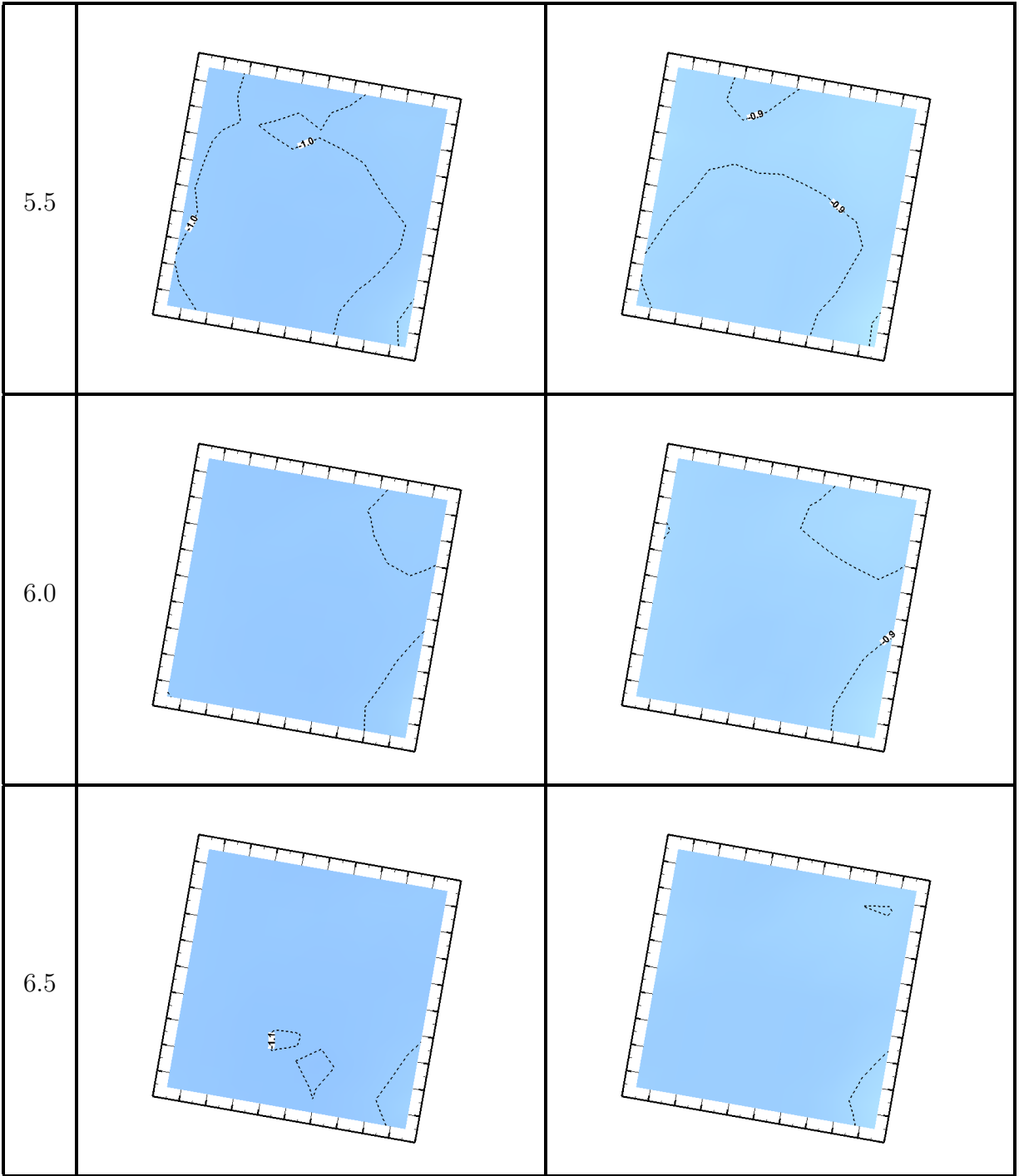


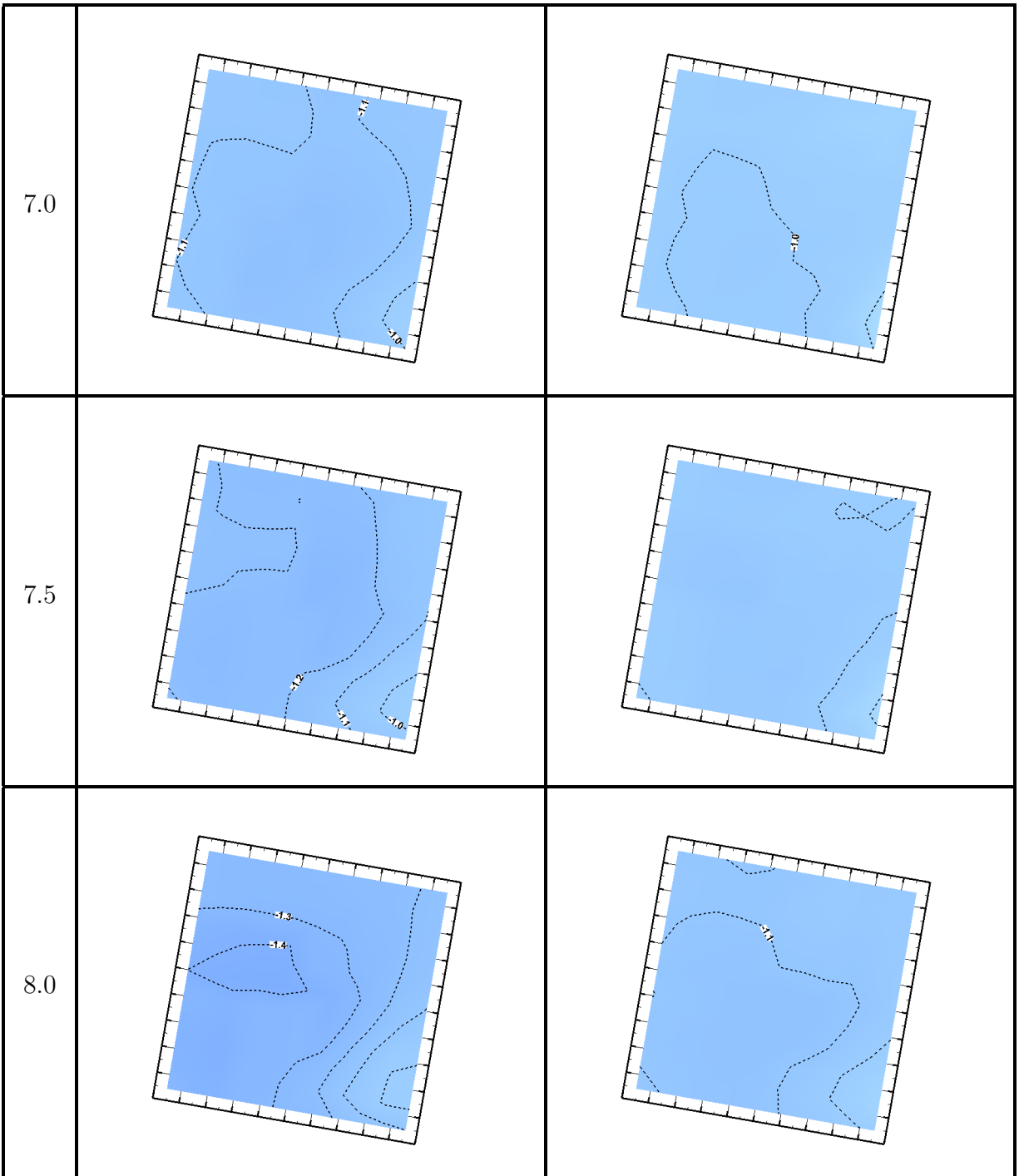
**Table A.2:** Free-end mean pressure distribution (contour lines of constant  $C_P$ ) at  $\alpha = 10^\circ$  for AR = 1 to 11. The flow is from left to right. See page 180 for the scale.

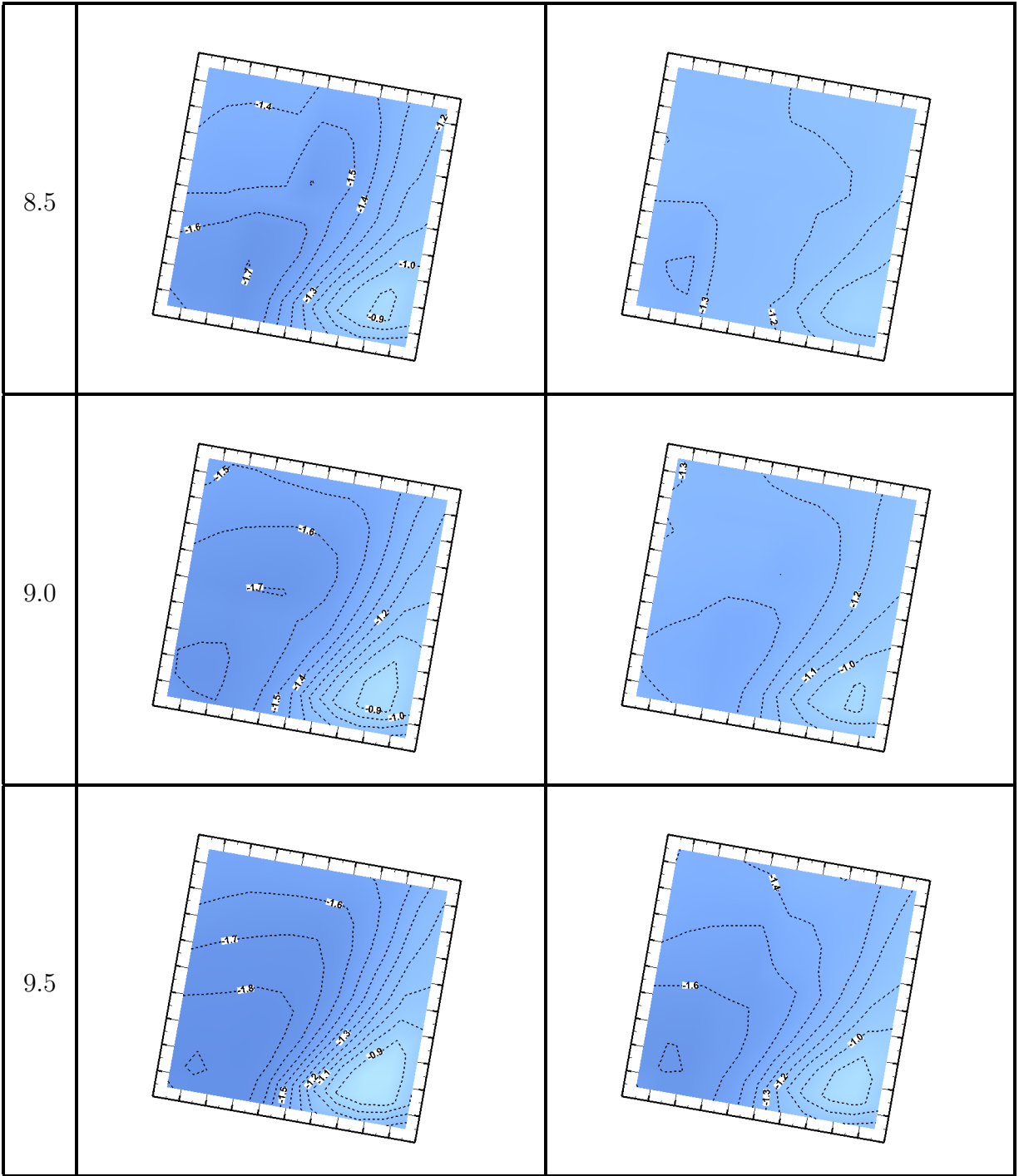


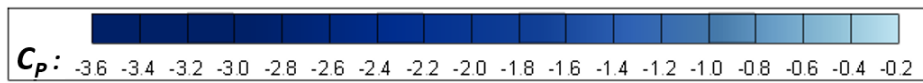
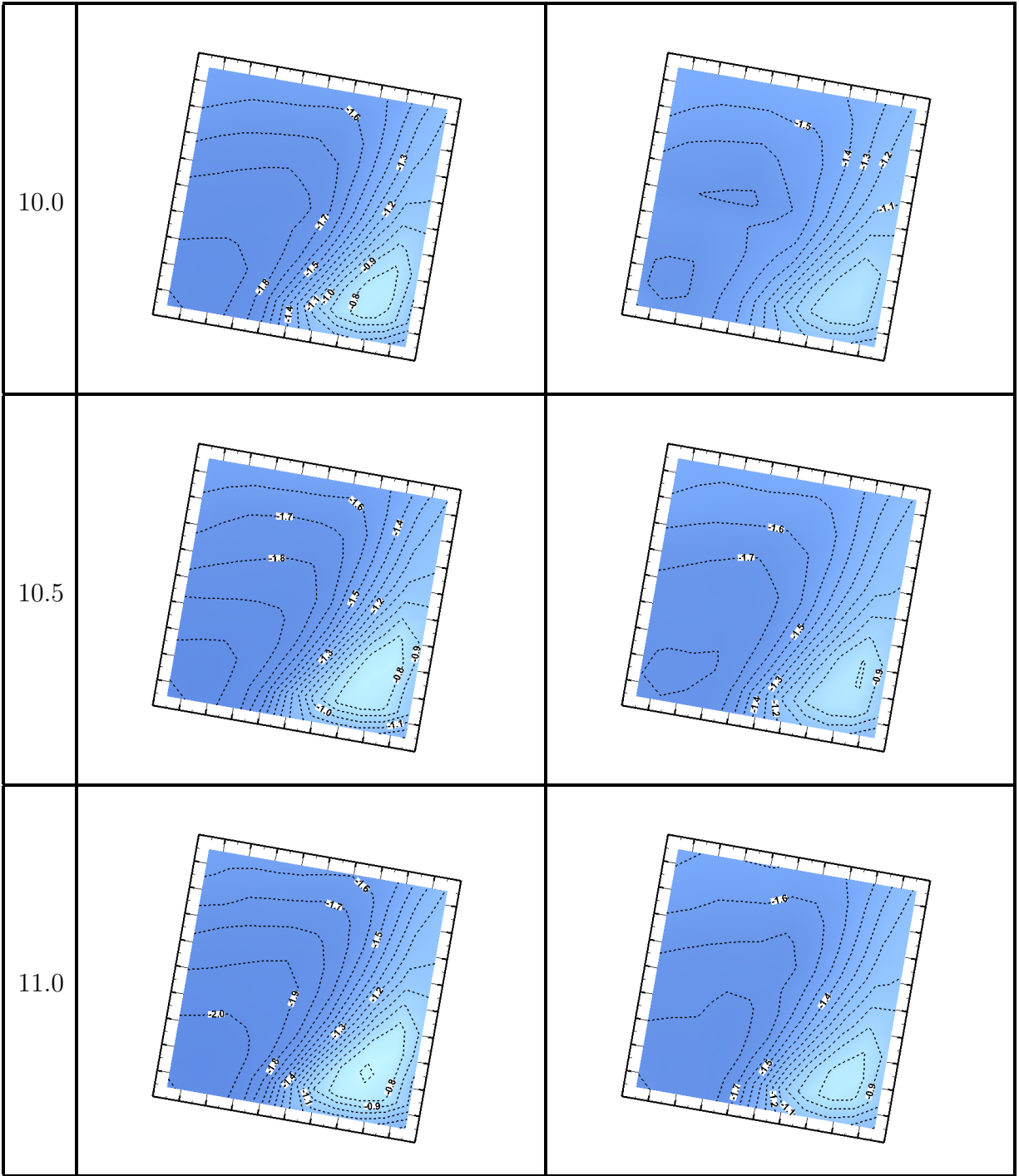




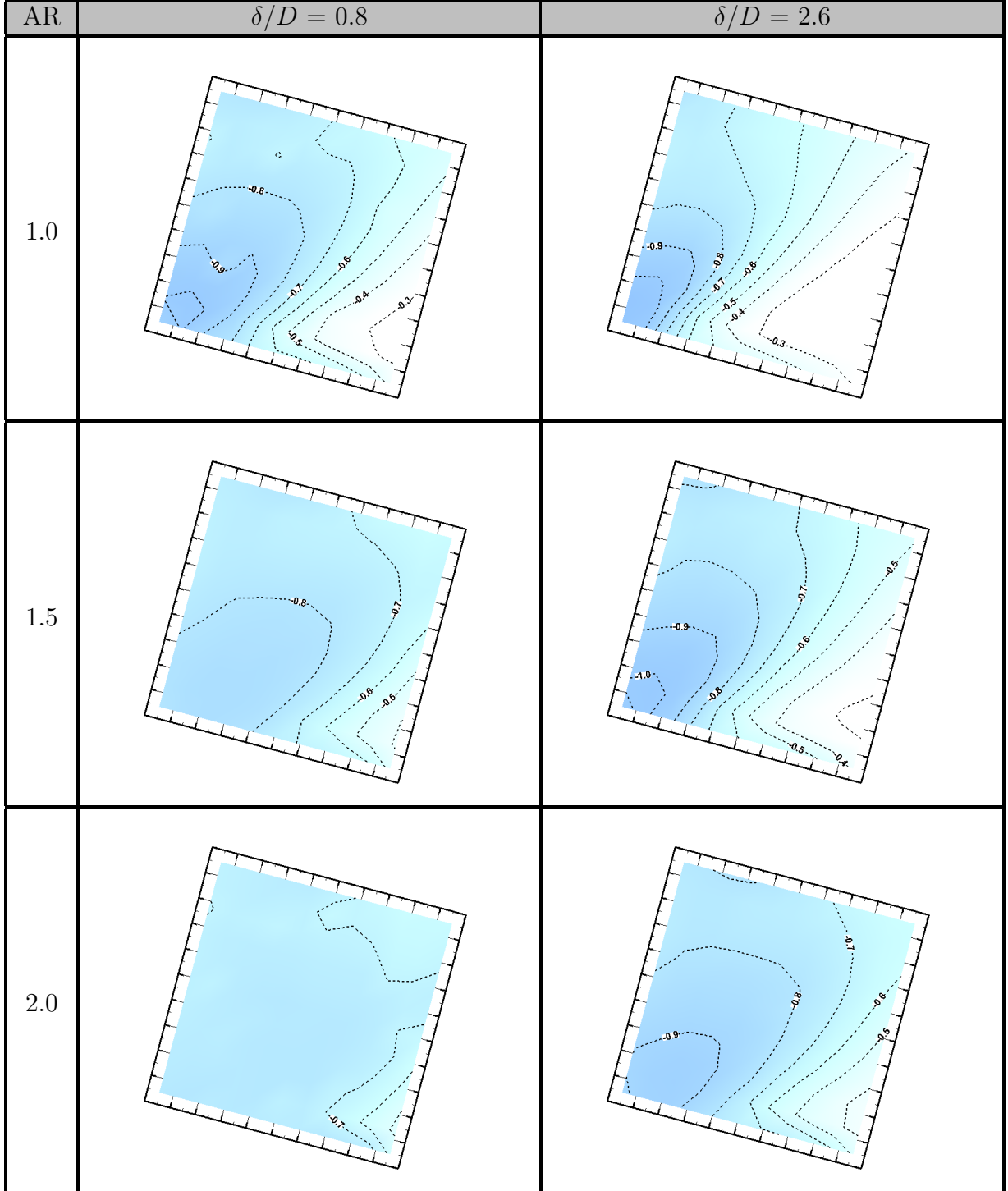


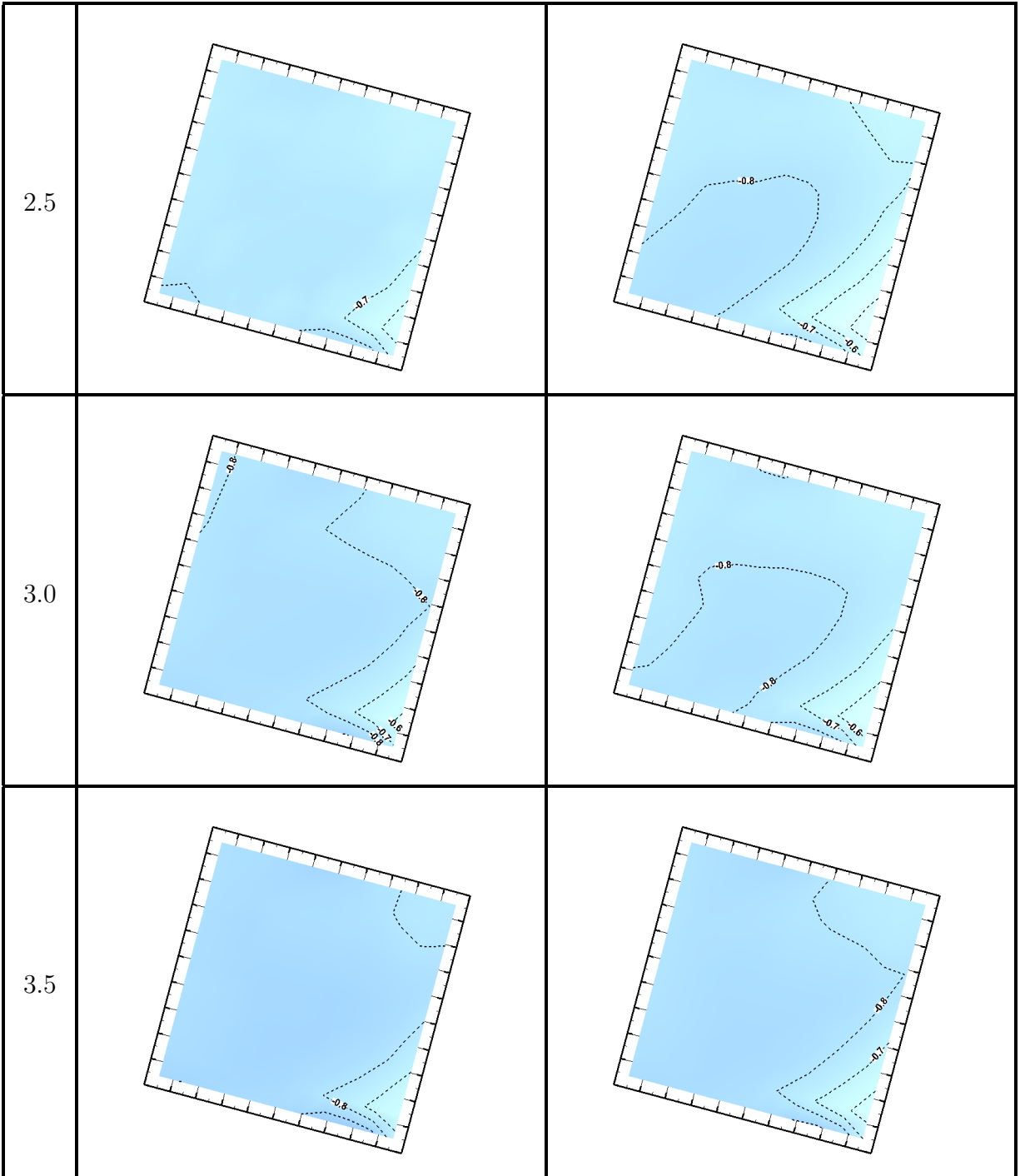


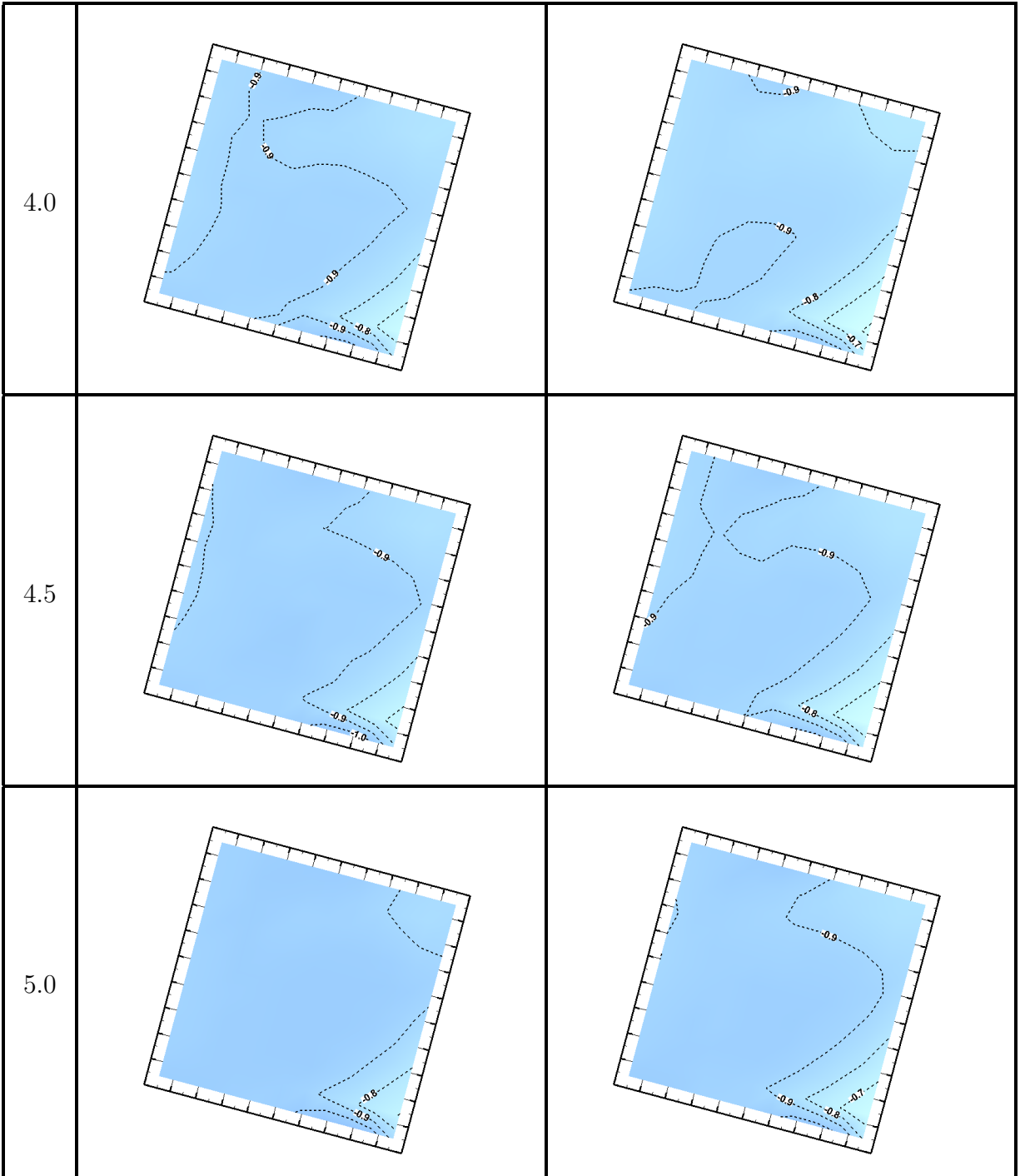


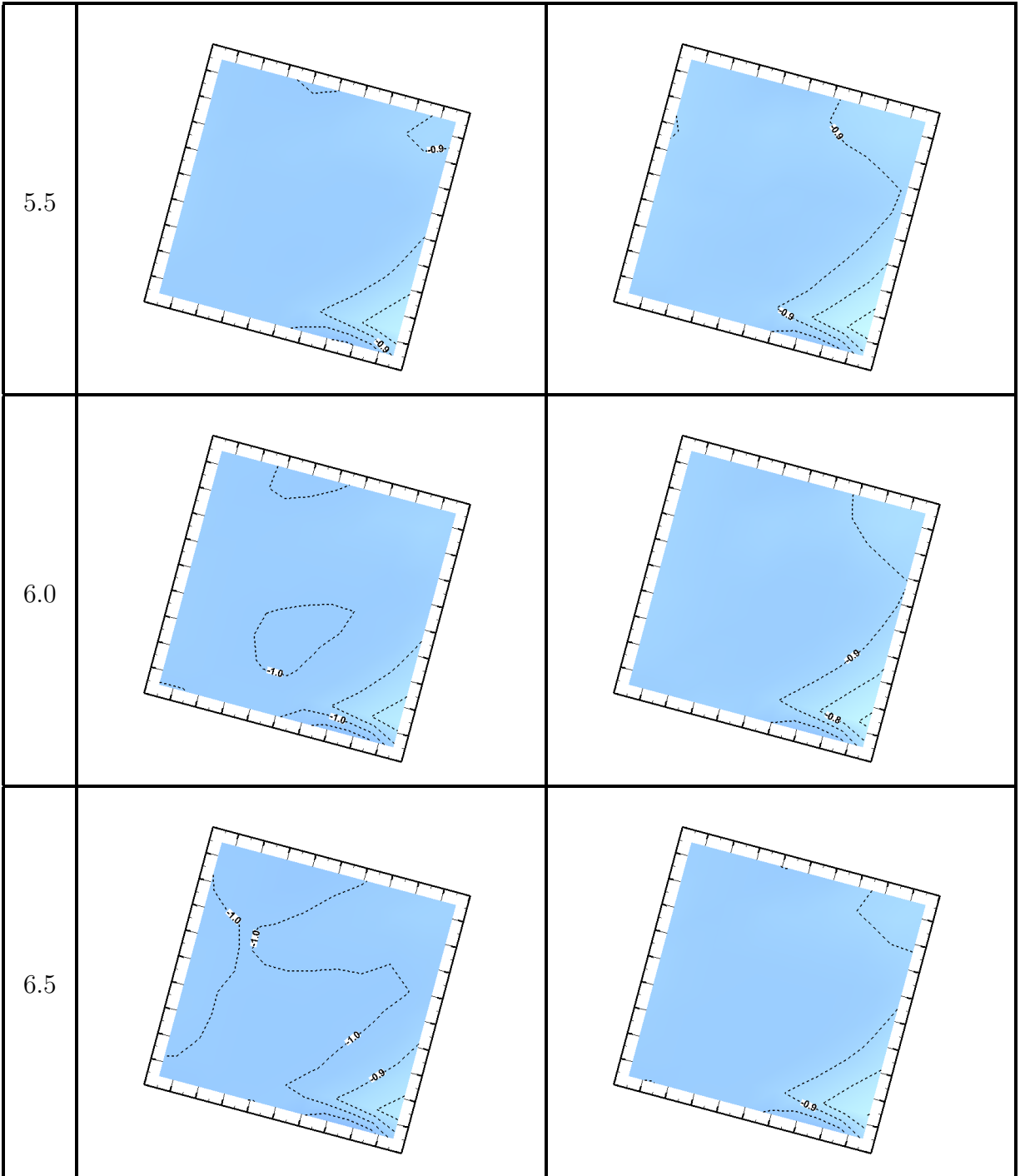


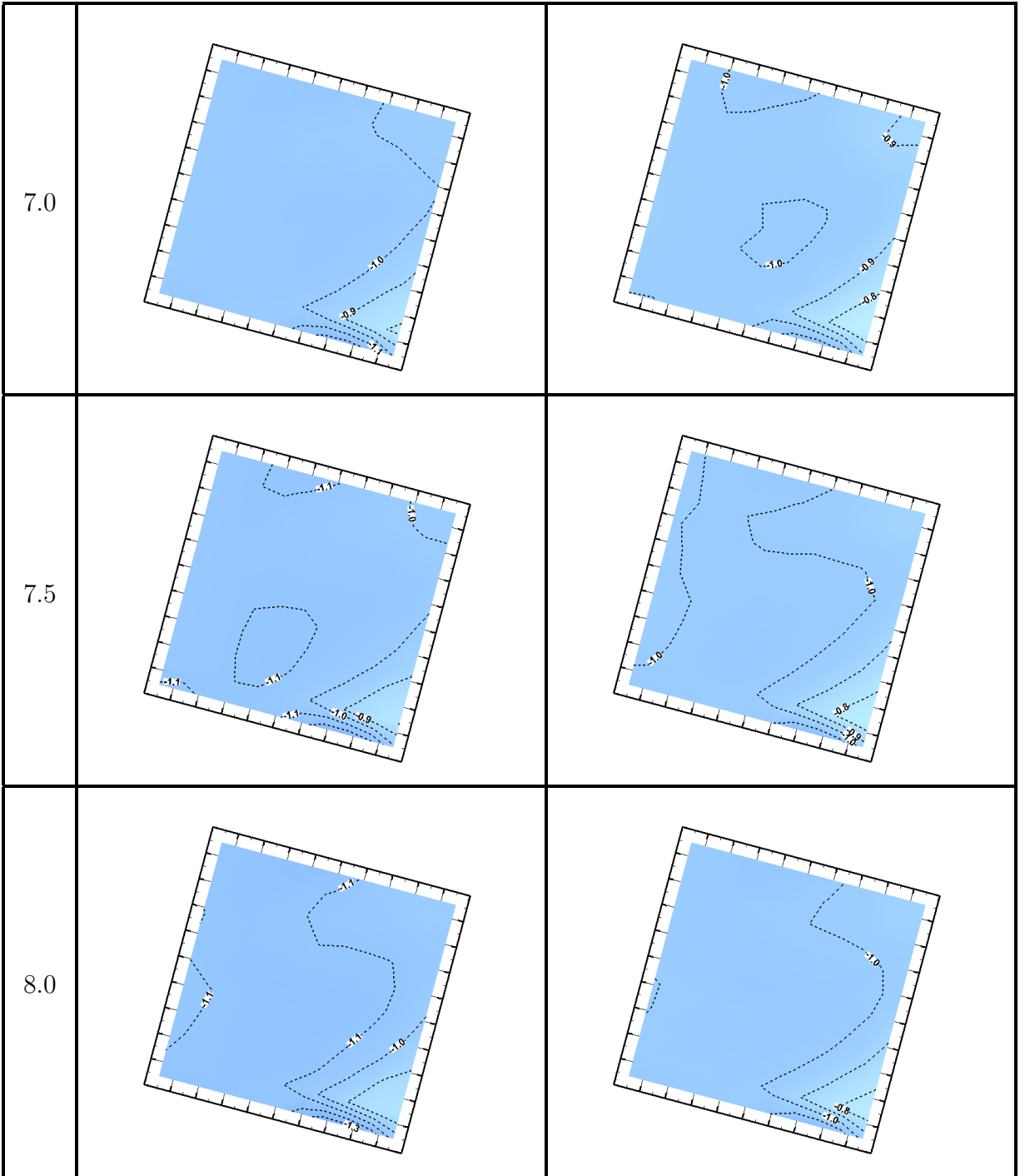
**Table A.3:** Free-end mean pressure distribution (contour lines of constant  $C_P$ ) at  $\alpha = 15^\circ$  for AR = 1 to 11. The flow is from left to right. See page 187 for the scale.



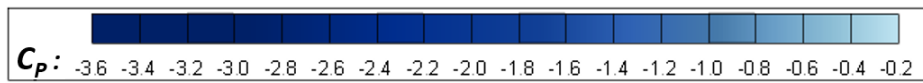
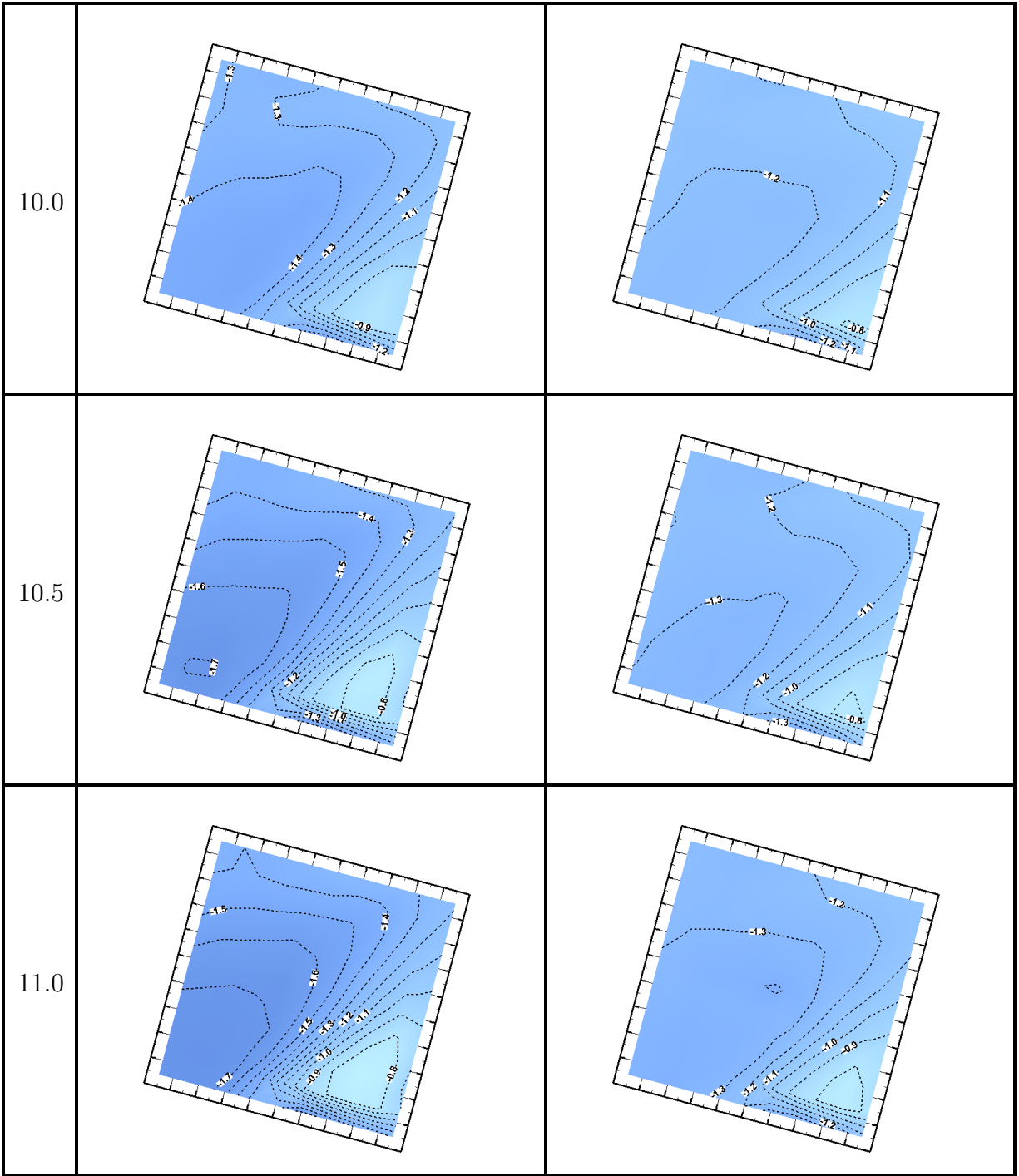




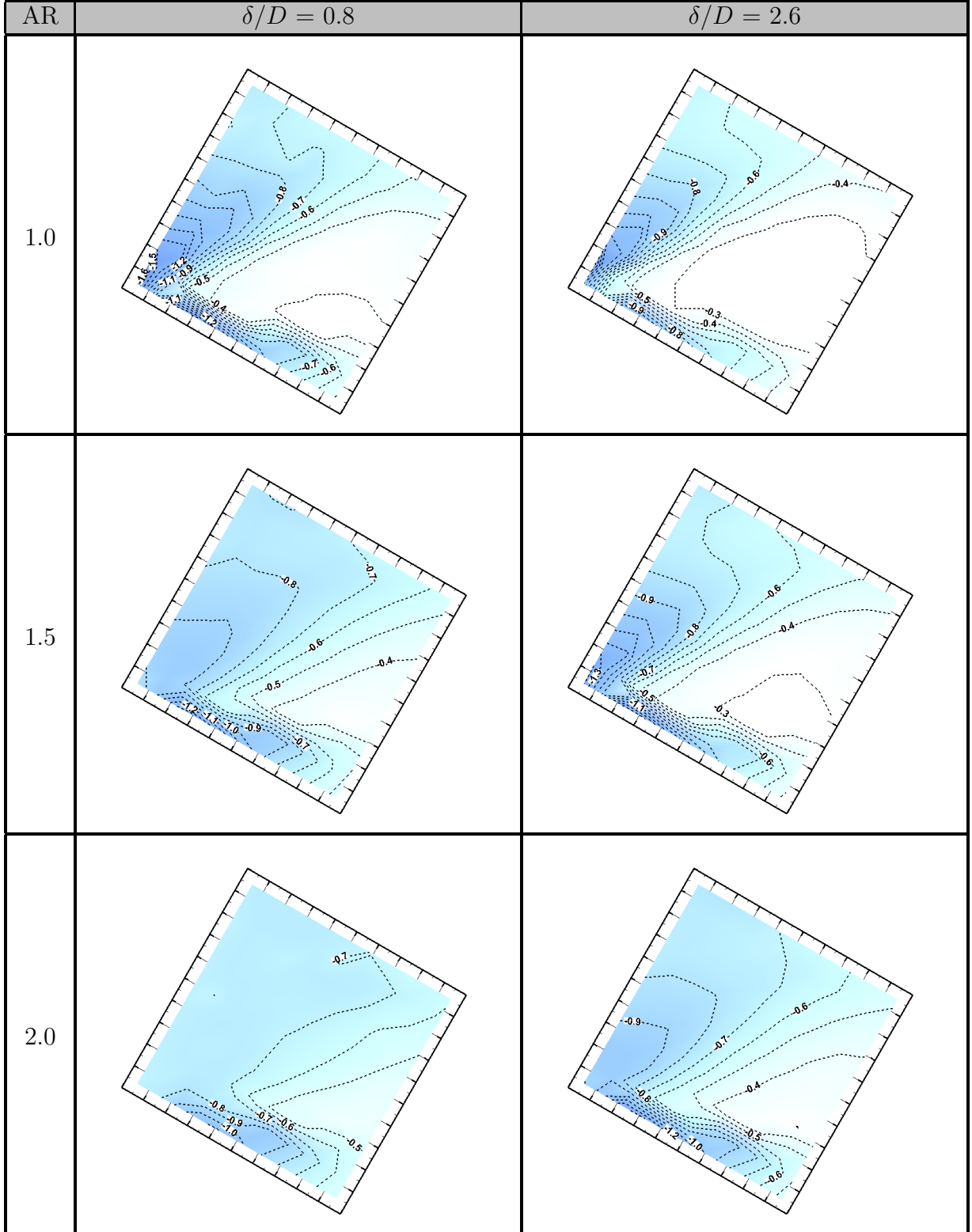


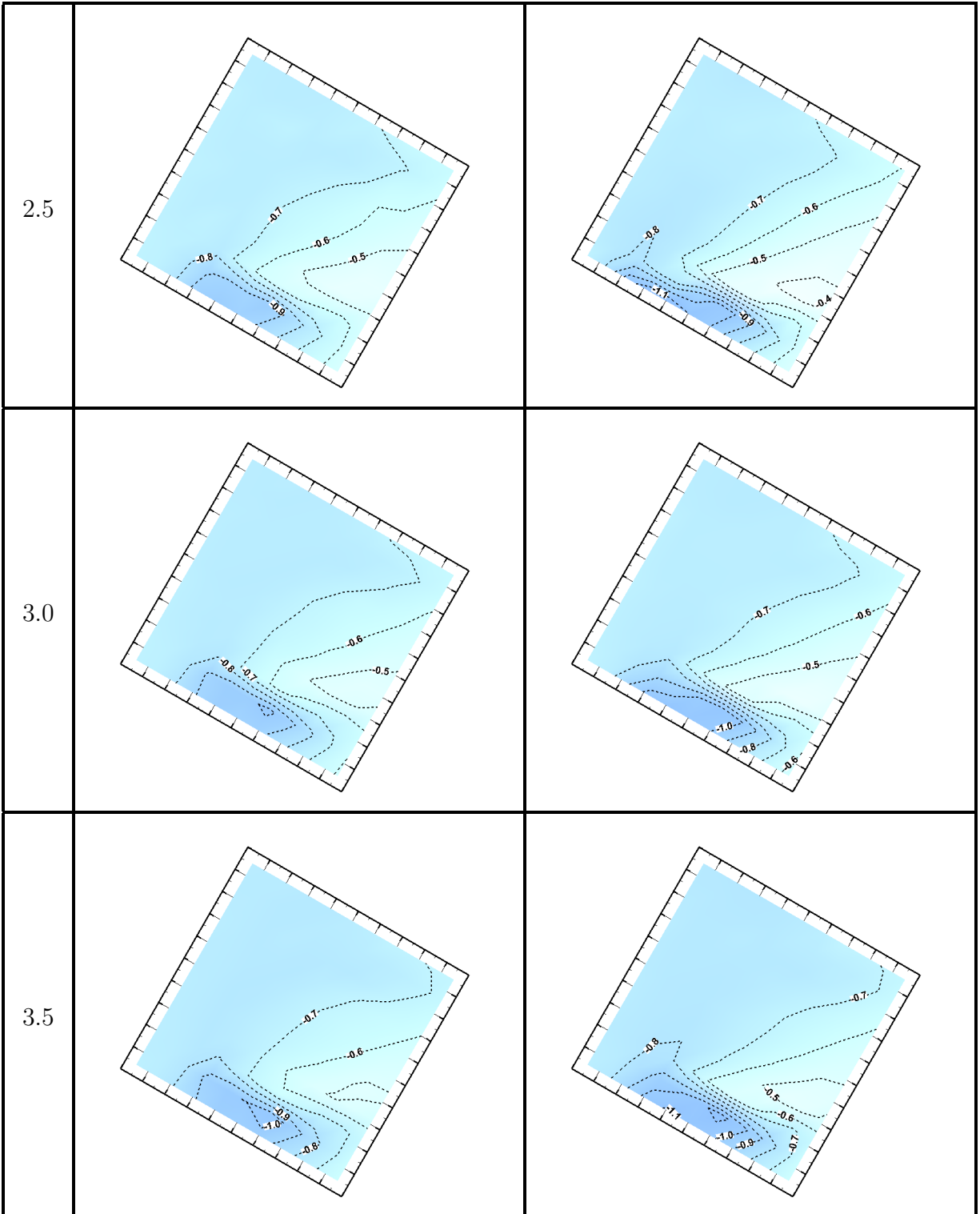


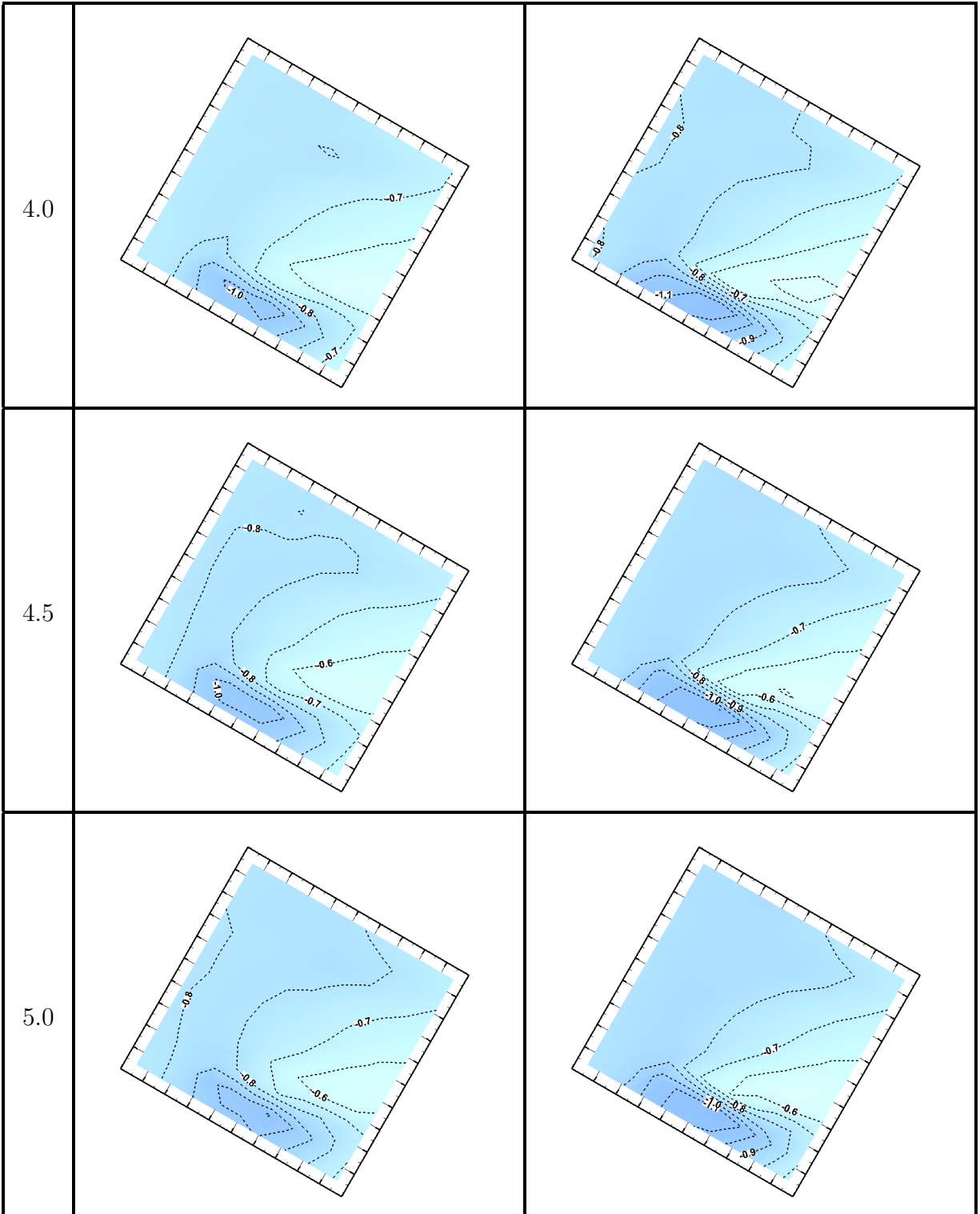


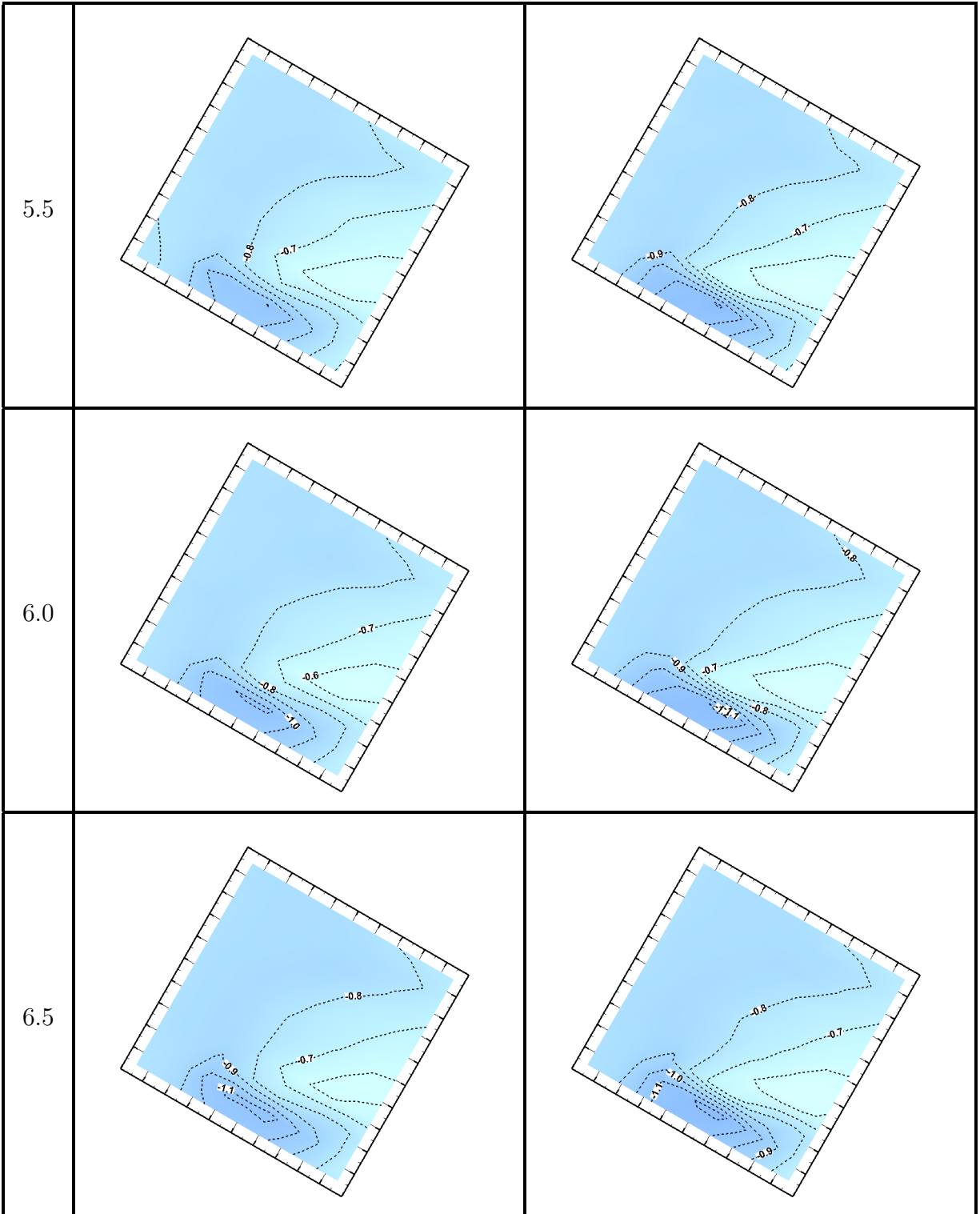


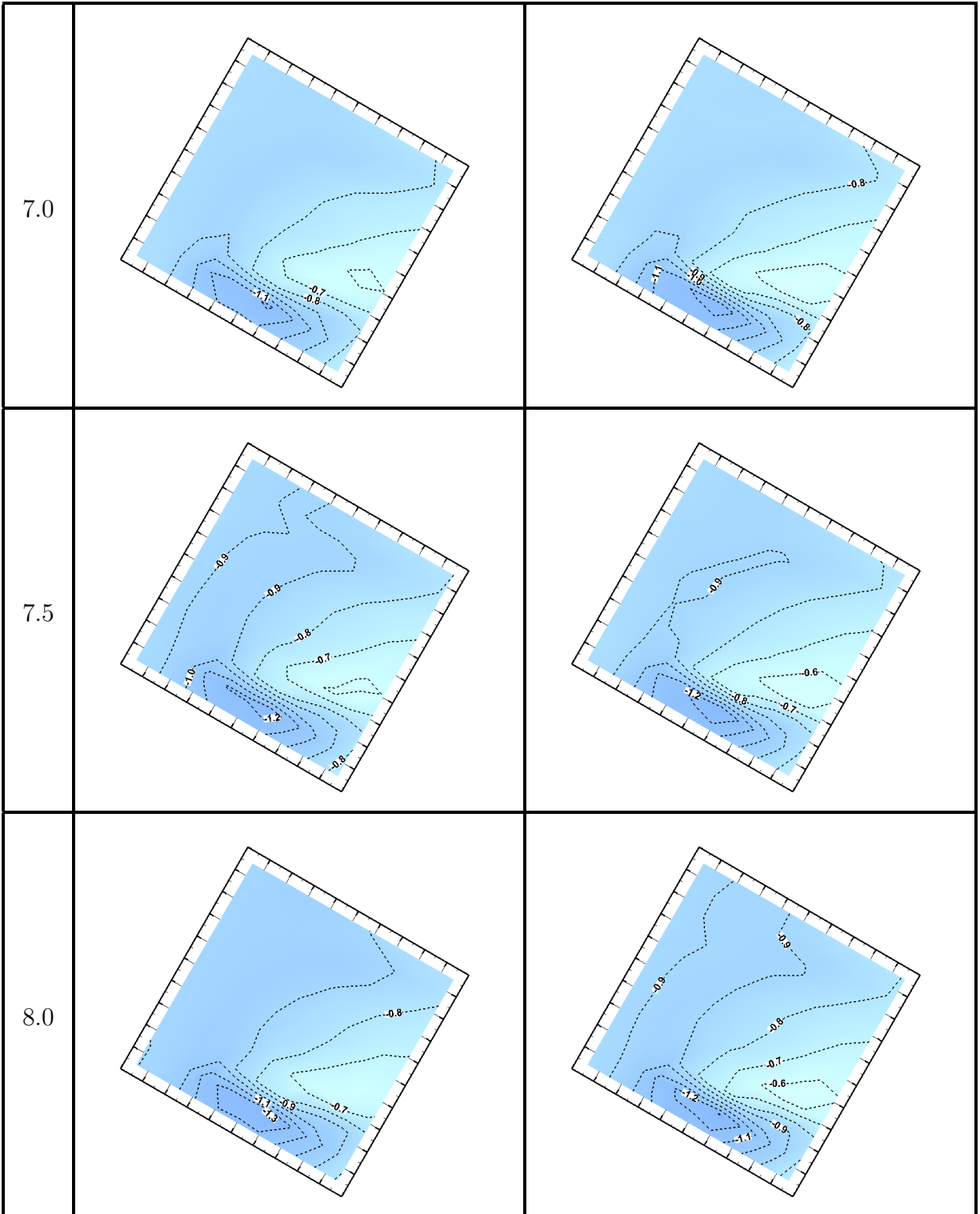
**Table A.4:** Free-end mean pressure distribution (contour lines of constant  $C_P$ ) at  $\alpha = 30^\circ$  for AR = 1 to 11. The flow is from left to right. See page 194 for the scale.

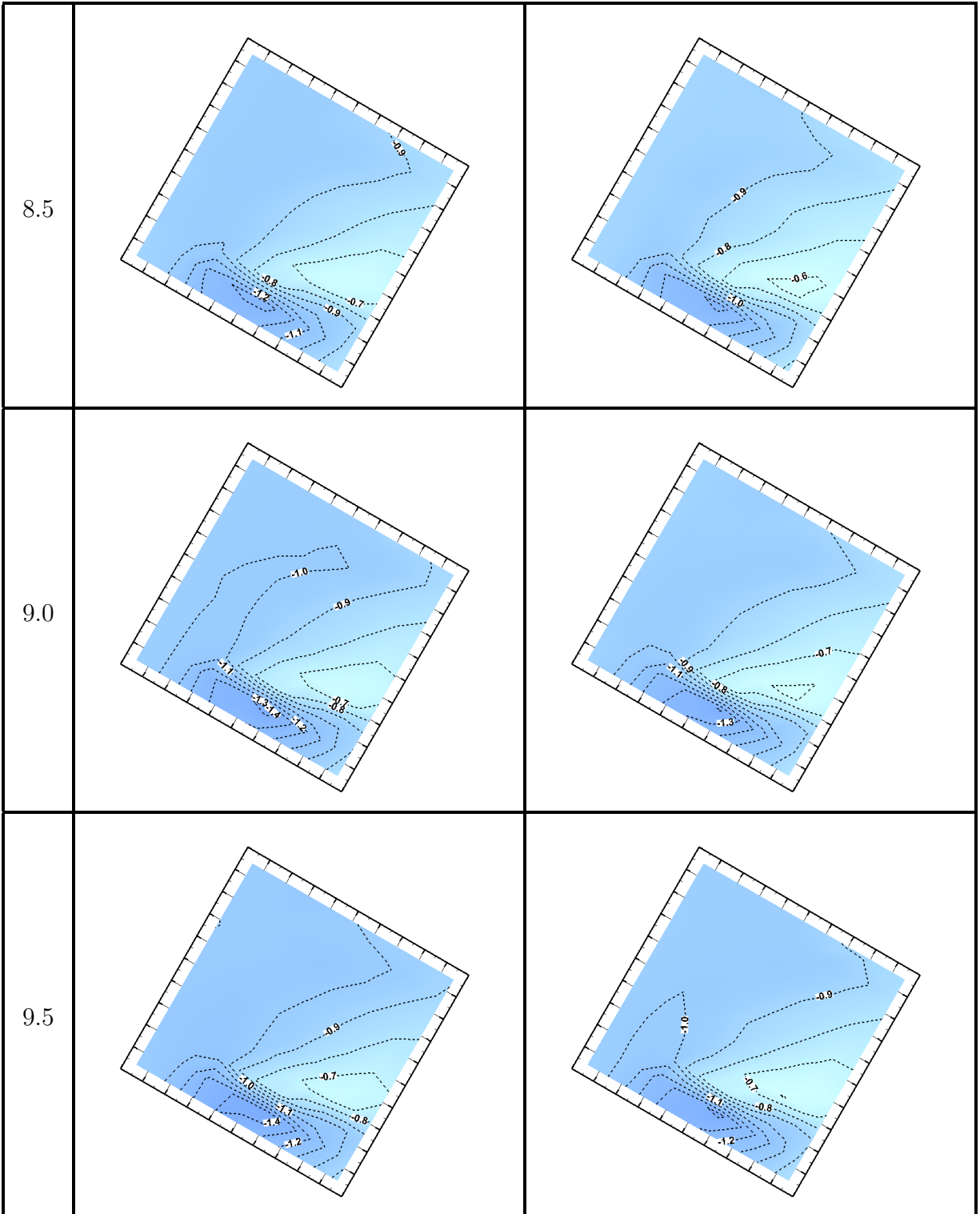


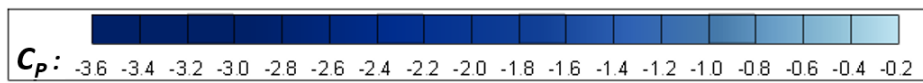
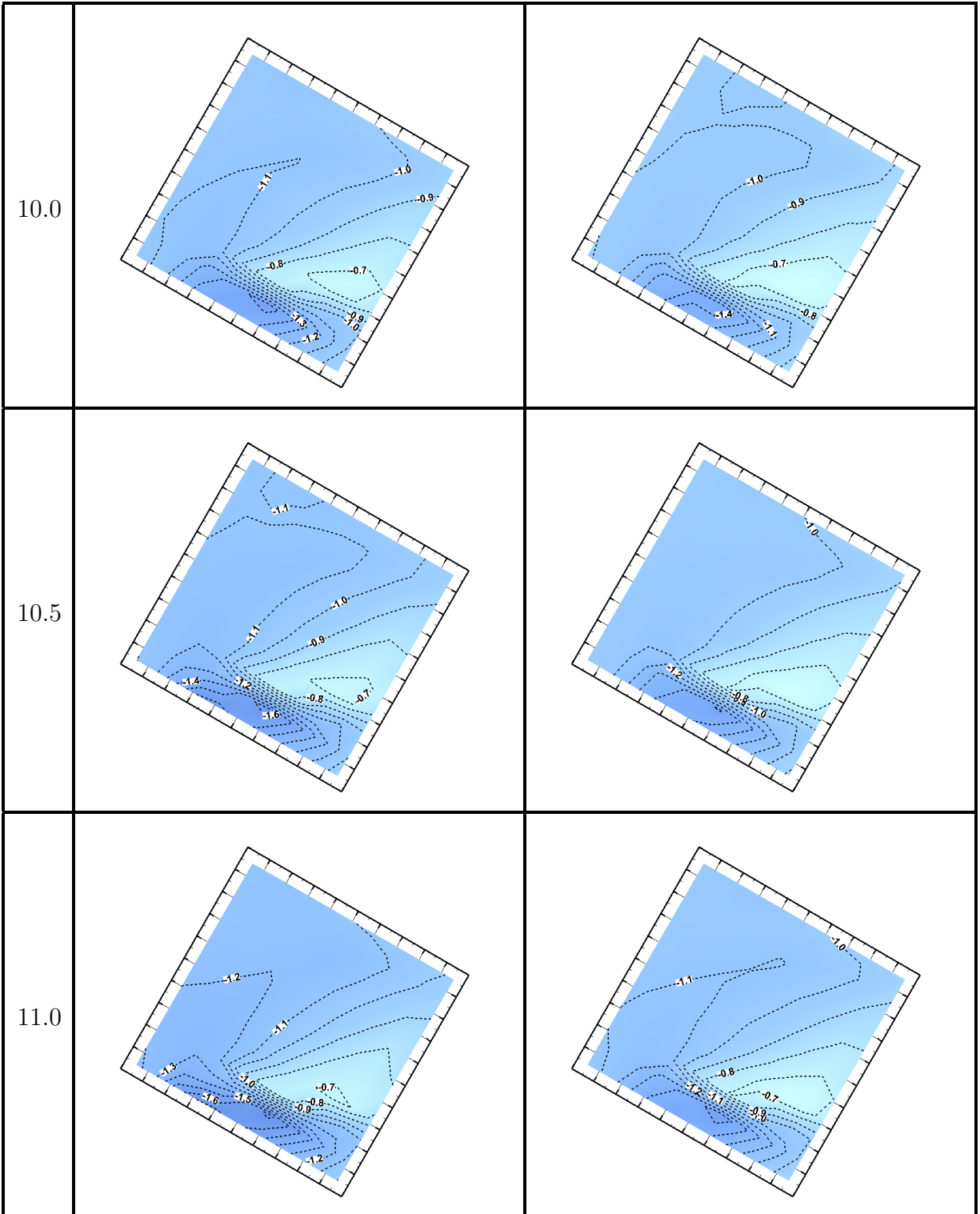




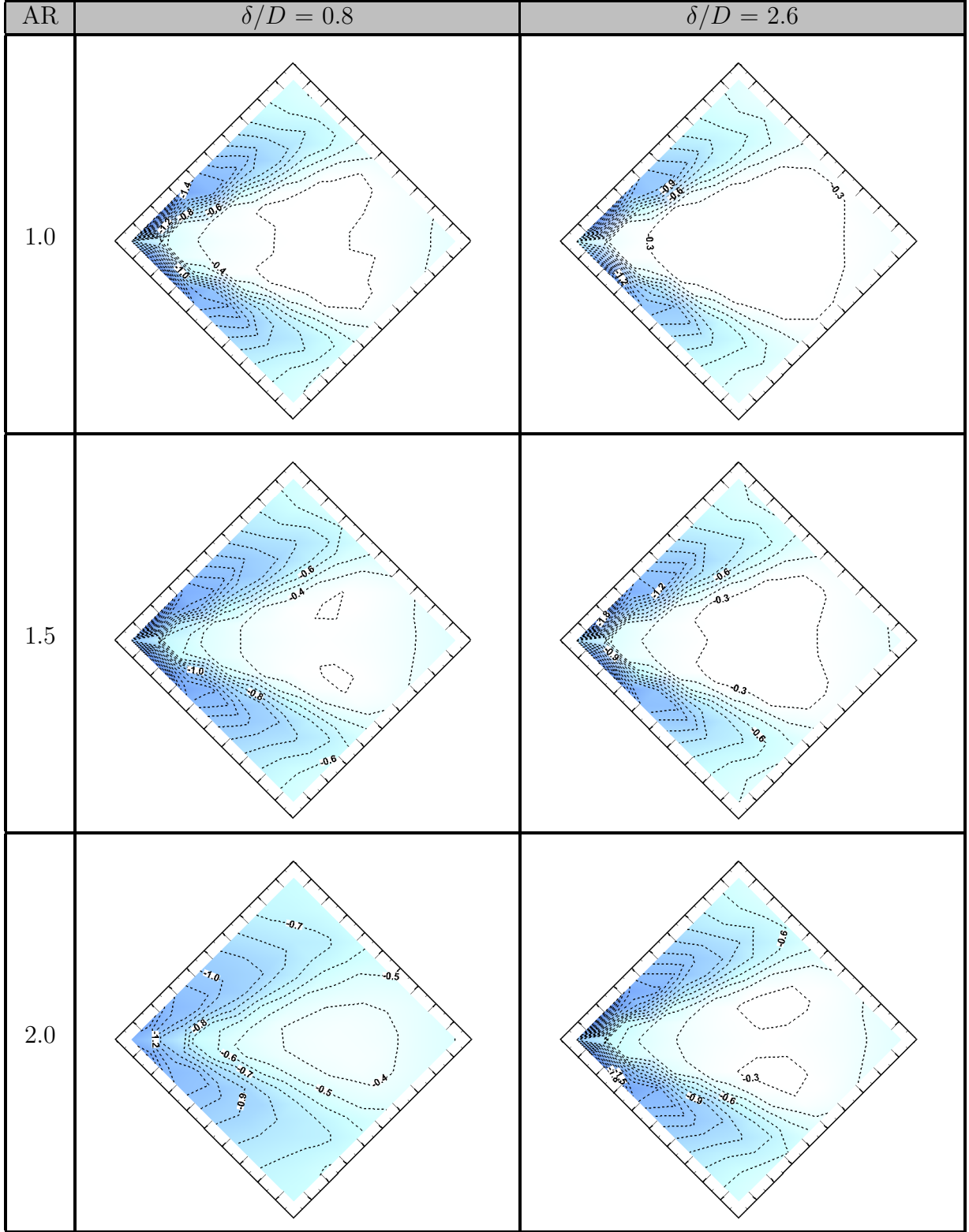


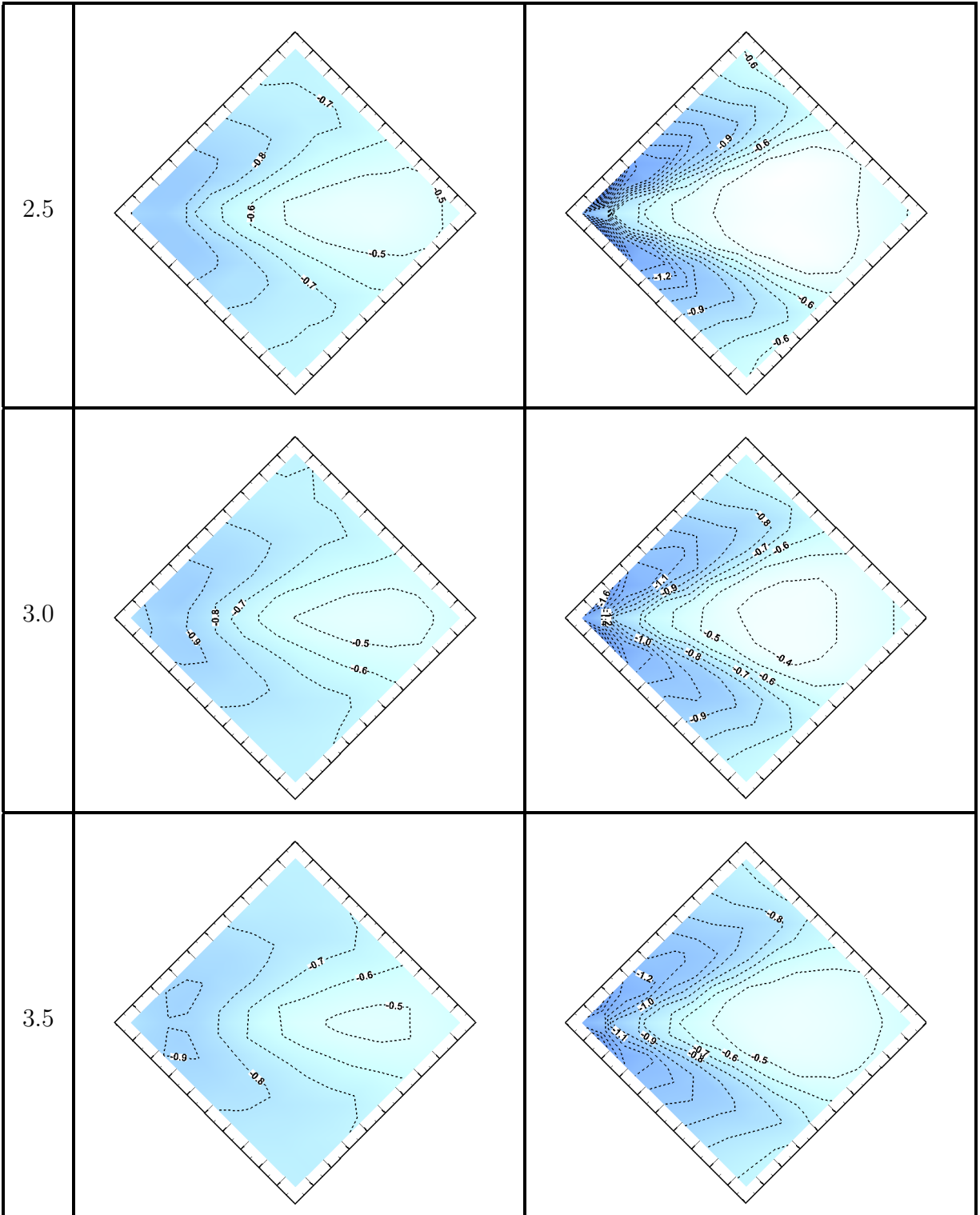


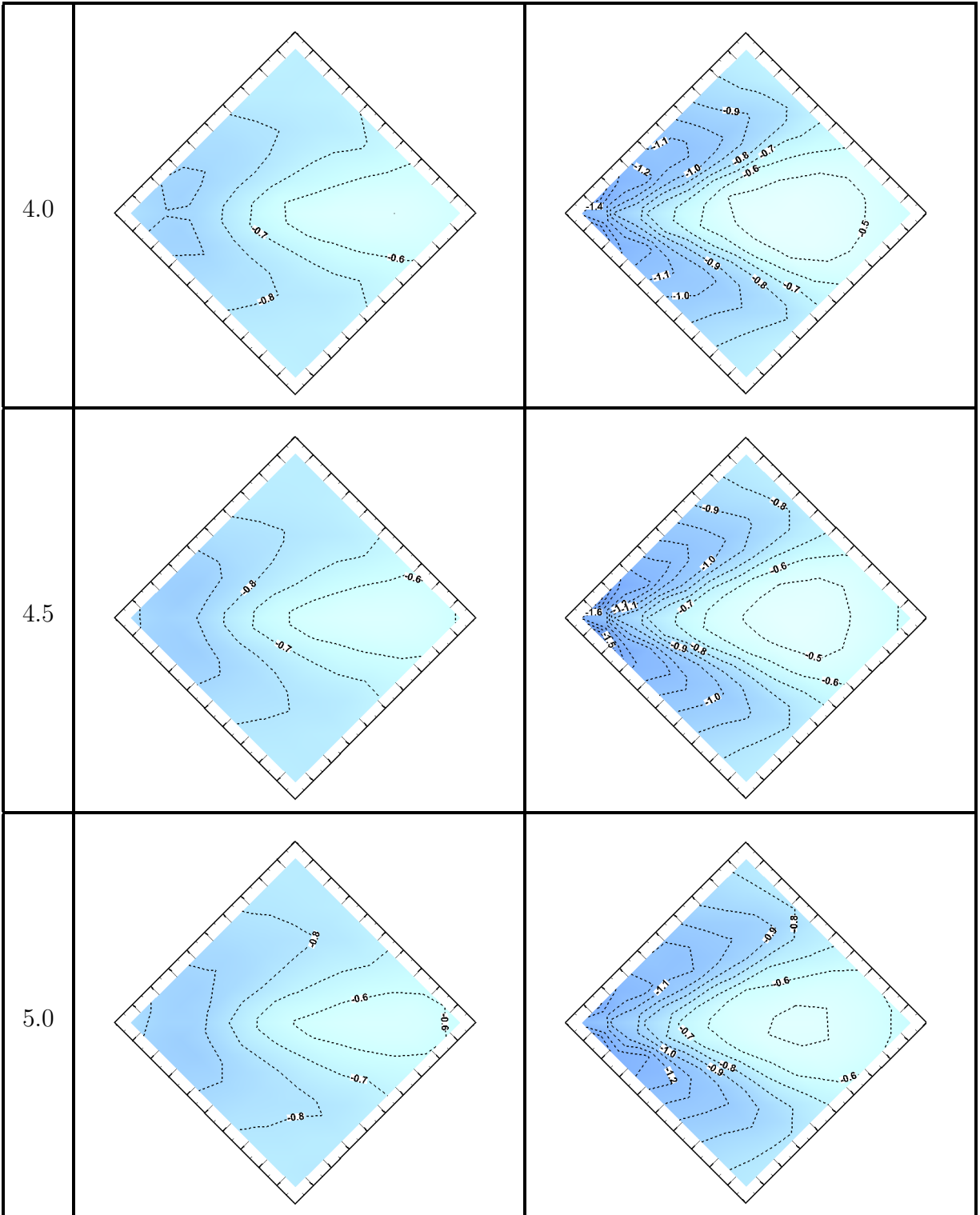


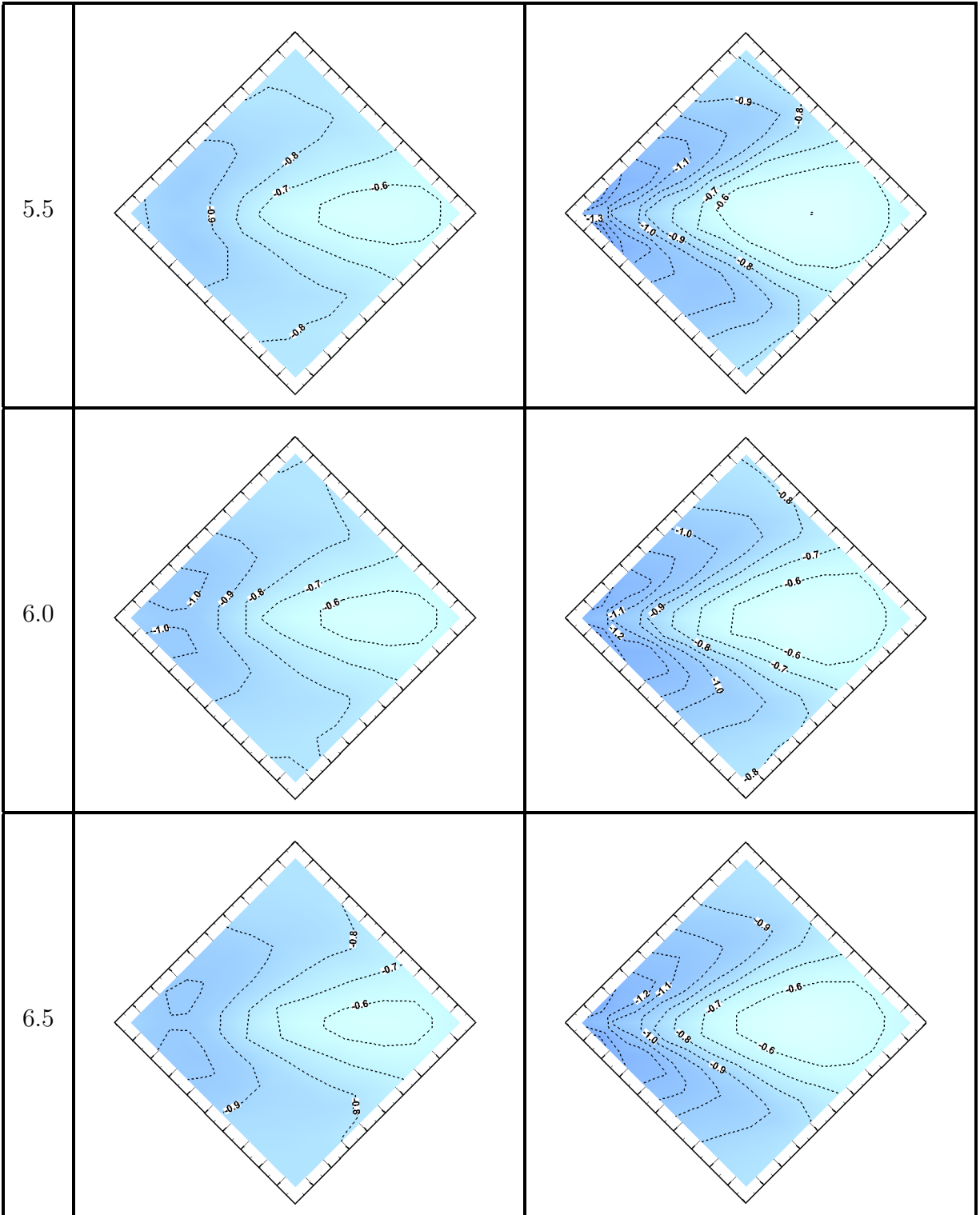


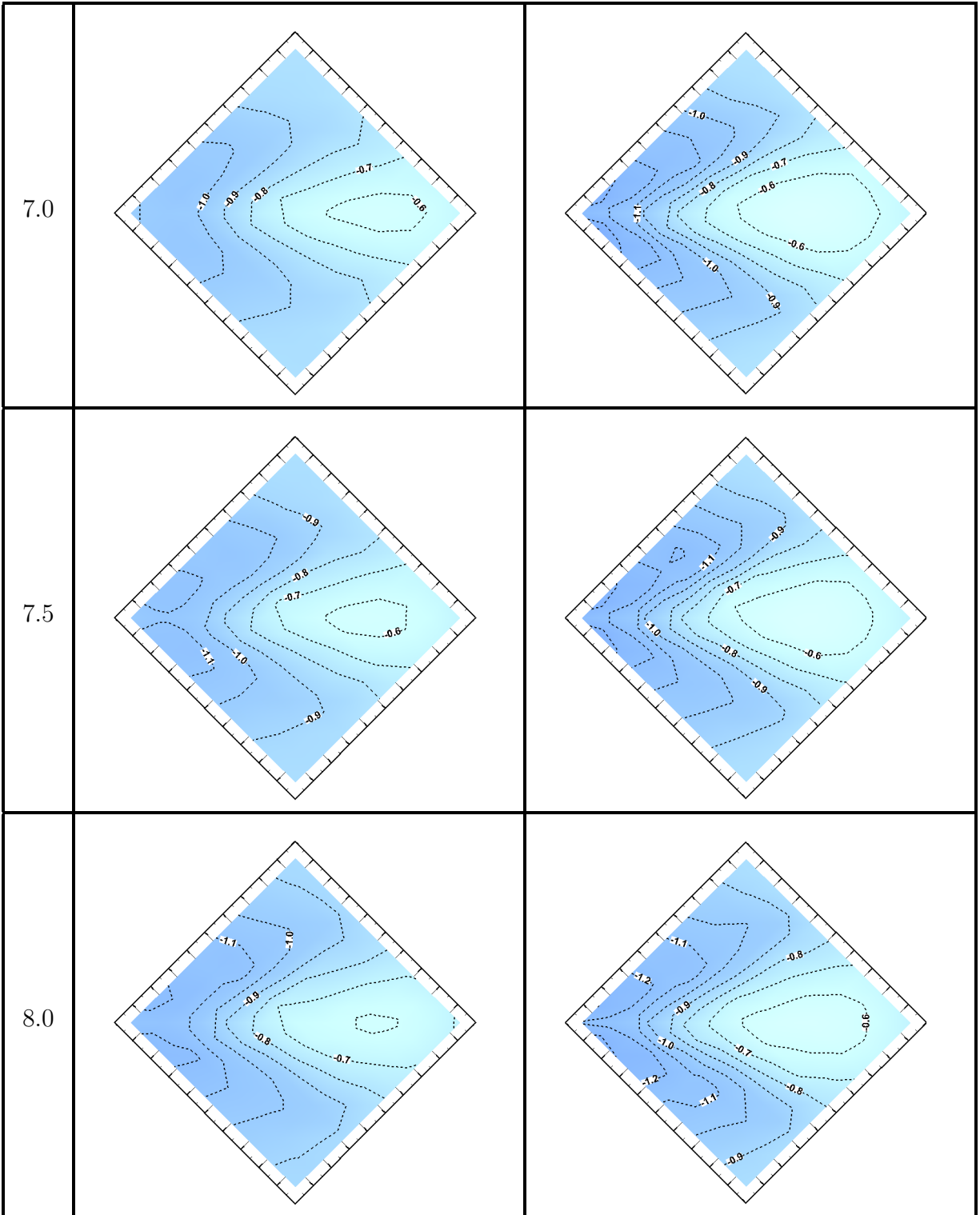
**Table A.5:** Free-end mean pressure distribution (contour lines of constant  $C_P$ ) at  $\alpha = 45^\circ$  for AR = 1 to 11. The flow is from left to right. See page 201 for the scale.

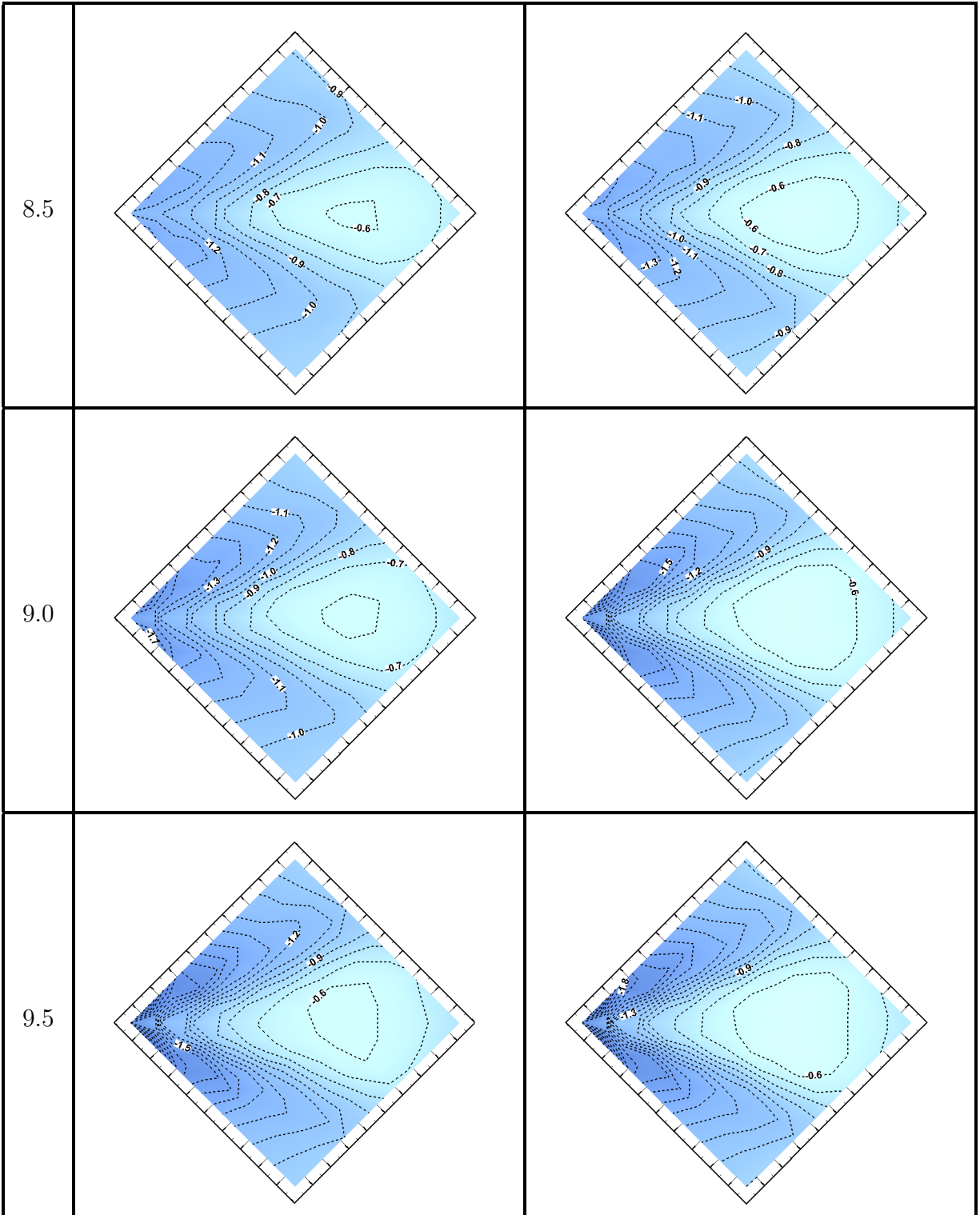


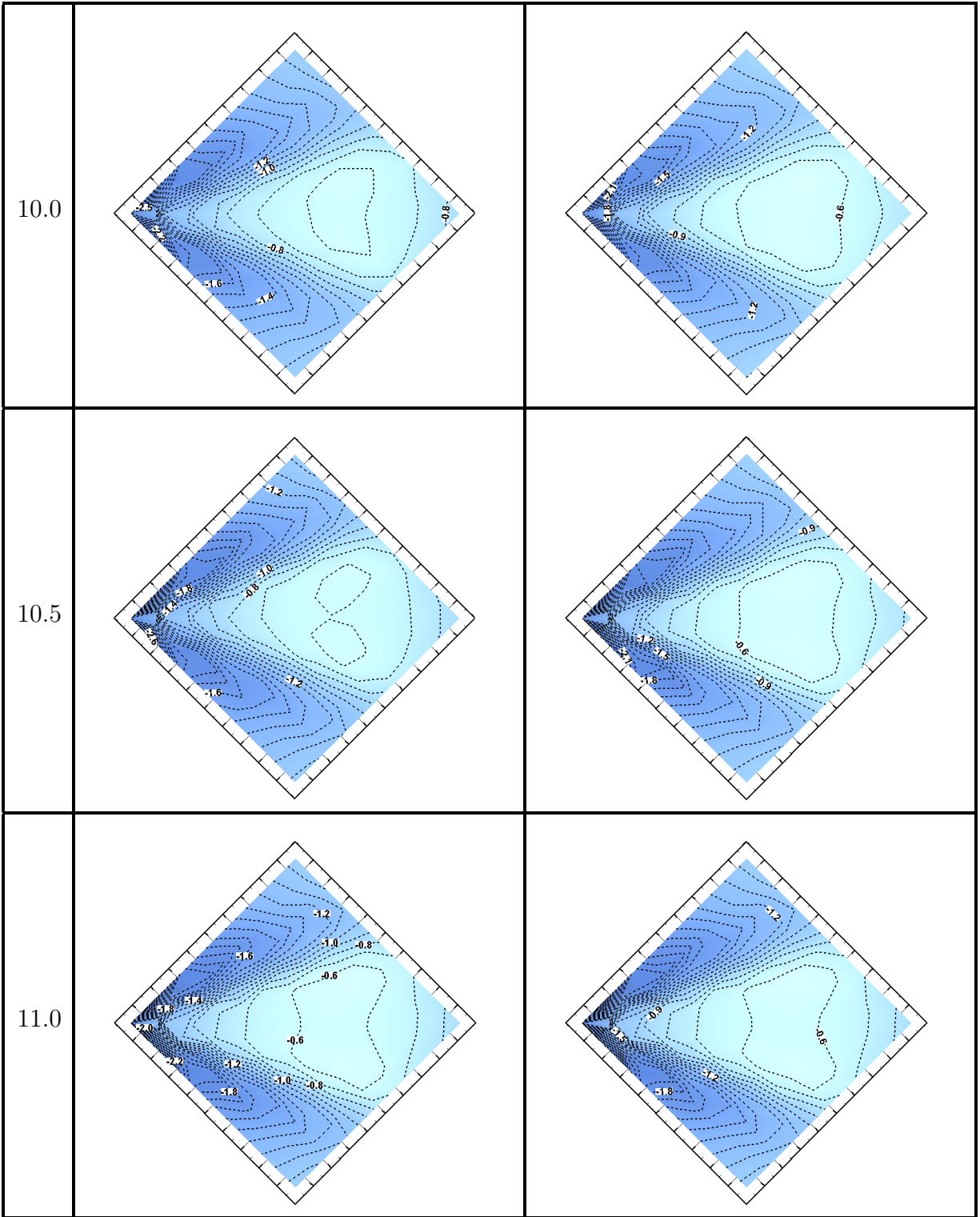










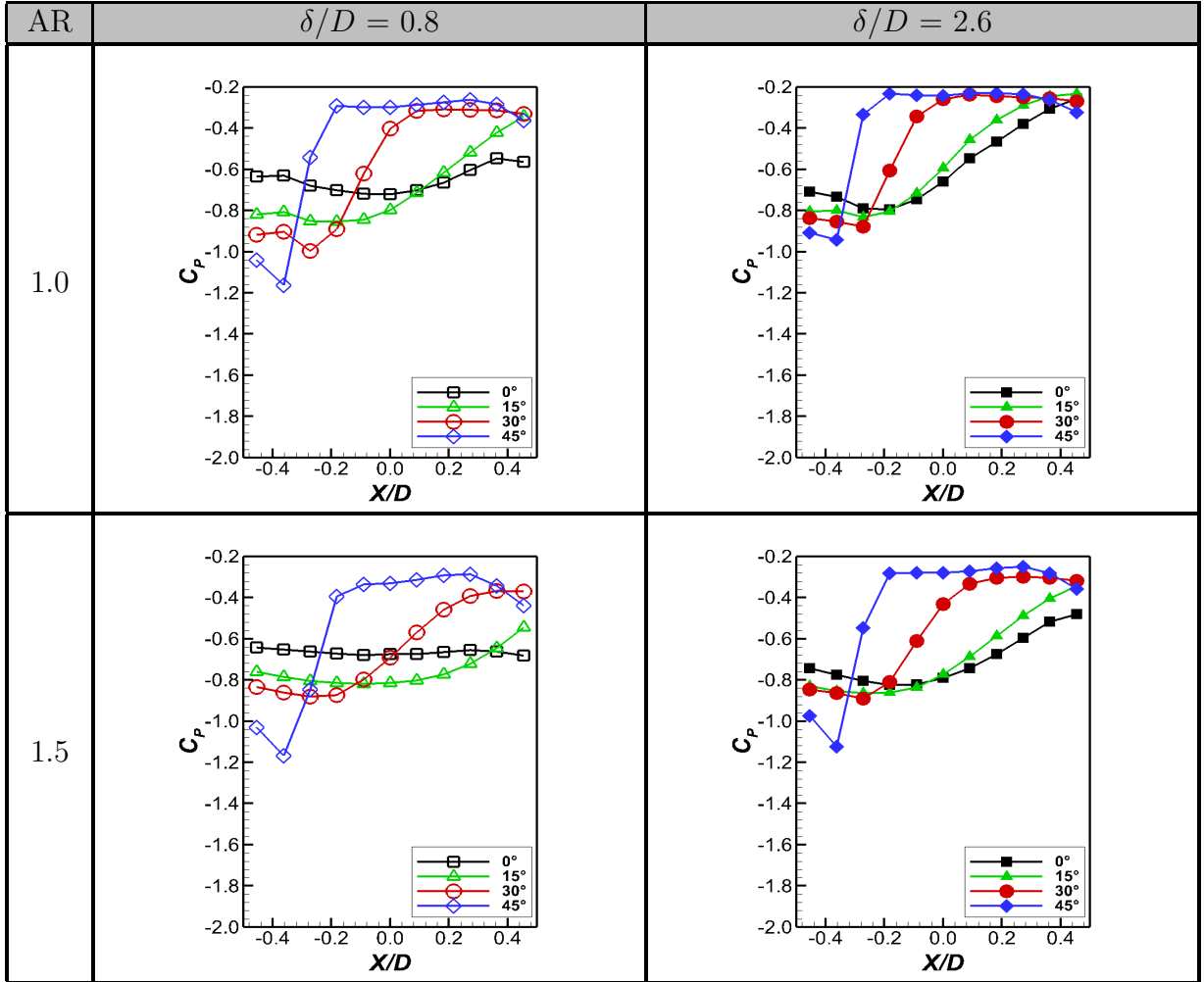


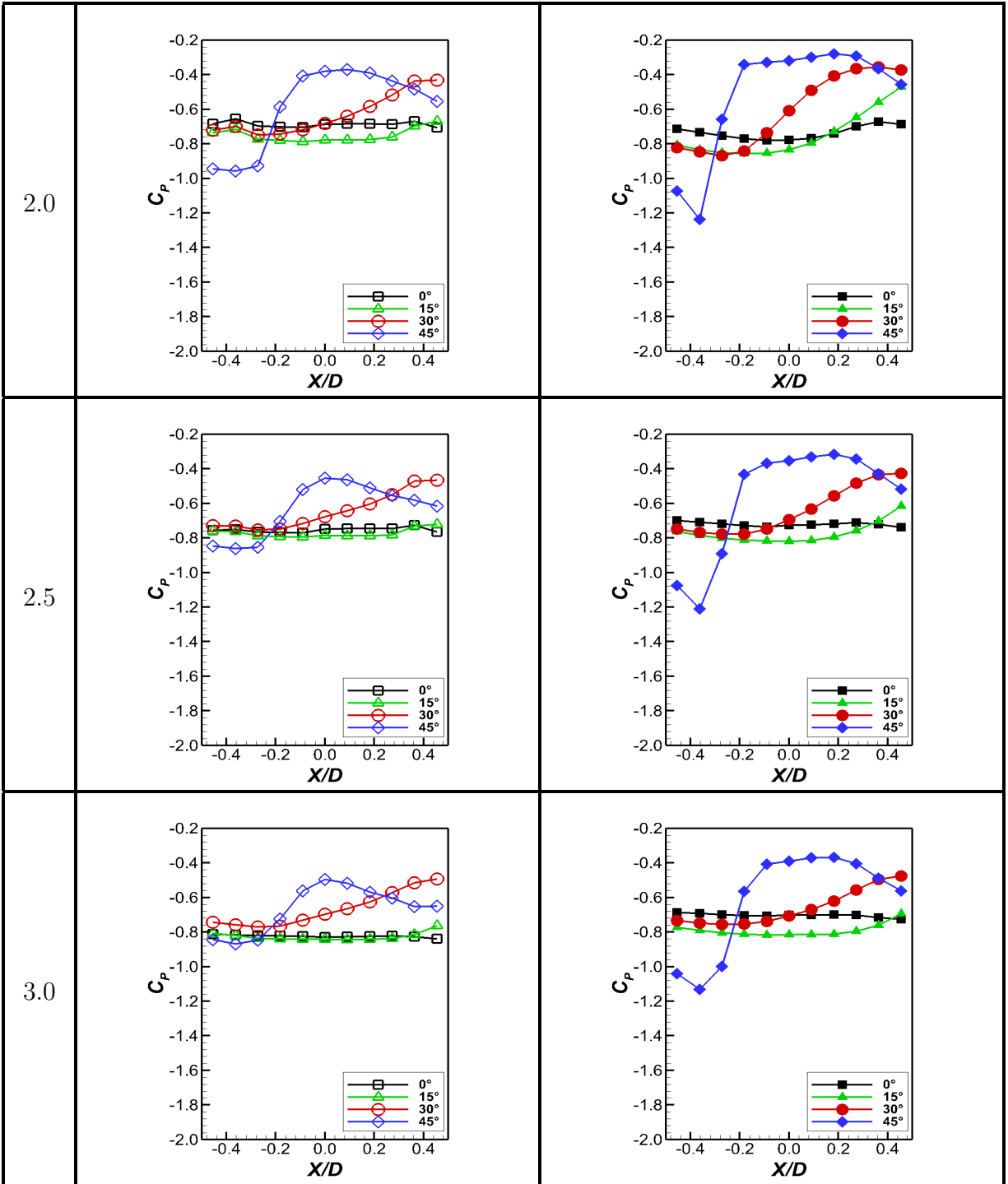
# APPENDIX B

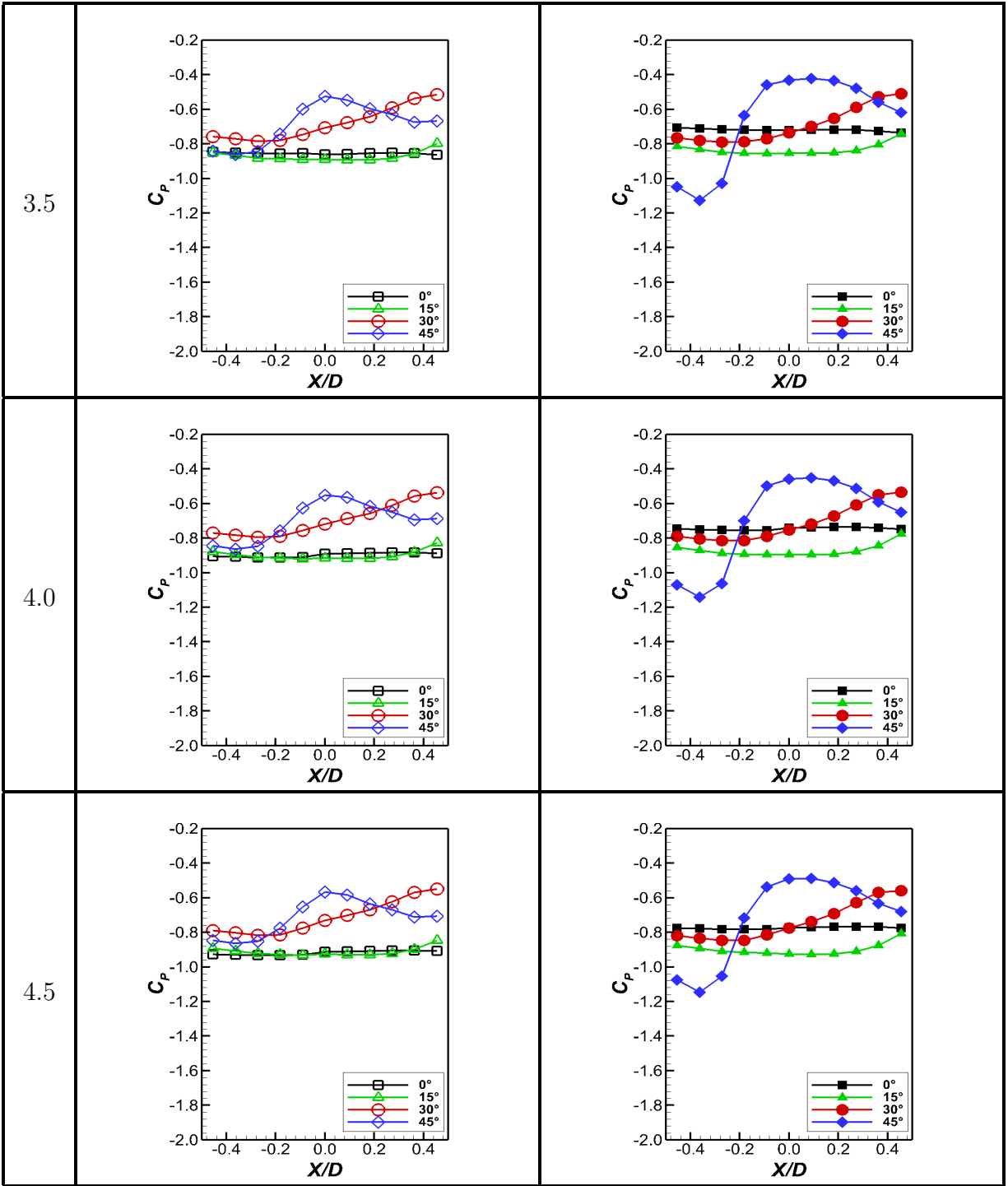
## CENTERLINE $C_P$ PROFILES

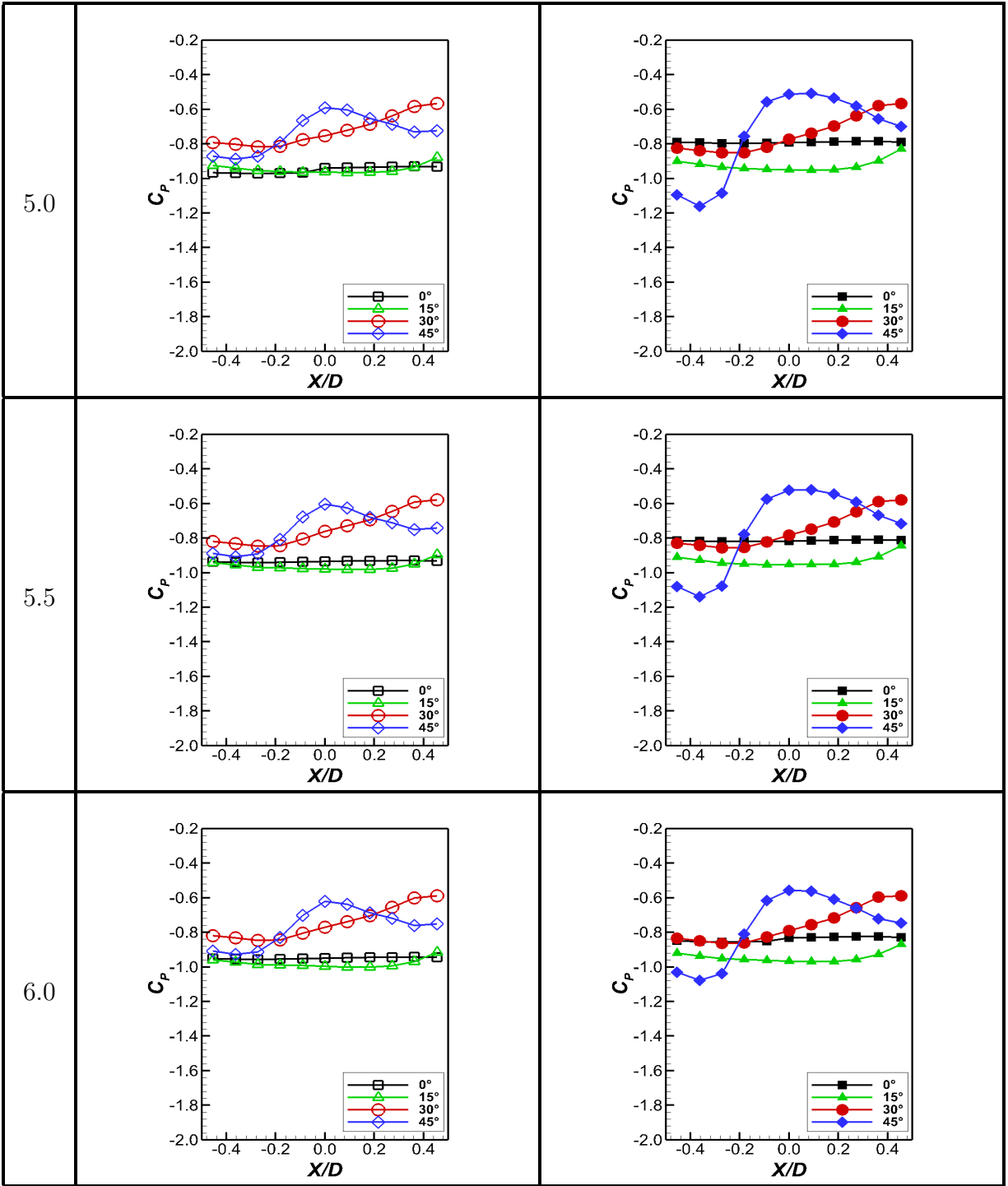
This appendix contains the information of the centerline pressure profiles at four selected incidence angles of  $= 0^\circ, 15^\circ, 30^\circ$ , and  $45^\circ$ , along the  $X$ -axis that is fixed with the free-end surface, and rotated with the prism. All the tested aspect ratios from  $AR = 1$  to  $11$  are presented for both boundary layers. The results of the thin and thick boundary layers are shown in the left and right, respectively.

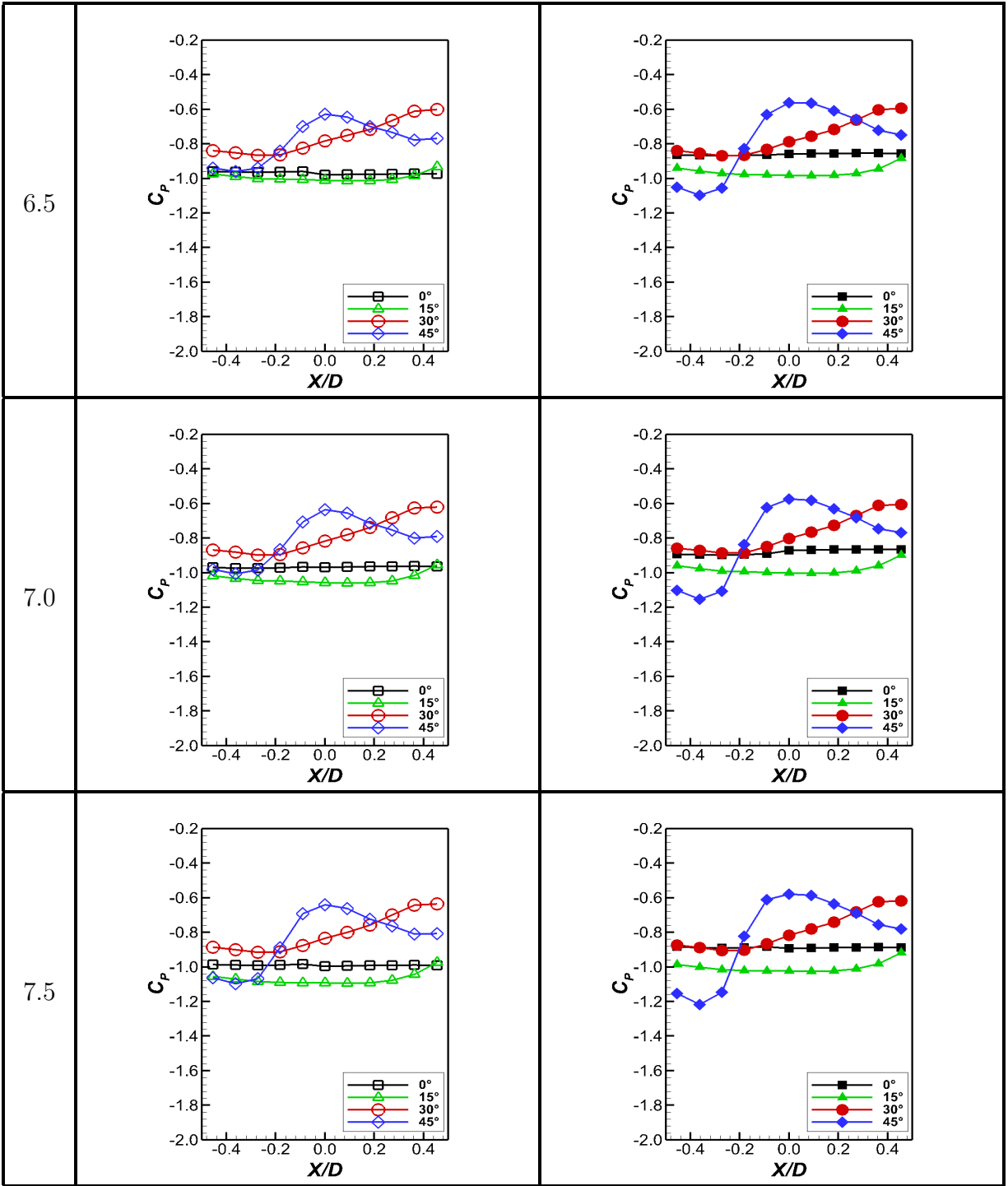
**Table B.1:** Centerline mean  $C_P$  profiles (where  $X =$  is a coordinate fixed to the prism free-end surface, and rotates with the prism) at (a)  $AR = 1$ , (b)  $AR = 1.5$ , (c)  $AR = 4.5$ , (d)  $AR = 7$ , (e)  $AR = 9$ , and (f)  $AR = 11$  at selected  $\alpha = 0^\circ, 15^\circ, 30^\circ$  and  $45^\circ$ .

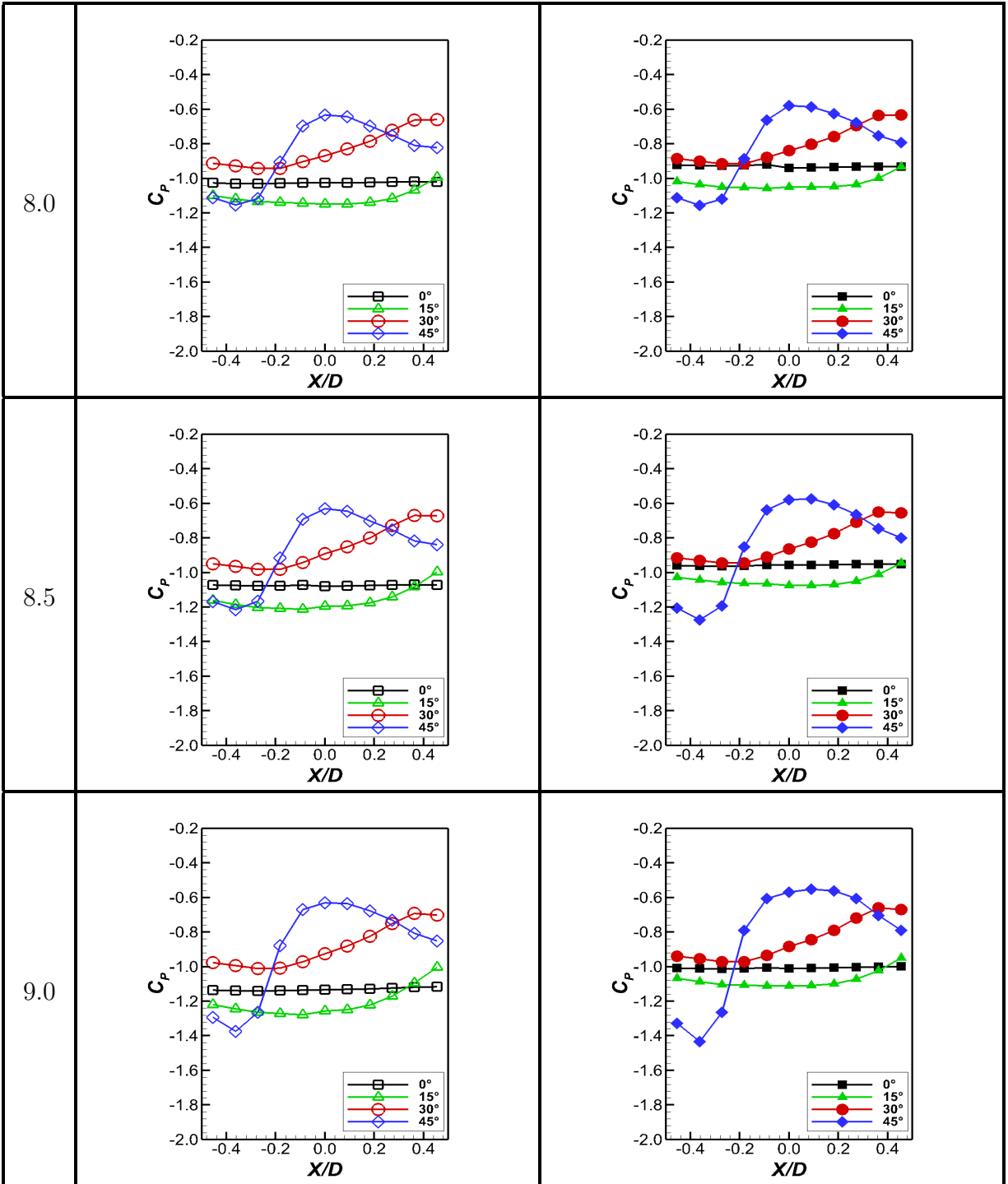


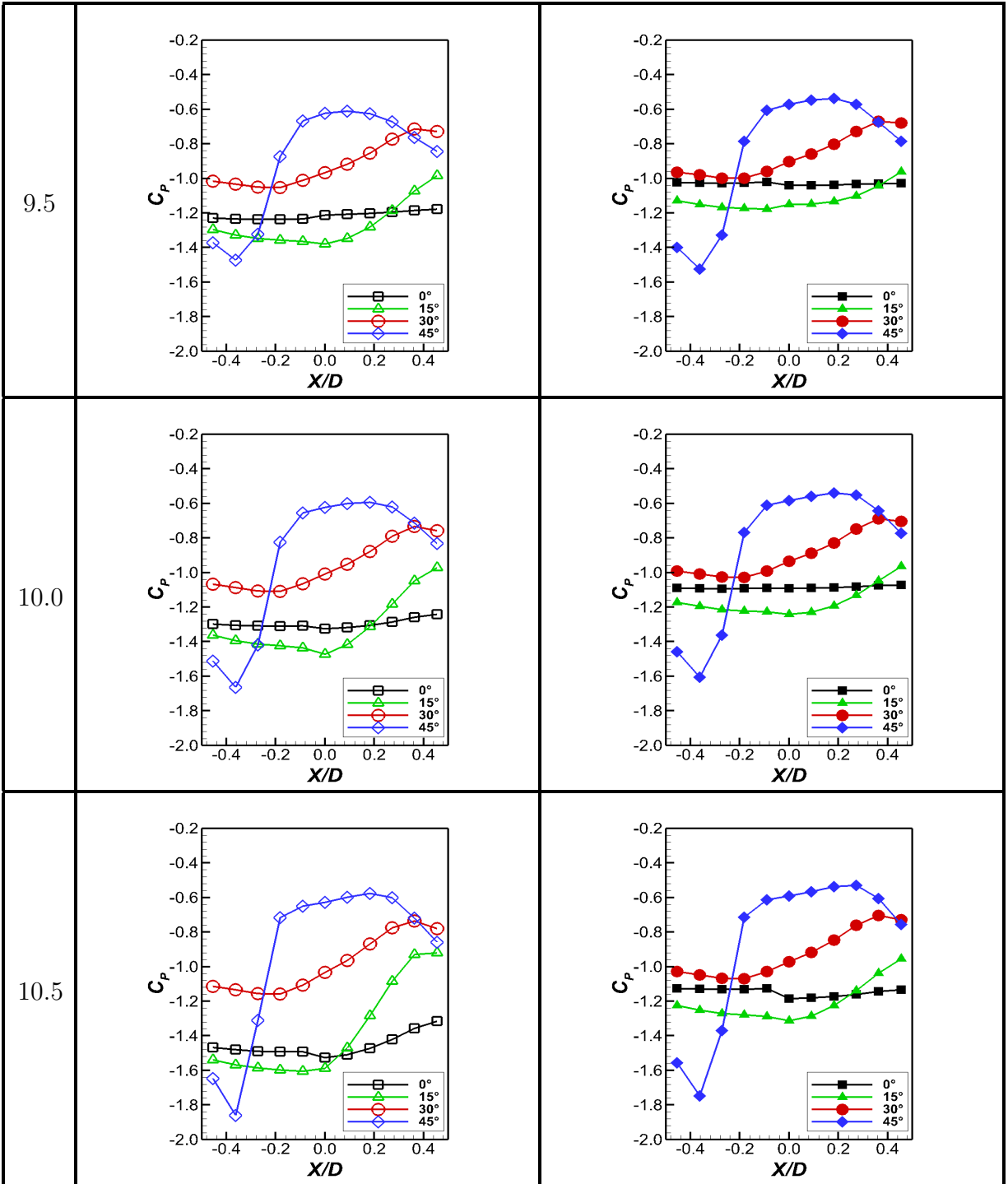




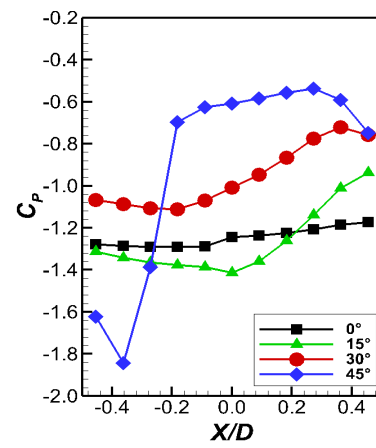
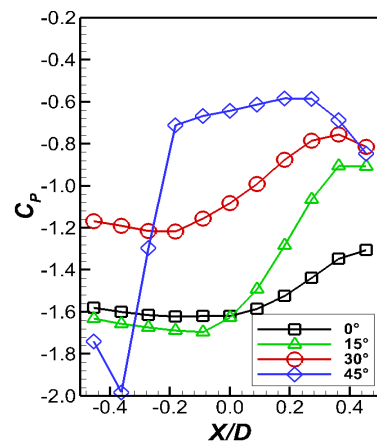








11.0

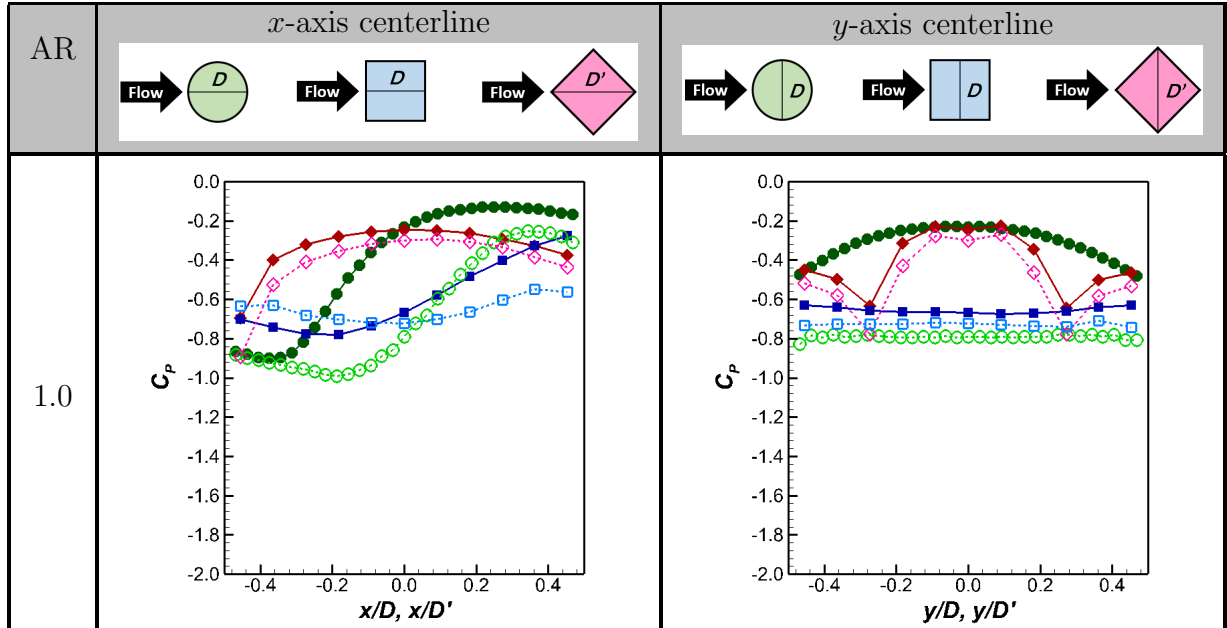


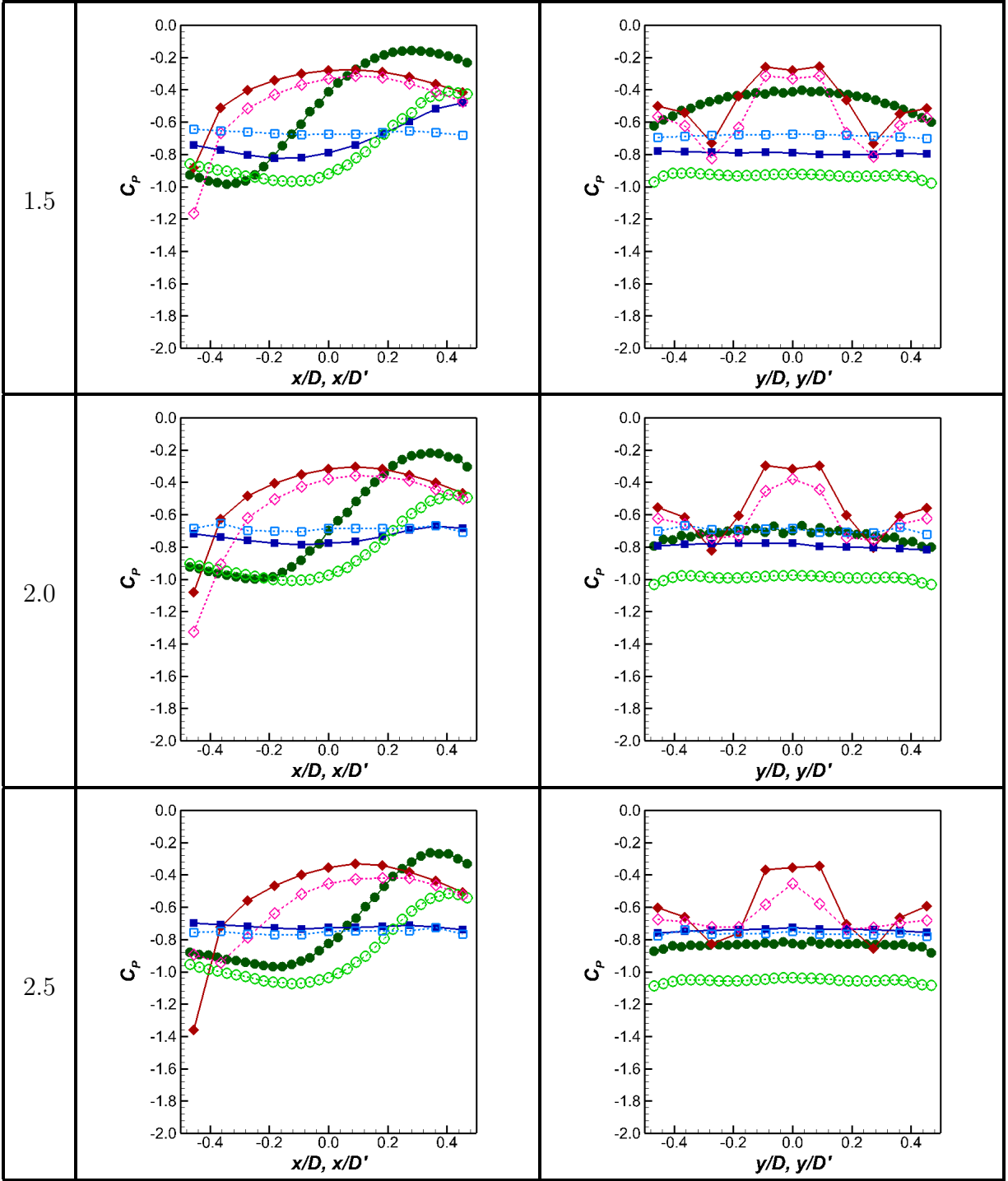
# APPENDIX C

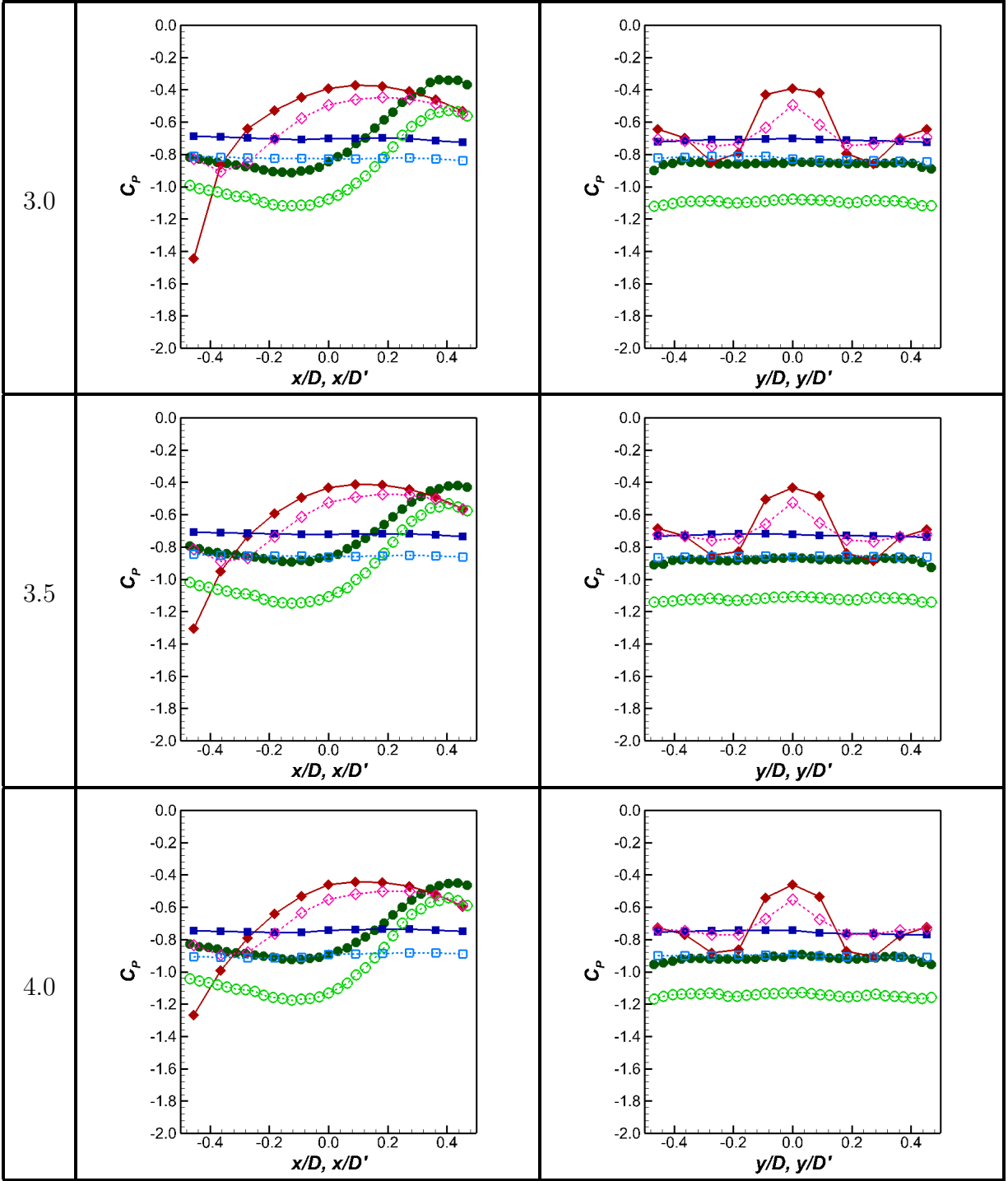
## COMPARISON OF THE $C_P$ PROFILES FOR THE CYLINDER AND SQUARE PRISM

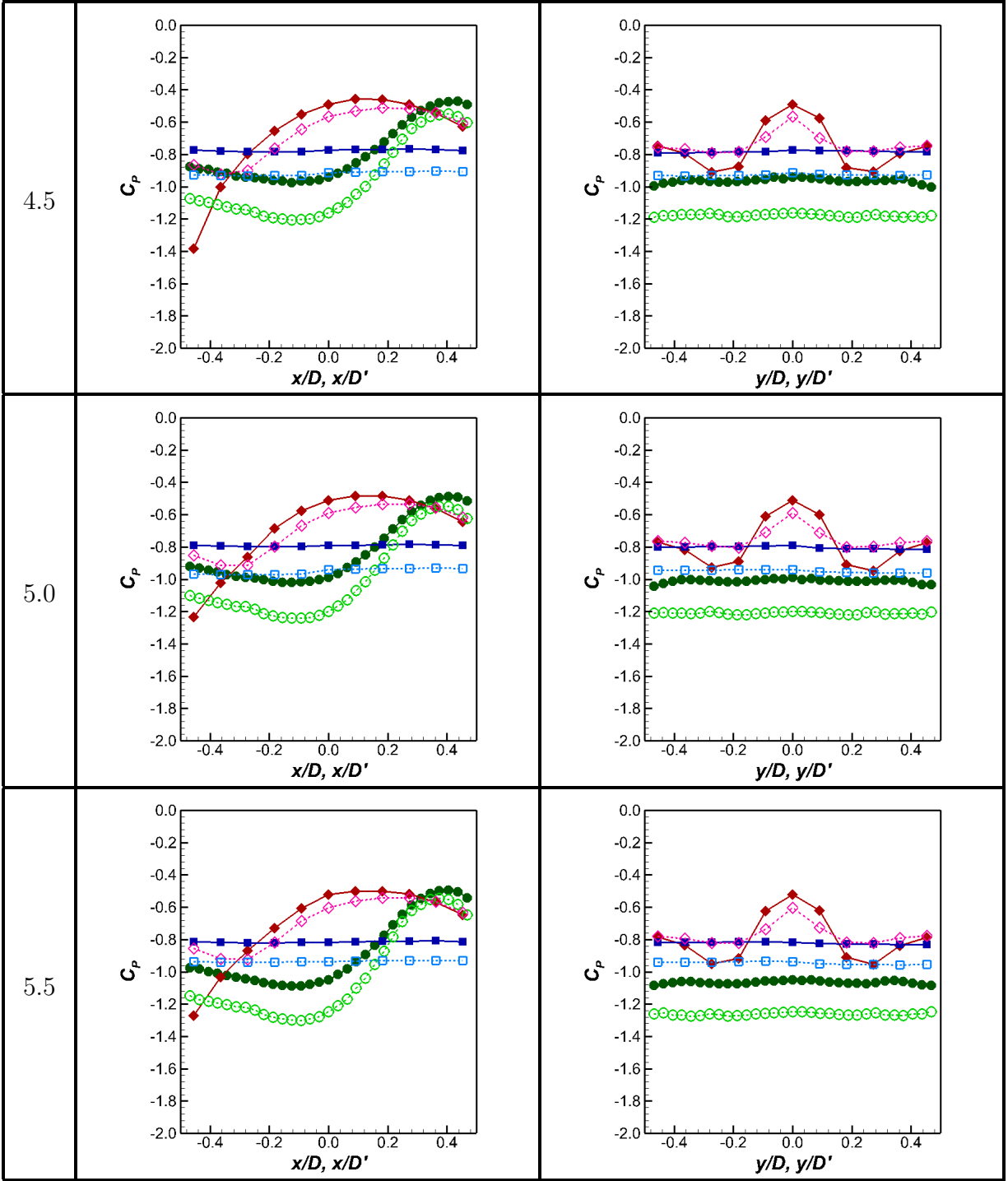
This appendix compares the results of the present thesis and the thesis of Beitel (2017) for the centerline  $C_P$  profile. The profiles along the  $x$ -axis (parallel to the flow) are shown in the left, while the profiles along the  $y$ -axis (perpendicular to the flow) are shown in the right. The square prisms of the present thesis are shown for two incidence angles of  $\alpha = 0^\circ$  and  $45^\circ$ . For both theses, the information of all the tested aspect ratios from  $AR = 1$  to 11 for both boundary layers are presented.

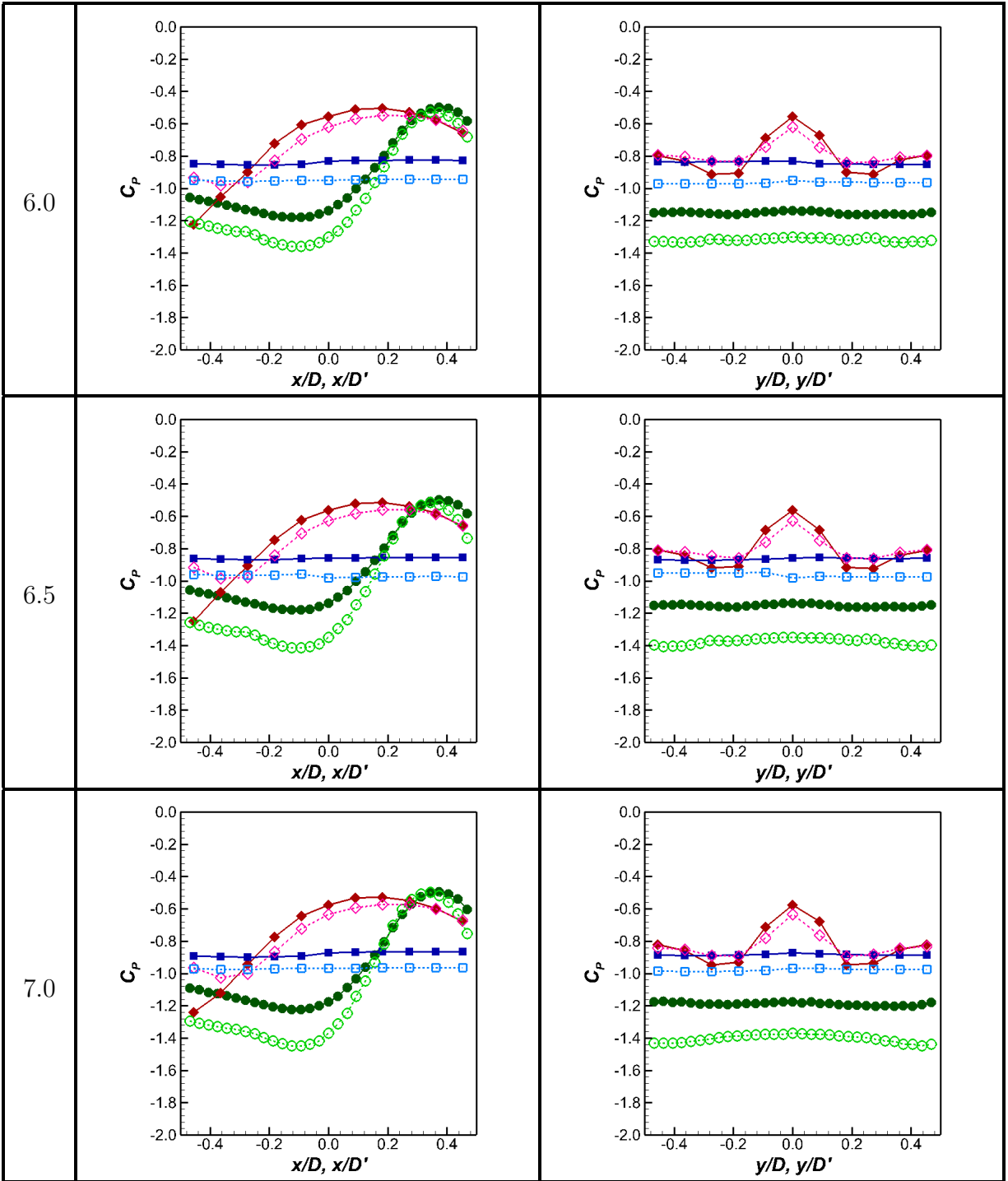
**Table C.1:** Comparison of  $x$ -axis and  $y$ -axis centerline  $C_P$  profile between square prisms at  $\alpha = 0^\circ$  (blue square) and  $\alpha = 45^\circ$  (normalized with projected width,  $D'$ ) (red diamond), and circular cylinder studied by Beitel (2017) (green circle), for  $AR = 1$  to 11.  $Re = 6.5 \times 10^4$  for both studies. Open symbol and dashed line represent the thin boundary layer ( $\delta/D = 0.8$  (present) and 0.6 (Beitel (2017)))); solid symbol and solid line represent the thick boundary layer ( $\delta/D = 2.6$  (present) and 1.9 (Beitel (2017)))).

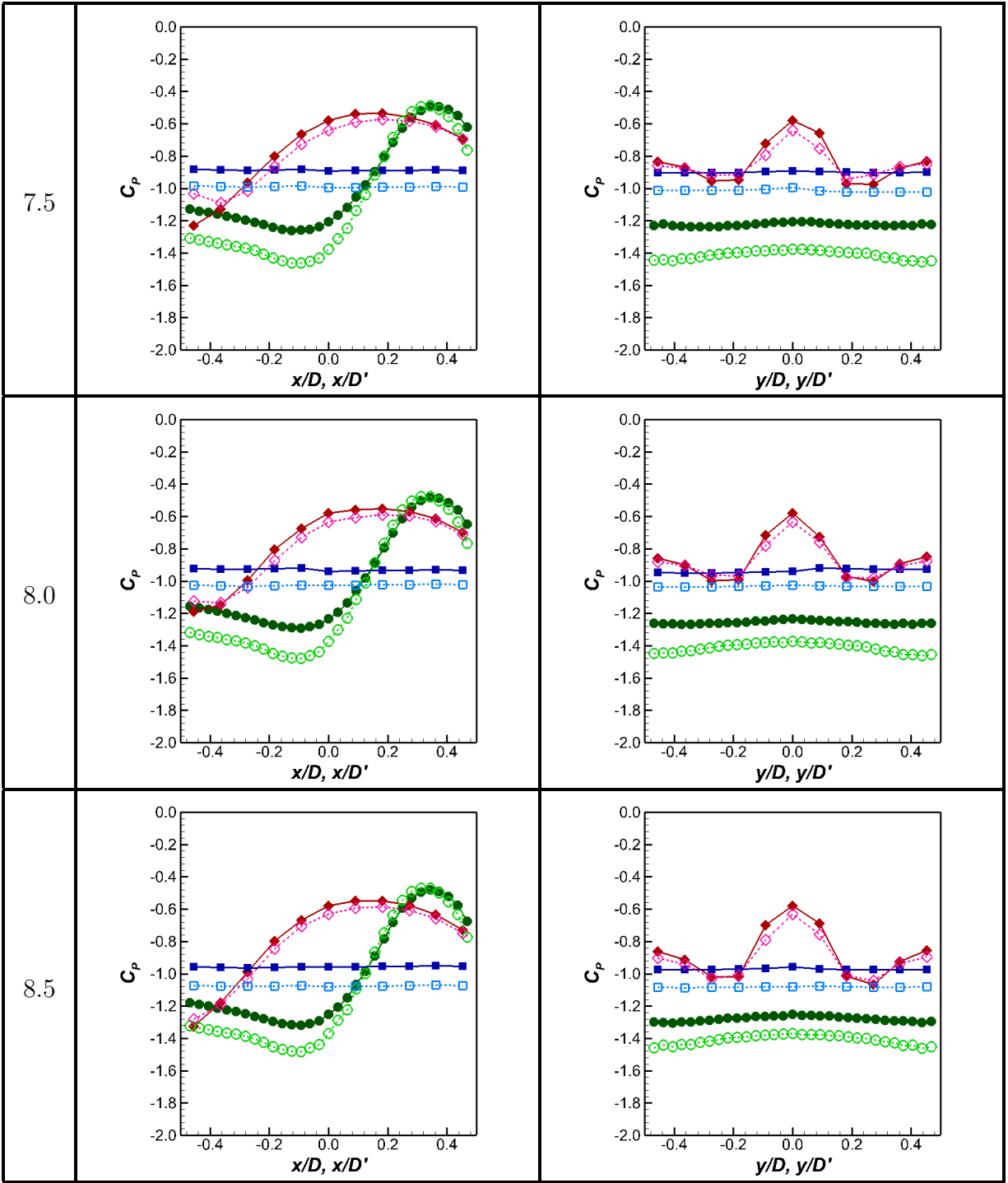


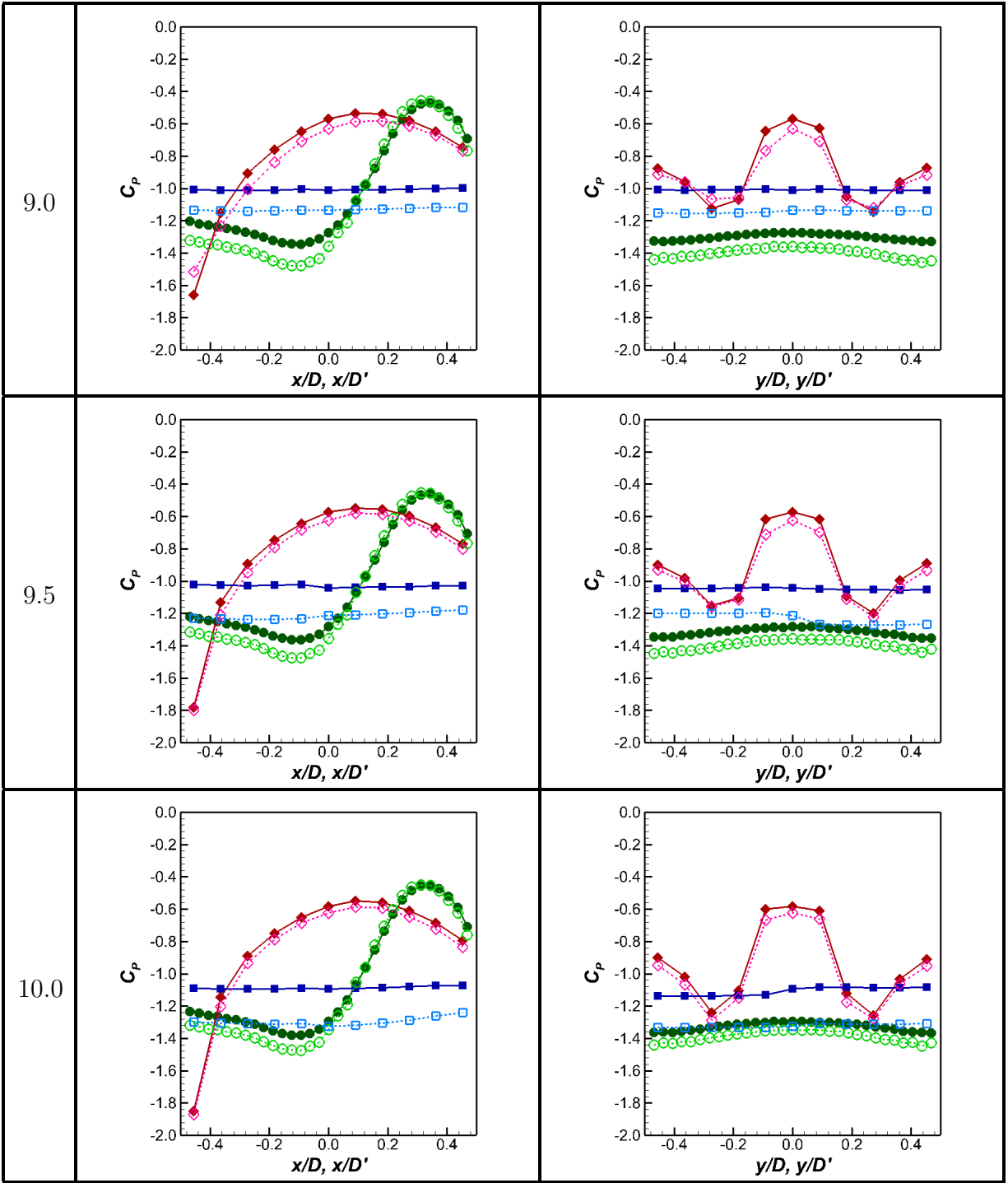


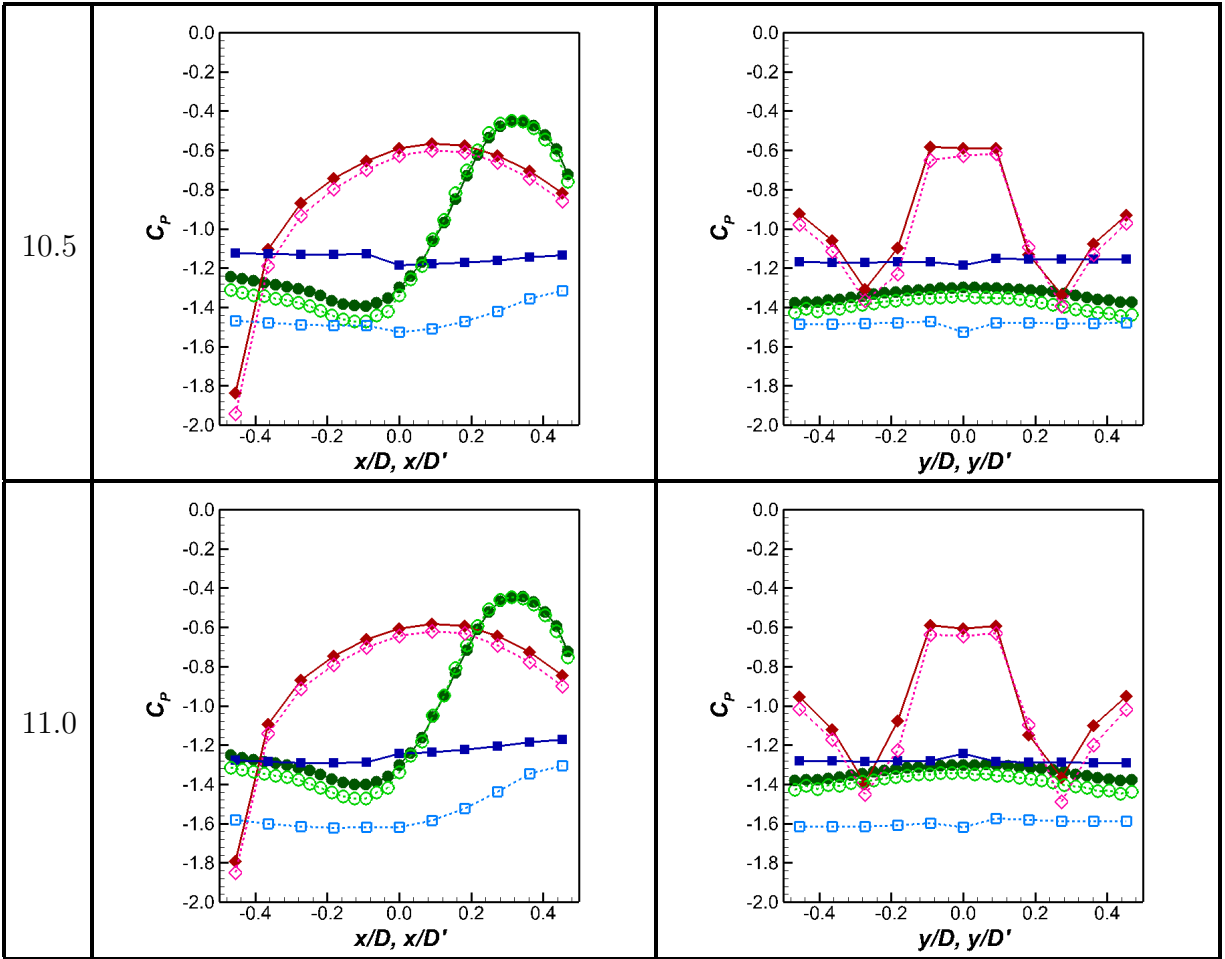












# APPENDIX D

## PERMISSION AGREEMENTS

This appendix contains the permissions obtained from the publishers for using the figures in the present thesis, presented in the order of appearance.

### CAMBRIDGE UNIVERSITY PRESS LICENSE TERMS AND CONDITIONS

Jul 08, 2019

This Agreement between University of Saskatchewan -- Herman Heng ("You") and Cambridge University Press ("Cambridge University Press") consists of your license details and the terms and conditions provided by Cambridge University Press and Copyright Clearance Center.

License Number	4624401127195
License date	Jul 08, 2019
Licensed Content Publisher	Cambridge University Press
Licensed Content Publication	The Journal of Fluid Mechanics
Licensed Content Title	The finite-length square cylinder near wake
Licensed Content Author	H. F. WANG, Y. ZHOU
Licensed Content Date	Oct 5, 2009
Licensed Content Volume	638
Licensed Content Issue	undefined
Start page	453
End page	490
Type of Use	Dissertation/Thesis
Requestor type	Author
Portion	Text extract
Number of pages requested	5
Author of this Cambridge University Press article	No
Author / editor of the new work	Yes
Order reference number	
Territory for reuse	World
Title of your thesis / dissertation	Experimental Investigation of the Free-end Pressure Distribution for Surface-Mounted Finite-Height Square Prisms
Expected completion date	Oct 2019
Estimated size(pages)	250
Requestor Location	University of Saskatchewan 57 Campus Drive  Saskatoon, SK S7N5A9 Canada Attn: University of Saskatchewan
Publisher Tax ID	123258667RT0001
Total	0.00 CAD

**ELSEVIER LICENSE  
TERMS AND CONDITIONS**

Jul 09, 2019

This Agreement between University of Saskatchewan -- Herman Heng ("You") and Elsevier ("Elsevier") consists of your license details and the terms and conditions provided by Elsevier and Copyright Clearance Center.

License Number	4624380025990
License date	Jul 08, 2019
Licensed Content Publisher	Elsevier
Licensed Content Publication	Journal of Wind Engineering and Industrial Aerodynamics
Licensed Content Title	Flow patterns and vortex shedding behavior behind a square cylinder
Licensed Content Author	Shun C. Yen, Chen W. Yang
Licensed Content Date	Aug 1, 2011
Licensed Content Volume	99
Licensed Content Issue	8
Licensed Content Pages	11
Start Page	868
End Page	878
Type of Use	reuse in a thesis/dissertation
Intended publisher of new work	other
Portion	figures/tables/illustrations
Number of figures/tables/illustrations	1
Format	both print and electronic
Are you the author of this Elsevier article?	No
Will you be translating?	No
Original figure numbers	Figure 4
Title of your thesis/dissertation	Experimental Investigation of the Free-end Pressure Distribution for Surface-Mounted Finite-Height Square Prisms
Expected completion date	Oct 2019
Estimated size (number of pages)	250
Requestor Location	University of Saskatchewan 57 Campus Drive  Saskatoon, SK S7N5A9 Canada Attn: University of Saskatchewan
Publisher Tax ID	GB 494 6272 12
Total	0.00 USD

**AIP PUBLISHING LICENSE  
TERMS AND CONDITIONS**

Jul 09, 2019

This Agreement between University of Saskatchewan -- Herman Heng ("You") and AIP Publishing ("AIP Publishing") consists of your license details and the terms and conditions provided by AIP Publishing and Copyright Clearance Center.

License Number	4624390563777
License date	Jul 08, 2019
Licensed Content Publisher	AIP Publishing
Licensed Content Publication	Physics of Fluids
Licensed Content Title	Alternating half-loop shedding in the turbulent wake of a finite surface-mounted square cylinder with a thin boundary layer
Licensed Content Author	J. A. Bourgeois, P. Sattari, R. J. Martinuzzi
Licensed Content Date	Sep 1, 2011
Licensed Content Volume	23
Licensed Content Issue	9
Type of Use	Thesis/Dissertation
Requestor type	Student
Format	Print and electronic
Portion	Figure/Table
Number of figures/tables	1
Title of your thesis / dissertation	Experimental Investigation of the Free-end Pressure Distribution for Surface-Mounted Finite-Height Square Prisms
Expected completion date	Oct 2019
Estimated size (number of pages)	250
Requestor Location	University of Saskatchewan 57 Campus Drive  Saskatoon, SK S7N5A9 Canada Attn: University of Saskatchewan
Total	0.00 USD

**AIP PUBLISHING LICENSE  
TERMS AND CONDITIONS**

Jul 09, 2019

This Agreement between University of Saskatchewan -- Herman Heng ("You") and AIP Publishing ("AIP Publishing") consists of your license details and the terms and conditions provided by AIP Publishing and Copyright Clearance Center.

License Number	4624390702547
License date	Jul 08, 2019
Licensed Content Publisher	AIP Publishing
Licensed Content Publication	Physics of Fluids
Licensed Content Title	Low-Reynolds-number flow around a wall-mounted square cylinder: Flow structures and onset of vortex shedding
Licensed Content Author	M. R. Rastan, A. Sohankar, Md. Mahbub Alam
Licensed Content Date	Oct 1, 2017
Licensed Content Volume	29
Licensed Content Issue	10
Type of Use	Thesis/Dissertation
Requestor type	Student
Format	Print and electronic
Portion	Figure/Table
Number of figures/tables	1
Title of your thesis / dissertation	Experimental Investigation of the Free-end Pressure Distribution for Surface-Mounted Finite-Height Square Prisms
Expected completion date	Oct 2019
Estimated size (number of pages)	250
Requestor Location	University of Saskatchewan 57 Campus Drive  Saskatoon, SK S7N5A9 Canada Attn: University of Saskatchewan
Total	0.00 USD

SPRINGER NATURE LICENSE TERMS AND CONDITIONS	
Jul 08, 2019	
<p>This Agreement between University of Saskatchewan -- Herman Heng ("You") and Springer Nature ("Springer Nature") consists of your license details and the terms and conditions provided by Springer Nature and Copyright Clearance Center.</p>	
License Number	4624390913834
License date	Jul 08, 2019
Licensed Content Publisher	Springer Nature
Licensed Content Publication	Experiments in Fluids
Licensed Content Title	Low-frequency dynamics in the turbulent wake of cantilevered square and circular cylinders protruding a thin laminar boundary layer
Licensed Content Author	Matthew G. Kindree, Maryam Shahroodi, Robert J. Martinuzzi
Licensed Content Date	Jan 1, 2018
Licensed Content Volume	59
Licensed Content Issue	12
Type of Use	Thesis/Dissertation
Requestor type	academic/university or research institute
Format	print and electronic
Portion	figures/tables/illustrations
Number of figures/tables/illustrations	1
Will you be translating?	no
Circulation/distribution	<501
Author of this Springer Nature content	no
Title	Experimental Investigation of the Free-end Pressure Distribution for Surface-Mounted Finite-Height Square Prisms
Institution name	University of Saskatchewan
Expected presentation date	Oct 2019
Portions	Figure 7
Requestor Location	University of Saskatchewan 57 Campus Drive  Saskatoon, SK S7N5A9 Canada Attn: University of Saskatchewan
Total	0.00 USD

**ELSEVIER LICENSE  
TERMS AND CONDITIONS**

Jul 09, 2019

---

This Agreement between University of Saskatchewan -- Herman Heng ("You") and Elsevier ("Elsevier") consists of your license details and the terms and conditions provided by Elsevier and Copyright Clearance Center.

License Number	4624380499363
License date	Jul 08, 2019
Licensed Content Publisher	Elsevier
Licensed Content Publication	International Journal of Heat and Fluid Flow
Licensed Content Title	The effect of incidence angle on the mean wake of surface-mounted finite-height square prisms
Licensed Content Author	S. Unnikrishnan,A. Ogunremi,D. Sumner
Licensed Content Date	Aug 1, 2017
Licensed Content Volume	66
Licensed Content Issue	n/a
Licensed Content Pages	20
Start Page	137
End Page	156
Type of Use	reuse in a thesis/dissertation
Intended publisher of new work	other
Portion	figures/tables/illustrations
Number of figures/tables/illustrations	1
Format	both print and electronic
Are you the author of this Elsevier article?	No
Will you be translating?	No
Original figure numbers	Figure 13(a)(b)(c)(d)
Title of your thesis/dissertation	Experimental Investigation of the Free-end Pressure Distribution for Surface-Mounted Finite-Height Square Prisms
Expected completion date	Oct 2019
Estimated size (number of pages)	250
Requestor Location	University of Saskatchewan 57 Campus Drive  Saskatoon, SK S7N5A9 Canada Attn: University of Saskatchewan
Publisher Tax ID	GB 494 6272 12
Total	0.00 USD

**ELSEVIER LICENSE  
TERMS AND CONDITIONS**

Jul 09, 2019

This Agreement between University of Saskatchewan -- Herman Heng ("You") and Elsevier ("Elsevier") consists of your license details and the terms and conditions provided by Elsevier and Copyright Clearance Center.

License Number	4624380931717
License date	Jul 08, 2019
Licensed Content Publisher	Elsevier
Licensed Content Publication	International Journal of Heat and Mass Transfer
Licensed Content Title	Local heat transfer around a wall-mounted cube in the turbulent boundary layer
Licensed Content Author	Hajime Nakamura,Tamotsu Igarashi,Takayuki Tsutsui
Licensed Content Date	Sep 1, 2001
Licensed Content Volume	44
Licensed Content Issue	18
Licensed Content Pages	11
Start Page	3385
End Page	3395
Type of Use	reuse in a thesis/dissertation
Intended publisher of new work	other
Portion	figures/tables/illustrations
Number of figures/tables/illustrations	2
Format	both print and electronic
Are you the author of this Elsevier article?	No
Will you be translating?	No
Original figure numbers	Figure 7, Figure 8(b)
Title of your thesis/dissertation	Experimental Investigation of the Free-end Pressure Distribution for Surface-Mounted Finite-Height Square Prisms
Expected completion date	Oct 2019
Estimated size (number of pages)	250
Requestor Location	University of Saskatchewan 57 Campus Drive  Saskatoon, SK S7N5A9 Canada Attn: University of Saskatchewan
Publisher Tax ID	GB 494 6272 12
Total	0.00 USD

**ELSEVIER LICENSE  
TERMS AND CONDITIONS**

Jul 09, 2019

This Agreement between University of Saskatchewan -- Herman Heng ("You") and Elsevier ("Elsevier") consists of your license details and the terms and conditions provided by Elsevier and Copyright Clearance Center.

License Number	4624370563074
License date	Jul 08, 2019
Licensed Content Publisher	Elsevier
Licensed Content Publication	Journal of Wind Engineering and Industrial Aerodynamics
Licensed Content Title	Conical vortices over side face of a three-dimensional square prism
Licensed Content Author	Y Okuda,Y Taniike
Licensed Content Date	Dec 1, 1993
Licensed Content Volume	50
Licensed Content Issue	n/a
Licensed Content Pages	10
Start Page	163
End Page	172
Type of Use	reuse in a thesis/dissertation
Intended publisher of new work	other
Portion	figures/tables/illustrations
Number of figures/tables/illustrations	1
Format	both print and electronic
Are you the author of this Elsevier article?	No
Will you be translating?	No
Original figure numbers	Figure 9
Title of your thesis/dissertation	Experimental Investigation of the Free-end Pressure Distribution for Surface-Mounted Finite-Height Square Prisms
Expected completion date	Oct 2019
Estimated size (number of pages)	250
Requestor Location	University of Saskatchewan 57 Campus Drive  Saskatoon, SK S7N5A9 Canada Attn: University of Saskatchewan
Publisher Tax ID	GB 494 6272 12
Total	0.00 USD

**American Society of Mechanical Engineers ASME LICENSE  
TERMS AND CONDITIONS**

Jul 16, 2019

This is a License Agreement between University of Saskatchewan -- Herman Heng ("You") and American Society of Mechanical Engineers ASME ("American Society of Mechanical Engineers ASME") provided by Copyright Clearance Center ("CCC"). The license consists of your order details, the terms and conditions provided by American Society of Mechanical Engineers ASME, and the payment terms and conditions.

**All payments must be made in full to CCC. For payment instructions, please see information listed at the bottom of this form.**

License Number	4630970044910
License date	Jul 08, 2019
Licensed content publisher	American Society of Mechanical Engineers ASME
Licensed content title	Journal of fluids engineering
Licensed content date	Jan 1, 1973
Type of Use	Thesis/Dissertation
Requestor type	Academic institution
Format	Print, Electronic
Portion	chart/graph/table/figure
Number of charts/graphs/tables/figures	7
The requesting person/organization is:	Herman Heng
Title or numeric reference of the portion(s)	Figure 1, Figure 2, Figure 4(a)(b)(c), Figure 10(a)(b)
Title of the article or chapter the portion is from	An experimental investigation of aspect ratio and incidence angle effects for the flow around surface-mounted finite-height square prisms
Editor of portion(s)	ASME
Author of portion(s)	McClellan J, Sumner D
Volume of serial or monograph.	136
Page range of the portion	081206
Publication date of portion	August 2014
Rights for	Main product
Duration of use	Life of current edition
Creation of copies for the disabled	no
With minor editing privileges	no
For distribution to	Worldwide
In the following language(s)	Original language of publication
With incidental promotional use	no
The lifetime unit quantity of new product	Up to 499
Title	Experimental Investigation of the Free-end Pressure Distribution for Surface-Mounted Finite-Height Square Prisms
Institution name	University of Saskatchewan
Expected presentation date	Oct 2019
Billing Type	Invoice
Billing Address	University of Saskatchewan 57 Campus Drive  Saskatoon, SK S7N5A9 Canada Attn: University of Saskatchewan
Total (may include CCC user fee)	0.00 USD

**ELSEVIER LICENSE  
TERMS AND CONDITIONS**

Jul 09, 2019

This Agreement between University of Saskatchewan -- Herman Heng ("You") and Elsevier ("Elsevier") consists of your license details and the terms and conditions provided by Elsevier and Copyright Clearance Center.

License Number	4624381166730
License date	Jul 08, 2019
Licensed Content Publisher	Elsevier
Licensed Content Publication	International Journal of Heat and Fluid Flow
Licensed Content Title	Influence of aspect ratio on the mean flow field of a surface-mounted finite-height square prism
Licensed Content Author	D. Sumner,N. Rostamy,D.J. Bergstrom,J.D. Bugg
Licensed Content Date	Jun 1, 2017
Licensed Content Volume	65
Licensed Content Issue	n/a
Licensed Content Pages	20
Start Page	1
End Page	20
Type of Use	reuse in a thesis/dissertation
Intended publisher of new work	other
Portion	figures/tables/illustrations
Number of figures/tables/illustrations	3
Format	both print and electronic
Are you the author of this Elsevier article?	No
Will you be translating?	No
Original figure numbers	Figure 6, Figure 8(a)(b)(c)(d), Figure 14(d)
Title of your thesis/dissertation	Experimental Investigation of the Free-end Pressure Distribution for Surface-Mounted Finite-Height Square Prisms
Expected completion date	Oct 2019
Estimated size (number of pages)	250
Requestor Location	University of Saskatchewan 57 Campus Drive  Saskatoon, SK S7N5A9 Canada Attn: University of Saskatchewan
Publisher Tax ID	GB 494 6272 12
Total	0.00 USD

**ELSEVIER LICENSE  
TERMS AND CONDITIONS**

Jul 09, 2019

This Agreement between University of Saskatchewan -- Herman Heng ("You") and Elsevier ("Elsevier") consists of your license details and the terms and conditions provided by Elsevier and Copyright Clearance Center.

License Number	4624370239975
License date	Jul 08, 2019
Licensed Content Publisher	Elsevier
Licensed Content Publication	Journal of Wind Engineering and Industrial Aerodynamics
Licensed Content Title	Investigation of wall pressures and surface flow patterns on a wall-mounted square cylinder using very high-resolution Cartesian mesh
Licensed Content Author	Yong Cao,Tetsuro Tamura,Hidenori Kawai
Licensed Content Date	May 1, 2019
Licensed Content Volume	188
Licensed Content Issue	n/a
Licensed Content Pages	18
Start Page	1
End Page	18
Type of Use	reuse in a thesis/dissertation
Portion	figures/tables/illustrations
Number of figures/tables/illustrations	2
Format	both print and electronic
Are you the author of this Elsevier article?	No
Will you be translating?	No
Original figure numbers	Figure 12, Figure 25
Title of your thesis/dissertation	Experimental Investigation of the Free-end Pressure Distribution for Surface-Mounted Finite-Height Square Prisms
Expected completion date	Oct 2019
Estimated size (number of pages)	250
Requestor Location	University of Saskatchewan 57 Campus Drive  Saskatoon, SK S7N5A9 Canada Attn: University of Saskatchewan
Publisher Tax ID	GB 494 6272 12
Total	0.00 CAD

**ELSEVIER LICENSE  
TERMS AND CONDITIONS**

Jul 09, 2019

This Agreement between University of Saskatchewan -- Herman Heng ("You") and Elsevier ("Elsevier") consists of your license details and the terms and conditions provided by Elsevier and Copyright Clearance Center.

License Number	4624380665401
License date	Jul 08, 2019
Licensed Content Publisher	Elsevier
Licensed Content Publication	International Journal of Heat and Fluid Flow
Licensed Content Title	Local heat transfer around a wall-mounted cube at 45° to flow in a turbulent boundary layer
Licensed Content Author	Hajime Nakamura,Tamotsu Igarashi,Takayuki Tsutsui
Licensed Content Date	Dec 1, 2003
Licensed Content Volume	24
Licensed Content Issue	6
Licensed Content Pages	9
Start Page	807
End Page	815
Type of Use	reuse in a thesis/dissertation
Intended publisher of new work	other
Portion	figures/tables/illustrations
Number of figures/tables/illustrations	1
Format	both print and electronic
Are you the author of this Elsevier article?	No
Will you be translating?	No
Original figure numbers	Figure 9(b)
Title of your thesis/dissertation	Experimental Investigation of the Free-end Pressure Distribution for Surface-Mounted Finite-Height Square Prisms
Expected completion date	Oct 2019
Estimated size (number of pages)	250
Requestor Location	University of Saskatchewan 57 Campus Drive  Saskatoon, SK S7N5A9 Canada Attn: University of Saskatchewan
Publisher Tax ID	GB 494 6272 12
Total	0.00 USD

**From:** Techno-press <[was@techno-press.com](mailto:was@techno-press.com)>  
**Sent:** Thursday, July 11, 2019 11:38 AM  
**To:** [info@techno-press.com](mailto:info@techno-press.com)  
**Subject:** RE: Republish or display content in Journal of Wind & Structures (copyrighted by Techno-Press)  
**Importance:** High

Dear Heng:

Thank you for your inquiry.

We are happy to grant a permission to use our copyright.

Sincerely yours,

Chang-Koon Choi  
Editor-in-Chief

CKC/hjl

---

**From:** Heng, Cloud <[cloud.heng@usask.ca](mailto:cloud.heng@usask.ca)>  
**Sent:** Tuesday, July 09, 2019 7:13 AM  
**To:** [info@techno-press.com](mailto:info@techno-press.com)  
**Subject:** Republish or display content in Journal of Wind & Structures (copyrighted by Techno-Press)

Dear Sir / Madam,

Good day. I would like to seek for some assistance on how to obtain permission from Techno-Press Ltd to reproduce / republish some copyrighted figures owned by Techno-Press. I am a Master of Science student at the University of Saskatchewan. These figures will be used in my thesis and only for academic purpose. Below are the details of the figures that I would like to obtain the permission from your side for reproducing:

**Journal title:** Journal of Wind and Structures

**Article title:** Detached eddy simulation of flow around rectangular bodies with different aspect ratios

**Author:** Lim H, Ohba M

**Volume:** 20

**No:** 1

**Year:** 2015

**Figure to be reproduced:** Figure 11(a)

**Journal title:** Journal of Wind and Structures

**Article title:** Pressure distribution on rectangular buildings with changes in aspect ratio and wind direction

**Author:** Lee Y, Boo S, Lim H, Misutani K

**Volume:** 23

**No:** 5

**Year:** 2016

**Figure to be reproduced:** Figure 7

**ELSEVIER LICENSE  
TERMS AND CONDITIONS**

Jul 09, 2019

This Agreement between University of Saskatchewan -- Herman Heng ("You") and Elsevier ("Elsevier") consists of your license details and the terms and conditions provided by Elsevier and Copyright Clearance Center.

License Number	4624370739948
License date	Jul 08, 2019
Licensed Content Publisher	Elsevier
Licensed Content Publication	Journal of Wind Engineering and Industrial Aerodynamics
Licensed Content Title	Wind interference effects of high-rise building on low-rise building with flat roof
Licensed Content Author	Bo Chen,Luxi Shang,Mengyi Qin,Xinzhong Chen,Qingshan Yang
Licensed Content Date	Dec 1, 2018
Licensed Content Volume	183
Licensed Content Issue	n/a
Licensed Content Pages	26
Start Page	88
End Page	113
Type of Use	reuse in a thesis/dissertation
Intended publisher of new work	other
Portion	figures/tables/illustrations
Number of figures/tables/illustrations	2
Format	both print and electronic
Are you the author of this Elsevier article?	No
Will you be translating?	No
Original figure numbers	Figure 3(a)(b), Figure 4(a)(b)
Title of your thesis/dissertation	Experimental Investigation of the Free-end Pressure Distribution for Surface-Mounted Finite-Height Square Prisms
Expected completion date	Oct 2019
Estimated size (number of pages)	250
Requestor Location	University of Saskatchewan 57 Campus Drive  Saskatoon, SK S7N5A9 Canada Attn: University of Saskatchewan
Publisher Tax ID	GB 494 6272 12
Total	0.00 USD

**ELSEVIER LICENSE  
TERMS AND CONDITIONS**

Jul 09, 2019

This Agreement between University of Saskatchewan -- Herman Heng ("You") and Elsevier ("Elsevier") consists of your license details and the terms and conditions provided by Elsevier and Copyright Clearance Center.

License Number	4624370962461
License date	Jul 08, 2019
Licensed Content Publisher	Elsevier
Licensed Content Publication	Journal of Wind Engineering and Industrial Aerodynamics
Licensed Content Title	Aerodynamic forces acting on a rectangular prism placed vertically in a turbulent boundary layer
Licensed Content Author	Hiroshi Sakamoto
Licensed Content Date	Apr 1, 1985
Licensed Content Volume	18
Licensed Content Issue	2
Licensed Content Pages	21
Start Page	131
End Page	151
Type of Use	reuse in a thesis/dissertation
Intended publisher of new work	other
Portion	figures/tables/illustrations
Number of figures/tables/illustrations	3
Format	both print and electronic
Are you the author of this Elsevier article?	No
Will you be translating?	No
Original figure numbers	Figure 8, Figure 10, Figure 14
Title of your thesis/dissertation	Experimental Investigation of the Free-end Pressure Distribution for Surface-Mounted Finite-Height Square Prisms
Expected completion date	Oct 2019
Estimated size (number of pages)	250
Requestor Location	University of Saskatchewan 57 Campus Drive  Saskatoon, SK S7N5A9 Canada Attn: University of Saskatchewan
Publisher Tax ID	GB 494 6272 12
Total	0.00 USD

**CAMBRIDGE UNIVERSITY PRESS LICENSE  
TERMS AND CONDITIONS**

Jul 08, 2019

This Agreement between University of Saskatchewan -- Herman Heng ("You") and Cambridge University Press ("Cambridge University Press") consists of your license details and the terms and conditions provided by Cambridge University Press and Copyright Clearance Center.

License Number	4624410132054
License date	Jul 08, 2019
Licensed Content Publisher	Cambridge University Press
Licensed Content Publication	The Journal of Fluid Mechanics
Licensed Content Title	The aeroacoustics of finite wall-mounted square cylinders
Licensed Content Author	Ric Porteous, Danielle J. Moreau, Con J. Doolan
Licensed Content Date	Oct 26, 2017
Licensed Content Volume	832
Licensed Content Issue	undefined
Start page	287
End page	328
Type of Use	Dissertation/Thesis
Requestor type	Author
Portion	Text extract
Number of pages requested	3
Author of this Cambridge University Press article	No
Author / editor of the new work	Yes
Order reference number	
Territory for reuse	World
Title of your thesis / dissertation	Experimental Investigation of the Free-end Pressure Distribution for Surface-Mounted Finite-Height Square Prisms
Expected completion date	Oct 2019
Estimated size(pages)	250
Requestor Location	University of Saskatchewan 57 Campus Drive  Saskatoon, SK S7N5A9 Canada Attn: University of Saskatchewan
Publisher Tax ID	123258667RT0001
Total	0.00 CAD